π-Conjugated Pyrenoimidazole Derivatives: Synthesis, Spectroscopic and Crystallographic Studies

by

A thesis submitted to the School of Graduate Studies in partial fulfilment of the requirements for the degree of

Ph.D.

Department of Chemistry

Memorial University of Newfoundland

July 2020

St. John's Newfoundland

Abstract

This PhD thesis was aimed at the design and synthesis of new functional phenyl-pyrenoimidazole derivatives and the development of these compounds as novel chromophores/fluorophores and supramolecular synthons for organic crystal engineering. An efficient and modular one-pot condensation reaction between 4,5-pyrenedione and various benzaldehydes in presence of ammonium acetate and acetic acid was used to prepare all the new phenyl-pyrenoimidazoles investigated in this thesis work. There are three major projects accomplished in this thesis. The first project investigated the properties of two new benzaldehyde-substituted pyrenoimidazoles, in which the electron-withdrawing formyl group is attached to the *para* and *meta* position of the phenyl group. These two isomers were characterized by various spectroscopic, X-ray single crystallographic analyses, in conjunction with density functional theory (DFT) calculations. The interactions of these two new compound with fluoride anions through hydrogen bonds were examined as well, and the results demonstrated the applicability of the *para*-benzaldehyde substituted pyrenoimidazole as an efficient ratiometric fluorescence probe for fluoride anion. In the second project, a series of phenyl-pyrenoimidazole substituted with various organic functional groups (including CH_3, Cl, Br, OCH_3, CHO, and NO_2) were synthesized and their structure photophysical property relationships were subsequently studied by UV-Vis absorption and fluorescence spectroscopy. X-ray crystallographic and molecular electrostatic potential (MEP) analyses were undertaken to disclose the interplay of various non-covalent forces that govern the crystal packing of these pyrenoimidazole molecules. The results indicated that the

substituent group is an important factor controlling the crystal structural properties, which attests to the possibility of using various phenylpyrenoimidazole derivatives as tunable supramolecular synthons for crystal engineering. In the third project, hydroxyl and alkoxyl-substituted phenyl-pyrenoimidazole derivatives were prepared and investigated for comparative studies of the effects of hydrogen bonding and $\pi - \pi$ interactions on their crystallization behaviors. To construct different organic crystals, various aromatic carboxylic acids were used with these pyrenoimidazoles. The resulting crystal structures were analyzed by X-ray crystallography to show the formation of different supramolecular network structures in the solid state. Based on the crystallographic data obtained, Hirshfeld surface analysis and quantum theory of atoms in molecules (QTAIM) calculations were carried out to quantitatively interpret and comprehensively visualize the various intermolecular forces, such as hydrogen bonding, $\pi - \pi$, C–H$\cdots\pi$, and H$\cdots$H interactions, in the pyrenoimidazole crystals and co-crystals.

Acknowledgements

First and foremost, I would like to express my sincere gratitude to my supportive supervisor, Prof. Yuming Zhao for his valuable guidance with excellence patience throughout my PhD research studies and thesis writing. I truly admire and am influenced by his motivation, enthusiasm, immense knowledge, and attention to details for all things in chemistry. I would like to thank my co-supervisor Prof. David W. Thompson for his wonderful advice and support. I would also like to acknowledge my supervisory committee member, Prof. Sunil Pansare for his insightful comments and helpful suggestion during committee meetings and critical reading and review of this dissertation. Sincere thanks to Dr. Jian-Bin Lin of Memorial University and Dr. Michael Ferguson of University of Alberta for analyzing and solving all the single crystal structures discussed in this thesis. I would also like to thank our collaborators, Prof. Graham Bodwell and his PhD student Joshua C. Walsh, for their generous supply of pyrene-4,5-dione to my synthetic studies and their valuable contribution to publishing our research results. I would also like to acknowledge Prof. Eyad A. Younes at University of Jordan for his assistance in density functional theory (DFT) calculations and his kind help for the experimental part of my first project. I would also like to thank all of the current and former members of the Zhao Group for their help and support during my study, especially to Dr. Mohammadreza Khadem for his assistance and insightful discussions. I would also like to extend my gratitude to all my labmates, their support and co-operation. I would also like to appreciate my mother and my brothers and sisters for their unfailing love and charitable consolation all through life. My special gratitude goes to my mother-in-law and my brothers-in-

law for their encouragement, and I wish them all lifelong health and happiness. Most importantly, I would like to express my deepest gratitude to my husband Masoud who has been consistently supportive to me during my study. Last but not the least, a tremendous gratitude to the MUN organic division, all the staff and faculty at Chemistry Department, C-CART members of the chemistry department, School of Graduate Studies (SGS) for the financial support and to Memorial University for creating such a great educational and friendly environment for students.

Contents

Abstract **ii**

Acknowledgements **iv**

List of Figures **xi**

List of Schemes **xxiv**

List of Abbreviations and Symbols **xxvi**

1 Introduction **1**

1.1 Concepts of Photoluminescence 1

1.1.1 History of Fluorescence 2

1.1.2 Fluorophores 3

1.1.3 Jablonski Diagram 4

1.1.4 The Stokes Shift and Mirror-Image Rule 6

1.1.5 Exceptions to the Mirror-Image Rule 7

1.1.6 Quantum Yield 8

1.1.7 Franck-Condon Principle 9

1.2 Pyrene and Pyrene Derivatives 9
1.2.1 Excimers and Exciplexes 11
1.2.2 Functionalization of Pyrene 12
1.2.3 *K*-region Oxidation of Pyrene 14
1.3 Imidazoles 16
1.3.1 Structures and Properties of Imidazoles 18
1.3.2 General Synthetic Methods for Preparation of Imidazoles . . . 19
1.4 Chemosensors Based on Pyrene and Imidazole 24
1.4.1 General Principles of Chemosensors 24
1.4.2 Recent Progress in Pyrene and Imidazole-Based Chemosensors 25
1.5 Recent Development of Pyrenoimidazoles as Functional Organic Fluorophores 31
1.6 Objectives of This Thesis Work 39

2 Pyrenoimidazolyl-Benzaldehyde Fluorophores: Synthesis, Properties, and Sensing Function for Fluoride Anions 42

2.1 Introduction 43
2.2 Results and Discussion 46
2.2.1 Synthesis of Pyrenoimidazolyl-Benzaldehyde (PI-BAL) Isomers **4** and **5** 46
2.2.2 Solid-State Structural Properties 47
2.2.3 Solvent Effects on UV-Vis Absorption and Fluorescence Properties 50
2.2.4 Electrochemical Redox Properties 53

2.2.5 Interactions with the Fluoride Ion 55
2.2.6 Theoretical Modelling Studies 63
2.3 Conclusions 67
2.4 Experimental Section 68

3 Crystal Engineering and Photophysical Properties of Phenyl-Pyrenoimidazole Systems 72

3.1 Introduction 73
3.2 Methodology 75
3.2.1 Materials 75
3.2.2 Characterizations 75
3.2.3 Computational Methods 76
3.3 Results and Discussion 77
3.3.1 Synthesis of Py-Im Derivatives 77
3.3.2 Single Crystal X-Ray Structural Analysis 77
3.3.2.1 Linear hydrogen bonded imidazole networks 78
3.3.2.2 Helical hydrogen bonded imidazole–alcohol networks 81
3.3.2.3 π-π Stacking dominated packing 84
3.3.2.4 Hydrogen bonded Py-Im dimers 86
3.3.3 Molecular Electrostatic Potentials and Correlation with Crystal Packing Properties 89
3.3.4 Substitution Effects on Photophysical Properties 92
3.3.5 Substitution Effects on Imidazolyl Deprotonation 94
3.4 Conclusions 107

4 Designed Synthesis and Crystallization of Pyrenoimidazole-based Supramolecular Synthons 108

4.1 Introduction 109

4.2 Experimental 112

4.2.1 Synthesis and Characterization 112

4.2.2 Crystallization Conditions and X-ray Crystallographic Analysis 114

4.3 Results and Discussion 115

4.3.1 Crystallization Behavior of Pyrenoimidazoles **1**–**3** 115

4.3.2 Co-crystallization of Pyrenoimidazole **4** with Aromatic Carboxylic Acids 122

4.4 Conclusions 129

5 Hirshfeld Surfaces Analysis of Pyrenoimidazole Crystal Structures 131

5.1 Introduction to Hirshfeld Surfaces Analysis 132

5.1.1 Surface Properties 134

5.1.2 Properties Encoded on the Hirshfeld Surface 135

5.1.3 Two-Dimensional Fingerprint Plots 136

5.2 Hirshfeld Surface Analysis of Pyrenoimidazole Crystals 139

5.2.1 Phenyl-Substituted Pyrenoimidazole 139

5.2.2 Tolyl-Substituted Pyrenoimidazole 140

5.2.3 *p*-Methoxyphenyl-Substituted Pyrenoimidazole 143

5.2.4 *p*-Chlorophenyl-Substituted Pyrenoimidazole 145

5.2.5 *p*-Nitrophenyl-Substituted Pyrenoimidazole 147

5.2.6 *p*-Formylphenyl-Substituted Pyrenoimidazole 157

5.2.7 *p*-Hydroxyphenyl-Substituted Pyrenoimidazole 159

5.2.8 *p*-Decyloxyphenyl-Substituted Pyrenoimidazole 161

5.2.9 *N*-decyl-*p*-decyloxyphenyl-Substituted Pyrenoimidazole 164

5.3 On the Close H···H Contacts Observed in the Crystal Structures of Pyrenoimidazoles 166

5.4 Conclusions 175

6 Conclusions and Future Work **177**

Bibliography **182**

List of Figures

1.1 Photographic image of a *Lignum nephriticum* cup made from the wood of the narra tree (*Pterocarpus indicus*), and a flask containing its fluorescent solution. 2

1.2 Exemplar applications of fluorescence. 3

1.3 Jablonski diagram illustrating the processes of photoexcitation and various deactivation pathways. 5

1.4 Experimental set up to observe energy differences between absorption and emission devised by G. G. Stokes. 7

1.5 Schematic illustration of the Franck-Condon principle. 10

1.6 Common substitution patterns of pyrene. 13

1.7 Structure of pyrene with K-region and non K-region labelled. 14

1.8 X-ray structure of a linear supramolecular assembly of imidazoles through intermolecular H-bonding interactions. CCDC 136337. 19

1.9 (A) Synthesis of pyrene-imidazole chemosensor **1-46** via reductive amination. (B) Formation of 1:1 complex of **1-46/SA** with salicylic acid through H-bonding and $\pi - \pi$ interactions. 27

1.10 Mechanochromic properties of pyrenoimidazole derivatives **1-64** and **1-66**. 33

1.11 Schematic illustration of the complementary $\pi - \pi$ stacking of pyrene and imidazole moieties in the crystal structure of **1-69**. 35

1.12 Molecular structures of pyrenoimidazole-based dye **1-76** and squaraine dye **1-77**. 37

1.13 Synthesis of two pyrenoimidazole-based isomers **1-80** and **1-81**. . . . 38

1.14 Concepts of developing D/A-substituted phenyl-pyrenoimidazole (**Ph-PyIm**) derivatives and aims of property studies. 39

2.1 Proposed intramolecular charge transfer (ICT) occurring upon hydrogen bonding interactions between an anion (A^-) and 10-phenyl-PI bearing an electron-withdrawing group (EWG). 46

2.2 (A) ORTEP plot (50% probability) of the hydrogen-bonded dimer of PI-BAL **4** (CCDC 1851836). (B) Solid-state packing diagram of **4**. The parallelogram highlights a hydrogen bonded dimer viewed from its side.(C) ORTEP plot (50% probability) of PI-BAL **5** co-crystallized with DMSO (CCDC 1851835). (D) Solid-state packing diagram of **5**. 48

2.3 (A) Normalized UV-Vis absorption and (B) fluorescence emission spectra of **4** measured in various solvents. (C) Normalized UV-Vis absorption and (D) fluorescence emission spectra of **5** measured in various solvents. 52

2.4 Cyclic voltammograms of PI-BAL **4** measured in (A) acetone and (B) DMSO, and PI-BAL **5** measured in (C) acetone and (D) DMSO. Experimental conditions: electrolyte: Bu_4NBF_4 (0.1 M), working electrode: glassy carbon, counter electrode: Pt wire, reference electrode: Ag/AgCl, scan rate: 100 mV/s. 54

2.5 ^{1}H NMR (300 MHz) spectra monitoring the titration of PI-BAL **4** with TBAF in acetone-d_6. 57

2.6 Titration of PI-BAL **4** with TBAF monitored by UV-Vis absorption spectroscopy in (A) acetone and (B) DMSO, fluorescence spectroscopy in (C) acetone and (D) DMSO. 58

2.7 Plots of the ratio of fluorescence intensities of PI-BAL **4** at two different wavelengths against the concentration of TBAF. (A) Fluorescence intensities at 507 nm and 561 nm (F_{507}/F_{561}) in acetone, (B) fluorescence intensities at 530 nm and 585 nm (F_{530}/F_{585}) in DMSO. Solid lines are the linear least squares fitting for data points in selected ranges and associated R^2 values are indicated. 60

2.8 ^{1}H NMR (300 MHz) spectra monitoring the titration of PI-BAL **5** with TBAF in acetone-d_6. 62

2.9 Titration of PI-BAL **5** with TBAF monitored by UV-Vis absorption spectroscopy in (A) acetone and (B) DMSO, fluorescence spectroscopy in (C) acetone and (D) DMSO. 63

2.10 Contour plots (isovalue = 0.02 e/Å^3) and eigenvalues of frontier molecular orbitals (FMOs) for PI-BALs **4** and **5** calculated at the B3LYP/6-31++G(d,p) level of theory in the gas phase. 64

2.11 Optimized geometries of the 1:1 complexes of (A) [**4**$\cdots F^-$] and (B) [**5**$\cdots F^-$] in the gas phase at the B3LYP/6-31++G(d,p) level of theory, and variation of hydrogen bond distances in different solvents calculated by the PCM solvent model. 66

3.1 Molecular structures of **Phen-Im** and **Py-Im**. 73

3.2 (A) ORTEP diagram of compound **3a** (50% ellipsoid probability). (B) Packing of **3a** molecules in the unit cell viewed along the *c* axis. (C) Linear network of **3a** molecules assembled via imidazolyl hydrogen bonds. CCDC 1851837. 79

3.3 (A) ORTEP diagram of compound **3b** co-crystalized with acetone (50% ellipsoid probability). (B) Packing of **3b** molecules in the unit cell viewed along the *b* axis. (C) Linear network of **3b** molecules assembled via hydrogen bonds. CCDC 1851835. 80

3.4 (A) ORTEP diagram of compound **3e** co-crystalized with methanol (50% ellipsoid probability, hydrogen bonds highlighted in Å). (B) Hydrogen bonds that interconnect the molecules of **3e** and methanol in the crystal structure (only the imidazolyl groups are shown for clarity and hydrogen bond distances are highlighted in Å.) (C) Packing of **3e** and methanol molecules in the unit cell viewed along the *c* axis. (D) Helical networks of **3e** and methanol molecules assembled via hydrogen bonding interactions (top: left-handed, bottom: right-handed). CCDC 1917379. 82

3.5 (A) ORTEP diagram of compound **3h** co-crystalized with *R*-(+)-1-phenylethanol (50% ellipsoid probability, hydrogen bonds highlighted in Å). (B) Solid-state assemblies of **3h** and *R*-(+)-1-phenylethanol molecules forming helical networks with a *P* helicity. CCDC 1957897. 83

3.6 (A) ORTEP diagram of compound **3c** co-crystallized with acetone (50% ellipsoid probability, hydrogen bonds highlighted in Å). (B) Packing of **3c** and acetone molecules in the unit cell viewed along the *c* axis. (C) Top view of the π-stacked assembly of [**3c**$\cdots$acetone] in crystal. (D) Crystal packing diagram of **3c** and acetone molecules. CCDC 1917380. 85

3.7 (A) ORTEP diagram of compound **3f** co-crystalized with two molecules of DMSO (50% ellipsoid probability, hydrogen bonds highlighted in Å). (B) Packing of **3f** and DMSO molecules in the unit cell. (C) Top view of the π-stacked assembly of [**3f**$\cdots$(DMSO)$_2$] in crystal. (D) Crystal packing diagrams of **3f** and DMSO molecules. CCDC 1851838. . . . 86

3.8 (A) ORTEP diagram of a hydrogen bonded dimer of compound **3g** (50% ellipsoid probability, hydrogen bonds highlighted in Å). (B) Packing of **3g** molecules in the unit cell viewed along the *b* axis. (C) and (D) Crystal packing diagram of **3g** viewed from different perspectives. CCDC 1851836. 88

3.9 (A) ORTEP diagram of a hydrogen bonded dimer of compound **3h** co-crystalized with acetone (50% ellipsoid probability, hydrogen bonds highlighted in Å). (B) Packing of **3h** molecules in the unit cell viewed along the *b* axis. (C) Crystal packing diagram of **3h**. CCDC 1917378. 99

3.10 MEP maps for **Py-Im** derivatives **3a**–**c**, **3e**–**h**, and relevant solvent molecules on the 0.002 au isodensity surface. Maximum potential energy values on the molecular edges are highlighted in $kJ \cdot mol^{-1}$. . . . 100

3.11 Correlations of the maximum electrostatic potentials of on the isodensity surface (0.002 au) with Hammett substituent constants. (A) At the imidazolyl N–H position, and (B) at the imidazolyl N=C position. 101

3.12 Normalized (A) UV-Vis absorption and (B) fluorescence spectra of **Py-Im** derivatives **3a**–**h** measured in acetone at room temperature. . 102

3.13 Photographic images of crystals of **Py-Im 3h** slowly grown in different solvent systems at room temperature. (A) EtOAc/acetone/hexanes (1:5:94), (B) DMSO/acetone/hexanes (1:5:94), (C) acetone/hexanes (5:95), (D) CH_3OH/acetone/hexanes (3:5:92), (E) Et_2O/acetone/hexanes (5:5:90), and (F) acetone/hexanes (5:95). . . . 103

3.14 (A) ORTEP diagram of compound **3h** co-crystalized with water molecules (50% ellipsoid probability, hydrogen bonds highlighted in Å). (B) Hydrogen bonded networks of **3h** and water molecules in the crystal structure of **3h-II**. (C) π-Stacking motif of **3h-II** in the crystal structure. CCDC 1957899. 104

3.15 Expanded ^1H NMR (300 MHz) spectra of (A) crystals of **3h-II** dissolved in acetone-d_6, (B) crystals of **3h-I** dissolved in acetone-d_6, and (C) crystals of **3h-I** dissolved in acetone-d_6 after addition of 5.6 equiv of CD_3OD. 105

3.16 (A) UV-Vis absorption and (B) fluorescence spectra monitoring the titration of **3a** (56.5 μM) with TBAF (0–20.0 molar equiv) in acetone. (C) Hydrogen bonding interactions of **3a** and fluoride anion and subsequent deprotonation reaction. 105

3.17 Contours (isovalue = 0.03 au) and eigenvalues (in eV) of FMOs of **3a** (left) and deprotonated **3a** anion (right) calculated at TD-B3LYP/6-311+G(d,p) level. 106

4.1 Supramolecular synthons investigated in this work. 110

4.2 (A) ORTEP drawing of molecules of **1** and methanol packed in the unit cell (30% ellipsoid probability, hydrogen bonds highlighted in Å). (B) ORTEP drawing of **1** and methanol molecules in the unit cell viewed along the *c*-axis. (C) Packing diagram of **1** and methanol molecules. (D) Alignment of **1** and methanol molecules showing the π–stacking motif (interplanar distance highlighted in Å). CCDC 1949991. 116

4.3 Hydrogen bonds among **1** and methanol molecules in the crystal structure. The pyrenyl group of **1** is hidden for clarity and the hydrogen bond distances are highlighted in Å. 117

4.4 (A) ORTEP drawing of molecules of **2** and water packed in the unit cell (30% ellipsoid probability, hydrogen bonds highlighted in Å). (B) Packing diagram of **2** and water molecules, with a complementary molecular pair of **2** in the unit cell highlighted by space filling model. (C) Alignment of two adjacent molecules of **2** showing C-H$\cdots\pi$ interactions. (D) Hydrogen bonds among **2** and water molecules in the crystal structure. The pyrenyl group of **2** is hidden for clarity and the hydrogen bond distances are highlighted in Å. CCDC 1972848. . . 119

4.5 (A) ORTEP drawing of molecules of **3** packed in the unit cell (30% ellipsoid probability). (B) Packing diagram of **3** where molecules are colored by symmetry operation (hydrogen atoms are hidden for clarity). (C) Alignment of two adjacent molecules of **3** showing C-H$\cdots\pi$ interactions (distances highlighted in Å). (D) Top view of a pair of **3** showing the geometry of pyrenoimidazole π-stacking (hydrogen atoms omitted). CCDC 1972837. 120

4.6 Proposed hydrogen-bonded assemblies between imidazolium and carboxylate ions. (A) Hydrogen bonding polymer, and (B) hydrogen-bonded "double-decker" assembly. 121

4.7 (A) Packing diagram of the co-crystal of **4** and benzoic acid (hydrogen atoms are hidden for clarity). (B) Hydrogen-bonded "double-decker" assemblies of **4** and benzoic acid molecules in the crystal structure (hydrogen bonds highlighted in Å). (C) Side view of the hydrogen-bonded "double-decker" assemblies of **4** and benzoic acid molecules, with interplanar distances (in Å) and tilt angle highlighted. CCDC 1972771. 123

4.8 (A) ORTEP drawing of two molecules of **4** in the unit cell (30% probability, close intermolecular contacts highlighted in Å, CCDC 1981368). (B) π–Stacking motif of compound **4** showing anti-parallel orientation between adjacent molecules. (C) Side view of π–stacking of **4** with interplanar distance (in Å) and angle highlighted. (D) Topology of a dimeric assembly of **4**/acetone reported in our previous paper. . 125

4.9 (A) Packing diagram of the co-crystal of **4**, trimesic acid, water, and acetone (hydrogen atoms molecules colored by operation symmetry). (B) Hydrogen bonds among **4**, trimesic acid, water, and acetone (distances highlighted in Å). (C) Hydrogen-bonded "double-decker" assemblies of **4** and trimesic acid molecules in the crystal structure (hydrogen bonds highlighted in Å). CCDC 1972772. 128

4.10 (A) Topology of hydrogen-bonded trimesic acid–imidazole frameworks, and (B) arrangement of solvent molecules in the co-crystal of **4**, trimesic acid, water, and acetone (highlighted by space filling model and colored by symmetry operation). 129

5.1 Hirshfeld surfaces of pyrene-4,5-dione. 135

5.2 (A) Hirshfeld surface mapping the O···H contacts in the crystal of pyrene-4,5-dione. (B) Fingerprint plot with the O···H contacts of pyrene-4,5-dione highlighted. 137

5.3 (A) Molecular structure of phenyl-pyrenoimidazole. (B) Hirshfeld surface mapped with d_{norm}. (C) Hirshfeld surface mapped with shape index. (D) Fingerprint plots with different intermolecular contacts highlighted. 141

5.4 (A) Molecular structure of tolyl-pyrenoimidazole. (B) Hirshfeld surface mapped with d_{norm}. (C) Hirshfeld surface mapped with shape index. (D) Fingerprint plots with different intermolecular contacts highlighted. 142

5.5 (A) Molecular structure of *p*-methoxyphenyl-pyrenoimidazole. (B) Hirshfeld surface mapped with d_{norm}. (C) Hirshfeld surface mapped with shape index. (D) Fingerprint plots with different intermolecular contacts highlighted. 144

5.6 (A) Molecular structure of *p*-chlorophenyl-pyrenoimidazole. (B) Hirshfeld surface mapped with d_{norm}. (C) Hirshfeld surface mapped with shape index. (D) Fingerprint plots with different intermolecular contacts highlighted. 146

5.7 (A) Molecular structure of *p*-nitrophenyl-pyrenoimidazole (co-crystallized with acetone). (B) Hirshfeld surface mapped with d_{norm}. (C) Hirshfeld surface mapped with shape index. (D) Fingerprint plots with different intermolecular contacts highlighted. 148

5.8 (A) Molecular structure of *p*-nitrophenyl-pyrenoimidazole (co-crystallized with water). (B) Hirshfeld surface mapped with d_{norm}. (C) Hirshfeld surface mapped with shape index. (D) Fingerprint plots with different intermolecular contacts highlighted. 150

5.9 (A) Molecular structure of *p*-nitrophenyl-pyrenoimidazole (co-crystallized with benzoic acid). (B) Hirshfeld surface mapped with d_{norm}. (C) Hirshfeld surface mapped with shape index. (D) Fingerprint plots with different intermolecular contacts highlighted. 152

5.10 (A) Molecular structure of *p*-nitrophenyl-pyrenoimidazole (co-crystallized with trimesic acid). (B) Hirshfeld surface mapped with d_{norm}. (C) Hirshfeld surface mapped with shape index. (D) Fingerprint plots with different intermolecular contacts highlighted. 155

5.11 (A) Molecular structure of *p*-nitrophenyl-pyrenoimidazole (without solvents). (B) Hirshfeld surface mapped with d_{norm}. (C) Hirshfeld surface mapped with shape index. (D) Fingerprint plots with different intermolecular contacts highlighted. 156

5.12 (A) Molecular structure of *p*-nitrophenyl-pyrenoimidazole. (B) Hirshfeld surface mapped with d_{norm}. (C) Hirshfeld surface mapped with shape index. (D) Fingerprint plots with different intermolecular contacts highlighted. 158

5.13 (A) Molecular structure of *p*-hydroxyphenyl-pyrenoimidazole. (B) Hirshfeld surface mapped with d_{norm}. (C) Hirshfeld surface mapped with shape index. (D) Fingerprint plots with different intermolecular contacts highlighted. 160

5.14 (A) Molecular structure of *p*-decyloxyphenyl-pyrenoimidazole. (B) Hirshfeld surface mapped with d_{norm}. (C) Hirshfeld surface mapped with shape index. (D) Fingerprint plots with different intermolecular contacts highlighted. 163

5.15 (A) Molecular structure of *p*-decyloxyphenyl-pyrenoimidazole. (B) Hirshfeld surface mapped with d_{norm}. (C) Hirshfeld surface mapped with shape index. (D) Fingerprint plots with different intermolecular contacts highlighted. 165

5.16 Examples of dihydrogen bonding. 167

5.17 Molecular graph of the dimer of *p*-chlorophenyl-substituted pyrenoimidazole obtained from QTAIM analysis. The closest intermolecular H$\cdots$H is highlighted by a oblong red shade, and related characteristics are indicated. 169

5.18 Molecular graph of the dimer of *p*-nitrophenyl-substituted pyrenoimidazole (co-crystallized with acetone) obtained from QTAIM analysis. The closest intermolecular H$\cdots$H is highlighted by a oblong red shade, and related characteristics are indicated. 170

5.19 Molecular graph of the dimer of *p*-nitrophenyl-substituted pyrenoimidazole (without solvents) obtained from QTAIM analysis. The closest intermolecular H$\cdots$H is highlighted by a oblong red shade, and related characteristics are indicated. 171

5.20 Molecular graph of the dimer of didecyl-substituted pyrenoimidazole obtained from QTAIM analysis. The closest intermolecular H$\cdots$H contacts are highlighted by oblong red and blue shades, respectively. Related characteristics are indicated. 173

5.21 Molecular graph of the dimer of *p*-formylphenyl-substituted pyrenoimidazole obtained from QTAIM analysis. The closest intermolecular H$\cdots$H is highlighted by a oblong red shade, and related characteristics are indicated. 174

5.22 (A) NCI isosurfaces and (B) 2-D plot of RDG versus sign(λ_2)$\times\rho$ of the dimer of *p*-formylphenyl-substituted pyrenoimidazole. 176

6.1 A targeted pyrenoimidazole macrocycle in the future work. 179

List of Schemes

1.1 Dewar localization energies of various positions in pyrene and phenanthrene and their direct oxidation reactions. 15

1.2 Synthesis of 4,5-pyrenedione through direct oxidation methods. 17

1.3 Imidazole and common imidazole derivatives. 17

1.4 Resonance scheme of imidazole. 18

1.5 General synthetic methods for imidazole derivatives. 20

1.6 General scheme of the Debus-Radziszewski synthesis. 21

1.7 Reaction mechanism for the Debus-Radziszewski synthesis. 22

1.8 Microwave-assisted synthesis of imidazole derivatives. 23

1.9 Solid-state synthesis imidazole derivatives with the assistance of grinding. 23

1.10 Py-BiimzH_2 as a ratiometric fluorescent sensor for cyanide anion. . . 26

1.11 (A) Synthesis of a pyrene-naphthalene derivative **1-48** through Schiff base condensation. (B) Proposed binding mode of **1-48** with histidine and plausible fluorescence turn-on sensing mechanism for histidine. . 28

1.12 (A) Synthesis of anthracene/pyrene-benzimidazole hybrids **1-52** and **1-53** through a one-step condensation reaction. (B) Transformation of **1-52** and **1-53** into corresponding Schiff bases and complexation with Al^{3+} ion. 29

1.13 Synthesis of pyrene-substituted benzoimidazopyrimidine derivatives through Biginelli condensation. 30

1.14 Synthesis of a pyrene-benzimidazole derivative through condensation reaction. 31

1.15 Synthesis of pyrenoimidazoles with AIEE and mechanochromic properties. 32

1.16 Synthetic routes for (A) benzene **1-69** and (B) oligothiophene-centered **1-73** bispyrenoimidazole derivatives with double *n*-dodecyl chains. . . 34

1.17 Synthesis of sterically hindered pyrenoimidazole and phenanthroimidazole derivatives as deep blue light emitters. 36

2.1 Synthesis of PI-BALs **4** and **5**. 47

2.2 Gibbs free energy changes for the interactions of **4** and **5** with fluoride ion in the gas phase and various solvents.Calculated at the B3LYP/6-31++G(d,p) with the PCM model used for solvents. 67

3.1 Synthesis of substituted **Py-Im** derivatives **3a**–**h** via condensation reactions. 78

List of Abbreviations and Symbols

A^-	anion
Ω	asphericity
ACQ	aggregation-caused quenching
AIEE	aggregation-induced emission enhancement
APPI	atmospheric pressure photo ionization
aq	aqueous
BCP	bond critical point
calcd	calculated
CSD	Cambridge Structural Database
cm	centimeter(s)
C-T	charge-transfer
ca.	circa
J	coupling constant

CV	cyclic voltammetry
D	Debye
DFT	density functional theory
DSC	differential scanning calorimetry
D/A	donor/acceptor
d	doublet
decomp	decomposition
BCP	bond critical point(s)
COF	covalent organic framework
J	coupling constant
DSSCs	dye-sensitized solar cells
eV	electron volt
EWG	electron-withdrawing group
Et	ethyl
M*	excited molecule
S_1	first excited state
FMOs	frontier molecular orbitals

Tg	glass transition temperature
G	globularity
g	gram(s)
S_0	ground state
σ	Hammett substituent constant
h	hour(s)
HOMO	highest occupied molecular orbital
HRMS	high-resolution mass spectrometry
Hz	hertz
IPCE	incident photon-to-current efficiency
IR	infrared
ICT	intramolecular charge transfer
ISC	intersystem crossing
LUMO	lowest unoccupied molecular orbital
OFETs	organic field effect transistors
OLEDs	organic light emitting devices
OPVs	organic photovoltaics

m/z	mass-to-charge ratio
MW	microwave
MALDI-TOF	matrix-assisted laser desorption/ionization-time of flight
Me	methyl
mg	milligram(s)
MHz	megahertz
min	minute(s)
mL	milliliter(s)
mmol	millimole(s)
mM	milimolar
M	molar
mol	mole(s)
m.p.	melting point
MS	mass spectrometry
mV	millivolt(s)
mW	milliwatt(s)
MEP	Molecular electrostatic potential

m	multiplet
nm	nanometer(s)
NMI	*N*-methylimidazole
NIPMAT	non-bonded interaction pattern matrix
NMR	nuclear magnetic resonance
PAH	polycyclic aromatic hydrocarbon
PCM	polarizable continuum model
ppm	parts per million
Ph-PyIm	phenyl-pyrenoimidazole
PET	photoinduced electron transfer
PTI	Photon Technology International
PXRD	powder X-ray diffraction
PI	pyrenoimidazole
PI-BAL	pyrenoimidazolyl-benzaldehyde
ϕ	quantum yield
QTAIM	quantum theory of atoms in molecules
TBAF	tetrabutylammonium fluoride

TGA	thermogravimetric analysis
TD-DFT	time-dependent density functional theory
T_1	triplet state
THF	tetrahydrofuran
TLC	thin-layer chromatography
UV	ultraviolet
UV-Vis	ultraviolet-visible
vdW	van der Waals
Vis	visible
V	volt(s)
XRD	X-ray diffraction
ΔG°	Gibbs free energy
δ	chemical shift
λ_{max}	maximum absorption wavelength

Chapter 1

Introduction

1.1 Concepts of Photoluminescence

For decades, fluorescence spectroscopy has been a very useful analytical tool in the fields of chemistry, biochemistry, and biophysics, owing to its high sensitivity and efficiency in detecting various organic/inorganic compounds and bio-materials. Emission of light from bodies at heated temperature is called incandescence, while luminescence is a name for all other forms of light emission. The term luminescence comes from a Latin root (*lumen* means light). It was first introduced by the German physicist and science historian, Eilhard Wiedemann, in 1888 for all phenomena of light emission other than incandescence.[1] Presently, luminescence is defined as a spontaneous emission of radiation from an electronically excited species or from a vibrationally excited species. Generation of luminescence through excitation of a molecule by ultraviolet (UV) or visible (Vis) light is a phenomenon termed photoluminescence, which is known as a "cold light". Photoluminescence can

be divided into fluorescence and phosphorescence, depending on the electronic configuration of the excited state and the emission pathway.[2]

1.1.1 History of Fluorescence

As early as 1565, Spanish physician Nicolás Monardes reported the peculiar blue color from the infusion of a wood known as *Lignum nephriticum* (Latin for "kidney wood", see Figure 1.1).[3] The chemical compound responsible for this intense blue fluorescence was later identified as *matlaline* (the Aztec word for blue), which is the oxidation product of the flavonoids found in this wood.[4]

(Cited from Fluorescence of supermolecules, polymers, and nanosystems, **2007**)
Figure 1.1: Photographic image of a *Lignum nephriticum* cup made from the wood of the narra tree (*Pterocarpus indicus*), and a flask containing its fluorescent solution.

In 1845 Fredrick W. Herschel discovered that UV light can excite a quinine solution (*e.g.*, tonic water) to emit blue light.[2,4] In 1852, George Gabriel Stokes further studied this discovery, and described the ability of fluorspar and uranium glass to change invisible light beyond the violet end of the visible spectrum into blue light. He

described this phenomenon of fluorescence as follows: "*I am almost inclined to coin a word, and call the appearance fluorescence, from fluor-spar [i.e., fluorite]*". In a key experiment he used a prism to isolate UV radiation from sunlight and observed blue light emitted by an ethanol solution of quinine exposed by it.[5,6]

Fluorescence has many practical applications, including mineralogy,[7] gemology,[8] medicine,[9] chemical sensors (fluorescence spectroscopy), fluorescent labelling,[10] dyes,[11] biological detectors,[12] cosmic-ray detection,[13] and most commonly fluorescent lamps (examples in figure 1.2).[14] Fluorescence also occurs frequently in nature in some minerals and in various biological states.[2]

Figure 1.2: Exemplar applications of fluorescence.

1.1.2 Fluorophores

A fluorophore can be intrinsic or extrinsic. Intrinsic fluorophores (*e.g.*, chlorophyll) are molecules with natural fluorescence properties. Extrinsic fluorophores are molecules labelled with a fluorescence dye, and they are added to the sample to induce or to change the spectral properties of the sample. An organic fluorophore is a fluorescent organic compound that can interact with light to yield re-emission of absorbed light energy at a specific wavelength(s). The magnitude of emitted energy and wavelength is related to both molecular components and chemical

environments.[15]

Typical organic fluorophores are polycyclic aromatic compounds with a conjugated π-electron system. As early as 1877, the fluorescence of fluorescein was utilized to demonstrate the connection of the rivers Danube and Rhine by underground streams. The well-known organic fluorophore, quinine, was used for the first spectrofluorometer devised in the 1950s. The emission of anthracene and perylene fluorophores can be used for environmental monitoring of oil pollution. Pyridine and rhodamine are frequently used in dye lasers.[16]

1.1.3 Jablonski Diagram

Jablonski diagram is a diagram for illustrating the processes of absorption and emission of light by molecules (Figure 1.3). It was named after Professor Alexander Jablonski, who is regarded as the father of fluorescence spectroscopy because of his many achievements in the studies of fluorescence of solutions.[17,18] Photoexcitation involving direct transitions from the ground state (S_0) to other singlet electronically-excited states (S_1, S_2, etc.) occurs within femtoseconds without changes in the positions nuclei in the molecule according to the Franck-Condon principle (1.1.7).[19] They are therefore called vertical transitions and can be represented by vertical lines in the Jablonski diagram.

Following light absorption, the fluorophore rapidly relaxes to the lowest vibrational level of the first excited state (S_1) by the process of internal conversion (IC) which is the radiationless transition between energy states of the same spin stat. Returning to the ground state (S_0) typically arrives at higher excited vibrational levels in the

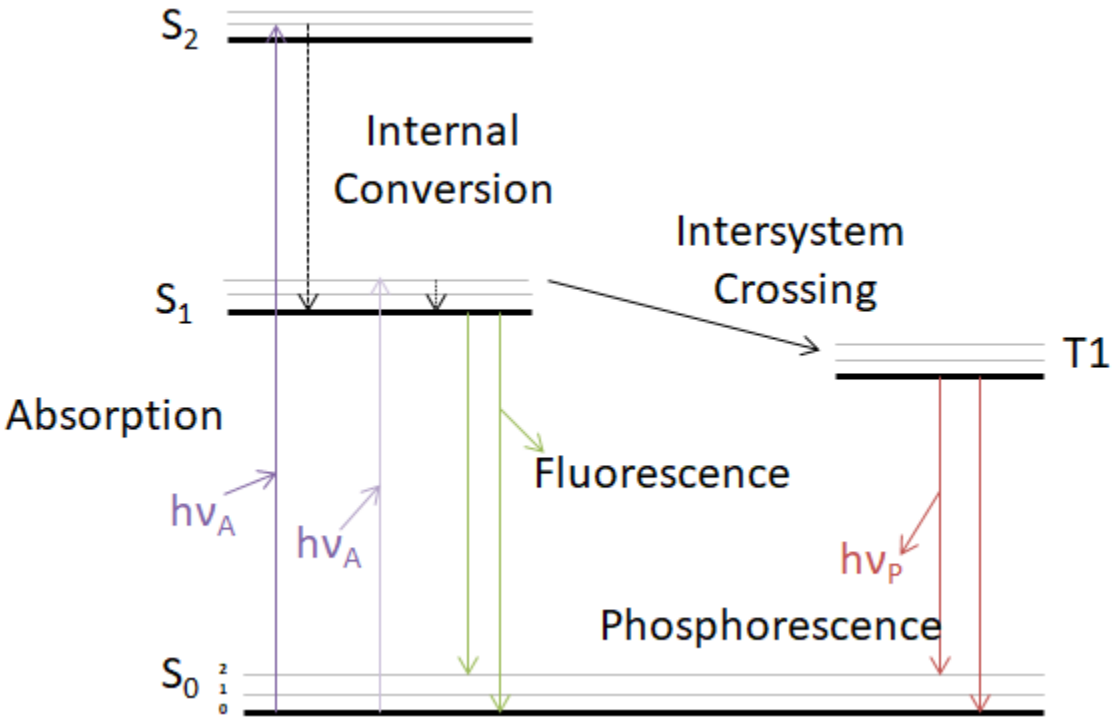

Figure 1.3: Jablonski diagram illustrating the processes of photoexcitation and various deactivation pathways.

ground state through photon emission, generating the emission spectrum. It is worth noting that emission spectrum would be a mirror image of the absorption spectrum, if the electronic excitation does not cause noticeable changes in the geometry of the nuclei.

The first excited state (S_1) may also find a pathway to reach the triplet state (T_1) by a process called intersystem crossing (ISC) Which is a radiationless process involving a transition between the two electronic states with different states spin multiplicity. The triplet state can release a photon to be deactivated back to the ground state (S_0) , giving rise to phosphorescence emission. Relative to fluorescence, phosphorescence features an longer wavelength emission. Since the ISC is spin-

forbidden, phosphorescence shows a considerably smaller rate constant than that of fluorescence. The emission rates in the phosphorescence are about (10^{-3} to 100 s^{-1}) while in the fluorescence are about (10^{-9} to 10^{-6}). Because some deactivation processes such as non-radiative decay and quenching occur simultaneously with emission, usually phosphorescence is not obvious at room temperature. Most likely phosphorescence can be observed from the emission of mixed singlet–triplet states in transition metal-ligand complexes.

1.1.4 The Stokes Shift and Mirror-Image Rule

The energy difference between light absorption and fluorescence emission is termed the Stokes shift. G. G. Stokes investigated this property by using very simple instrumentation (Figure 1.4).[20] A blue glass filter and sunlight were used as the source of UV excitation. This filter selectively transmits light below 400 nm, which can be absorbed by quinine (Figure 1.4). The proceeding light was prevented from reaching the detector (eye) by a yellow glass (of wine) filter. Quinine fluorescence occurs near 450 nm and is therefore easily visible.

Energy losses between excitation and emission are observed universally for fluorescent molecules in solution. One common cause of the Stokes shift is the rapid decay to the lowest vibrational level of S_1. Furthermore, a fluorophore generally decays to higher vibrational levels of S_0 (Figure 1.3), resulting in another loss of excitation energy by thermalization of the excess vibrational energy. In addition to these effects, fluorophores may show Stokes shifts due to solvent effects, excited-state reactions, complex formation, and/or energy transfer.

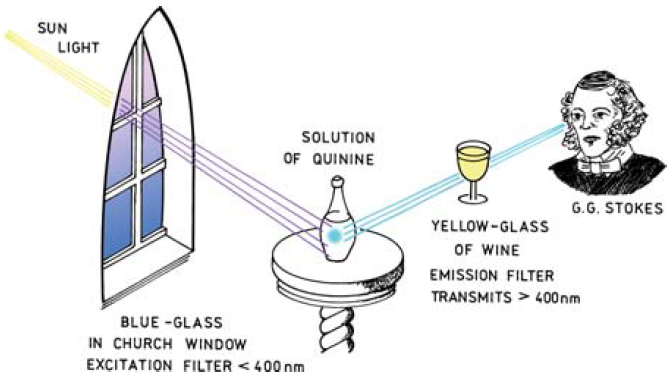

(Cited from *P*hil. Trans. Royal Soc. London **1852**)

Figure 1.4: Experimental set up to observe energy differences between absorption and emission devised by G. G. Stokes.

According to the Kasha's rule, photon emission (fluorescence or phosphorescence) occurs in an appreciable yield only from the lowest excited state of a given multiplicity.[21] For instance, quinine shows two peaks in the absorption spectrum, and its emission spectrum shows a pattern as only the mirror image of its S_0 to S_1 absorption band, but not the entire absorption spectrum.[22] Since the spacings of the energy levels in the vibrational manifolds of the ground state and first excited electronic states are usually similar accounts for the fact that the emission and absorption spectra are approximately mirror images.[23]

1.1.5 Exceptions to the Mirror-Image Rule

Excited-state reactions such as proton dissociation or formation of a charge-transfer (C-T) complex can result in deviations from the mirror symmetry rule. The unstructured emission at longer wavelengths is due to formation of a C-T complex between the excited state of two species or a dimer of a fluorophore that is referred

to as the exciplex or excimer. As a good example, pyrene at low concentrations has a highly structured emission, but at higher concentrations displays an emission in the visible region due to the formation of excimers.[24]

1.1.6 Quantum Yield

The quantum yield (ϕ) is the ratio of the number of photons emitted against the number of photons absorbed. If all molecules in the excited state release their absorbed energy through photon emission, the quantum yield equals unity (i.e., 100%). However, in reality non-radiative decay often contributes to the deactivation processes besides the radiative decay, making the quantum yield between 100% and 0% . In the research of organic fluorophores, the quantum yield is determined as a measure for the probability of the excited state being deactivated by fluorescence rather than by other non-radiative mechanisms.[25]

In routine fluorescence characterization of organic fluorophores, *relative* quantum yield can be determined by equation 1.1,

$$\phi_x = \frac{A_s}{A_x} \times \frac{F_x}{F_s} \times (\frac{n_x}{n_s})^2 \times \phi_s \tag{1.1}$$

where ϕ is the fluorescence quantum yield, A is the absorbance at the excitation wavelength, F is the area under the corrected emission curve (expressed in number of photons), and n is the refractive index of the solvents used. Subscripts s and x in this equation refer to the standard and the unknown, respectively. Additionally, modern fluorescence spectrophotometers allow the quantum yield to be directly obtained by detecting all sample fluorescence through the use of an integrating sphere.

1.1.7 Franck-Condon Principle

In the field of absorption and emission spectroscopy, the Franck–Condon principle has been widely applied to interpret vertical electronic transition properties. According to this principle, a molecular electronic transition is most likely to occur without changes in the positions of the nuclei of the entire molecule as well as its environment, because the nuclear motion (10^{-13} s) is negligible during the time required for an electronic excitation (10^{-16} s). As shown in Figure 1.5, when a molecule absorbs photonic energy to be electronically excited, it undergoes a vertical electronic transition, reaching a non-equilibrium state called the Franck-Condon state. The Franck-Condon state then comes to thermal equilibrium in picoseconds by collision with solvent molecules, causing a practically continuous absorption band. According to the Kasha's rule, relaxation of the excited state quickly occurs to the lowest vibrational level and always undergoes emission through the lowest-lying excited singlet state to the electronic ground state.[26]

1.2 Pyrene and Pyrene Derivatives

Pyrene ($C_{16}H_{10}$) is a polycyclic aromatic hydrocarbon (PAH) consisting of four fused benzene rings, resulting in a flat aromatic system that has become one of the most studied organic molecules in terms of its photophysical properties and pyrene derivatives have attracted enormous attention in synthetic materials chemistry.[27] Pyrene can be extracted from coal tar in a significant yield.[28] The rigid π-conjugated molecular backbone makes pyrene an excellent chromophore/fluorophore. The name pyrene (Greek for "fire") was coined since Laurent first discovered and believed that it

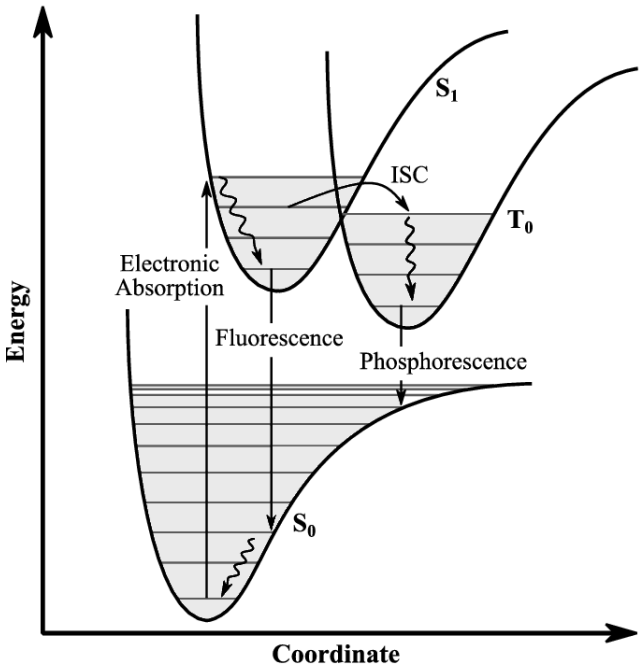

Figure 1.5: Schematic illustration of the Franck-Condon principle.

was frequently obtained via the distillation of organic substances with fire.[29] Initially, several derivatives such as pyranthrone were synthesized from pyrene for application in the synthetic industry. In 1954 Forster and Kasper reported the first observation of intermolecular excimers in a pyrene solution. The formation of excimers along with other intriguing properties, such as long-lived excited state, high fluorescence quantum yield, and high sensitivity to environmental changes at the micro-level, have made pyrene a precious standard in most organic photophysical studies.[30–32]

The excimer fluorescence of pyrene and derivatives can be utilized to sensitively detect the changes in environmental parameters (e.g., temperature, pH, pressure) as well as to recognize the binding of various guest molecules, ranging from small gaseous molecules and aromatic compounds to metal cations and anions.[33,34] Application of pyrene as a functional molecular building block in advanced organic

optoelectronic materials has resulted in significant advancement in devices such as organic light emitting devices (OLEDs), organic photovoltaics (OPVs), organic field effect transistors (OFETs), organic lasers and memory cells. In contrast to inorganic semiconductors, the properties of organic materials such as energy gap, solubility, electron affinity and stability in ambient air can be readily adjusted and finely tuned by means of chemical functionalization, which provides a powerful approach for the preparation of materials with desired properties and functions.[35,36] In recent pyrene-oriented research, many efforts have been dedicated to efficient and selective functionalization of pyrene with the aims to produce useful pyrene materials in a cost-effective way and to gain control over their electronic, photophysical properties, and supramolecular ordering.[27]

1.2.1 Excimers and Exciplexes

Pyrene is a well-established chromophore that can be applied in detecting guest molecules by monitoring its sensitive changes of optic and electronic properties. Pyrene is a polycyclic aromatic hydrocarbon (PAH) with both electron-donating and electron-withdrawing properties. Pyrene exhibits interesting optical behaviors in the solution, aggregated, and solid states. In the excited state, pyrene can form an excimer or an exciplex.[37] An excimer (i.e., excited dimer) is formed, in the solid state or concentrated solution, through binding an excited molecule with the same molecule in the ground state (equation 1.2). An exciplex (i.e., excited complex) is a complex between an excited molecule (M*) and a different molecule in the ground-state (N) (equation 1.3). Fluorescence emission spectra of both excimer and

exciplex are broad, unstructured and red-shifted related to the emission features of their monomers. Excimer/exciplex formation can also cause fluorescence quenching of the initially excited chromophores, which can be used as a mean to indirectly investigate the aggregation properties of pyrene and pyrene derivatives. The changes in environmental parameters or the binding of pyrene with a guest molecule can be readily detected by fluorescecence analysis that monitors the changes in the intensity of excimer/exciplex of pyrene.

$$M + M^* \rightarrow (MM)^* excimer \tag{1.2}$$

$$N + M^* \rightarrow (NM)^* exciplex \tag{1.3}$$

1.2.2 Functionalization of Pyrene

Pyrene is a readily available and inexpensive chemical with interesting electronic electrooptical properties; however, the blue light emitting property of pyrene has limited the use of pyrene as an emissive material in OLEDs due to its strong tendency to form excimers in condensed media or to aggregate in the solid state via intermolecular $\pi - \pi$ stacking. Aggregation of pyrene results in considerable redshift in its emission wavelength and quenching of its fluorescence. To overcome this downside, numerous studies have been attempted in the structural modification of pyrene in order to avoid aggregation and improve the fluorescence quantum yield for the application in OLEDs.[38] Two approaches have been found particularly useful: (1) introduction of bulky aryl/alkyl substituents, and (2) incorporation of heteroatoms into the π-conjugated backbone of pyrene. Such chemical functionalizations can

effectively diminish the $\pi - \pi$ stacking of pyrene in the aggregated states and thus preventing aggregation-caused quenching (ACQ) of fluorescence. As such, many functionalized pyrenes exhibit much higher degrees of photoluminescence than pyrene itself.

Pyrene can undergo electrophilic substitution reactions, for example, bromination. The brominated products of pyrene can be further modified through various cross-coupling reactions such as Suzuki, Heck, and Sonogashira couplings.[39–42] Chemical functionalization on the pyrene core can lead to a range of mono-, di-, and poly-substituted pyrene derivatives, and the commonly seen substituted patterns are illustrated in Figure 1.6.

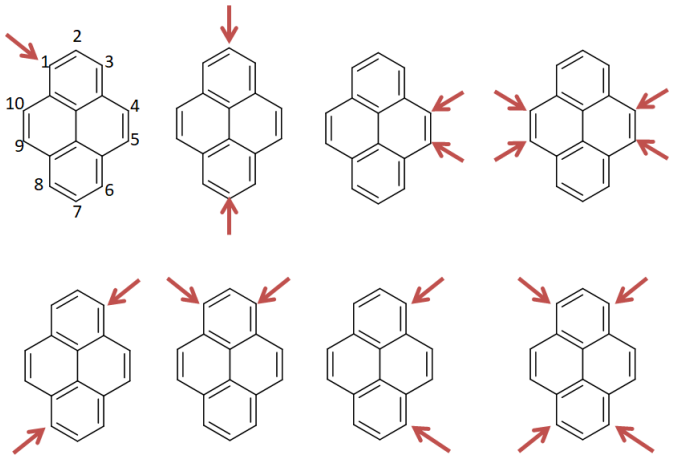

Figure 1.6: Common substitution patterns of pyrene.

Pyrene can be directly functionalized through bromination, borylation, oxidation, formylation, and *tert*-butylation reactions to generate new pyrene derivatives. Generally speaking, the 1, 3, 6, and 8 positions of pyrene are more reactive than the *K*-region (4, 5, 9, 10) and nodal plane (2, 7) sites on the pyrene core (Figure 1.7). In recent literature, however, selective synthetic methods for functionalization of the

K-region of pyrene have also been reported.[27]

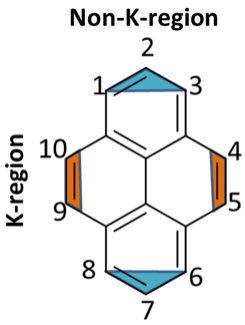

Figure 1.7: Structure of pyrene with K-region and non K-region labelled.

Substitution on the 4, 5, 9, and 10 positions of pyrene can generate interesting π-conjugated building blocks for the preparation of extended aromatic hydrocarbons. However, in the past few decades synthetic access to tetra- and di-substituted pyrenes in these positions such as pyrene-4,5-dione and pyrene-4,5,9,10-tetraone was somewhat limited due to the difficulties in their preparation. Several studies have been made on the preparation of pyrene-4,5-dione and pyrene-4,5,9,10-tetraone directly from pyrene.[43–45] K-region (4, 5, 9, 10) substituted pyrenes are not readily accessible unless the more reactive 1, 3, 6, and 8 positions are blocked with bulky *tert*-butyl groups at the 2 and 7 positions. The most common procedure to prepare these compounds involves the oxidation of pyrene under ruthenium catalysis.[40,43]

1.2.3 *K*-region Oxidation of Pyrene

The selective oxidation of pyrene in the K-region is a critical approach for pyrene functionalization, as the oxidized products can be further modified to produce various interesting pyrene derivatives. K-region oxidation products of pyrene and related

PAHs are both chemically and biologically important, as they are useful precursors to larger π-conjugated systems. In general, pyrene or similar PAHs can be oxidized in the K-region to form corresponding *ortho*-quinones by treatment with strong oxidants such as chromic acid. During the oxidation of a PAH, the positions with the lowest localization energy will react more easily. According to Dewar's calculations, the K-region of phenanthrene (1-1) shows the lowest localization energy (see Scheme 1.1).[46] However, for other PAHs (e.g., pyrene) the K-regions are rarely the position(s) of the lowest localization energy. As a result, the synthesis of K-region *ortho*-quinones from direct oxidation of pyrene and other PAHs is difficult. For instance, direct oxidation of pyrene (1-3) with CrO_3 in the presence of H_2SO_4 would result in 1,6- or 1,8-quinione (1-4 or 1-5) products, since these positions have lower localization energies than the K-region (see Scheme 1.1).[47]

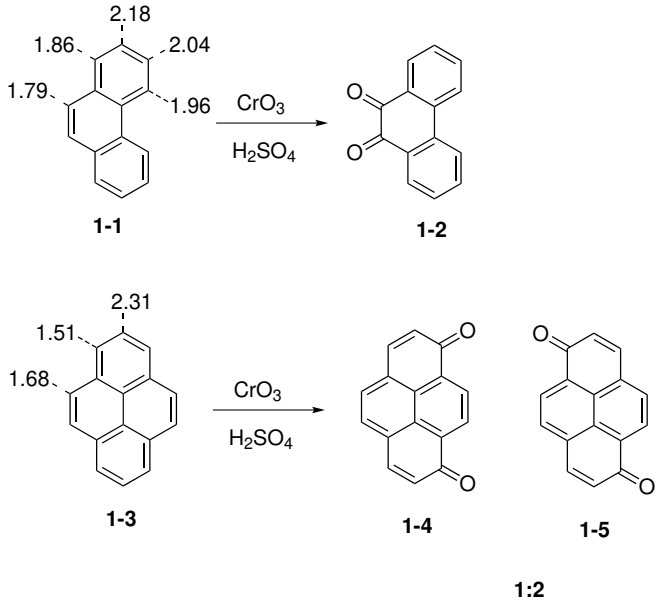

Scheme 1.1: Dewar localization energies of various positions in pyrene and phenanthrene and their direct oxidation reactions.

Harvey and co-workers reported a direct approach for *K*-region oxidation of PAHs in the 1970s,[48] but this strategy has not been widely adopted because of the use of osmium tetroxide, an expensive and highly toxic chemical, as the oxidant. In 2005, Zhang and Harris reported that the use of ruthenium chloride/sodium metal periodate as an oxidant could lead to *K*-region oxidation of pyrene through a single step reaction, which yielded pyrene-4,5-dione and pyrene-4,5,9,10-tetraone as products depending on the reaction temperature and the amount of oxidant used (see Scheme 1.2).[44] Harris' procedure, although quite straightforward, is not very easy to control and hence unsuitable for large-scale application. The Bodwell group optimized the reaction conditions by changing the solvents and adding a small amount of additive, *N*-methylimidazole (NMI). Bodwell's modifications not only resulted in shortened reaction time and improved reaction yield, but also eliminated the difficulty of messy workup in the previous oxidation methods. Such advantages make this method more suitable for relatively large-scale synthesis.[49,50]

1.3 Imidazoles

Imidazoles are aromatic heterocyclic compounds belonging to the alkaloid family. The pristine imidazole is a 5-membered ring compound with a chemical formula of $C_3H_4N_2$, and it appears as a white or colorless solid. 1,3-Diazole is the systematic name of imidazole that has been used in some literature, but the term imidazole for this kind of molecules was introduced officially by Hantzsch.[51] Imidazoles contain a variety of compounds with the same 5-ring core and various substituents. Imidazoles can act as both base and acid as well as biological building blocks, which

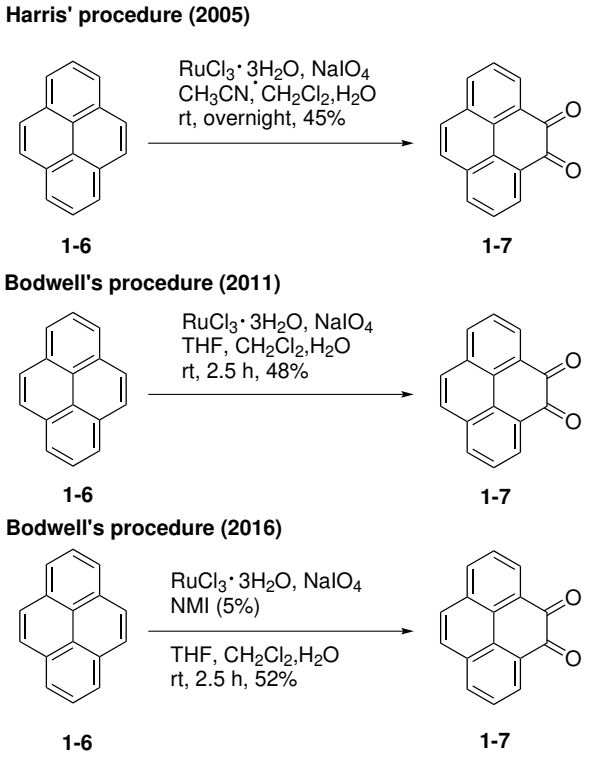

Scheme 1.2: Synthesis of 4,5-pyrenedione through direct oxidation methods.

show diverse biological, physiological, and pharmacological properties. Many drug compounds, antifungal, antibiotic, and sedative agents contain the imidazole ring in their molecular structures. Imidazole, histidine, related hormone histamine, and nitroimidazole are illustrated in Scheme1.3.[52]

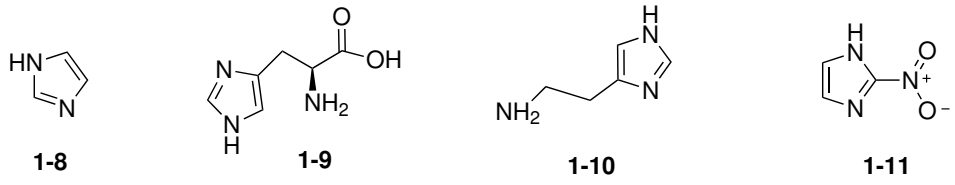

Scheme 1.3: Imidazole and common imidazole derivatives.

1.3.1 Structures and Properties of Imidazoles

Imidazole is a small heterocyclic compound with a planar five-membered ring. Imidazole is highly soluble in water and other polar solvents because of its high polarity. It is known as an aromatic compound, due to the sextet of π-electrons in the ring. Scheme 1.4 illustrates the resonance scheme of imidazole, from which one can see a significant degree of π-electron delocalization. Imidazole can undergo tautomerization, through which the acidic proton can readily change its location from 1 to 3 positions.

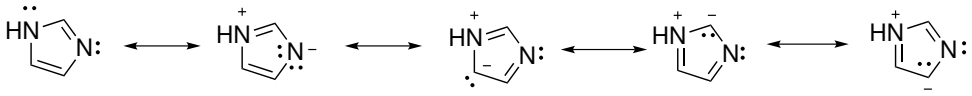

Scheme 1.4: Resonance scheme of imidazole.

Imidazole is an amphoteric compound with both an acidic and basic site. The pK_a of its N–H group is 14.5, while protonated imidazole shows a pK_a value around 6.95, which is a weaker acidity than that of pyridinium ion (5.25).[53] As such, imidazole has a basicity that is about 100 time stronger than that of pyridine, and this can be attributed to the strong resonance effect of the imidazole five-member ring. Compared to other five-membered ring organic compounds, imidazole has a high boiling point (256 °C) due to strong intermolecular hydrogen bonding interactions. Figure 1.8 shows the formation of a linear network in the X-ray single crystal structure of imidazole, resulting from hydrogen bonding interactions.[54] Herein, the N–H group of imidazole acts as a hydrogen bond donor, while the C=N group as a hydrogen bond acceptor.

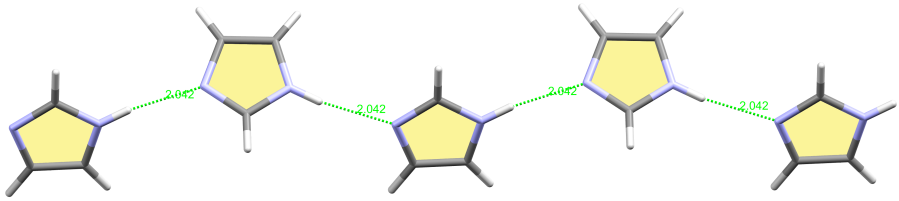

Figure 1.8: X-ray structure of a linear supramolecular assembly of imidazoles through intermolecular H-bonding interactions. CCDC 136337.

1.3.2 General Synthetic Methods for Preparation of Imidazoles

Imidazole and its derivatives can be synthesized by numerous methods. Scheme 1.5 summarizes the reactions that are commonly used for imidazole synthesis. Imidazole was first synthesized by Debus in 1858 through a condensation reaction between glyoxal and formaldehyde in ammonia as illustrated method (a) of Scheme 1.5[55]. In 1882, Radiszewski reported a condensation approach using α-diketones, benzaldehyde, and ammonia as reactants (see method (b), Scheme 1.5)[56]. These methods gave imidazole products in a one-pot manner. Later on, other methods such as dehydrogenation of imidazolines (method (c)), Wallach synthesis (method (d)), from α-halo ketones (method (e)), Marckwald synthesis (method (f)), and from aminonitrile and aldehyde (method (g)) were reported for C-substituted imidazoles.[51] It is worth nothing that 1-substituted imidazoles are formed by using primary amines instead of one equivalent of ammonia.[52]

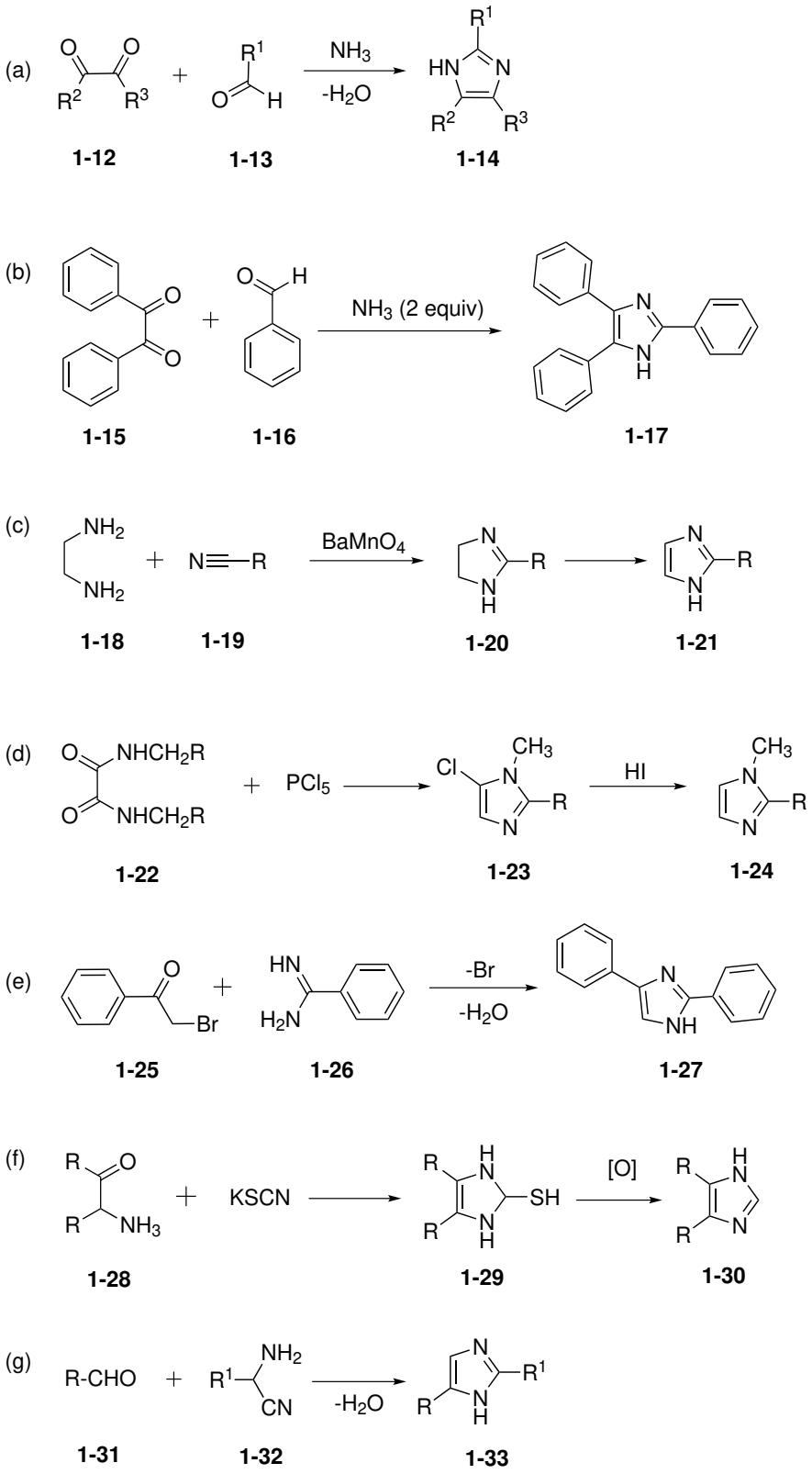

Scheme 1.5: General synthetic methods for imidazole derivatives.

As mentioned above, there have been numerous methods available for the synthesis of imidazoles. Commercially, the commonly used one is the so-called Debus-Radziszewski imidazole synthesis, in which a dicarbonyl (usually glyoxal) and an aldehyde are reacted with ammonia through a multi-component condensation approach.[57,58] As shown in Scheme 1.6, the reaction involves two stages. In the first stage, the dicarbonyl and ammonia are condensed to give a diimine intermediate (**1-34**), and in the second stage this diimine is condensed with the aldehyde to generate an imidazole product (**1-14**).

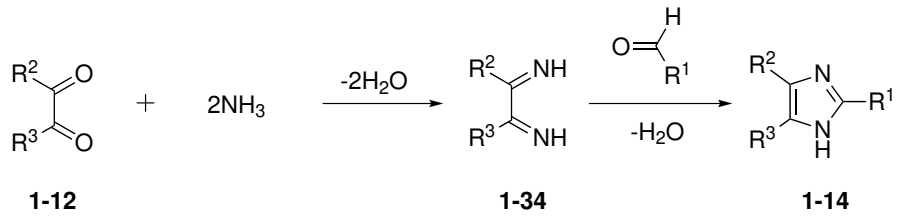

1-12 **1-34** **1-14**

Scheme 1.6: General scheme of the Debus-Radziszewski synthesis.

The detailed mechanism for the Debus-Radziszewski synthesis is outlined in Scheme 1.7.[59,60] It is worth noting that, according to this mechanism, oxazole can also be possibly generated as a by-product of the reaction.

While most reactions for imidazole synthesis are conducted under traditional heating conditions, microwave (MW) radiation can also be used as an efficient heating source. Microwave irradiation has several advantages over conventional heating. Under microwave irradiation, reactions proceed faster and give higher yields than conventional heating conditions.[52,61] The magnitude of the energy transfer is related to the dielectric properties of the molecules. The higher dielectric constants the compounds possess, the more microwave energy they

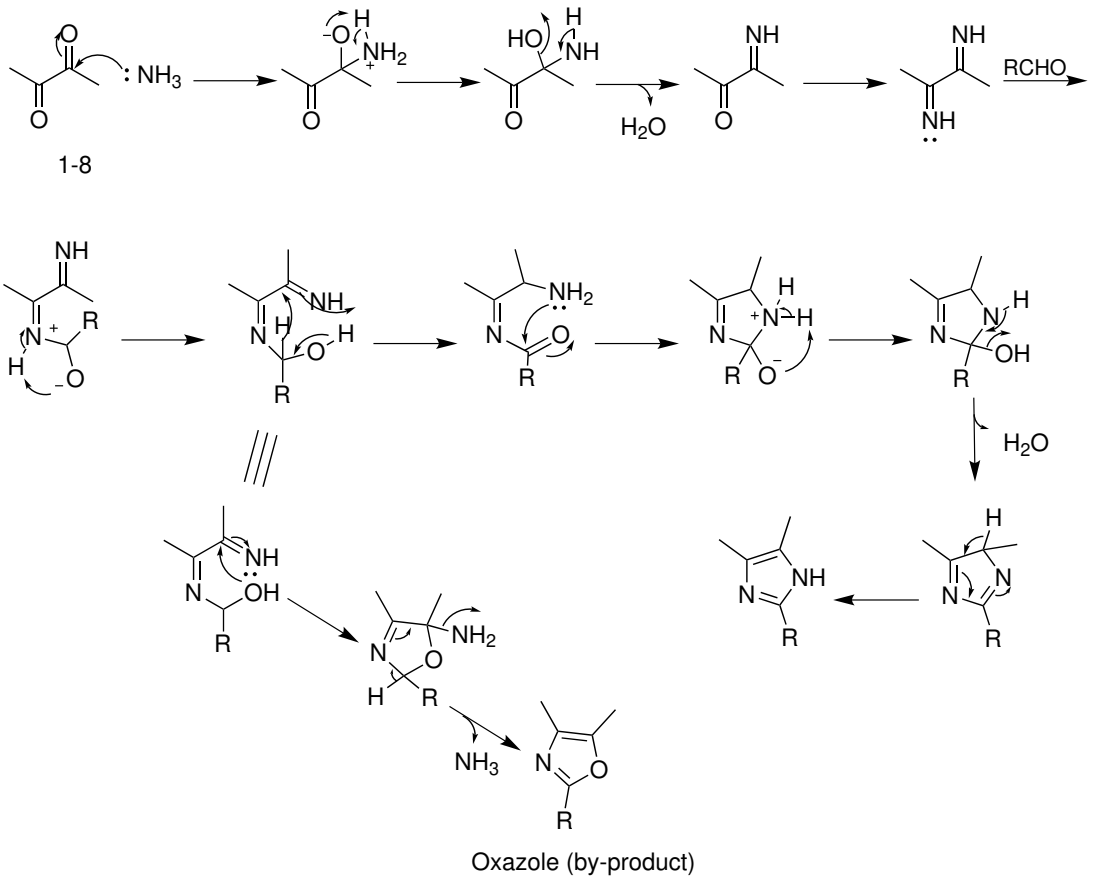

Scheme 1.7: Reaction mechanism for the Debus-Radziszewski synthesis.

absorb. For this reason, the synthesis of imidazole derivatives can be substantially promoted by microwave irradiation. For instance, in 2005 Zhao *et al.* reported the synthesis of three benzimidazoles through reactions of 1,2-phenylenediamine (**1-35**) with carboxylic acids and acetoacetic esters without the use of any catalysts (Scheme 1.8).[61] In 2011, Qasim *et al.* reported a solventless synthesis of 2-phenylimidazo[4,5-*f*][1,10]phenanthroline derivatives (**1-40**) by condensation of *p*-substituted benzaldehyde (**1-39**) with a dicarbonyl compound (**1-38**) in the presence of a neutral ionic liquid (Scheme 1.8).[62]

Imidazole synthesis can also be performed in the solid state without the use of

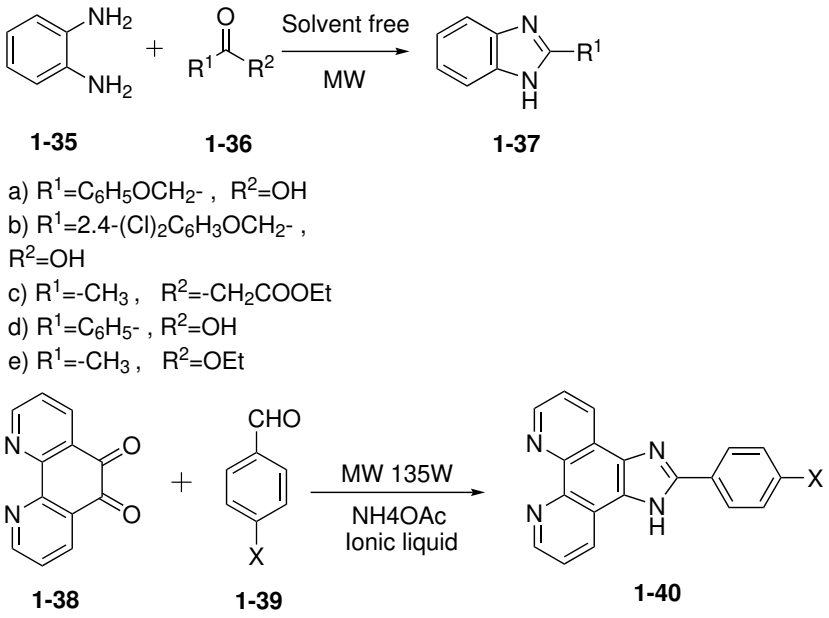

Scheme 1.8: Microwave-assisted synthesis of imidazole derivatives.

solvents.[52] In 2011, Qasim and co-workers reported the synthesis of the some imidazole derivatives through grinding the mixture of a substituted benzaldehyde (**1-39**), benzil (**1-15**), and NH_4OAc in the presence of a catalytic amount of NaH_2PO_4 under solvent-free conditions at room temperature (Scheme 1.9).[63]

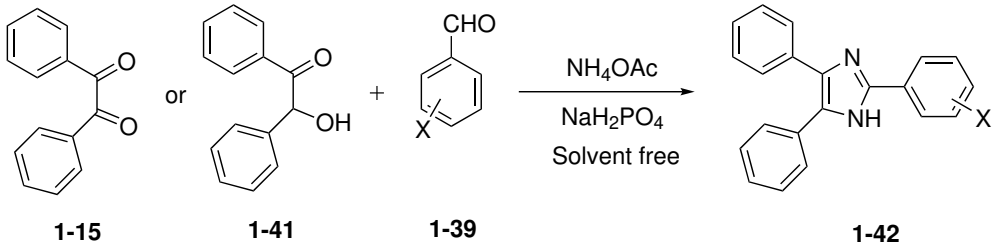

Scheme 1.9: Solid-state synthesis imidazole derivatives with the assistance of grinding.

1.4 Chemosensors Based on Pyrene and Imidazole

1.4.1 General Principles of Chemosensors

Chemosensors are compounds that can give detectable signals (e.g., changes in optical, electrical, and magnetic properties) upon binding with certain analytes, such as cations, anions, small organic molecules as well as large biomolecules, in a selective manner.[64] Generally speaking, the molecular structure of a chemosensor should contain at least two essential parts, receptor and reporter. The receptor unit has functional group(s) that can selectively interact with the desired analyte through covalent and/or non-covalent forces, while the reporter unit responds to the binding of receptor with analyte by showing detectable changes in its electronic and photophysical properties.[65]

Of numerous molecular properties, the optical properties of a molecule are often useful in chemical sensing. For example, a molecule that sensitively responds to the binding with an analyte by exhibiting dramatic color changes can act as a colorimetric sensor, while a fluorophore that changes in emission wavelength and/or intensity in response to an analyte serves as a fluorescent chemosensor. Compared with colorimetric chemosensors, fluorescent chemosensors have advantages of rapid response, enhanced selectivity/sensitivity, and real-time detection via portable sensing units.[63,66]

The π-conjugated structure of pyrene gives rise to versatile fluorescence properties that are not only of high emission efficiency but also sensitive to the microenvironment where it is located. As a result, many designed fluorescent chemosensors have utilized pyrene as the fluorescence reporter in conjugation with other functional units.[67]

Imidazolyl as a stable heterocyclic aromatic group has both acidic N–H and basic C=N sites that can effectively bind with a variety of cations and anions through ion-dipole and hydrogen bonding interactions. In recent years, there has been a growing interest in the design and synthesis of novel fluorescence sensors containing pyrene and/or imidazole as the key building components. In the following section, the progress in recent studies of fluorescent chemosensors based on pyrene and imidazole are briefly reviewed.

1.4.2 Recent Progress in Pyrene and Imidazole-Based Chemosensors

In 2015, Baitalik *et al.* prepared a simple Py–BiimzH_2 system (**1-43**, Scheme 1.10) and found it can act as an efficient fluorogenic ratiometric sensor for CN^- anion.[68] As shown in Scheme 1.10, the binding of **1-43** with CN^- anion is achieved through H-bonding interactions and involves three stages of changes. In the first stage, the anion binds with the bisimmidazole unit through double hydrogen bonds to form a 1:1 complex. With increasing addition of CN^- anion, stepwise deprotonation of the NH of imidazoles occurs. The deprotonated **1-43** shows substantially altered electronic properties, which cause the emission band of **1-43** at 404 nm to attenuate and a longer-wavelength charge-transfer (C-T) band to emerge at 476 nm. The ratio of the intensity at the two emission wavelengths shows a good linear correlation with the concentration of CN^- anion, allowing for sensitive detection and quantification of CN^- anion in the concentration range of 10^{-5} to 10^{-3} M. Besides the facile synthesis and structural simplicity, sensor **1-43** gives the ratiometric sensing performance that

is advantageous over typical sensors, which rely on merely single-wavelength emission signal. Although it is straightforward to monitor the emission of a fluorophore at a single wavelength to achieve fluorescence sensing, this type of sensing mechanism has some drawbacks; particularly, the fluorescence signals are often dependent on various instrumental and environmental parameters. These properties limit the certainty and accuracy of analyte detection. To overcome these problems, the ratiometric sensing method is often used, since examination of the variations of two correlated signals can substantially reduce systematic errors and improve accuracy and reliability.[69] The fusion of pyrene and imidazole in **1-43** yields a π-conjugated system, the electron density over which can be readily altered through the binding of anions with the imidazolyl unit. This feature enhances the intramolecular charge transfer (ICT) process to facilitate anion sensing. (Scheme 1.10)

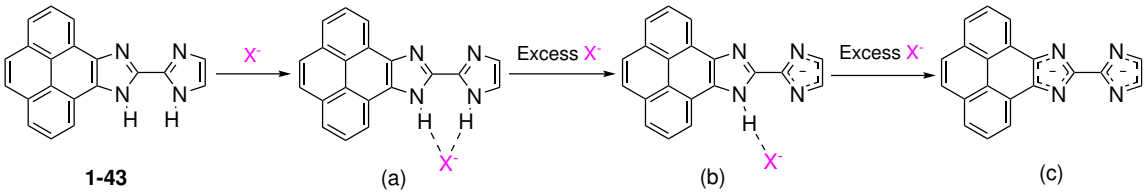

Scheme 1.10: Py-BiimzH_2 as a ratiometric fluorescent sensor for cyanide anion.

In 2014, Kim *et al.* reported the synthesis of a pyrene-imidazole hybrid **1-46** through a reductive amination approach (Scheme 1.9A).[70] Compound **1-46** was found to show high binding strength with aromatic carboxylic acids, especially salicylic acid derivatives, through multiple H-bonding and $\pi - \pi$ interactions (Scheme 1.9B). Fluorescence spectroscopic studies indicated that **1-46** can form 1:1 complexes with various salicylic acids. Particularly, electron-deficient salicylic acids, such as 5-

nitrosalicylic acid gave a high binding constant (7.18×10^4 M) and the binding resulted in prominent fluorescence enhancement.

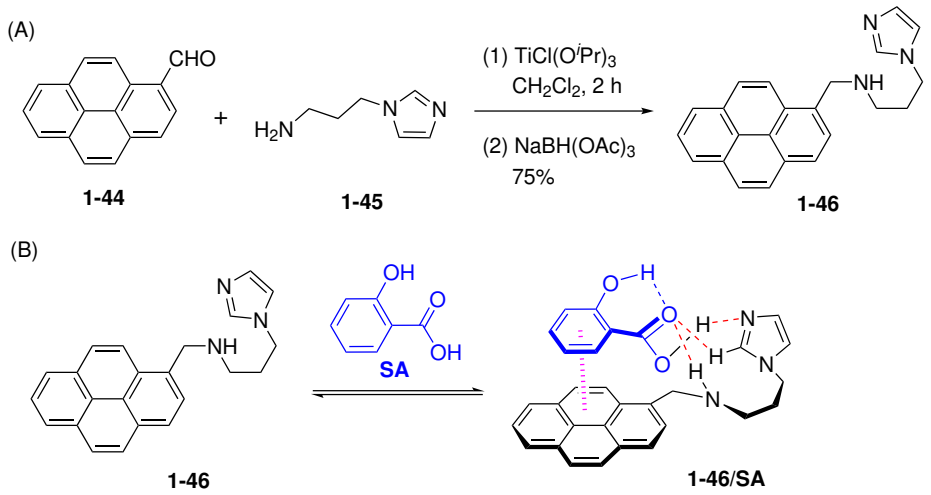

Figure 1.9: (A) Synthesis of pyrene-imidazole chemosensor **1-46** via reductive amination. (B) Formation of 1:1 complex of **1-46/SA** with salicylic acid through H-bonding and $\pi - \pi$ interactions.

In 2014, Das and co-workers synthesized a pyrene-naphthalene derivative **1-48** through a Schiff base condensation (Scheme 1.11).[71] The compound is a visible light excitable fluorescent probe. As shown in Scheme 1.11, **1-48** can bind with histidine through H-bonding interactions. Before binding, the molecular skeleton of **1-48** is flexible and can freely rotate. The fluorescence of the pyrene unit is quenched by photoinduced electron transfer (PET). After binding with histidine through two hydrogen bonds, the molecular rotation of **1-48** is restricted and becomes rigid. The PET process is consequently disrupted and the fluorescence of pyrene is enhanced. Through this mechanism, compound **1-48** shows fluorescence turn-on responses to histidine. Das and co-workers further demonstrated that it could be used as a selective

fluorescence probe for *in vivo* monitoring the concentration of histidine in living cells. Since the level of histidine in the human body has an essential function in nervous system, fluorescence probe **1-48** was expected to have a great potential in biological application.

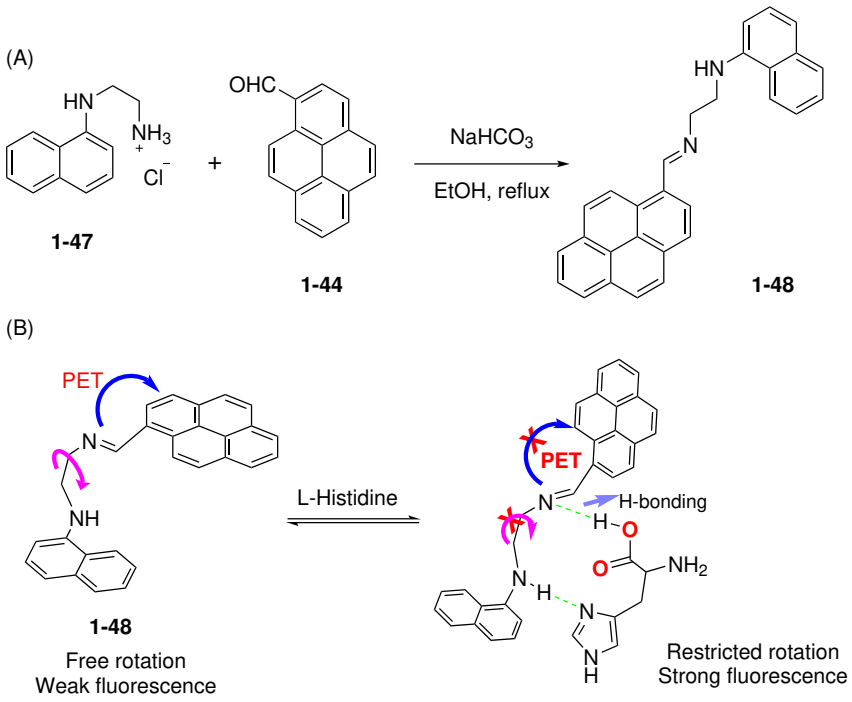

Scheme 1.11: (A) Synthesis of a pyrene-naphthalene derivative **1-48** through Schiff base condensation. (B) Proposed binding mode of **1-48** with histidine and plausible fluorescence turn-on sensing mechanism for histidine.

In 2019, Shree and co-workers designed and synthesized two fluorescent turn-on chemosensors **1-52** and **1-53**, the structures of which contain a benzimidazole group in conjunction with an anthracene and pyrene group, respectively.[72] As shown in Scheme 1.12A, the synthesis of **1-52** and **1-53** was achieved through a one-step condensation of an arene-aldehyde with 2-aminophenylbenzimidazole (**1-51**) in

ethanol. Compounds **1-52** and **1-53** exhibited high selectivity and sensitivity towards Al^{+3} ion. As shown in Scheme 1.12B, the two compounds can undergo a ring opening process via a 1,5 H-shift mechanism, forming corresponding a Schiff base that favors the chelation with Al^{3+} ion at a 1:1 ratio through the imine and imidazolyl sites. The binding with Al^{3+} ion resulted in significant fluorescence enhancement and the two chemosensors were found to be effective in fluorescence imagining of Al^{3+} ion in living cells.

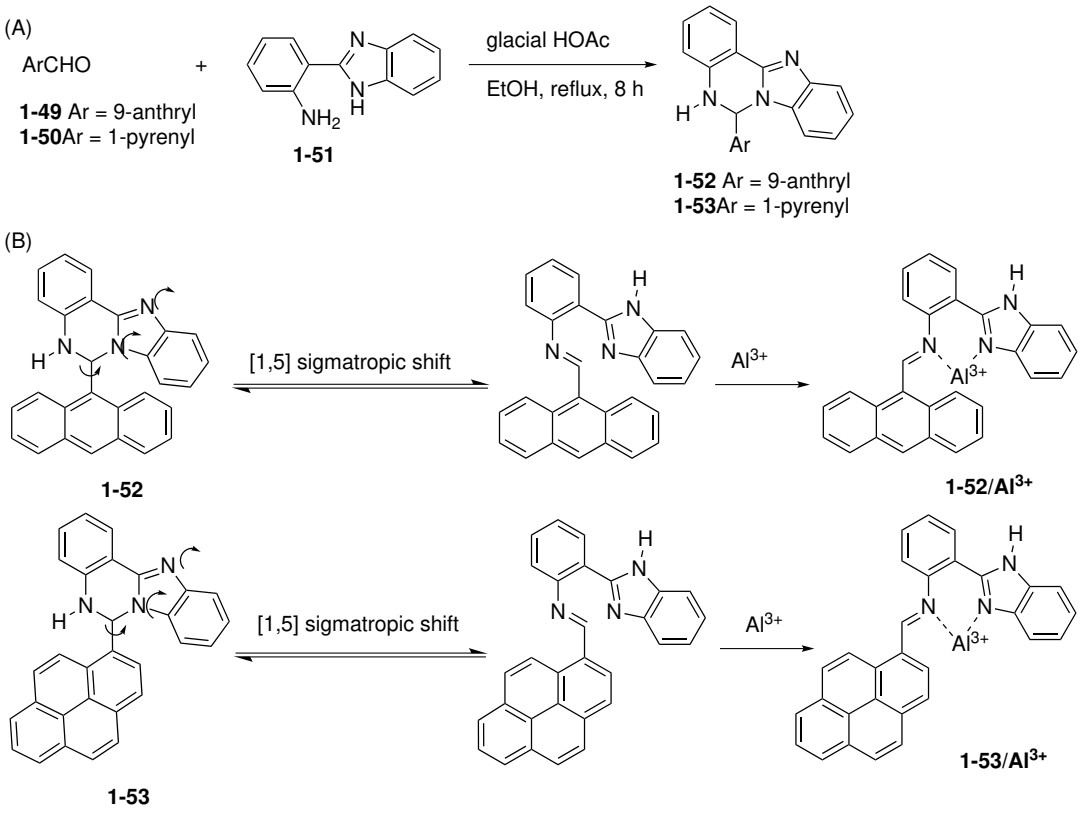

Scheme 1.12: (A) Synthesis of anthracene/pyrene-benzimidazole hybrids **1-52** and **1-53** through a one-step condensation reaction. (B) Transformation of **1-52** and **1-53** into corresponding Schiff bases and complexation with Al^{3+} ion.

Singh and co-workers in 2014 reported the synthesis of a series of pyrenyl-substituted benzimidazopyrimidine derivatives **1-57** and **1-58** through the Biginelli reaction (Scheme 1.13).[64] The two compounds were found to selectively bind with Zn^{2+} ion in acetontitrile and show fluorescence quenching. Nanoaggregates of **1-57** and **1-58** in aqueous media exhibited fluorescence turn-off sensing properties for Fe^{3+} ion.

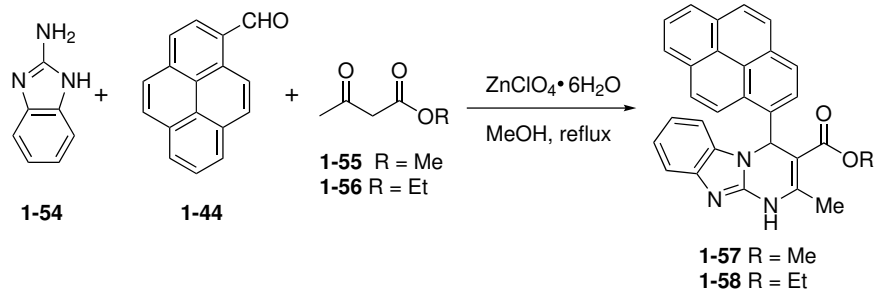

Scheme 1.13: Synthesis of pyrene-substituted benzoimidazopyrimidine derivatives through Biginelli condensation.

In 2018, Das and co-workers prepared a series of benzimidazole derivatives, including a 1-pyrenylbenzimidazole compound **1-59** (Scheme 1.14), through condensation reactions.[73] (^{19}F and ^{1}H) NMR analysis confirmed that compound **1-59** can strongly bind with F^- anion through hydrogen bonding interactions, with the imidazole N–H acting as the hydrogen bond donor. UV-Vis absorption and fluorescence analyses showed that compound **1-59** can selectively discriminate fluoride anion among numerous anions through both colorimetric and fluorescence sensing approaches. They even built a molecular logic gate based on compound **1-59** to demonstrated a "write-read-erase-read" function.[74]

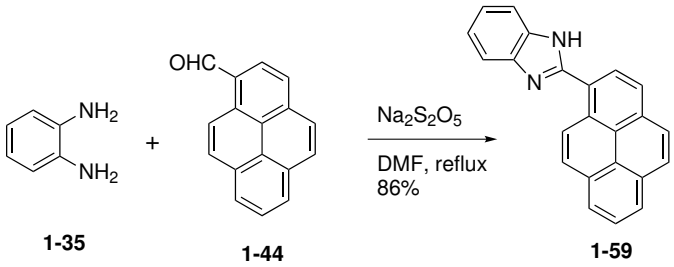

Scheme 1.14: Synthesis of a pyrene-benzimidazole derivative through condensation reaction.

1.5 Recent Development of Pyrenoimidazoles as Functional Organic Fluorophores

Additionally, the application in synthetic chemosensors, pyrene and imidazole have also been frequently used as the essential building components in molecular materials for advanced optoelectronic application. Of many pyrene-imidazole hybrids, pyrenoimidazoles have attracted increasing attention in recent years, mainly because of their highly delocalized π-electron properties, versatile intermolecular interactions, and flexible structural tunability. The following section summarizes the development of pyrenoimidazole-based materials reported in the recent literature.

In 2015, Misra *et al.* designed and synthesized a class of phenylethene-substituted pyrenoimidazoles **1-64** and **1-66** (Scheme 1.15).[75] Their synthesis began with a multi-component condensation reaction, in which pyrene-4,5-dione (**1-7**) was reacted with aniline and *p*-bromobenzaldehyde in the presence of NH_4OAc and glacial acetic acid. The reaction yielded compound **1-62**, which was then subjected to Suzuki-Miyaura cross coupling with tetraphenylethene boronate **1-63** and triphenylethene boronate **1-65** to give pyrenoimidazole derivatives **1-64** and **1-66**, respectively.

Incorporation of the crowded tetraphenylethene (TPE) and triphenylacrylonitrile (TPAN) units brought about interesting aggregation-induced emission enhancement (AIEE) properties. In general, π-conjugated organic chromophores favor strong $\pi-\pi$ stacking in aggregated states and thus show aggregation caused quenching (ACQ) effect on their fluorescence properties. However, in some special cases, particularly sterically crowded arenes, the aggregation of chromophores can result in enhanced emission, originated from restricted intramolecular motion (RIM) mechanisms.[76–78] Indeed, the twisted conformations of TPE and TPAN groups in **1-64** and **1-66** help suppress the $\pi-\pi$ stacking of pyrene and promote AIEE in the solid state.

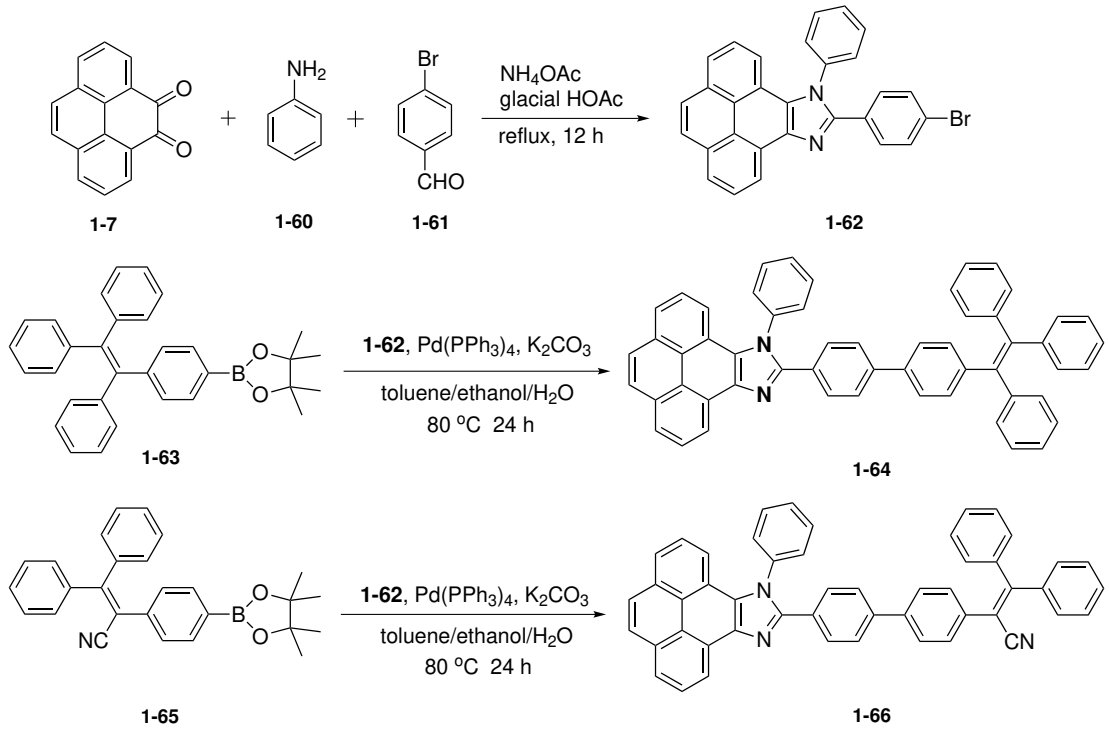

Scheme 1.15: Synthesis of pyrenoimidazoles with AIEE and mechanochromic properties.

More interestingly, pyrenoimidazole derivatives **1-64** and **1-66** exhibit reversible

mechanochromic behavior due to the transformation of the twisted crystalline state to their planar amorphous state resulting in π-conjugation enhancement (see Figure 1.10). Obviously, there is an equilibrium between the emission behavior of the crystalline form and powdery form of the compounds. The crystalline form of **1-64** yields blue-colored emission light under UV irradiation, while **1-66** affords a sky-blue light emission in the crystalline state. After mechanical grinding, the solid-state emission shows significant color changes (yellowish green light). This behavior is reversible through annealing or fuming with dichloromethane vapor.

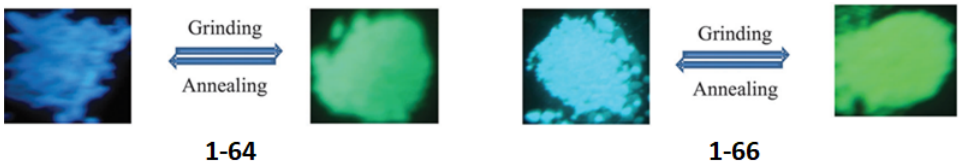

Figure 1.10: Mechanochromic properties of pyrenoimidazole derivatives **1-64** and **1-66**.

In 2014, Huang *et al.* synthesized a series of symmetrical benzene and oligothiophene-centered bispyrenoimidazole oligomers **1-69** and **1-73** (Scheme 1.16).[79] In their synthesis, pyrenoimidazoles were first constructed through a condensation reaction of pyrene-4,5-dione (**1-7**) with an aldehyde counterpart in the presence of NH_4OAc and glacial acetic acid. The imidazolyl N–H sites of the oligomers were also alkylated with *n*-decyl groups. The electronic absorption and emission properties were investigated by UV-Vis and fluorescence spectroscopy. Benzene-centered bisimidazole oligomer **1-69** exhibited the highest fluorescence efficiency, while oligothiophene-centered derivatives **1-73** showed much higher thermal stability with bathochromic shifts in absorption and emission peaks compared with benzene-

centered **1-69**. These features can be ascribed to that the thiophene rings are more electron-rich than benzene, which facilitates ICT and induces fluorescence quenching. Their studies indicated that the length and type of π-conjugated bridges have significant influence on the optoelectrical properties.

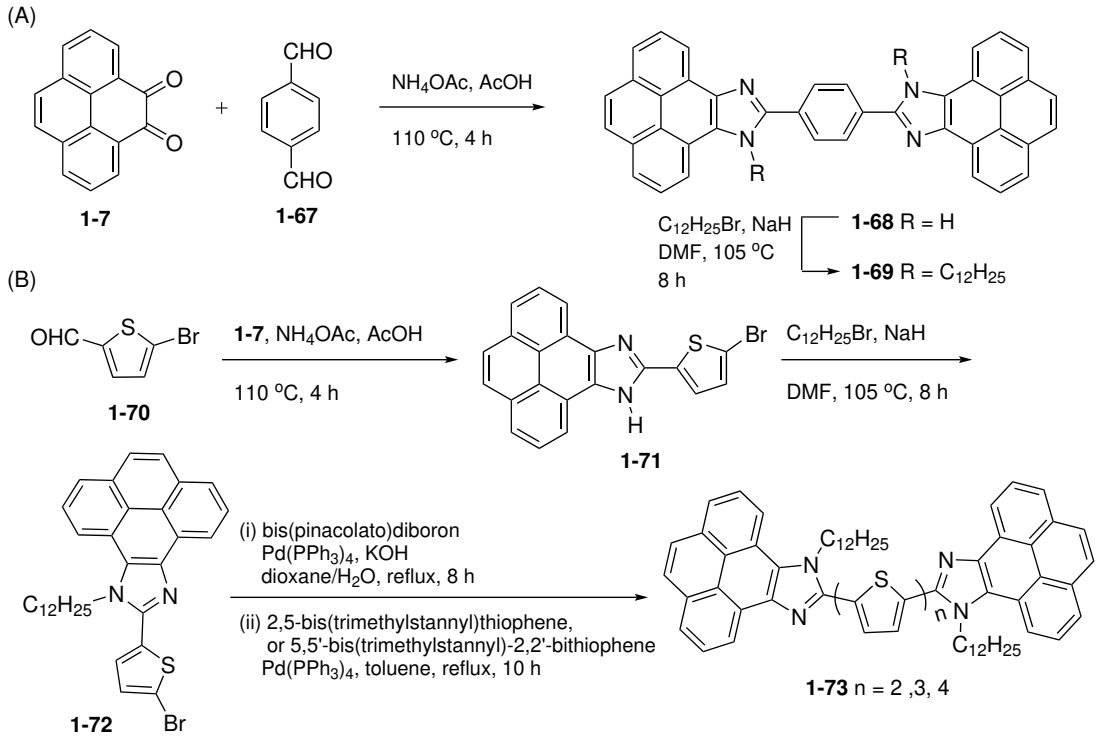

Scheme 1.16: Synthetic routes for (A) benzene **1-69** and (B) oligothiophene-centered **1-73** bispyrenoimidazole derivatives with double *n*-dodecyl chains.

Moreover, the solid-state structural properties of **1-69** were investigated by X-ray single crystallographic analysis. The results showed strong π–π stacking taking place between neighboring pyrene and imidazole moieties (see Figure 1.11) and suggested that the pyrenomidazole unit may serve as a controllable structural component for crystal engineering.

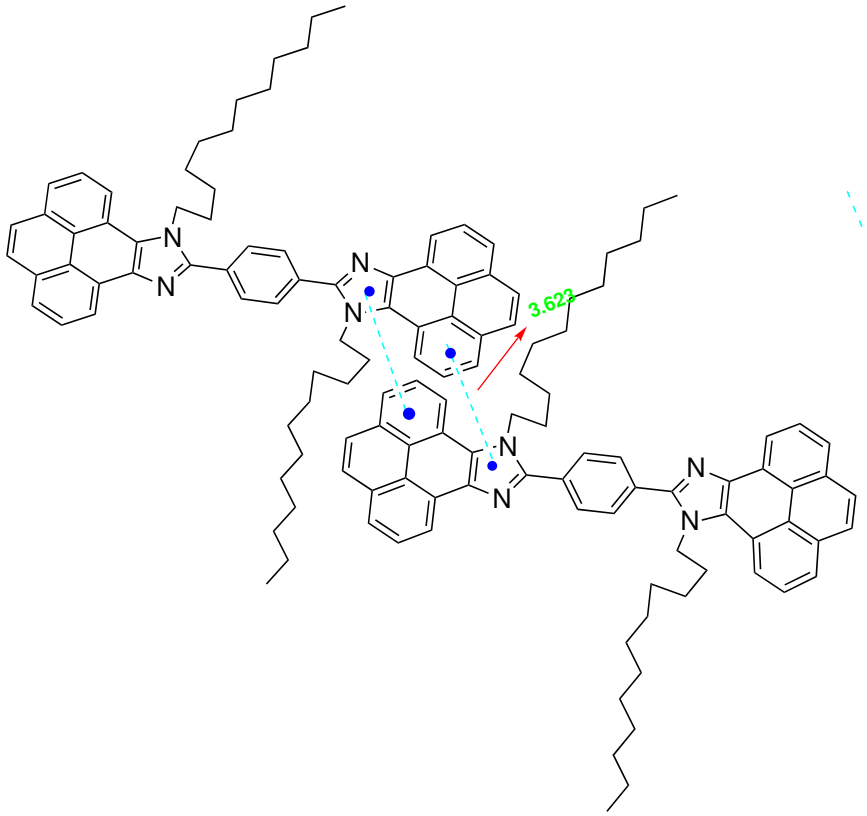

Figure 1.11: Schematic illustration of the complementary $\pi - \pi$ stacking of pyrene and imidazole moieties in the crystal structure of **1-69**.

In 2016, Lu and co-workers synthesized and investigated a group of pyrenoimidazole and phenanthroimidazole derivatives **1-74** and **1-75** (Scheme 1.17) through one-pot multi-component condensation of pyrene-4,5-dione or phenanthrene-9,10-dione with 1-naphthaldehyde and aniline in glacial acetic acid under heating.[80] The resulting compounds **1-74** and **1-75** were characterized to be efficient deep-blue emitters. Incorporation of a 1-naphthyl group into the pyrenoimidazole and phenanthroimidazole systems resulted in increased steric hindrance and hence attenuated the charge transfer (CT) states in both structures. Thermogravimetric analysis (TGA) and differential scanning calorimetric (DSC) analysis showed that

they retain excellent thermal stability up to 400 °C and have high glass transition temperature (Tg) at about 100 °C without crystallization. The remarkable luminescence properties and high thermal stability of these two blue light emitters make them a really good candidate materials for deep blue organic light emitting devices (OLEDs).

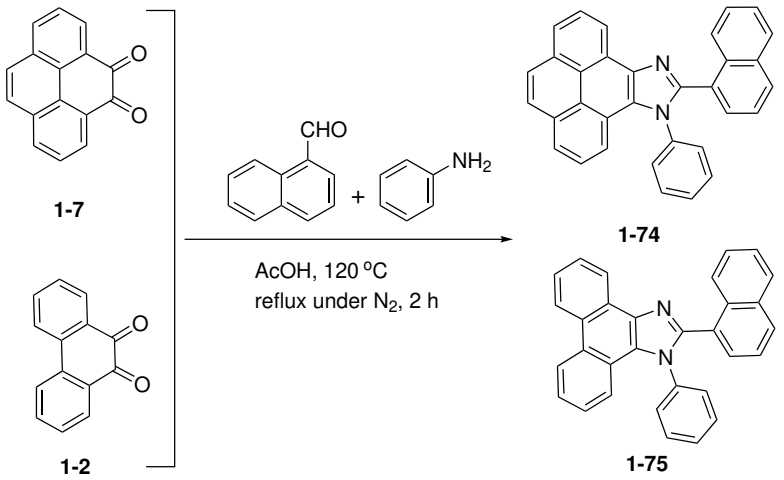

Scheme 1.17: Synthesis of sterically hindered pyrenoimidazole and phenanthroimidazole derivatives as deep blue light emitters.

Dye-sensitized solar cells (DSSCs) are low-cost alternatives to conventional solar cells and they have received considerable attention since the first type of DSSC was demonstrated in the early 1970s. A modern DSSC is usually composed of a porous layer of TiO_2 nanoparticles covered with molecular dyes that can efficiently absorb sunlight. Application of metal-free organic dyes in DSSCs has been actively sought after in recent years.[81] To improve DSSC performance, the organic dye is desired to either sufficiently absorb a wide range of wavelength (400–900 nm) or be able to induce efficient co-sensitization with other dyes.[82,83] In 2013, Ho and co-

workers reported a co-sensitized DSSC based on a pyrenoimidazole organic dye (**1-76**) together with squaraine-based organic dye (**1-77**) (Scheme 1.12).[84] The co-sensitizer showed a sharper and broader complementary absorption band compared with the individual dyes. The pyrenoimidazole dye **1-76** absorbs light from 360 nm to 520 nm, while the absorption of squaraine dye **1-77** appears in the range of 550–710 nm with higher extinction coefficient (319,000 $M^{-1}cm^{-1}$) at 662 nm than the pyrenoimidazole dye (44,900 $M^{-1}cm^{-1}$) at 464 nm. The DSSC attained a power conversion efficiency as high as 6.24% when the squaraine and pyrenoimidazole dyes were mixed at a molar ratio of 4:6. The incident photon-to-current efficiency (IPCE) spectra of the DSSCs showed a broadened and enhanced response when the two organic dyes were co-adsorbed on the TiO_2 film, which was confirmed by the absorption spectral results. Moreover, the co-sensitized photoanodes investigated with a binary-ionic electrolyte at room temperature showed a good durability (up to 1,000 hours).

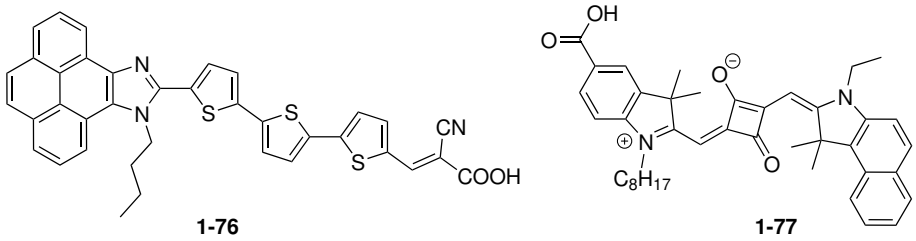

Figure 1.12: Molecular structures of pyrenoimidazole-based dye **1-76** and squaraine dye **1-77**.

Fu and co-workers in 2019 reported two pyrenoimidazole-based fluorophores **1-80** and **1-81**, which are *syn* and *anti* isomers with different molecular symmetries.[85] As shown in Scheme 1.13, their synthesis began with a *t*-butylation reaction that generated 2,7-di-*t*-butylpyrene (**1-78**). Ru-promoted oxidation was then

conducted to give 2,7-di-*t*-butylpyrene-4,5,9,10-tetraone (**1-79**). In the last step, a condensation reaction of **1-79** with benzaldehyde and aniline was performed in the presence of NH_4OAc and acetic acid under heating. Two isomeric products, centrosymmetric **1-80** and axisymmetric **1-81**, were obtained after column chromatographic separation. The molecular structures of these two pyrenoimidazole derivatives were unambiguously confirmed by X-ray structural analysis. Thermal analyses showed that the two compounds possess superb thermal stability, while fluorescence spectroscopic analysis suggested they could be used as blue light emitting materials.

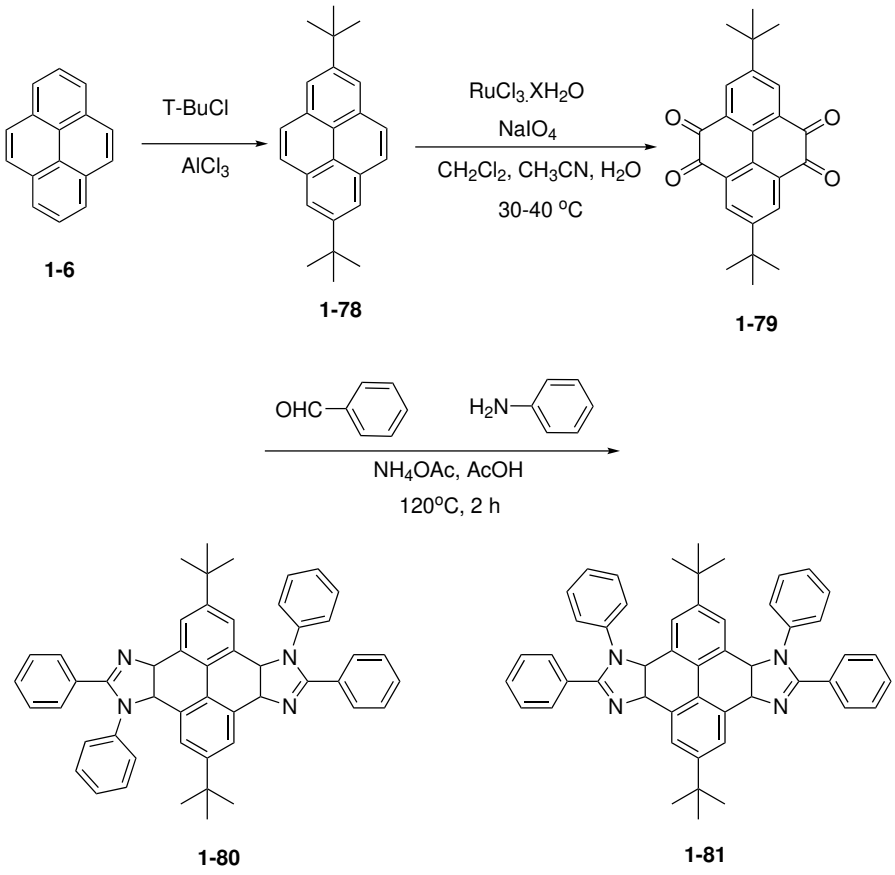

Figure 1.13: Synthesis of two pyrenoimidazole-based isomers **1-80** and **1-81**.

1.6 Objectives of This Thesis Work

Based on the aforementioned background and literature review, this thesis work was focused on the development of new pyrene and imidazole based organic fluorophores, particularly those contain the 9*H*-pyreno[4,5-*d*]imidazole structure. At the outset of this thesis study, the possibility of tailoring the electronic and photophysical properties of pyrenoimidazoles through a donor/acceptor (D/A) substitution strategy was conceived. As shown in Figure 1.14, pyrene-4,5-dione, a readily available synthetic precursor, was identified as a key starting material for a series of condensation reactions with various D/A-substituted benzaldehydes. The condensation products contain π-conjugated frameworks in which the electronic properties of the pyrene unit were expected to be significantly influenced by the substituent group attached to the phenyl ring. As already demonstrated in the literature, the condensation reactions to produce such phenyl-pyrenoimidazole (**Ph-PyIm**) derivatives should be cost-effective, straightforward, and easily scaled up. The simplicity and efficiency of the synthesis are indeed advantageous for real application in organic fluorescent materials and devices.

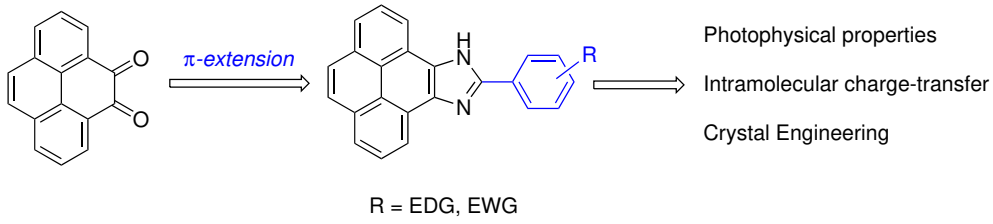

Figure 1.14: Concepts of developing D/A-substituted phenyl-pyrenoimidazole (**Ph-PyIm**) derivatives and aims of property studies.

With these **Ph-PyIm** derivatives in hand, the thesis work was then concentrated on three objectives. The first objective was to investigate the rudimentary photophysical properties of these **Ph-PyIm** derivatives. Research tools such as UV-Vis absorption and fluorescence spectroscopy in combination with density functional theory (DFT) calculations were employed in this thesis work to comprehensively determine the photophysical properties of the D/A substituted **Ph-PyIm** systems. Understanding of the substitution-property relationships was clearly established based on the spectroscopic and computational studies. In view of the versatile binding properties of imidazole, the development of highly efficient fluorescent chemosensors based on **Ph-PyIm** was targeted. Intramolecular charge-transfer (ICT) mechanism was conceived as a key mechanism to achieve both sensitive fluorescence recognition of anions (e.g., fluoride anion) and accurate quantification via the ratiometric sensing approach. Finally, the ability of imidazole to act as both H-bond donor and acceptor was considered for the design of organic crystalline materials with ordered supramolecular network structures. To achieve this objective, single-crystal X-ray diffraction (XRD) analysis was utilized to examine and elucidate the detailed structures of **Ph-PyIm** in the solid state. It was expected that the **Ph-PyIm** derivatives would act as controllable tectons to assemble into different solid-state network structures through specific intermolecular forces, such as hydrogen bonding, $\pi - \pi$ stacking, dipole-dipole interactions. It is worth noting that prior to this work, studies on pyrenoimidazole derivatives in the literature had been primarily focused on their electronic absorption and fluorescence properties as well as application in optoelectronic devices. Although there were a few crystal structures published, the crystallographic studies were mainly aimed at characterization of molecular

structures. Systematic crystal engineering of pyrenoimidazoles had not yet been reported in the literature prior to this thesis work. The studies carried out herein have made a new and important contribution to the field of pyrenoimidazole chemistry, which complements the current literature and significantly widens the application scope of pyrenoimidazole-based organic materials.

Chapter 2

Pyrenoimidazolyl-Benzaldehyde Fluorophores: Synthesis, Properties, and Sensing Function for Fluoride Anions

The contents of this chapter were published as a full article in *ACS Omega* **2018**, *3*, 16387–16397. Contributions of authors are described below:

Zahra A. Tabasi is the first author, who conducted the synthesis of all the pyrenoimidazole compounds and relevant spectroscopic characterizations, and contributed to the manuscript preparation and editing.

Dr. Eyad A. Younes is a co-author who assisted in density functional theory (DFT) calculations.

Joshua C. Walsh and Prof. Graham J. Bodwell are collaborators of this project,

who synthesized pyrene-4,5-dione and assisted in manuscript editing.

Profs. David W. Thompson and Yuming Zhao are the supervisors of Z. A. Tabasi, and they helped develop the concepts and design of this project. Prof. Y. Zhao is the corresponding author of this paper.

2.1 Introduction

The design and synthesis of functional organic $\pi-$conjugated molecules are of considerable importance to the field of nanoscale electronics and optoelectronics,[86–91] as research in this area continuously adds new molecular building blocks to the synthetic toolbox and accelerates the development of materials and devices in this area. Pyrene is a small polycyclic aromatic hydrocarbon (PAH) with a planar, rigid $\pi-$conjugated molecular backbone and hence exhibits fascinating photophysical, electrochemical, and supramolecular properties.[92] For decades, pyrene has been widely used as an active fluorophore in materials science. Currently, the number of pyrene-based molecules is growing rapidly owing to the great efforts made by synthetic chemists.[92–94]

9*H*-Pyreno[4,5-*d*]imidazole (PI) is a heterocycle-fused pyrene system that can be readily prepared by the condensation reaction between 4,5-pyrenedione and a suitable aldehyde in the presence of ammonium acetate.[95,96] The extended $\pi-$framework and the ability of imidazole to form complexes with various metal ions and acids have rendered PI an active component in the preparation of functional molecules, ranging from ligands for metal ions,[97] fluorescence emitters,[98–101] dye-sensitized solar cells,[84] and electrocatalysts.[96] The imidazole unit in the PI system is important

because it provides effective binding sites for the capture of anions and/or metal cations.[102–105] In particular, hydrogen bonding can occur between the imidazolyl N–H proton and various anions. Indeed, a number of PI-based sensors has relied upon these interactions. For example, Baitalik and co-workers prepared Ru(II) and Os(II) complexes containing a PI ligand and demonstrated their colorimetric and fluorescence sensing function toward a range of anions.[106,107] Fluorescence quenching was observed when these complexes were mixed with some basic anions, such as F^-, CN^-, and CH_3COO^-, due to deprotonation of the imidazolyl moiety. Acidic anions (*e.g.*, $H_2PO_4^-$), on the other hand, interacted with the pyrenoimidazolyl unit through hydrogen bonding to induce fluorescence enhancement. In 2015, a pyrene-bisimidazole system was reported by the Baitalik group and it showed significant absorption and emission responses to CN^- and Cu^{2+} ions.[108] Such properties allowed this compound to act as a ratiometric optical sensor for CN^- in aqueous media and a molecular memory device. Most recently, Karthik *et al.* reported the synthesis of a series of substituted 10-aryl-PIs and investigated their photophysical properties and reactivity toward Ru(II)-catalyzed oxidative annulation.[101]

Synthetically, aryl-PIs (particularly the phenyl-PIs) can be easily and economically prepared owing to the abundant availability of benzaldehyde precursors from commercial sources. They should therefore constitute a versatile platform for the development of novel chromophores/fluorophores with diverse functionalities and activities. In the literature, however, the family of phenyl-PIs is still underdeveloped and there is a lack of demonstration of their applicability in molecule-based optoelectronic devices, such as colorimetric and fluorescence chemosensors. Awareness of this background thus motivated us to design and characterize some

new classes of 10-phenyl-PIs in which the phenyl group is functionalized with an electron-withdrawing group. Generally speaking, the imidazolyl group is electron-accepting in nature and can provide an acidic N–H proton to interact with various anions through hydrogen bonds.[66,109–113] The hydrogen bonding interaction, in theory, polarizes the imidazolyl N–H bond to alter the electron density on the imidazolyl ring. In a phenyl-PI system such as that illustrated in Figure 2.1, intramolecular charge transfer (ICT) can conceivably occur through $\pi-$electron delocalization.[114,115] Such an effect might be expected to significantly modulate the electronic and photophysical properties, particularly the fluorescence behavior. So far, there has been no report of PI-based chemosensors that operate with an ICT mechanism. In the design of chemosensors, the ICT mechanism has often been used to achieve ratiometric fluorescence sensors, which detect analytes (*e.g.*, anions) at two or more significant emission wavelengths. For practical application, ratiometric fluorescence measurements are advantageous over the detection methods that rely on only single wavelength emission in terms of accuracy, reproducibility, and detection range.[116–121] In this work, we have investigated the fundamental properties of benzaldehyde-substituted PI systems in terms of their structural, crystallographic, and electronic properties. Furthermore, the interactions of these new PI systems with fluoride anions were examined to demonstrate the possibility of tuning this type of fluorophores to give ratiometric fluorescence sensing function for fluoride anions.

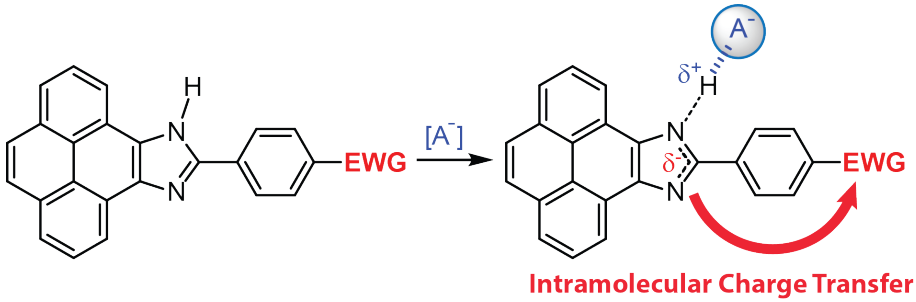

Figure 2.1: Proposed intramolecular charge transfer (ICT) occurring upon hydrogen bonding interactions between an anion (A^-) and 10-phenyl-PI bearing an electron-withdrawing group (EWG).

2.2 Results and Discussion

2.2.1 Synthesis of Pyrenoimidazolyl-Benzaldehyde (PI-BAL) Isomers 4 and 5

In this work, two PI-BAL derivatives (**4** and **5** in Scheme 2.1) were designed and synthesized. In the structures of the two compounds, an electron-withdrawing formyl group is attached to the phenyl group at the *para* and *meta* positions, respectively. The two structural isomers were expected to help understand their photophysical properties in relation to substitution patterns, particularly the effects of resonance (*para*) versus induction (*meta*). The synthesis of compounds **4** and **5** was conducted through a direct condensation reaction between the readily-available 4,5-pyrenedione (**1**)[122] and terephthalaldehyde (**2**) or isophthalaldehyde (**3**), in the presence of ammonium acetate and glacial acetic acid. In the reactions, the molar ratio of 4,5-pyrenedione (**1**) versus **2** or **3** was set as 1:3, so that only one of the formyl groups in **2** or **3** underwent condensation and the other remained intact. The

condensation reactions proceeded smoothly upon heating at 110 °C for 1 to 3 hours. Compounds **4** and **5** were obtained in reasonably good yields (50-60%) after silica flash column chromatographic separation.

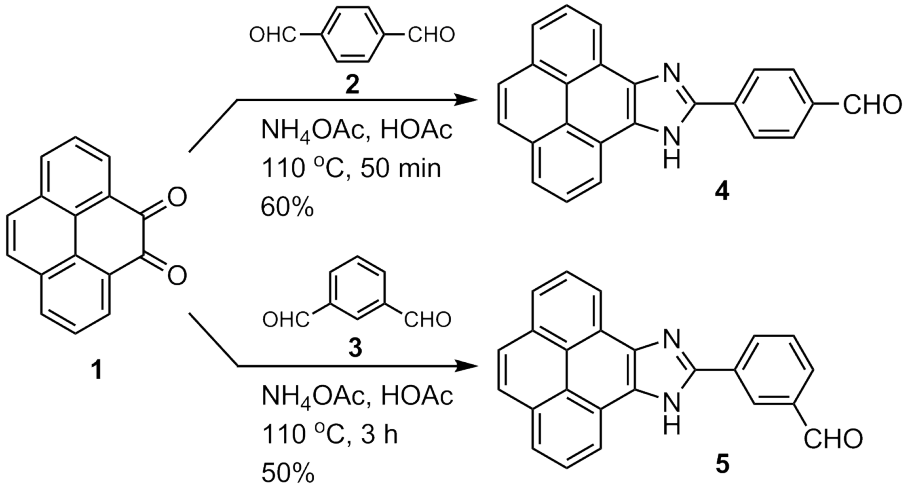

Scheme 2.1: Synthesis of PI-BALs **4** and **5**.

2.2.2 Solid-State Structural Properties

The obtained PI-BALs **4** and **5** were characterized initially by IR, MS, ^{1}H and ^{13}C NMR analyses. Detailed spectroscopic data are included in the ESI†. Recrystallization of compound **4** from acetone/hexane (3:7, v/v) resulted in the formation of crystals in different forms; fast recrystallization afforded thin orange needles, whereas slow crystallization yielded larger translucent single crystals with a brownish color. A crystal of **4** was subjected to single crystal X-ray crystallographic analysis to determine its solid-state structure.

In the crystal structure of **4**, the phenyl ring does not assume the expected co-planar orientation relative to the PI moiety, even though co-planarity is favored

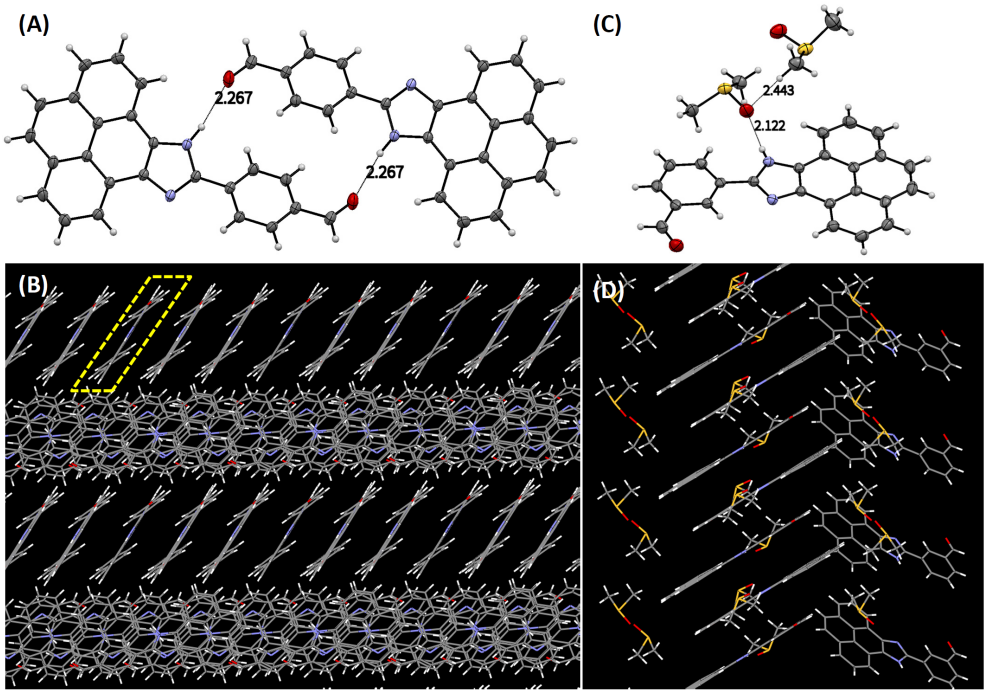

Figure 2.2: (A) ORTEP plot (50% probability) of the hydrogen-bonded dimer of PI-BAL **4** (CCDC 1851836). (B) Solid-state packing diagram of **4**. The parallelogram highlights a hydrogen bonded dimer viewed from its side.(C) ORTEP plot (50% probability) of PI-BAL **5** co-crystallized with DMSO (CCDC 1851835). (D) Solid-state packing diagram of **5**.

by maximal $\pi-$conjugation. Instead, the phenyl group is rotated by 21.6° with respect to the PI group. The slightly twisted conformation can be ascribed to crystal packing forces, since density functional theory (DFT) calculations show that the minimum-energy structure of compound **4** in the gas phase or solvents is fully planar when intermolecular interactions are not taken into consideration (*vide infra*). One interesting feature observed in the solid-state packing of compound **4** is that hydrogen bonded dimers are formed through the interactions of the imidazolyl N–H protons (donor) and the C=O oxygens (acceptor) with an intermolecular O$\cdots$H distance of

2.27 Å and an N–H$\cdots$O angle at 169.5° as shown in Figure 2.2A. In the solid state, the hydrogen bonded dimers are closely packed together through π-stacking as revealed by Figure 2.2B, and such a tight packing motif leaves no space for solvent molecules to co-crystalize. Overall, intermolecular hydrogen bonding and π-stacking are the two major factors dictating the solid-state structure of compound **4**.

PI-BAL **5** was recrystallized from a mixed solvent of hexanes/DMSO (9:1, v/v) to give dark-brown single crystals. X-ray structural analysis showed that, in contrast to **4**, the molecule of **5** adopts a fully planar conformation when packed in the solid state (see Figure 2.2C). Also of note is that two molecules of DMSO are present with compound **5** in the unit cell, whereby multiple hydrogen bonds among them can be identified. In particular, the imidazolyl N–H proton forms a significant hydrogen bond with the oxygen atom of one DMSO molecule at an O$\cdots$H distance of 2.12 Å, while another DMSO molecule interacts with the first DMSO molecule through S–O and CH_3 interactions (Figure 2.2C). The crystal structure of **5** also reveals that the phenyl and pyrenyl protons, which are in close proximity to the imidazolyl N–H group, form hydrogen bonds with the first DMSO molecule. The participation of DMSO molecules in the crystallization of **5** thus leads to a solid-state packing motif dramatically different than that of its *para*-isomer **4**. As shown in Figure 2.2D, π-stacking occurs but there are no hydrogen bonding interactions among the molecules of **5**. The association of DMSO molecules with **5** through hydrogen bonds makes the crystal packing less tight than the case of **4**.

2.2.3 Solvent Effects on UV-Vis Absorption and Fluorescence Properties

The UV-Vis absorption and fluorescence emission properties of PI-BALs **4** and **5** were studied in a range of organic solvents to assess the solvent effects. Figure 3.12 illustrates the UV-Vis and fluorescence spectra measured in three organic solvents (toluene, DMSO, and methanol) which are highlighted here to represent non-polar, dipolar aprotic, and dipolar protic solvents, respectively. For compound **4**, the UV-Vis absorption spectrum features two long-wavelength bands at 394 nm and 410 nm in toluene (Figure 3.12A). A similar pattern can be seen in the spectrum measured in benzene. When the solvents are switched to methylene chloride and chloroform, which are also non-polar in nature, only one absorption band appears in this spectral region (see Figure S-7 in the ESI for details). In view of the hydrogen-bonded dimer observed in the crystal structure of **4**, the spectral variations are rationalized as follows: in aromatic solvents (benzene and toluene), compound **4** forms a hydrogen-bonded dimer, in which the hydrogen bonds polarize the imidazolyl N–H and the C=O groups to enhance the "push-and-pull" effect, resulting in the $\pi \rightarrow \pi^*$ transition bands being bathochromically shifted. UV-Vis analysis of **4** in toluene at various concentrations (*ca.* 10^{-5} to 10^{-3} M) shows that the relative intensity of the peak at 410 nm decreases with decreasing concentration of **4** (see Figure S-11A in the ESI). When the toluene solution of **4** was titrated with methanol, the two long-wavelength bands gradually merged into one absorption peak (Figure S-11B in the ESI). Based on these experimental observations, the peak at 394 nm in toluene is attributed to the free molecule of **4**, while the peak at 410 nm is assigned to the hydrogen-bonded

dimer of **4**.

In polar solvents, the long-wavelength absorption band of **4** shows only a small degree of bathochromic shift relative to those measured in non-polar solvents. This trend generally agrees with the DFT computational analysis, which shows that in the solution phase compound **4** becomes more delocalized when the solvent polarity increases. Time-dependent density functional theory (TD-DFT) calculations reveal that the lowest-energy absorption band of **4** is mainly due to the HOMO $\rightarrow$ LUMO transition, and it does not vary very significantly in different solvents (see Table S-2 in the ESI), which is in agreement with the experimentally observed weak solvent effects in the UV-Vis analysis. Similarly, the absorption profiles of **5** show only slight variations when changing the solvent polarity from non-polar to polar (Figure 3.12C). But in methanol the UV-Vis absorption bands show notable hypsochromic shift relative to the others. It can be rationalized that in a dipolar protic solvent such as methanol the imidazolyl C=N group, which is a hydrogen bond acceptor, can form hydrogen bond(s) with the solvent molecule(s). Such interactions would be expected to cause the hypsochromic shift of UV-Vis peaks in methanol. Overall, the UV-Vis absorption analysis indicates that the $\pi \rightarrow \pi^*$ transitions in both compounds **4** and **5** are more significantly influenced by the protic nature of solvent than solvent polarity.

The fluorescence spectra of **4** and **5** exhibit a high degree of dependence on both solvent polarity and hydrogen bonding interactions. As can be seen in Figure 3.12B, the maximum emission wavelength of **4** in toluene appears at 464 nm and it is bathochromically shifted to 529 nm in DMSO, which is a hydrogen bond acceptor. In methanol, which acts as both hydrogen bond donor and acceptor, the emission of **4** is almost completely quenched. For compound **5**, the maximum emission wavelength

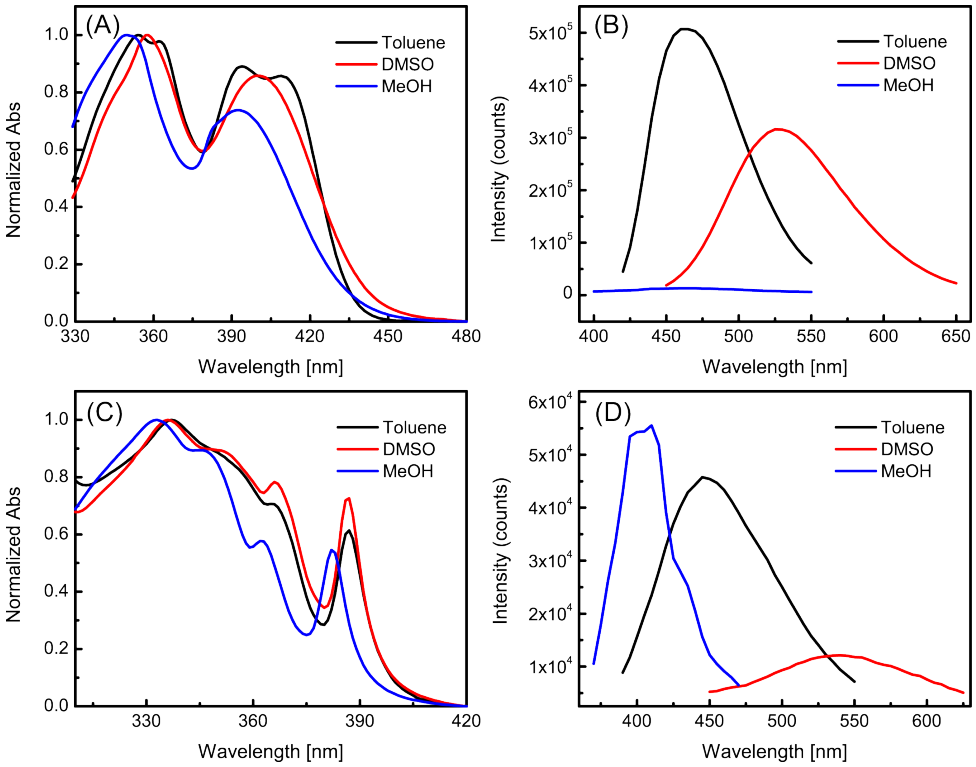

Figure 2.3: (A) Normalized UV-Vis absorption and (B) fluorescence emission spectra of **4** measured in various solvents. (C) Normalized UV-Vis absorption and (D) fluorescence emission spectra of **5** measured in various solvents.

is shifted from 445 nm (in toluene) to 542 nm (in DMSO), but in methanol it is blueshifted to 403 nm (see Figure 3.12D). The drastic solvent effects observed in the fluorescence spectra of **4** and **5** suggest that the excited states of these compounds undergo diverse radiative and non-radiative deactivation pathways which are sensitive to solvent-solute interactions; especially, the mechanism of imidazole-based excited-state proton transfer[123–126] could play an important role in the photo-excitation/deactivation processes.

2.2.4 Electrochemical Redox Properties

The electrochemical redox activities of PI-BALs **4** and **5** were examined by cyclic voltammetry (CV). As shown in Figure 2.4, compounds **4** and **5** exhibit very similar redox features in their CV profiles. In acetone, two redox couples were detected in the cyclic voltammograms of both compounds, while in DMSO the two compounds were found to undergo three distinctive redox processes in the negative potential window. The three steps of electron transfers are tentatively assigned to the injection of electrons to the benzaldehyde, imidazolyl, and pyrenyl groups respectively. The positions of the formyl group (*para* and *meta*) appear to have the same impact on the overall electrochemical redox properties of the PI-BAL system.

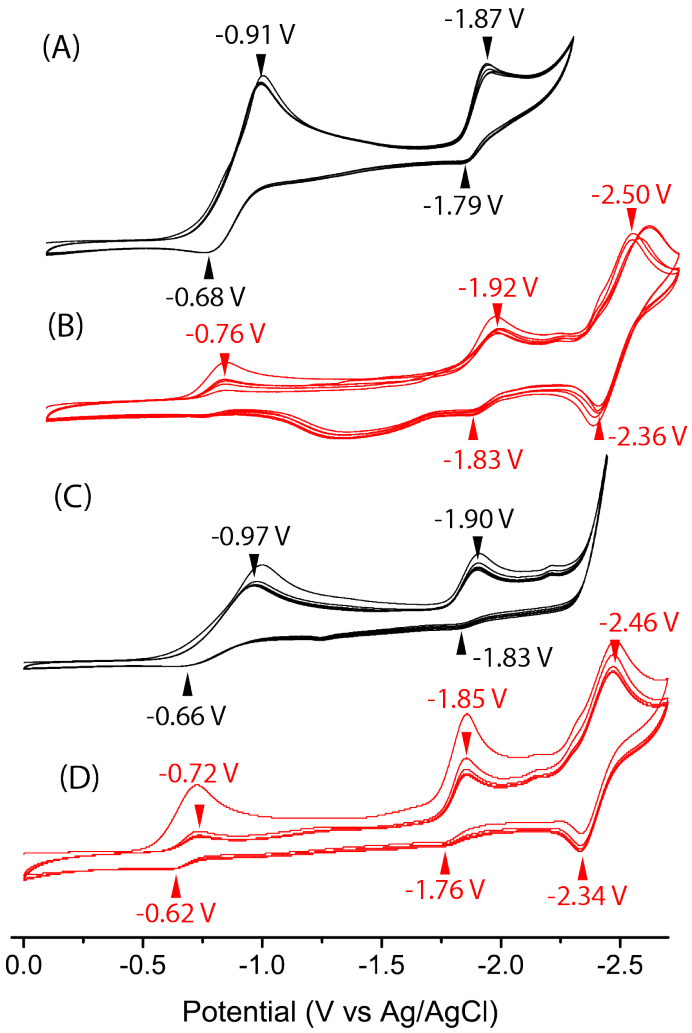

Figure 2.4: Cyclic voltammograms of PI-BAL **4** measured in (A) acetone and (B) DMSO, and PI-BAL **5** measured in (C) acetone and (D) DMSO. Experimental conditions: electrolyte: Bu_4NBF_4 (0.1 M), working electrode: glassy carbon, counter electrode: Pt wire, reference electrode: Ag/AgCl, scan rate: 100 mV/s.

2.2.5 Interactions with the Fluoride Ion

As mentioned previously, the acidic imidazolyl N–H group in the PI system can participate in hydrogen bonding interactions with various hydrogen bond acceptors (*e.g.*, anions).[66,109–113] The binding in theory would modulate the electronic properties of the PI system, leading to significant changes in electronic absorption and emission behavior. In a sense, this could serve as the mechanism for efficient colorimetric and fluorescence sensing of certain anions. To investigate these properties, PI-BALs **4** and **5** were subjected to titration with tetrabutylammonium fluoride (TBAF) as a fluoride anion source in acetone and/or DMSO, and the titration processes were monitored by ^{1}H NMR, UV-Vis absorption and fluorescence spectroscopic analyses, respectively.

Figure 2.5 shows the results of ^{1}H NMR titration of compound **4** with TBAF in acetone-d_6. Before titration, the eight pyrenyl protons of **4** appear as discrete signals without degeneracy in the ^{1}H NMR spectrum, suggesting that the imidazolyl proton (N–H) does not undergo very rapid exchange processes (*e.g.*, tautomerization) in acetone. Upon addition of TBAF at *ca.* 0.2 molar equivalent, the ^{1}H NMR spectral pattern changes immediately to feature twofold symmetry and degeneracy for the pyrenyl protons; for instance, the pyrenyl protons at the 4,5-positions (labelled as **g** and **g'** in Figure 2.5) can be now seen as a singlet in the spectra. Such an observation suggests that the interactions of fluoride anion with **4** considerably accelerate the tautomerization of the imidazolyl moiety, rendering the PI unit twofold symmetric in the ^{1}H NMR spectrum. DFT calculations show that fluoride anion can form a hydrogen bond with the imidazolyl N–H group (*vide infra*), which weakens the N–H bond and facilitates more rapid tautomerization. It is also noted that the N–H signal

at 13.04 ppm disappears after *ca.* 0.1 molar equivalent of TBAF is added, due to rapid proton exchange processes, most likely tautomerization. As the titration continues, the aldehyde proton (labelled as **a** in Figure 2.5) shows a notable upfield shift, from 10.14 ppm to 9.97 ppm, and the titration reaches an equilibrium after the addition of more than two molar equivalents of TBAF. The results suggest that PI-BAL **4** interacts with fluoride anion through two steps as outlined in Figure 2.5. In the first step, a 1:1 complex is formed through hydrogen bonding interactions, while in the second step compound **4** is deprotonated along with the formation of $[HF_2^-]$ ion.[117] During each of the two steps, the imidazolyl group experiences increased electron density which can be delocalized to the *para*-formyl group through the resonance effect, causing the aldehyde proton to significantly shift towards upfield. Some of the aryl protons of **4** also show significant upfield or downfield shifts during the titration, and these shifts can be reasonably correlated with the fluoride anion binding and subsequent deprotonation of the imidazolyl N–H group of **4**.

The electronic absorption and emission properties of compound **4** in response to the interactions with fluoride anion were examined by UV-Vis absorption and fluorescence spectroscopic analyses. Figure 2.6A shows the UV-Vis titration results of **4** with TBAF in acetone. Upon addition of TBAF from 0 to *ca.* 3 molar equivalents, the long-wavelength absorption region (*ca.* 400–520 nm) shows a steady increase in intensity and the absorption band at 355 nm decreases significantly. Two isosbestic points at 382 nm and 399 nm are clearly observable, and this stage of spectral changes can be attributed to the formation of a 1:1 complex between **4** and fluoride anion through hydrogen bonding interactions. After titration with more than 3 molar equivalents of TBAF, the UV-Vis spectra exhibit another stage of changes in which

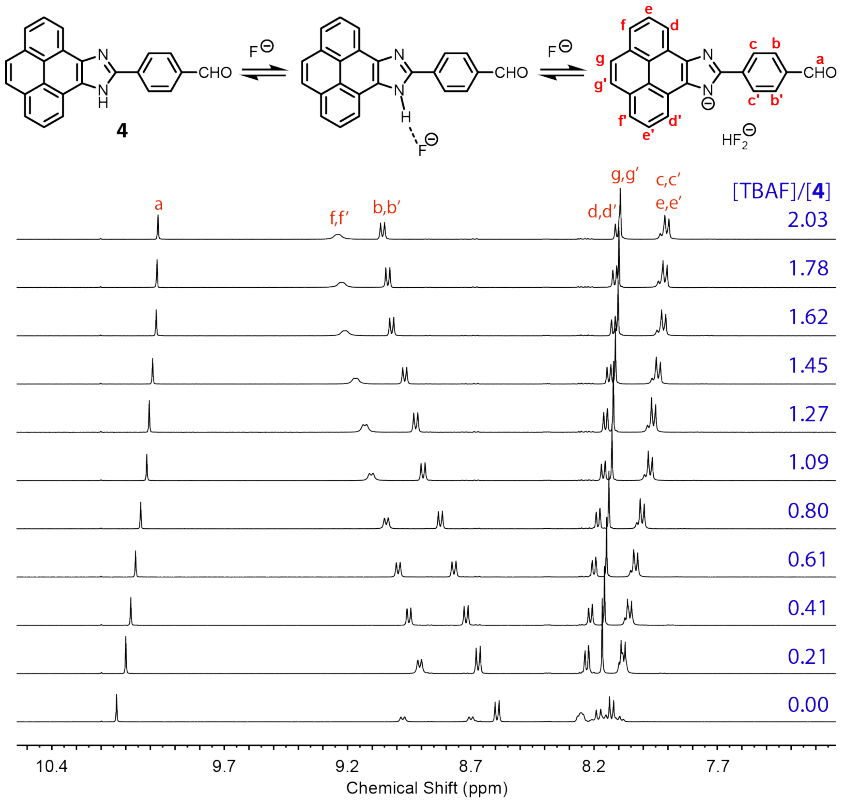

Figure 2.5: ^{1}H NMR (300 MHz) spectra monitoring the titration of PI-BAL **4** with TBAF in acetone-d_6.

a long-wavelength absorption band at 448 nm grows prominently, while the short-wavelength absorption bands in the region of 350 nm to 400 nm continuously decrease. TD-DFT calculations suggest that the strongly increasing new band is consistent with the HOMO→LUMO transition of deprotonated **4**. Accordingly, the second stage of spectral changes is linked to the deprotonation of compound **4**, through which an anionic product [**4**$^-$] is formed. This species is stabilized by the resonance effect exerted by the electron-withdrawing formyl group at the *para* position of the phenyl ring.

In DMSO, the UV-Vis absorption of **4** responds to TBAF titration in a different

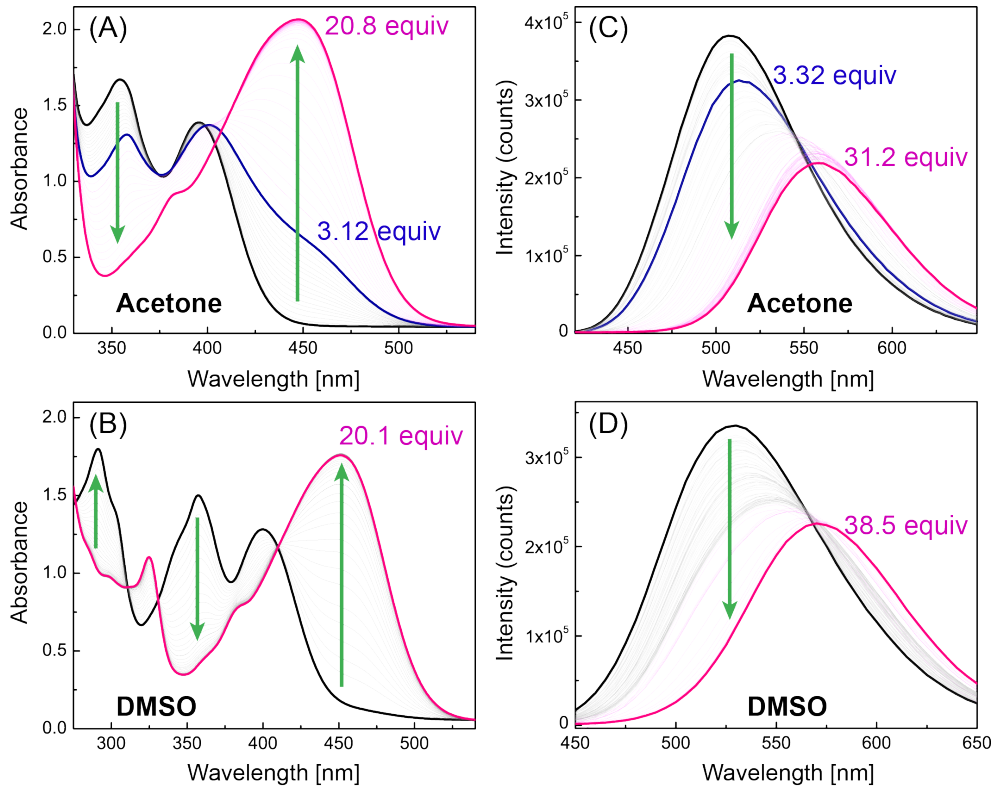

Figure 2.6: Titration of PI-BAL **4** with TBAF monitored by UV-Vis absorption spectroscopy in (A) acetone and (B) DMSO, fluorescence spectroscopy in (C) acetone and (D) DMSO.

way than in acetone. As shown in Figure 2.6B, there is only one stage of spectral changes observed during the whole process of titration, with three isosbestic points clearly observable at 409 nm, 330 nm, and 311 nm. Compared to the titration results obtained in acetone, the different spectral responses observed in DMSO suggest that in DMSO the second step (i.e., deprotonation) occurs more readily than the first hydrogen bond forming step.

Subsequent to the UV-Vis titration experiments, the fluorescence spectral changes of compound **4** upon titration with TBAF in acetone or DMSO were determined. In acetone, the maximum emission peak of **4** shows a dramatic redshift from 506 nm

to 557 nm during the titration of up to more than 30 molar equivalents of TBAF, with the intensity of emission peak attenuated by approximately 50% (see Figure 2.6C). In DMSO, similar fluorescence spectral changes can be observed (2.6D). As discussed above, the interactions of **4** with fluoride anion result in deprotonation of the imidazolyl N–H group to form a delocalized anion. The resonance effect between the imidazolyl anion and the electron-withdrawing formyl group at the *para* positions should facilitate access to an emissive charge-transfer (CT) state during the photoexcitation processes, leading to the bathochromic shift of its emission band. In this way, compound **4** behaves as an ICT fluorophore and could therefore function as an effective ratiometric fluorescence probe for the detection and quantification of fluoride anion in solution. To evaluate such sensory function, correlations of the ratio of fluorescence intensities at two different wavelengths with the concentration of TBAF were made. Herein the two fluorescence intensities were determined at the maximum emission wavelengths before the addition of TBAF and after saturation of titration was reached. As can be seen from Figure 2.7A, in acetone the ratio of fluorescence intensities at 507 nm and 561 nm versus the concentration of TBAF shows two linear relationships. In the sub-mM range the correlation features satisfactory sensitivity for quantification of fluoride anion. In DMSO (Figure 2.7B), the correlations appear to be more complex, with three linear relationships identified. The linearity in the low-concentration range (< 0.3 mM) shows the best sensitivity in terms of sensor performance, but the detection range is a bit narrower than that in acetone.

The interactions of compound **5** with TBAF in the solution phase were also studied. Figure 2.8 shows the ^{1}H NMR titration spectra obtained in acetone-d_6.

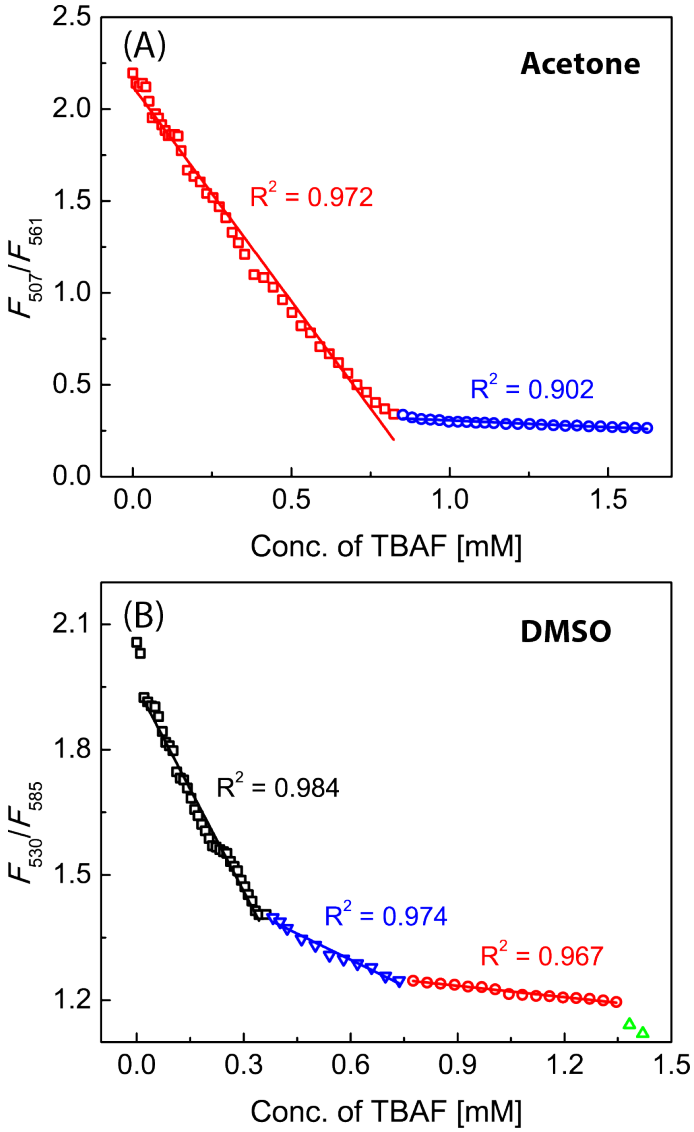

Figure 2.7: Plots of the ratio of fluorescence intensities of PI-BAL **4** at two different wavelengths against the concentration of TBAF. (A) Fluorescence intensities at 507 nm and 561 nm (F_{507}/F_{561}) in acetone, (B) fluorescence intensities at 530 nm and 585 nm (F_{530}/F_{585}) in DMSO. Solid lines are the linear least squares fitting for data points in selected ranges and associated R^2 values are indicated.

During the titration, the aldehyde proton shows an upfield shift from 10.21 ppm to 10.14 ppm. The magnitude of this shift (0.07 ppm) is significantly smaller than that

observed in the titration of **4** with TBAF (0.17 ppm). This can be explained by the *meta* relationship between the formyl group and the PI unit, which precludes a direct resonance interaction between the negatively-charged N atom and the formyl group. It is also interesting to note that the chemical shifts of the other aryl proton signals all change only slightly during the addition of the first equivalent of TBAF. This observation suggests that the formation of a 1:1 complex between **5** and fluoride anion does not polarize the imidazolyl N–H bond as much as in the case of **4**. In principle, the imidazolyl N–H of **5** is less acidic than that of **4** due to the lack of a direct resonance interaction with the formyl group. As such, **5** is predicted to form a weaker hydrogen bond with fluoride ion than its *para*-isomer **4**. This point is corroborated by DFT computational analysis (*vide infra*).

The results of the UV-Vis titration of PI-BAL **5** with TBAF in acetone and DMSO are shown in Figure 2.9A and B. As in the case of its *para*-isomer **4**, the UV-Vis absorption of **5** shows a two-stage response to fluoride anion in acetone. Upon titration from 0 to *ca.* 3.9 molar equivalents of TBAF, the spectra shows an increase in absorption intensity in the long-wavelength region (390–480 nm) and a slight decrease in intensity in the short-wavelength region. There are three isosbestic points observed at 386 nm, 382 nm, and 368 nm in the first stage of spectral change. In the second stage, a long-wavelength band at 409 nm grows pronouncedly and it can be assigned to the $\pi \rightarrow \pi^*$ transition of the deprotonated **5** upon interactions with the second equivalent of fluoride anion. In DMSO, the UV-Vis absorption spectra only exhibit a one-stage responses to the titration with TBAF, with five isosbestic points observed at 388 nm, 384 nm, 375 nm, 337 nm, and 307 nm. In contrast to the fluorescence titration results of **4**, *meta*-pyrenoimidazolyl benzaldehyde **5** responds to

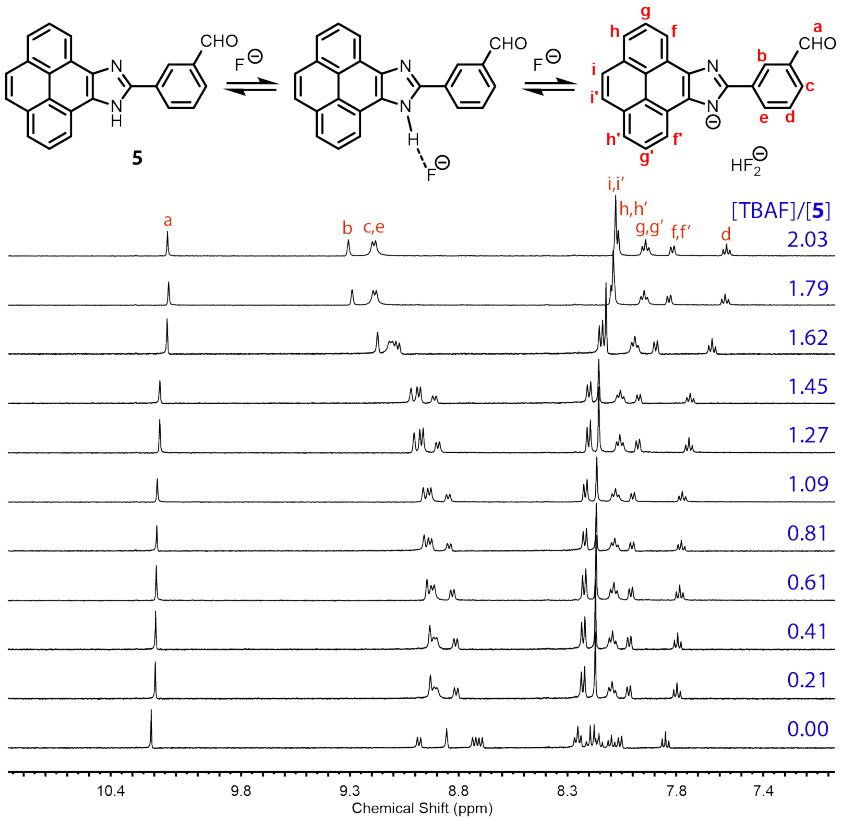

Figure 2.8: ^{1}H NMR (300 MHz) spectra monitoring the titration of PI-BAL **5** with TBAF in acetone-d_6.

fluoride ion in acetone and DMSO with only fluorescence attenuation (see Figure 2.9C and D). Comparing the different fluorescence behavior of the two structural isomers, **4** and **5**, in response to fluoride anion titration, it is evident that the resonance effect plays a crucial and indispensable role in inducing ICT emission for the PI system. Further understanding of the detailed structure-photophysical property relationship will be of great value for the rational design and tuning of highly efficient and sensitive fluorescence sensors based on the PI fluorophore.

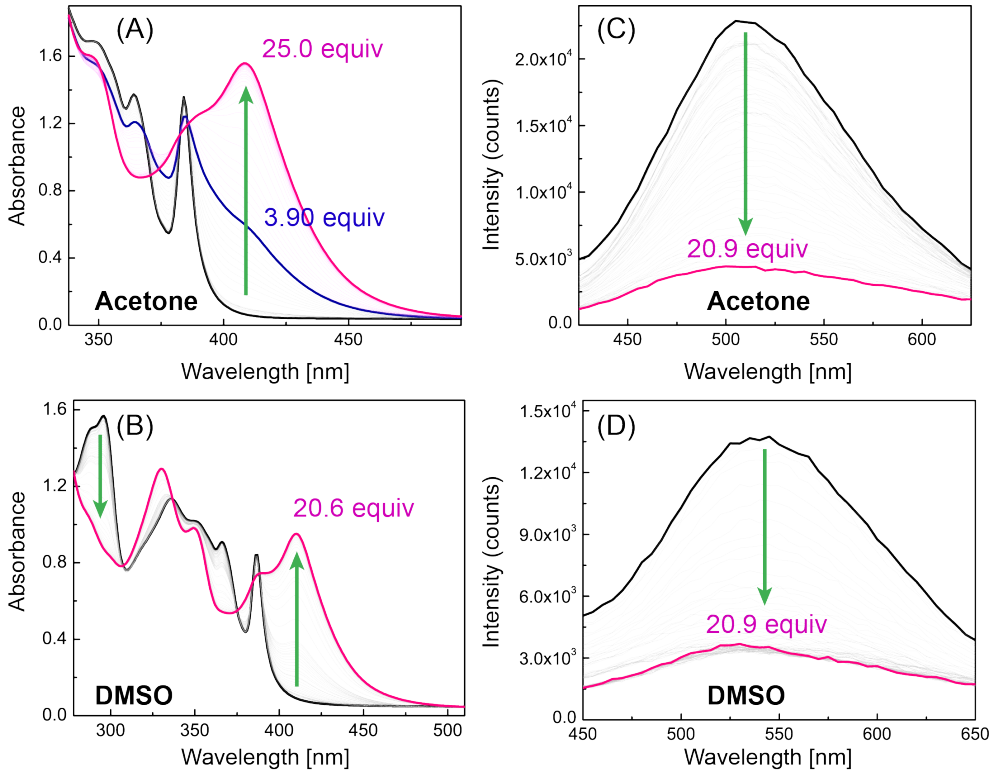

Figure 2.9: Titration of PI-BAL **5** with TBAF monitored by UV-Vis absorption spectroscopy in (A) acetone and (B) DMSO, fluorescence spectroscopy in (C) acetone and (D) DMSO.

2.2.6 Theoretical Modelling Studies

DFT computational analysis was carried out on PI-BALs **4** and **5** to gain deeper insight into their structural and electronic properties. Figure 2.10 illustrates the optimized ground-state structures of compounds **4** and **5** in the gas phase, with their frontier molecular orbitals (FMOs) displayed as well. It can be seen that the major differences between the structural isomers lie in their unoccupied (anti-bonding) orbitals (*e.g.*, LUMO and LUMO + 1), while the occupied (bonding) orbitals (HOMO and HOMO – 1) of the two compounds appear to be very similar in shape and spatial distribution. Owing to the resonance effect, the LUMO of *para*-isomer **4**

is more delocalized than that of *meta*-isomer **5**. For the LUMO + 1 of *meta*-isomer **5**, however, the orbital exhibits more extended spatial distribution than that of *para*-isomer **4**. Also of note is that *para*-isomer **4** has a smaller HOMO–LUMO gap (3.04 eV) than *meta*-isomer **5** (3.23 eV) because of the resonance effect. The different FMO energies and distributions thus account for their different electronic transition properties in the ground and excited states.

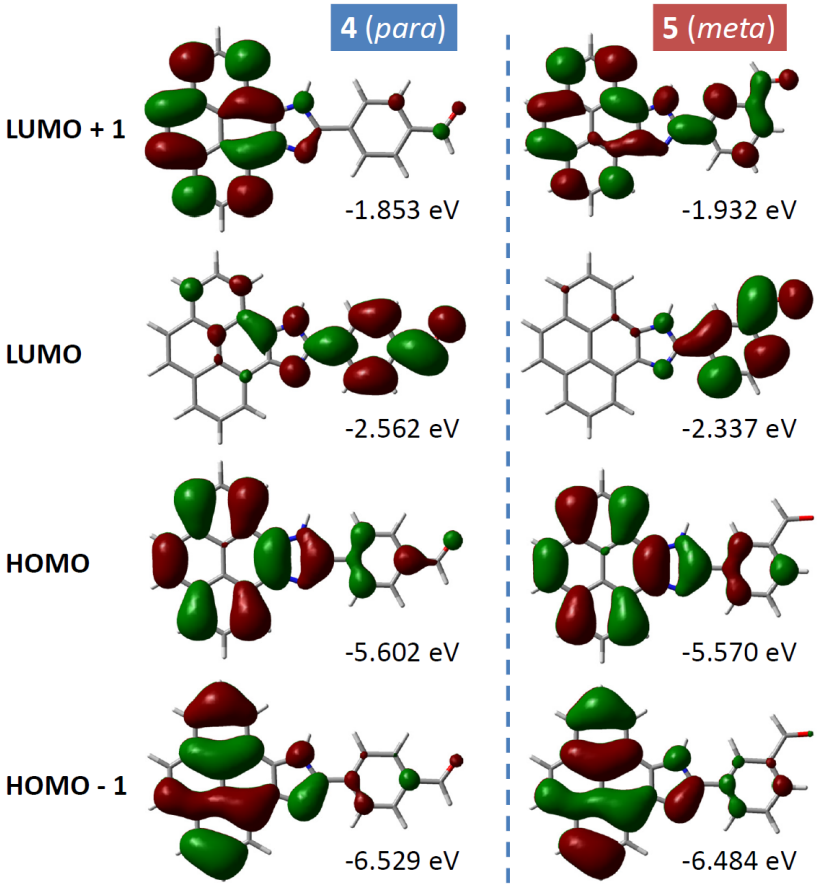

Figure 2.10: Contour plots (isovalue = 0.02 e/Å^3) and eigenvalues of frontier molecular orbitals (FMOs) for PI-BALs **4** and **5** calculated at the B3LYP/6-31++G(d,p) level of theory in the gas phase.

To better understand the interactions (particularly, hydrogen bonding) between PI-BALs and fluoride anion, the 1:1 complexes of [**4**$\cdots F^-$] and [**5**$\cdots F^-$] were modelled by DFT calculations. Herein the computational studies took both the gas and solution phases into consideration, with three representative solvents (benzene, acetone, and DMSO). As shown in Figure 2.11A, the fluoride anion binds with compound **4** through three hydrogen bonding interactions in the gas phase. The primary binding force comes from the imidazolyl N–$H_1\cdots F^-$ interaction, while the pyrenyl proton H_1 and phenyl proton H_3 also contribute hydrogen bonds to bind with the fluoride anion in a way similar to the [DMSO$\cdots$**5**] interactions observed in the crystal structure of **5** (Figure 2.2C). In the gas phase, $H_1\cdots F^-$ shows a bond distance at 1.04 Å and N–H_1 distance at 1.42 Å, indicating a significant degree of deprotonation at the imidazolyl N–H position upon binding with fluoride ion. The nature of the bonding interactions between **4** and F^- were also assessed by quantum theory of atoms in molecules (QTAIM) analysis.[127] Through the analysis, three bond critical points (BCPs) were identified between F^- anion and each of the three protons labelled as H_1, H_2, and H_3 in Figure 2.11. The imidazolyl $H_1\cdots F^-$ interaction shows a weak covalent bond character, with ρ(BCP) = 0.240 a.u. and $\nabla^2\rho$(BCP) = -0.879. The two BCPs between F^- and pyrenyl H_2/phenyl H_3 show similar ρ(BCP) values(*ca.* 0.011–0.013 a.u.), which are in the range of 0.002 to 0.040 a.u. for a hydrogen bond.[128,129] In the solution phase, however, the $H_1\cdots F^-$ bond elongates and the imidazolyl N–H_1 bond shortens with increasing solvent polarity, suggesting that the degree of N–H deprotonation is attenuated in polar organic media. QTAIM analysis also reveals that the $H_1\cdots F^-$ interaction is weakened to exhibit a hydrogen bond character in polar organic solvents (see Table S-8 in the ESI for details).

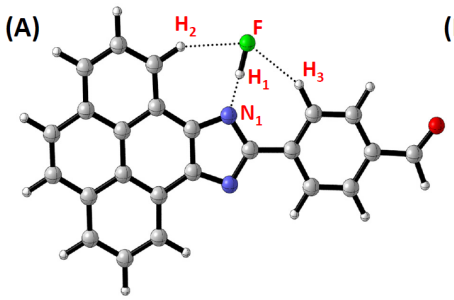

	Bond distance (Å)			
	N_1–H_1	F–H_1	F–H_2	F–H_3
Gas	1.42	1.04	2.33	2.27
Benzene	1.32	1.11	2.34	2.24
Acetone	1.11	1.37	2.37	2.19
DMSO	1.11	1.38	2.37	2.19

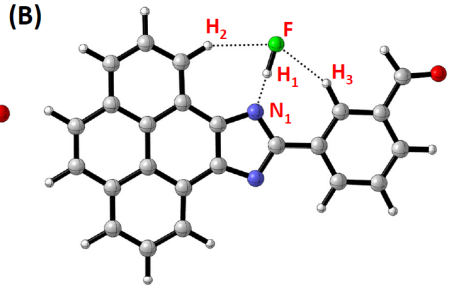

	Bond distance (Å)			
	N_1–H_1	F–H_1	F–H_2	F–H_3
Gas	1.39	1.06	2.38	2.22
Benzene	1.22	1.20	2.35	2.19
Acetone	1.11	1.39	2.40	2.16
DMSO	1.10	1.40	2.40	2.17

Figure 2.11: Optimized geometries of the 1:1 complexes of (A) $[\mathbf{4}\cdots F^-]$ and (B) $[\mathbf{5}\cdots F^-]$ in the gas phase at the B3LYP/6-31++G(d,p) level of theory, and variation of hydrogen bond distances in different solvents calculated by the PCM solvent model.

For the optimized structures of $[\mathbf{5}\cdots F^-]$ in the gas phase and various solvents (see Figure 2.11B), the N–H_1 and $H_1\cdots F^-$ bonds are shorter than those of $[\mathbf{4}\cdots F^-]$. These results suggest that the N–$H_1\cdots F^-$ interaction in $[\mathbf{5}\cdots F^-]$ is relatively weak. Again, this can be attributed to the *meta* relationship between the formyl group and the imidalzolyl unit in **5**, which rules out a direct resonance interaction between them. To quantitatively assess the thermodynamic properties of the fluoride anion interactions with **4** and **5**, the Gibbs free energy changes (ΔG°) for the 1:1 complexation reactions between fluoride anion with **4** and **5** and subsequent deprotonation reactions in the gas phase and various solvents were computed. Scheme 2.2 lists the detailed thermodynamic data, which show that the two steps of fluoride interactions are both exergonic and increasing the solvent polarity reduces the thermodynamic driving force significantly.

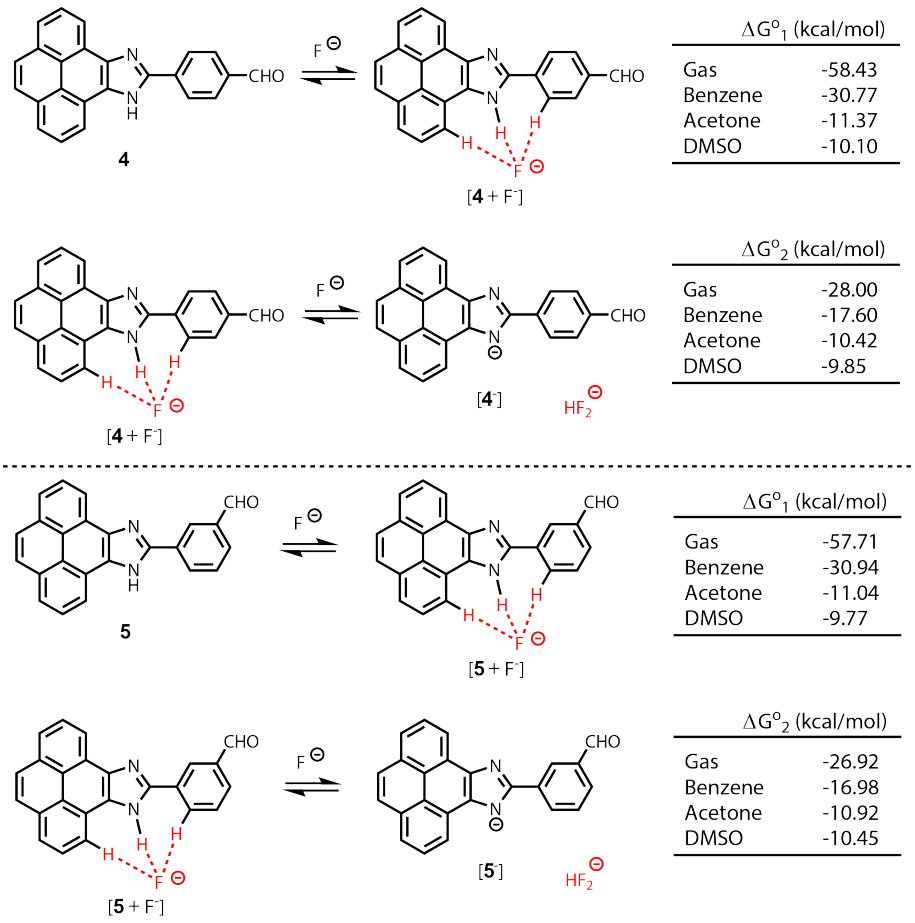

	ΔG^{o}_{1} (kcal/mol)
Gas	-58.43
Benzene	-30.77
Acetone	-11.37
DMSO	-10.10

	ΔG^{o}_{2} (kcal/mol)
Gas	-28.00
Benzene	-17.60
Acetone	-10.42
DMSO	-9.85

	ΔG^{o}_{1} (kcal/mol)
Gas	-57.71
Benzene	-30.94
Acetone	-11.04
DMSO	-9.77

	ΔG^{o}_{2} (kcal/mol)
Gas	-26.92
Benzene	-16.98
Acetone	-10.92
DMSO	-10.45

Scheme 2.2: Gibbs free energy changes for the interactions of **4** and **5** with fluoride ion in the gas phase and various solvents.Calculated at the B3LYP/6-31++G(d,p) with the PCM model used for solvents.

2.3 Conclusions

In conclusion, we have synthesized and studied the structural and electronic properties of two structural isomers of PI-BALs. Hydrogen bonding interactions have been found to play an important role in the solid-state structures of these compounds. Of particular note is that *para*-isomer **4** tends to form hydrogen-bonded dimers while *meta*-isomer can co-crystalize with hydrogen bond acceptors, such as DMSO.

Significant solvents effects were observed in the UV-Vis absorption and fluorescence emission properties of compounds **4** and **5**. Cyclic voltammetric studies show that both compounds **4** and **5** have similar redox activities in polar solvents (acetone and DMSO). In the presence of fluoride anion, the two compounds undergo similar two-step reactions in polar solvents: (i) forming a hydrogen-bonded 1:1 complex, and (ii) deprotonation of the imidazolyl N–H group. The UV-Vis absorption spectra of the two compounds in response to fluoride ion titration are similar, showing colorimetric responses as a result of fluoride-induced deprotonation of the PI chromophore. The fluorescence responses of **4** and **5** to fluoride anion titration, however, are dramatically different. For *para*-isomer **4** the fluorescence is retained to some extent but the maximum emission band is bathochromically shifted. Such properties enable compound **4** to act as a fluorescence ratiometric sensor for detection of fluoride ion in solution. The interactions of fluoride anion with *meta*-isomer **5**, on the other hand, results in fluorescence attenuation. Comparison of the fluorescence properties of the two pyrenoimidazolyl benzaldehyde isomers underscores the key role of the resonance effect in inducing the ICT mechanism. Our current studies lay a fundamental foundation for further efforts to design and develop new functional ICT fluorophores based on the PI motif.

2.4 Experimental Section

Reagents and solvents were purchased from commercial sources and used without purification unless otherwise noted. ^{1}H and ^{13}C NMR spectra were recorded on a Bruker 300 MHz Advance III spectrometer. Infrared (IR) spectra were recorded

using a Bruker Alfa spectrometer. High resolution APPI-TOF MS analyses were performed on a GCT premier Micromass Technologies instrument. UV-Visible absorption spectra were recorded using a Cary 6000i spectrophotometer. Fluorescence spectra were measured on a Photon Technology International (PTI) quantamaster spectrofluorometer. Cyclic voltammetry analyses were performed on a standard three-electrode setup (glassy carbon working electrode, Ag/AgCl reference electrode, and Pt wire counter electrode) controlled by a BASi Epsilon potentiostat. Single crystal X-ray diffraction analysis was conducted on a Bruker D8/APEX II CCD diffractometer equipped with a Cu-Kα (1.54178 Å) microfocus source. Crystal structures were solved and refined with the SHELXL software package. DFT and TD-DFT computational studies were carried out using the hybrid B3LYP functional[130,131] with the 6-31++G(d,p) basis set as implemented in the Gaussian 09 software package.[132] Optimized ground-state geometries were confirmed by frequency calculations to show the presence of no imaginary frequencies. Solvent effects were calculated using the polarizable continuum model (PCM)[133] implemented in Gaussian 09. Visualization of molecular structures and orbitals were done using CYLview[134] and GaussView 5.[135] QTAIM analysis was carried out using the Multiwfn program.[136]

Synthesis of compound 4. A mixture of 4,5-pyrenedione (**1**) (0.200 g, 0.861 mmol), terephthalaldehyde (**2**) (0.350 g, 2.58 mmol), ammonium acetate (1.33 g, 17.2 mmol), and glacial acetic acid (99.7%, 7 mL) was heated at 110 °C for 50 min. The solution was slowly cooled to room temperature and the resulting precipitate was collected by vacuum filtration and sequentially washed with glacial acetic acid, saturated aqueous $NaHCO_3$ solution and water. The crude product was purified by

silica flash column chromatography using acetone/hexanes (3:7, v/v) as eluent to afford pure compound **4** as an orange solid (0.178 g, 0.516 mmol, 60%). mp > 280 °C (decomp.); FTIR (neat): 3361, 3052, 2849, 1662, 1602, 1569, 1432, 1162, 821, 713 cm^{-1}; ^{1}H NMR (300 MHz, DMSO-d_6): δ 14.00 (s, 1H), 10.12 (s, 1H), 8.86 (d, J = 8.5 Hz, 2H), 8.60 (d, J = 8.3 Hz, 2H), 8.34–8.19 (m, 8H) ppm; ^{13}C NMR (75 MHz, DMSO-d_6): δ 192.6, 148.0, 138.0, 136.0, 135.4, 131.6, 131.4, 130.2, 128.9, 127.9, 127.4, 126.5, 126.3, 126.0, 124.7, 124.4, 122.0, 121.5, 119.2, 119.1 ppm; HRMS (APPI–TOF, positive mode): m/z calcd for $C_{24}H_{15}N_2O$ $[M + H]^+$ 347.1184, found 347.1172.

Synthesis of compound 5. A mixture of 4,5-pyrenedione (**1**) (0.200 g, 0.861 mmol), isophthalaldehyde (**3**) (0.350 g, 2.58 mmol), ammonium acetate (1.33 g, 17.2 mmol), and glacial acetic acid (99.7%, 7 mL) was heated at 110 °C for 3 h. The solution was slowly cooled to room temperature and the resulting precipitate was collected by vacuum filtration and sequentially washed with glacial acetic acid, saturated aqueous solution of $NaHCO_3$ and water. The crude product was purified by silica flash column chromatography using acetone/hexanes (1:9, v/v) as eluent to afford pure compound **5** as a dark brown solid (0.149 g, 0.430 mmol, 50%). mp > 272 °C (decomp.); FTIR (neat): 3341, 3033, 2916, 2815, 2732, 1685, 1604, 1446, 1309, 1280, 1181, 977, 908, 831, 722, 674 cm^{-1}; ^{1}H NMR (300 MHz, DMSO-d_6): δ 13.96 (s, 1H), 10.21 (s, 1H), 8.93–8.80 (m, 3H), 8.73–8.69 (m, 1H), 8.30–8.13 (m, 6H), 8.09–8.05 (m, 1H), 7.88 (t, J = 7.7 Hz, 1H); ^{13}C NMR (75 MHz, DMSO-d_6): δ 193.1, 161.9, 148.2, 137.6, 136.9, 131.8, 131.6, 131.4, 131.2, 130.7, 130.0, 128.5, 127.9, 127.5, 126.4, 126.3, 126.2, 126.0, 124.4, 124.3, 121.90, 121.86, 121.6, 119.0 ppm; HRMS (APPI–TOF, positive mode): m/z calcd for $C_{24}H_{15}N_2O$ $[M + H]^+$ 347.1184, found

347.1173.

Chapter 3

Crystal Engineering and Photophysical Properties of Phenyl-Pyrenoimidazole Systems

The contents of this chapter were published as a full article in *Cryst. Growth Des.* **2020**, *20*, 1681–1693. Contributions of authors are described below:

Zahra A. Tabasi is the first author, who conducted the synthesis of all the pyrenoimidazole compounds, growth of all the single crystals, and relevant spectroscopic characterizations. She also contributed to the manuscript preparation and editing.

Joshua C. Walsh and Prof. Graham J. Bodwell are collaborators of this project, who synthesized pyrene-4,5-dione and assisted in manuscript editing.

Profs. David W. Thompson and Yuming Zhao are the supervisors of Z. A. Tabasi, and they helped develop the concepts and design of this project. Prof. Y. Zhao is the

corresponding author of this paper.

3.1 Introduction

Organic fluorophores with rigid and extended π-frameworks have captured enormous interest in the field of organic electroluminescent materials and light-emitting devices.[137–139] Fused polycyclic aromatic hydrocarbons (PAHs) containing imidazole units such as 1*H*-phenanthro[9,10-*d*]imidazole (**Phen-Im**, Figure 3.1) and its derivatives have been particularly attractive owing to their easy synthesis, rich photophysical properties, and intriguing application in organic light emitting materials and chemical sensors.[140–146] Fusion of a pyrene system to imidazole gives a more extended analogue of **Phen-Im**, namely 9*H*-pyreno[4,5-*d*]imidazole (**Py-Im**). Over the past years, growing efforts have been dedicated to the studies of π-conjugated systems derived from **Py-Im**; however, the family of **Py-Im** derivatives is still relatively small, and their fundamental properties and potential application require continued exploration.

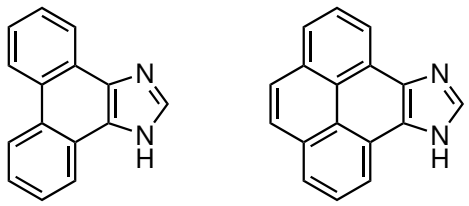

Phen-Im **Py-Im**

Figure 3.1: Molecular structures of **Phen-Im** and **Py-Im**.

In the literature, a number of **Py-Im** derivatives has been synthesized and investigated as useful materials for chemical sensors, light-emitting devices, organic

solar cells, and electrocatalysis.[68,80,84,95,98–101,147] In many of these applications the non-covalent forces arising from the **Py-Im** core, such as π-π stacking, hydrogen bonding, and C–H$\cdots\pi$ interactions, play pivotal roles in material properties and device performance.[68,99,101] Recently, we reported a study of two **Py-Im** derivatives bearing *para*-benzaldehyde and *meta*-benzaldehyde groups (**3f** and **3g**, Scheme 3.1).[148] Some of the imidazolyl and pyrenyl protons in these molecules were found to show hydrogen bonding interactions with fluoride anion in solution, resulting in significant photophysical responses that brought about colorimetric and fluorescence turn-on sensing functions. Besides the sensory properties, it was also observed that the solid-state structures of the two compounds are very different from one another. Clearly, substituent groups attached to **Py-Im** impose a pronounced effect on their solid-state structures. In the literature, single crystal structures of **Py-Im** derivatives have been sparsely documented.[68,99,101] In-depth understanding of their solid-state properties, especially the correlation between molecular structure and crystal packing, may be of great value for crystal engineering and could eventually fuel the development of novel **Py-Im** based materials with broad applications in advanced organic optoelectronics.

In this work, we systematically analyzed the crystal packing properties of a series of **Py-Im** derivatives and some correlations with substitution effects were observed. Molecular electrostatic potential (MEP) analysis based on density functional theory (DFT) calculations was utilized as an effective tool to investigate the roles of significant non-covalent forces (e.g., hydrogen bond and π-π stacking) in solid-state supramolecular organization. Furthermore, the effects of substituents on the electronic and photophysical properties of **Py-Im** systems were assessed by UV-Vis

absorption, fluorescence, and NMR spectroscopic analyses in conjunction with time-dependent density functional theory (TD-DFT) studies. Our results have established a deeper understanding of their structure-photophysical property relationships.

3.2 Methodology

3.2.1 Materials

All reagents were purchased from commercial suppliers and used as received without further purification. All reactions were carried out in standard glassware. Thin layer chromatographic (TLC) analysis was done on TLC sheets pre-coated with silica gel with UV_{254} fluorescent indicator (Macherey-Nagel), and flash silica column chromatographic purification was performed through SilicaFlash silica gel (230–400 mesh, Silicycle Inc.)

3.2.2 Characterizations

^{1}H and ^{13}C NMR spectra were recorded on a Bruker 300 MHz AVANCE III spectrometer. Infrared (IR) spectra were recorded on a Bruker Alfa spectrometer. High-resolution mass spectrometric (HRMS) analyses were performed on a GCT premier Micromass Technologies instrument. UV–Vis absorption spectra were recorded using a Cary 6000i spectrophotometer. Fluorescence spectra were measured on a Photon Technology International (PTI) QuantaMaster spectrofluorometer. Relative fluorescence quantum yields (ϕ_F) were measured following reported procedures[149,150] using quinine sulfate ($\phi_F = 0.546$) as the standard. Single crystal

X-ray diffraction (XRD) analysis was performed on a Bruker PLATFORM/APEX II CCD diffractometer, and the crystal structures were solved by direct methods using the SHELXD program[151] and refined by full-matrix least-squares methods with SHELXL–2014.[152]

3.2.3 Computational Methods

In the DFT computational studies, molecular geometry optimization was performed using the M06-2X/Def2-SV(P) method[153,154] implemented in the Spartan'18 Parallel Suite.[155] Each optimized geometry was then subjected to frequency calculation to confirm that it is a ground-state minimum (zero imaginary frequencies). Electrostatic potential maps were calculated at the same level of theory by using Spartan'18. For quantum theory of atoms in molecules (QTAIM) analysis, the molecular geometries were taken from corresponding crystal structures and then subjected to single-point calculations at the M06-2X/Def2-SV(P) level using the Gaussian 16 software packages.[156] The Gaussian output files were subjected to QTAIM analysis using the Multiwfn software[136] and the results were visualized by using the VMD software package.[157] TD-DFT calculations were performed using Gaussian 16 at the B3LYP/6-311+G(d,p) level of theory and based on the ground-state molecular geometries optimized at the M06-2X/Def2-SV(P) level.

3.3 Results and Discussion

3.3.1 Synthesis of Py-Im Derivatives

The synthesis of eight **Py-Im** derivatives (**3a**–**h**) was carried out through a one-pot condensation reaction between 4,5-pyrenedione (**1**)[50] and the corresponding benzaldehydes (**2a**–**h**) respectively in the presence of NH_4OAc and glacial acetic acid. Of the eight **Py-Im** derivatives, **3b**–**d** are new compounds, while the synthesis of the other five compounds was previously reported.[101,148] The reactions were conducted at 110 °C for varied periods of time depending on the benzaldehyde that was used to afford the corresponding **Py-Im** products **3a**–**h** (46–85%). Benzaldehydes with strong electron-withdrawing groups (e.g., NO_2, CHO) were found to undergo the condensation reactions considerably faster than those carrying electron-donating groups (e.g., OMe, CH_3). The eight **Py-Im** derivatives were characterized by NMR, IR, and HRMS analyses, which both confirmed the structures and provided evidence of purity. Details are given in the Supporting Information.

3.3.2 Single Crystal X-Ray Structural Analysis

Single crystals of compounds **3a**–**c** and **3e**–**h** were successfully grown in different organic solvent systems. Their molecular structures and solid-state packing properties were examined by single crystal XRD analysis. Their crystallographic properties are discussed in the following section with emphasis on the dominant supramolecular assembly features that are present.

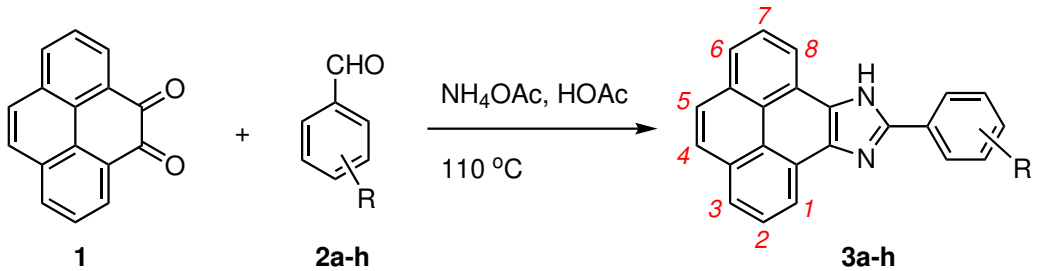

Entry	R	Time (h)	Yields of **3** (%)	Entry	R	Time (h)	Yields of **3** (%)
a	H	12	62	**e**	4-OMe	8	46
b	4-Me	12	48	**f**	3-CHO	2	50
c	4-Cl	5	57	**g**	4-CHO	0.8	60
d	4-Br	5	44	**h**	4-NO_2	2	85

Scheme 3.1: Synthesis of substituted **Py-Im** derivatives **3a**–**h** via condensation reactions.

3.3.2.1 Linear hydrogen bonded imidazole networks

Py-Im 3a was found to pack in a monoclinic $P2_1/c$ space group in the crystalline state. The molecule of **3a** (Figure 3.2A) shows a slightly twisted conformation with a torsion angle of 26.3° between the phenyl ring and pyrenoimidazolyl unit. The unit cell comprises four molecules which can be divided into two pairs. In each pair of molecules there is an intermolecular hydrogen bond between the adjacent imidazolyl groups, with the NH$\cdots$N distance at 2.048 Å and the N–H$\cdots$N angle at 169.5°. The two hydrogen bonded molecules are oriented at an interplanar angle of 89.7° between the pyrenoimidazolyl moieties. Among the pairs, close π-π interaction can be seen between the pyrenyl units at an interplanar distance of 3.478 Å (Figure 3.2B). Viewing along the direction of hydrogen bonded imidazolyl groups, one can also see the arrangement of an infinite linear network (Figure 3.2C), which is similar to the crystal structures of benzimidazole[158] and phenanthroimidazole[159] reported in the literature.

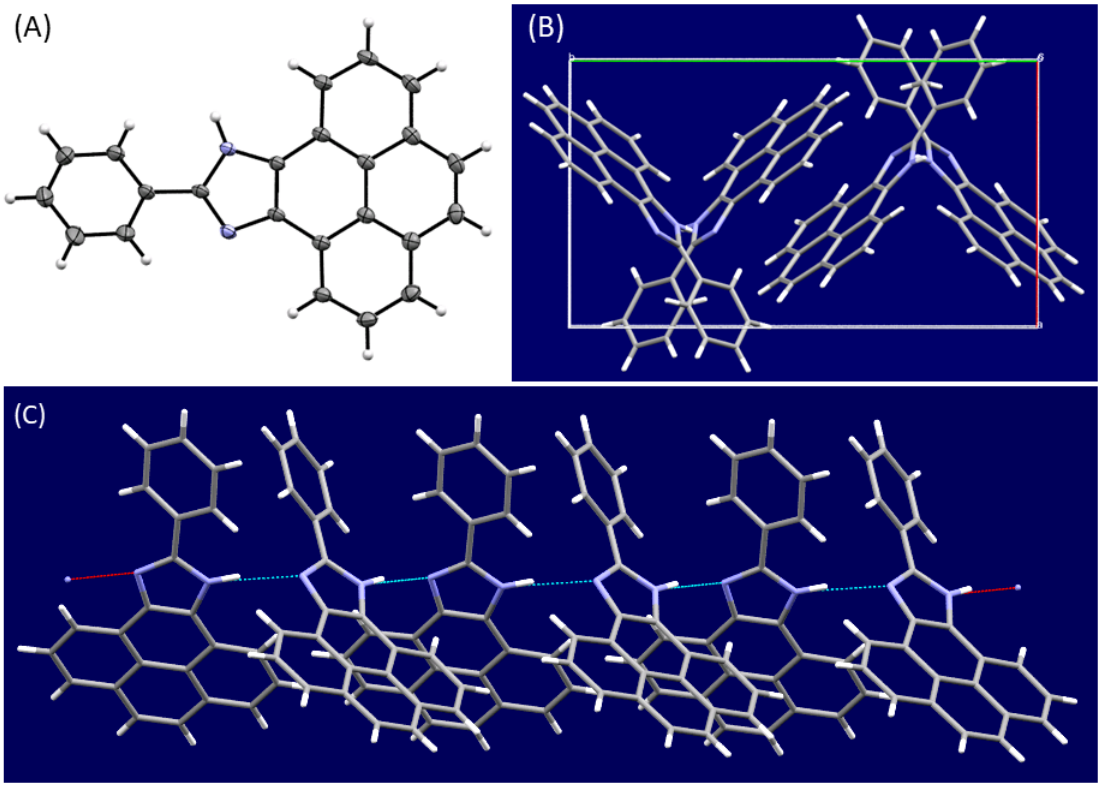

Figure 3.2: (A) ORTEP diagram of compound **3a** (50% ellipsoid probability). (B) Packing of **3a** molecules in the unit cell viewed along the c axis. (C) Linear network of **3a** molecules assembled via imidazolyl hydrogen bonds. CCDC 1851837.

Compound **3b** was found to co-crystalize with acetone in the monoclinic $P2_1/c$ space group similar to **3a**. As shown in Figure 3.3A, the torsion angle between tolyl and pyrenoimidazolyl groups is 24.5°, which is slightly smaller than that of **3a**. The unit cell contains four molecules of **3b** and four molecules of acetone. Like the packing of **3a**, both hydrogen bonding and π-π stacking play important roles in the solid-state structure of **3b**. For the hydrogen bonding interactions, the NH$\cdots$N distance is at 2.105 Å and the N–H$\cdots$N angle at 169.6°. Along the hydrogen bonding direction, a linear hydrogen bonded network is formed as well (Figure 3.3C), but the interplanar

angle between each adjacent pair of hydrogen bonded pyrenoimidazolyl moieties is 62.1°, which is significantly smaller than that of **3a**. The presence of a *para*-CH_3 group in **3b** gives rise to void space in its solid-state packing, which is filled with acetone molecules to form co-crystals (Figure 3.3C).

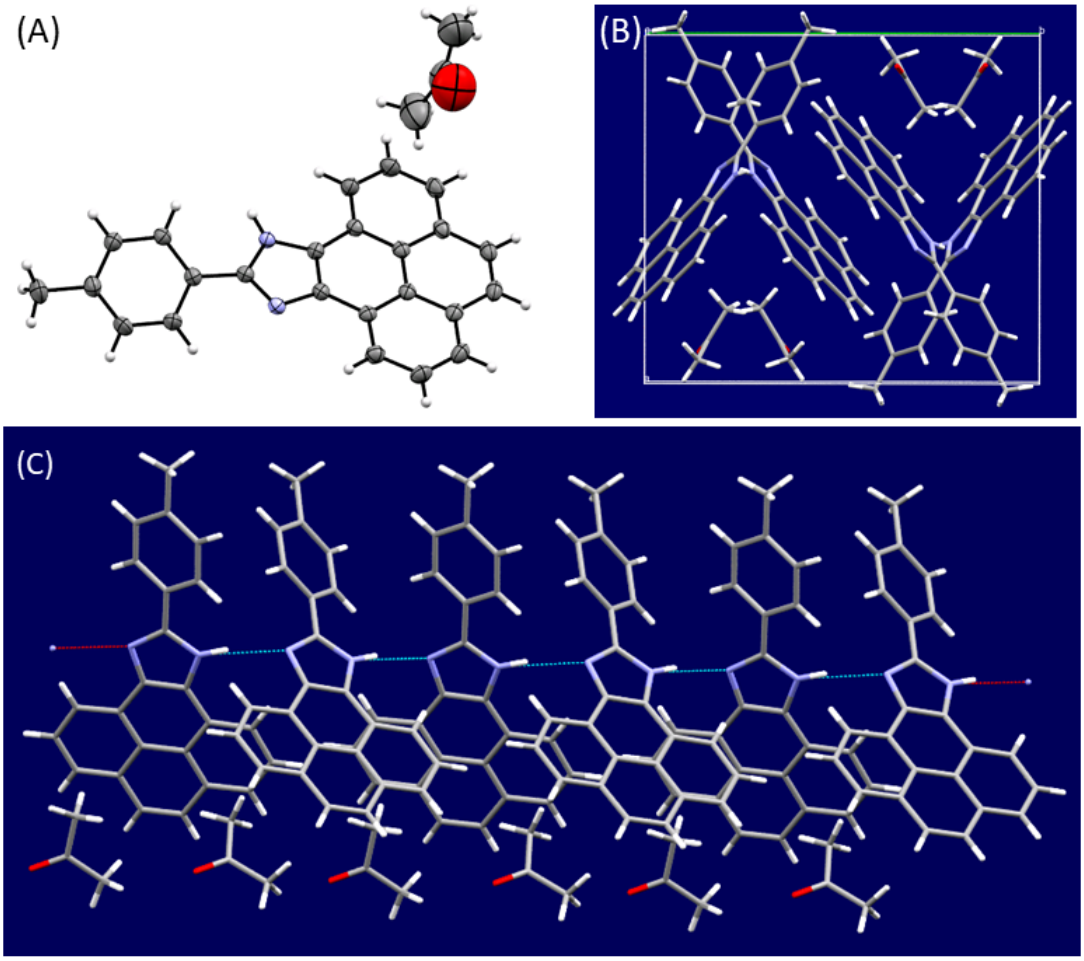

Figure 3.3: (A) ORTEP diagram of compound **3b** co-crystalized with acetone (50% ellipsoid probability). (B) Packing of **3b** molecules in the unit cell viewed along the *b* axis. (C) Linear network of **3b** molecules assembled via hydrogen bonds. CCDC 1851835.

3.3.2.2 Helical hydrogen bonded imidazole–alcohol networks

OMe-substituted **Py-Im 3e** co-crystallized with methanol to yield good-quality single crystals. As shown in Figure 3.4A, the imine nitrogen of **3e** forms a hydrogen bond with the hydroxy proton of methanol at a distance of 1.955 Å. The methanol oxygen also shows attractive interactions with the adjacent phenyl and pyrenyl protons (highlighted as red dashed lines in Figure 3.4A), which can also be ascribed to hydrogen bonding interactions according to QTAIM analysis (see Fig. S-14 in the Supporting Information). Such interactions not only flatten the molecular structure of **3e**, with the torsion angle between the phenyl and pyrenoimidazolyl groups being 19.0°, but also alter the intermolecular hydrogen bonding interactions between the imidazolyl groups. As can be seen in Figure 3.4C, the crystal unit cell consists of sixteen molecules of **3e** and sixteen molecules of methanol (space group $I4_1/a$). The solid-state packing is dominated by hydrogen bonding and π-π interactions, but the packing structure appears to be more complex than those of **3a** and **3b**. The imidazolyl unit of **3e** and the OH group of methanol are interconnected through the hydrogen bonds illustrated in Figure 3.4B. Viewing along the b axis of the unit cell, one can see two strands of helical networks assembled in opposite helicity (racemate). The *para*-MeO group of **3e** is believed to play an important role in the formation of such unique solid-state supramolecular structures, although it does not directly participate in intermolecular interactions. Most likely, the electron-donating nature of the OMe group affects the hydrogen bond donor ability of the imidazolyl unit, making it more prone to interact with methanol rather than to form linear hydrogen bonded imidazolyl networks such as those in **3a** and **3b**.

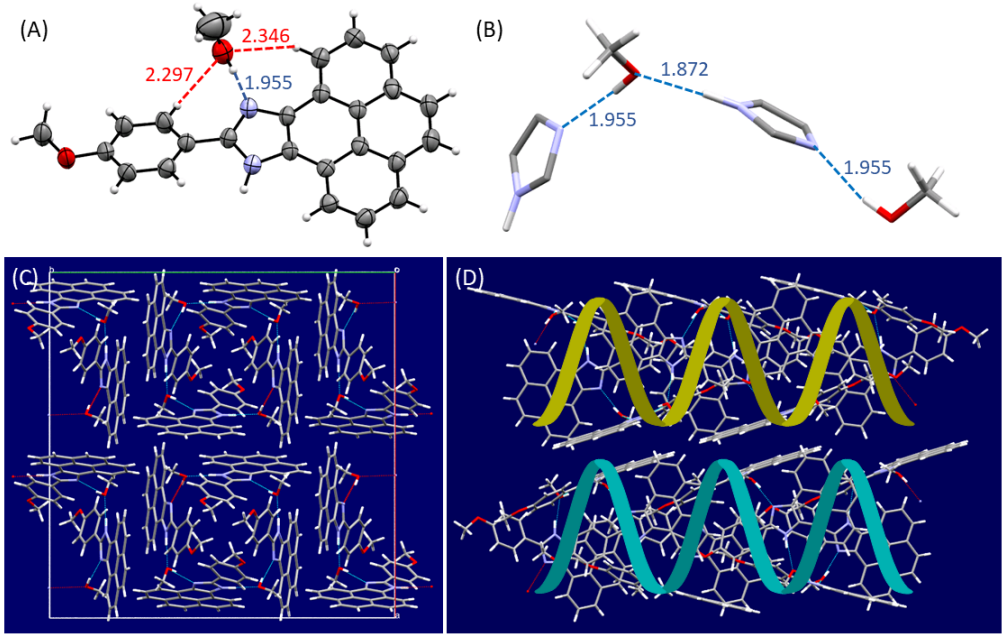

Figure 3.4: (A) ORTEP diagram of compound **3e** co-crystalized with methanol (50% ellipsoid probability, hydrogen bonds highlighted in Å). (B) Hydrogen bonds that interconnect the molecules of **3e** and methanol in the crystal structure (only the imidazolyl groups are shown for clarity and hydrogen bond distances are highlighted in Å.) (C) Packing of **3e** and methanol molecules in the unit cell viewed along the *c* axis. (D) Helical networks of **3e** and methanol molecules assembled via hydrogen bonding interactions (top: left-handed, bottom: right-handed). CCDC 1917379.

The complementary hydrogen bond donor–acceptor interactions between **3e** and methanol lead to the helical supramolecular assemblies in the co-crystallized state. The crystallographic packing data also suggest the possibility of building chiral crystals by co-crystalization of pyrenoimidazoles with suitable chiral hydrogen bond donors/acceptors (e.g., chiral alcohols). The subject of hydrogen bond-assembled helical crystals has attracted growing interest in recent years.[160,161] To shed light on this respect, we made attempts to co-crystalize a chiral alcohol, *R*-(+)-1-

phenylethanol, with the **Py-Im** derivatives **3a**–**h**. NO_2-substituted **Py-Im 3h** was found to co-crystalize with *R*-(+)-1-phenylethanol in a mixed solvent of benzene and acetone (1:1, v/v) to afford good-quality single crystals suitable for X-ray single crystallographic analysis. In the crystal structure, **3h** and *R*-(+)-1-phenylethanol are packed together in the monoclinic $P2_1$ space group. As can be seen in Figure 3.5A, the imidazolyl group of **3h** interacts with *R*-(+)-1-phenylethanol through two types of hydrogen bonds, N$\cdots$HO (1.807 Å) and NH$\cdots$O (1.826 Å). Such hydrogen bonding interactions connect the molecules of **3h** and *R*-(+)-1-phenylethanol to form an infinite chiral strand with a right-handed helicity. This example clearly demonstrates that pyrenoimidazoles can serve as supramolecular synthons to generate organized helical crystals with chiral alcohols. Further exploration in the application of pyrenoimidazole-based chiral crystals is currently underway.

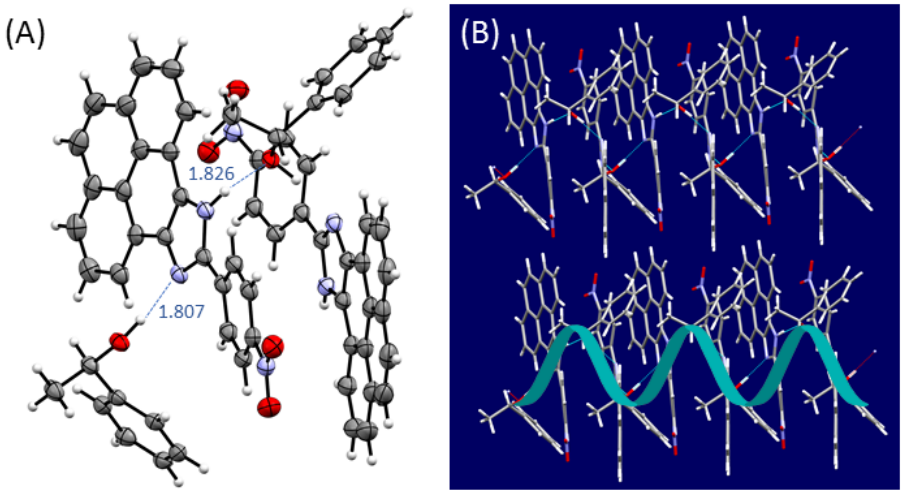

Figure 3.5: (A) ORTEP diagram of compound **3h** co-crystalized with *R*-(+)-1-phenylethanol (50% ellipsoid probability, hydrogen bonds highlighted in Å). (B) Solid-state assemblies of **3h** and *R*-(+)-1-phenylethanol molecules forming helical networks with a *P* helicity. CCDC 1957897.

3.3.2.3 π-π Stacking dominated packing

Cl-substituted **Py-Im 3c** formed a 1:1 hydrogen bonded complex with acetone in the crystal structure (Figure 3.6A), in which the imidazolyl N–H acts as the donor and the acetone oxygen as the acceptor (H$\cdots$O distance = 1.975 Å). Additionally, one of the phenyl hydrogens and one of the pyrenyl hydrogens also show hydrogen bonding interactions with the acetone oxygen at H$\cdots$O distances of 2.502 Å and 2.604 Å, respectively. Such interactions make **3c** adopt a nearly planar molecular conformation, with the torsion angle between the phenyl and pyrenoimidazolyl groups being as small as 8.35°. The flattened molecular shape of **3c** allows them to stack as pairs in a complementary face-to-face arrangement (see Figure 3.6C). In each of these molecular pairs, the polar C–Cl and imidazolyl N–H bonds point to the opposite directions, respectively, so as to attain a minimal net dipole moment. The single crystal packing of **3c** and acetone takes an orthorhombic *Pbcn* space group (Figure 3.6B). Close contact between pyrenyl units appears to be a dominant feature in the crystal packing, with an interplanar distance of 3.42 Å. Such intermolecular π-π interactions of **3c** lead to the herringbone stacking as illustrated in Figure 3.6D.

Compound **3f** co-crystallized with two molar equivalents of DMSO in the solid state. As shown in Figure 3.7A, **3f** and two molecules of DMSO are bound together through hydrogen bonding interactions. The imidazolyl N–H group acts as a hydrogen bond donor that interacts with the oxygen atom of one of the DMSO molecules, while two adjacent phenyl and pyrenyl protons also show close contact with this DMSO oxygen. The three hydrogen bonds with the DMSO molecule makes **3f** adopt a nearly planar conformation, in which the torsion angle between the phenyl and

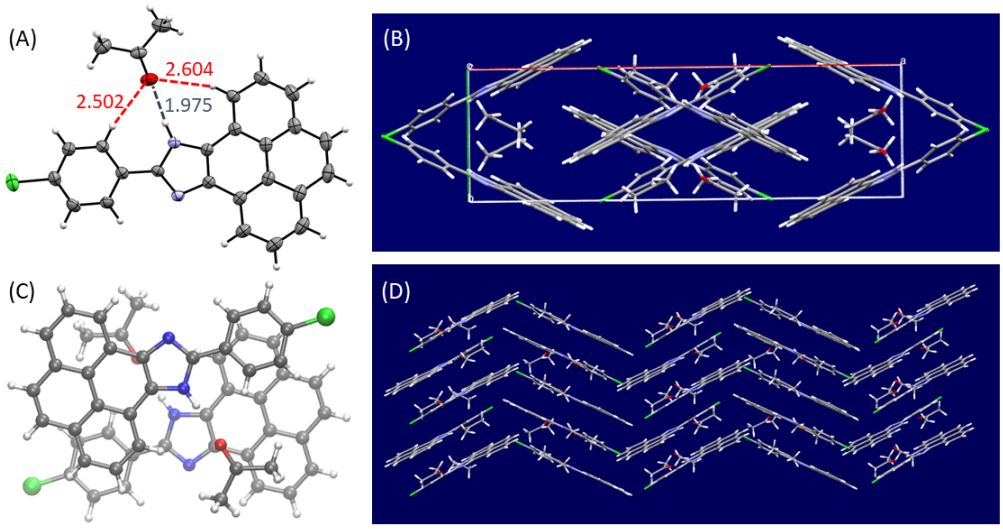

Figure 3.6: (A) ORTEP diagram of compound **3c** co-crystallized with acetone (50% ellipsoid probability, hydrogen bonds highlighted in Å). (B) Packing of **3c** and acetone molecules in the unit cell viewed along the c axis. (C) Top view of the π-stacked assembly of [**3c**$\cdots$acetone] in crystal. (D) Crystal packing diagram of **3c** and acetone molecules. CCDC 1917380.

pyrenoimdazolyl groups is only 3.85°. In addition, there is a second DMSO molecule bound to the first DMSO molecule via a $CH_3\cdots O$ bond. Compound **3f** exhibits a slipped stacking pattern in the crystal structure. Figure 3.7C illustrates a pair of **3f** molecules packed in a complementary fashion similar to that of **3c**. The interplanar distance between the molecules of **3f** is 3.22 Å, which is significantly shorter than that observed in the crystal packing of **3c**. Figure 3.7D highlights the stacking of **3f** in one direction to form a columnar assembly, in which the DMSO molecules are intercalated between the layers through hydrogen bonding interactions.

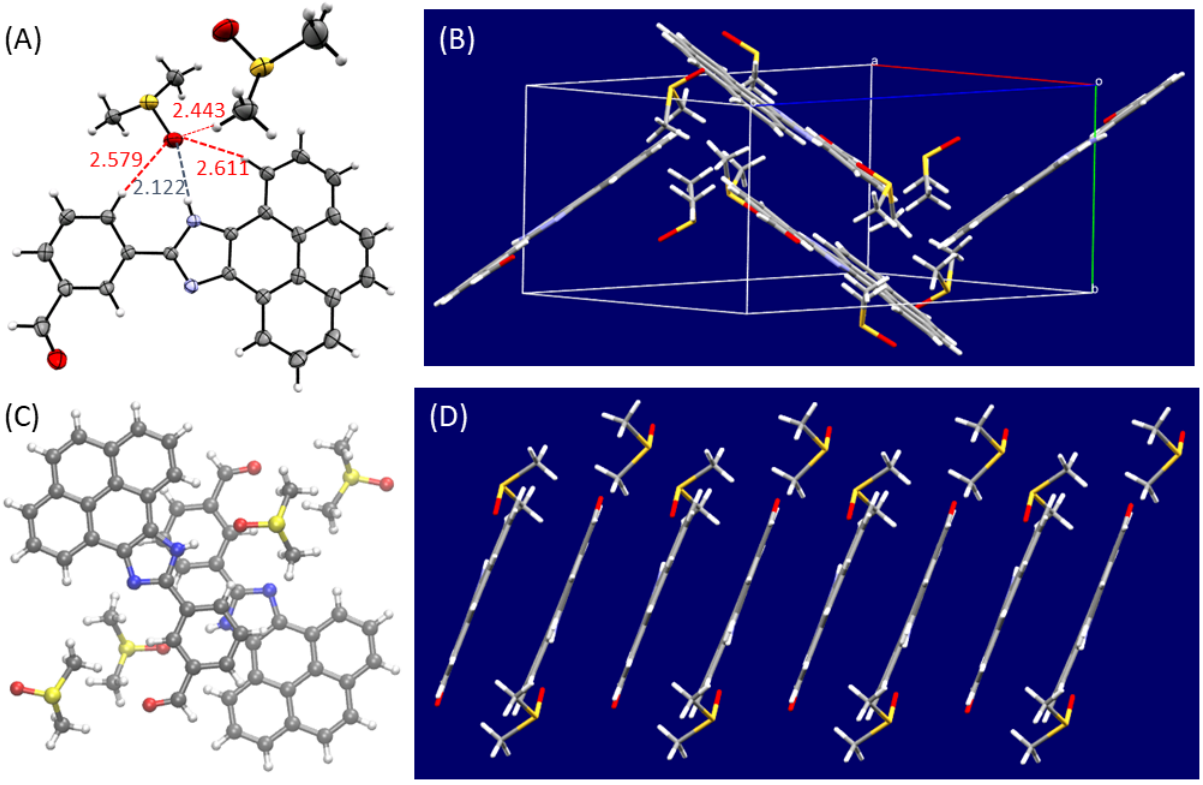

Figure 3.7: (A) ORTEP diagram of compound **3f** co-crystalized with two molecules of DMSO (50% ellipsoid probability, hydrogen bonds highlighted in Å). (B) Packing of **3f** and DMSO molecules in the unit cell. (C) Top view of the π-stacked assembly of [**3f**$\cdots$(DMSO)$_2$] in crystal. (D) Crystal packing diagrams of **3f** and DMSO molecules. CCDC 1851838.

3.3.2.4 Hydrogen bonded Py-Im dimers

Compound **3g**, a structural isomer of **3f**, has a carboxaldehyde group at the *para*-position of the phenyl ring. Such a molecular structure allows hydrogen bonded dimers to be formed in the solid state. Figure 3.8A shows that each dimer is assembled primarily by two intermolecular hydrogen bonds between imidazolyl N–H and aldehyde oxygen with a H$\cdots$O bond distance of 2.261 Å. In addition, each

aldehyde group is in close contact with an adjacent pyrenyl hydrogen at a distance of 2.657 Å. To accommodate the dimer formation, the phenyl and pyrenoimidazolyl groups in each molecule of **3g** adopt a torsion angle of 21.6°. QTAIM analysis also reveals non-covalent intermolecular attraction between the edges of the two adjacent phenyl rings (see Figure S-16 in the Supporting Information for details). Four molecules exist in the unit cell ($P2_1/c$ group) as shown in Figure 3.8B. In the crystal structure, the hydrogen bonded dimers are found to pack in a tilted face-to-face stacking motif as highlighted in Figure 3.8C. The interplanar distance of the stacks is 3.50 Å, indicating significant π-π stacking among the layers. Also, the packing of **3g** takes different directions to form a tightly packed crystal lattice that does not leave enough void space for trapping any solvent molecules (Figure 3.8D). It is also worth mentioning that compounds **3g** and **3a** are the only two cases that do not show co-crystallization with solvent molecules.

Compound **3h** co-crystallized with one molar equivalent of acetone in the single crystal structure bonded through hydrogen bonding interactions. As shown in Figure 3.9A, the imidazolyl N–H interacts with the acetone oxygen atom at a distance of 1.955 Å, while the adjacent phenyl and pyrenyl hydrogens also show close contact with acetone in a way similar to the **3c**$\cdots$acetone interactions. The molecule of **3h** has a fairly flat conformation, in which the torsion angle between the phenyl and pyrenoimidazolyl units is 3.85°. The presence of a strong electron-withdrawing *para*-nitro group in **3h** facilitates the formation of a supramolecular pair (dimer) through edge-to-edge attractions between nitro and pyrenyl groups. As shown in Figure 3.8A, the distance between the nitro oxygen and pyrenyl hydrogen is 2.636 Å. The nature of these intermolecular interactions was further examined by QTAIM

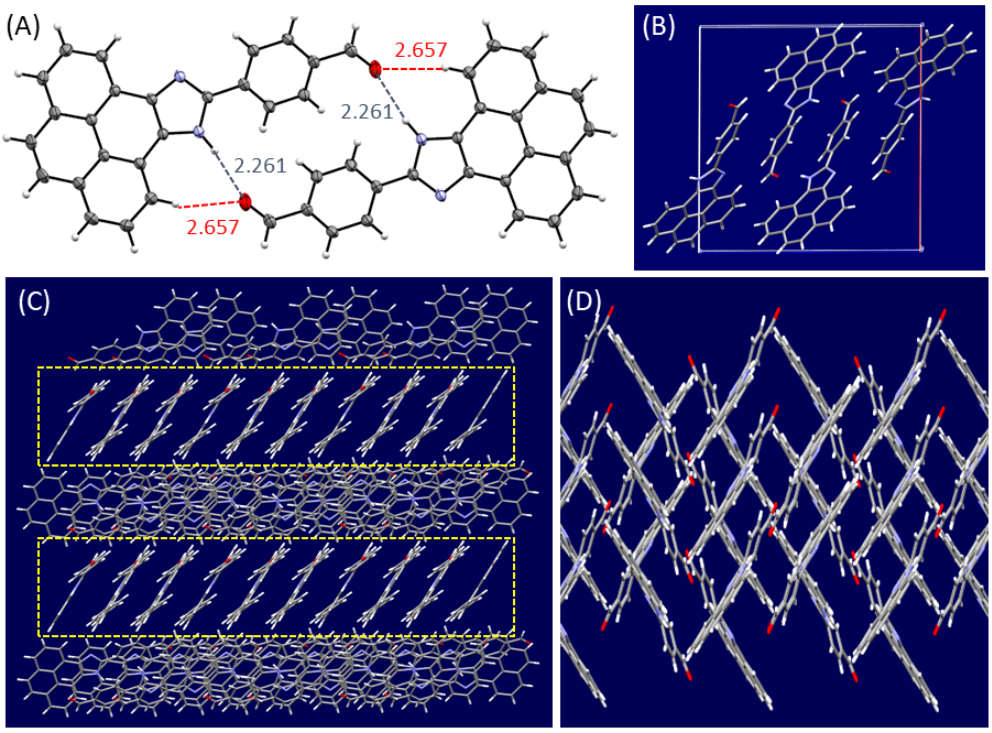

Figure 3.8: (A) ORTEP diagram of a hydrogen bonded dimer of compound **3g** (50% ellipsoid probability, hydrogen bonds highlighted in Å). (B) Packing of **3g** molecules in the unit cell viewed along the *b* axis. (C) and (D) Crystal packing diagram of **3g** viewed from different perspectives. CCDC 1851836.

analysis which reveals that they are weak hydrogen bonds (see Figure S-17 in the Supporting Information). The single crystal of **3h** belongs to the monoclinic $P2_1/c$ space group, with four molecules in the unit cell (Figure 3.8B). The nearly planar structure of the hydrogen bonded dimers allows them to form a co-facially stacked assembly with an interplanar distance of 3.19 Å between adjacent dimers (Figure 3.8C).

3.3.3 Molecular Electrostatic Potentials and Correlation with Crystal Packing Properties

The diverse solid-state packing motifs of **Py-Im** derivatives revealed by the above single crystallographic analysis indicate that the intermolecular interactions of **Py-Im** can be greatly influenced by the functional groups attached to the phenyl ring. Prediction of organic crystal structures is a highly complex and challenging subject.[162] To achieve this goal, continued efforts in data collection and analysis of relevant structure-property relationships are warranted. Electrostatic potentials have been often used as a straightforward interpretative tool for understanding intermolecular interactions in organic crystal structures.[163–165] Hence **Py-Im** derivatives **3a**–**c** and **3e**–**h** were subjected to DFT calculations to gain insight into this issue. Figure 3.10 illustrates the molecular electrostatic potential (MEP) maps of these compounds calculated at the M06-2X/Def2-SV(P) level. Maximum electrostatic potentials on the molecular surfaces (isodensity = 0.002 au) are highlighted to reveal the most significant interacting points of the molecules.

The MEP map of unsubstituted **Py-Im 3a** shows that the most positive electrostatic potential point is located at the imidazolyl N–H group, while the most negative electrostatic potential at the imidazolyl N=C site. These two groups act as hydrogen bond donor and acceptor respectively in the crystal packing of **3a**, and the intermolecular attraction between them dictates the formation of linear hydrogen bonded imidazolyl networks. With **3a** as a reference, one can readily see that the substituent group exerts a direct effect on the electrostatic potentials at the N–H and N=C groups. The Hammett substituent constant (σ) was found to show reasonably

good linear correlation with the maximum electrostatic potential values at the two groups (see Figure 3.11). The general trend can be stated as follows: when the **Py-Im** system is substituted with an electron-withdrawing group, the N–H group becomes more attractive to negative charge (i.e., better hydrogen bond donor) and the N=C group becomes less attractive to positive charge (poorer hydrogen bond acceptor), and vice versa for the electron-donating substitution.

For *para*-CH_3 substituted **3b** and *para*-OMe substituted **3e**, the maximum electrostatic potentials of their N–H and N=C groups show changes in a slight-to-moderate degree compared to those of **3a**. As such the imidazolyl groups in these compound serve as hydrogen bond donors and acceptors in a way similar to that of **3a** in crystal packing. It is worth noting that the acetone oxygen atom shows a slightly less negative electrostatic potential than the N=C group, which accounts for the absence of hydrogen bonding interactions between the two molecules in the co-crystallization of **3b** and acetone. For the co-crystallization of **3e** and methanol, however, the methanol oxygen has a much greater negative electrostatic potential than the N=C group. Hence in the crystal structure, methanol oxygen wins over the N=C group in forming hydrogen bond with the N–H group, leaving the N=C hydrogen bonded to methanol O–H. Herein, the pairing of the most positive electrostatic potential and the most negative electrostatic potential sites appears to be a dominating factor in the intermolecular interactions.

In the case of Cl-substituted **3c**, the electrostatic potential of imidazolyl N=C is significantly less negative than that of **3a**, which manifests itself as weakened hydrogen bond accceptor ability as a result of the electron-withdrawing Cl substituent. In this way, the co-crystallization of **3c** with acetone is dictated by interactions between

imidazolyl N–H (donor) and acetone oxygen (acceptor). The imidazolyl N=C group, albeit a hydrogen bond acceptor, has no participation in any direct intermolecular interactions.

For **Py-Im** derivatives **3f–h**, much stronger electron-withdrawing groups (CHO, NO_2) are attached to the phenyl ring. These groups can greatly deplete the electron density of the pyrenoimidazolyl moiety and hence result in significantly increased electrostatic potential of N–H. As such, strong hydrogen bonding interactions take place at this position in their crystal structures. In the case of *meta*-CHO substituted **3f**, the N=C group has more negative electrostatic potential than that of **3a**, which is against the general trend of substitution effects shown in Figure 3.11B. It is also noted that the CHO group has a slightly more negative electrostatic potential than the N=C site in **3f**, but neither of these groups is a sufficient competitor with the DMSO oxygen in terms of electrostatic attraction. As such, the N–H$\cdots$DMSO interactions prevail in the crystal packing of **3f**.

In the MEP map of *para*-CHO substituted **3g**, the most positive site is located at the imidazolyl N–H group and the most negative site at the *para*-CHO oxygen. The N=C group, on the other hand, is significantly weakened in terms of its positive charge attracting ability. This feature is consistent with the hydrogen bonded dimer structure in the crystal packing of **3g**, where the N–H and CHO interactions play the dominant role. Compared with its structural isomer **3f**, the molecular shape of **3g** can also be identified as a key factor enabling the two molecules to be hydrogen bonded in a complementary, anti-parallel orientation. Another feature worth mentioning in the MEP map of **3g** is that the electrostatic potential of the 7-hydrogen of the pyrenyl group (for detailed atomic labeling see Scheme 3.1) is considerably increased

compared to the unsubstituted **3a**. This allows the pyrenyl edge (7-position) to participate in hydrogen bonding interactions with the CHO group. The nature of such interactions was also examined by QTAIM analysis (see Figure S-16 in the Supporting Information).

The imidazolyl N–H of *para*-nitro substituted **3h** features the most positive electrostatic potential among the **Py-Im** derivatives examined in this work, because nitro has the strongest electron-withdrawing power. The N=C of **3h**, on the other hand, has the least negative electrostatic potential compared with other **Py-Im** derivatives. This effect reduces its competitiveness in terms of forming intermolecular interactions with other groups. In the crystal structure, the most electrostatic positive–negative attraction occurs between N–H and acetone oxygen. This prevents the imidazolyl unit from forming hydrogen bonded networks; however, the formation of **3h** dimer is enabled through the intermolecular attraction between the nitro oxygen and the pyrenyl hydrogen at the 2-position. Like the case of **3h**, an anti-periplanar orientation in the dimer of **3f** is also formed as a result of shape complementarity. The shape of **3h** dimer is more planar than that of **3g** dimer. Hence, the face-to-face stacking in the crystal of **3h** is in a much tighter and less tilted motif.

3.3.4 Substitution Effects on Photophysical Properties

The photophysical properties of **Py-Im** derivatives **3a**–**h** were probed by UV-Vis absorption and fluorescence spectroscopic analysis, and detailed data are illustrated in Figure 3.12. The UV-Vis absorption spectrum of unsubstituted **3a** shows two major absorption peaks, a sharp low-energy band at 383 nm ($S_\circ \rightarrow S_1$) and a relatively high-

energy band at 364 nm ($S_\circ \rightarrow S_2$). TD-DFT calculations indicate that the band at 383 nm is mainly due to the HOMO→LUMO transition, while the band at 364 nm is predominantly contributed by the HOMO→LUMO+1 transition (see Table S-2 in the Supporting Information). The absorption spectra of substituted **Py-Im** derivatives **3b**–**e** show spectral patterns very similar to those of **3a** with barely noticeable shifts in the maximum absorption wavelengths. The results suggest that electron-donating (i.e., CH3, OMe) and weakly electron-withdrawing groups (i.e., Cl, Br) have rather insignificant effects on the vertical electronic transition properties of **Py-Im**. For *meta*-CHO substituted **3f**, the $S_\circ \rightarrow S_1$ transition band is slightly redshifted relative to that of **3a** (by ca. 2 nm), but the lineshape of this band becomes notably broadened. The high-energy $\pi \rightarrow \pi^*$ absorption bands, however, are nearly unchanged compared to the spectrum of **3a**. In the case of *para*-CHO substituted **Py-Im 3g**, the $S_\circ \rightarrow S_1$ band is not only significantly redshifted to 396 nm, but also considerably broadened with the absorption tail extending to 450 nm. Such a trend of shift is even more dramatic in the spectrum of *para*-nitro substituted **3h**, in which a very broad low-energy absorption band emerges at 412 nm and its tail reaches as far as 500 nm.

The fluorescence spectra of **3a**–**e** also show similar spectral patterns in which the maximum emission peaks appear at *ca.* 408 nm (Figure 3.12B). These results indicate that the substitution effects are not significant on their first-excited state (S_1) properties either. Interestingly, CHO-substituted **Py-Im** isomers, **3f** and **3g**, show nearly identical maximum emission wavelengths at 507 nm. The presence of electron-withdrawing carboxaldehyde group causes the maximum emission band to redshift considerably relative to unsubstituted **3a**; however, the substitution position of the CHO group (*meta* or *para*) does not cause much difference in their emission

energies, but the fluorescence quantum yield of **3g** is far greater than its isomer **3f**. The emission of *para*-nitro substituted **3h** was observed to be not only considerably weakened but also redshifted to the largest extent in comparison to the other **Py-Im** derivatives. Overall, the absorption and emission spectroscopic studies show that only strong electron-withdrawing groups (CHO and NO_2) can cause significant changes in photophysical properties. The origin of such effects can be linked to the deprotonation of imidazolyl, a process that shows dependence on the nature of substituent group(s) attached (*vide infra*).

3.3.5 Substitution Effects on Imidazolyl Deprotonation

As discussed above, the **Py-Im** system shows greatly altered electrostatic potentials at the imidazolyl N=C and N–H positions when a strongly electron-withdrawing group such as nitro is attached to the phenyl ring. In theory, the electron-withdrawing effect results in lowered pK_a value of the imidazolyl N–H group, making it more prone to proton exchange reactions (e.g., tautomerization). A very interesting phenomenon observed during the recrystallization of nitro-substituted **Py-Im 3h** is that the crystallized solid can exist in various crystalline forms. Figure 3.13 illustrates photographic images of **3h** in these crystalline forms, among which a type of brown-colored translucent single crystals (herein referred to as **3h-I**, Figure 3.13A) was characterized by X-ray single crystallographic analysis as co-crystals of **3h** with acetone. The detailed structure of **3h-I** are illustrated in Figure 3.9. Another type of black-colored single crystals (**3h-II**, Figure 3.13B) was also obtained and their solid-state structure was elucidated by X-ray single crystallographic analysis as well. In

addition to these two crystalline forms, some aesthetically pleasing needle and tree-like crystals were formed under different crystallization conditions (Figure 3.13C–F).

Figure 3.14A shows that **3h-II** is actually a co-crystal of **3h** with water molecules at a 1:2 ratio. Herein, both the imidazolyl and nitro groups in **3h** form hydrogen bonds with water molecules, forming a 2-dimensional hydrogen bonded network in a fluted ribbon-like shape (see Figure 3.14B). Viewing from the edges of these "ribbons", one can also see close π-π stacking among them, with the interplanar distance between pyrenyl units measured to be 3.41 Å. Compared with the crystal structures of **3h-I**, the π-π stacking in **3h-II** appears to be more efficient. It is also noted that the phenyl and pyrenoimidazolyl units show a torsion angle of 14.0°, which is more twisted than the conformation observed in crystal of **3h-I**. Such dramatic differences in solid-state structures are probably the main reason for the two crystals to show very different colors and appearance.

The crystals of **3h-I** and **3h-II** were re-dissolved in acetone-d_6 and then immediately analyzed by ^{1}H NMR. The spectrum of **3h-II** (Figure 3.15A) suggests that the pyrenyl unit has two sets of chemically equivalent protons, whereas in the spectrum of **3h-I** (Figure 3.15B) pyrenyl protons appear as different signals without any chemical equivalence. Given that the imidazolyl unit forms hydrogen bonds with water molecules on both sides in the crystal structure of **3h-II**, it can be reasoned that rapid proton exchange occurs in the solution phase, which effectively introduces a plane of symmetry in the molecule and thus simplifies the spectrum (Figure 3.15A). On the other hand, the imidazolyl unit in the crystal structure of **3h-I** interacts with an acetone molecule only from one side. After dissolving in acetone-d_6, the association of imidazolyl with acetone is still retained; as a result, the two sides of

the imidazole (and thus also the pyrene) unit are not chemically equivalent (Figure 3.15B). It was also observed that the spectral pattern of **3h-I** could be dramatically changed after addition of CD_3OD. As shown in Figure 3.15C, the spectral pattern of **3h-I** added with CD_3OD bears resemblance to that of **3h-II**, suggesting that CD_3OD can considerably disrupt the hydrogen bonding of **3h** to acetone and facilitate rapid proton exchange around the imidazolyl unit.

To further understand the effects of imidazolyl proton transfer on the photophysical properties of **Py-Im**, unsubstituted **3a** was subjected to UV-Vis and fluorescence titrations with tetrabutylammonium fluoride (TBAF) in acetone, and detailed spectral results are given in Figure 3.16. During the UV-Vis titration, the absorption band of **3a** at 383 nm decreases in intensity with increasing addition of TBAF. In the meantime, a broad long-wavelength band emerges at 407 nm and grows steadily. This new band can be attributed to deprotonated **3a**, since it has been known that the fluoride anion released by TBAF is a hard base capable of interacting with the imidazolyl N–H of **Py-Im**, forming a H$\cdots$F hydrogen bond and then leading to deprotonation of the imidazolyl group (see Figure 3.16C).[148] TD-DFT computed $S_\circ \rightarrow S_1$ transition bands of **3a** (368 nm) and deprotonated **3a** anion (429 nm) exhibit a consistent trend of shift (see Tables S-2 and S-3 in the Supporting Information), corroborating the spectral assignment as well. The significantly broadened line shape of the growing band at 407 nm is likely a result of increased degree of free rotation about the imidazolyl and phenyl units after deprotonating the imidazolyl N–H. The fluorescence titration results show that the maximum emission band of **3a** is shifted from 397 nm to 490 nm with increasing addition of TBAF. It can also be seen from Figure 3.16B that the emission band of **3a** shows higher intensity and more distinct

vibronic features than those of TBAF-deprotonated **3a**. The increased rotational freedom about the phenyl and imidazolyl units in **3a** anion can explain the broadening and attenuation of its maximum emission band.

The TBAF titration results for **3a** also shed light on the photophysical properties of substituted **Py-Im** derivatives; in particular, a clear explanation for the dramatically different UV-Vis and fluorescence spectral patterns of (**3f**–**h**) in comparison to the others can be made as follows. The broad and long-wavelength absorption bands in the UV-Vis absorption spectra of **3g** and **3h** (Figure 3.12A) bear resemblance to that of the deprotonated **3a**. Hence the origin of the long-wavelength bands of **3g** and **3h** can be reasonably attributed to deprotonation of the imidazolyl group. The strong electron-withdrawing effects of *para*-CHO and *para*-nitro can greatly increase the acidity of imidazolyl N–H through the resonance effect, making it more easily undergo proton exchange in solution compared to other **Py-Im** derivatives, resulting in deprotonation at the imidazolyl moiety of **Py-Im**. Such a process has a great impact on the frontier molecular orbital (FMO) properties, leading to very different UV-Vis and fluorescence properties than those of the parent **Py-Im** species. Figure 3.17 depicts the calculated FMOs of **3a** and [**3a** – H]$^-$ anion. It can been seen that the HOMO and LUMO of **3a** show similar spatial distribution across its π-conjugated molecular backbone. While TD-DFT analysis indicated that HOMO$\rightarrow$LUMO transition is the dominant contributor to the $S_\circ \rightarrow S_1$ band, it can be concluded that the vertical electronic excitation of **Py-Im** is a typical $\pi \rightarrow \pi*$ transition with insignificant charge-transfer (C-T) character. When deprotonation occurs on the **Py-Im** system, e.g., during the formation of **3a** anion, the FMO properties are greatly altered. In particular, the HOMO features greater population

at the imidazolyl group and the LUMO at the pyrenyl segment. Such different spatial distribution suggests that the HOMO→LUMO transition of deprotonated **Py-Im** should have a significant degree of C-T character.

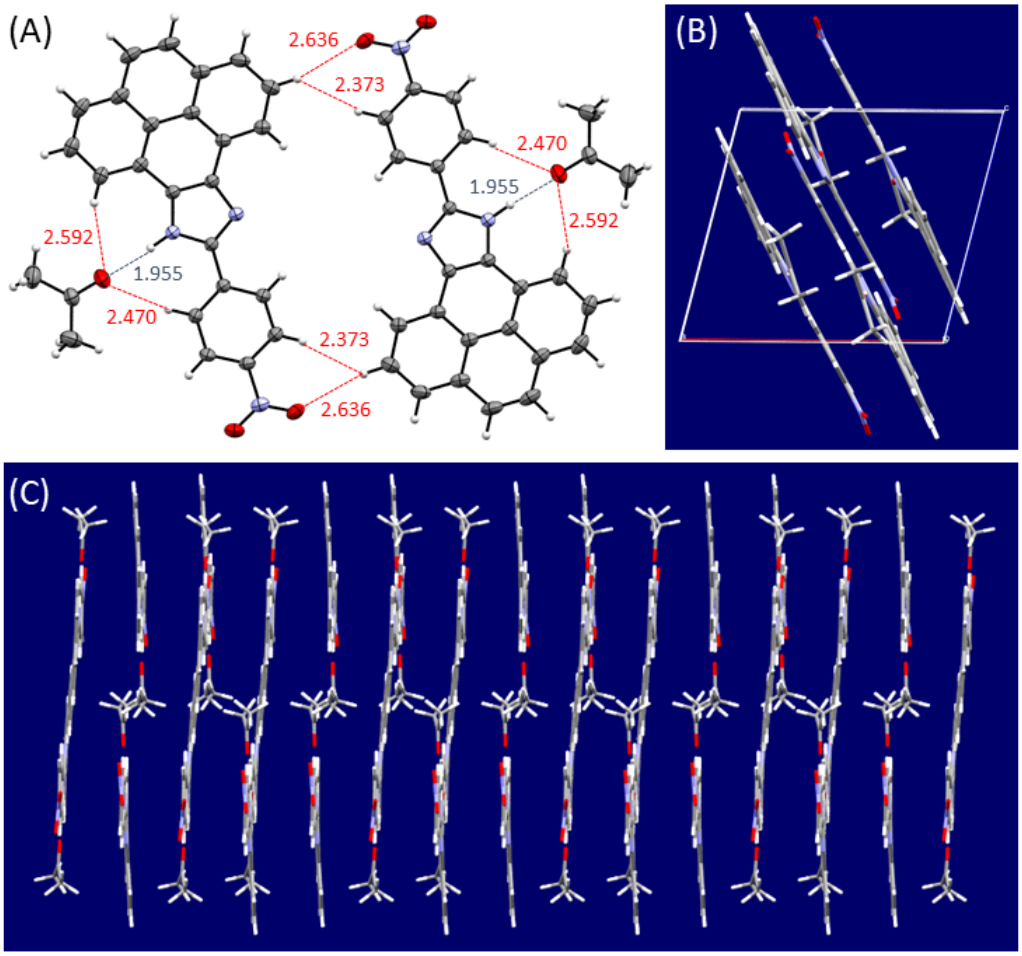

Figure 3.9: (A) ORTEP diagram of a hydrogen bonded dimer of compound **3h** co-crystalized with acetone (50% ellipsoid probability, hydrogen bonds highlighted in Å). (B) Packing of **3h** molecules in the unit cell viewed along the *b* axis. (C) Crystal packing diagram of **3h**. CCDC 1917378.

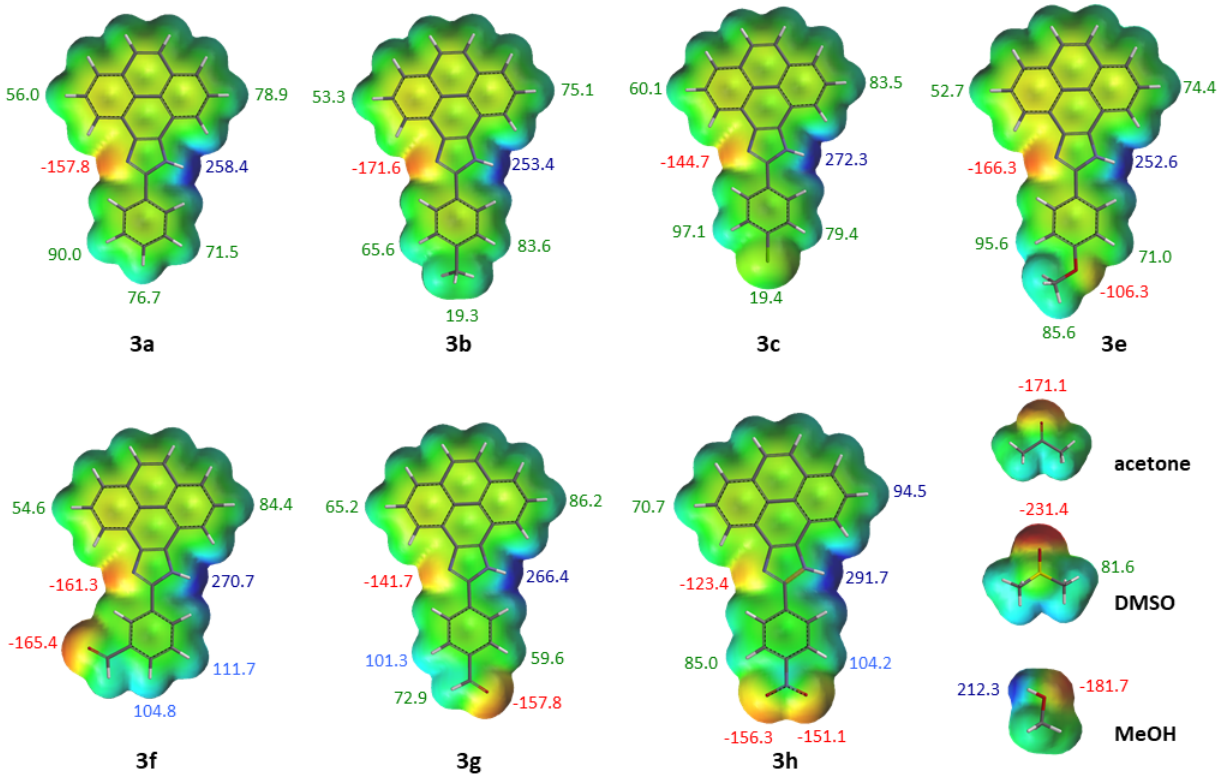

Figure 3.10: MEP maps for **Py-Im** derivatives **3a**–**c**, **3e**–**h**, and relevant solvent molecules on the 0.002 au isodensity surface. Maximum potential energy values on the molecular edges are highlighted in kJ·mol^{-1}.

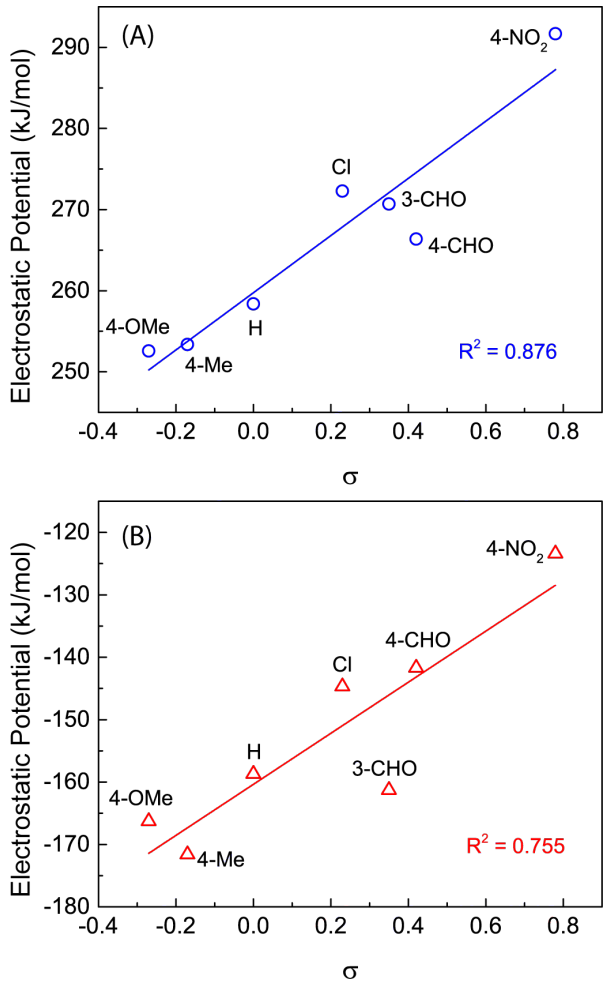

Figure 3.11: Correlations of the maximum electrostatic potentials of on the isodensity surface (0.002 au) with Hammett substituent constants. (A) At the imidazolyl N–H position, and (B) at the imidazolyl N=C position.

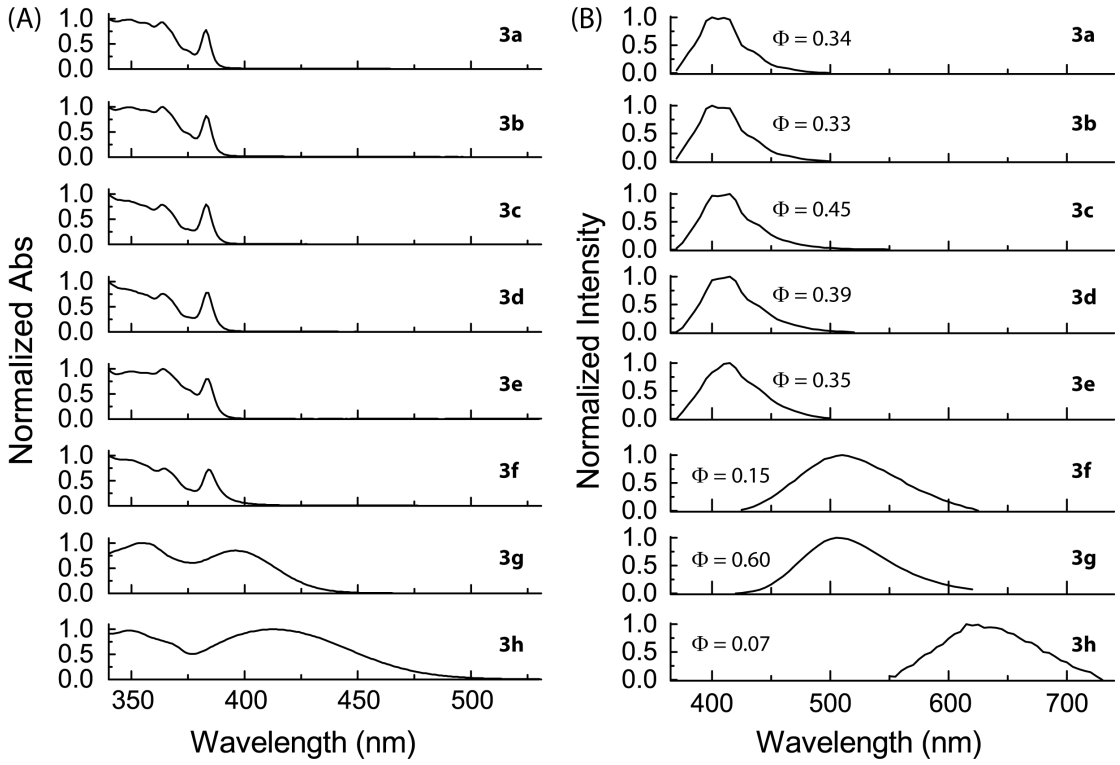

Figure 3.12: Normalized (A) UV-Vis absorption and (B) fluorescence spectra of **Py-Im** derivatives **3a**–**h** measured in acetone at room temperature.

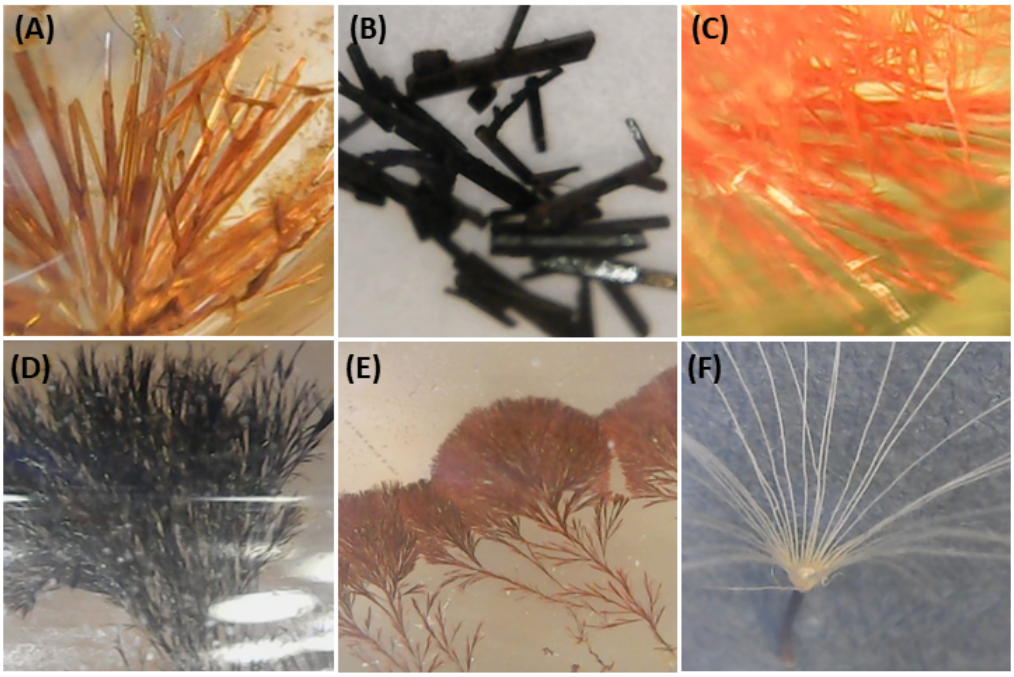

Figure 3.13: Photographic images of crystals of **Py-Im 3h** slowly grown in different solvent systems at room temperature. (A) EtOAc/acetone/hexanes (1:5:94), (B) DMSO/acetone/hexanes (1:5:94), (C) acetone/hexanes (5:95), (D) CH_3OH/acetone/hexanes (3:5:92), (E) Et_2O/acetone/hexanes (5:5:90), and (F) acetone/hexanes (5:95).

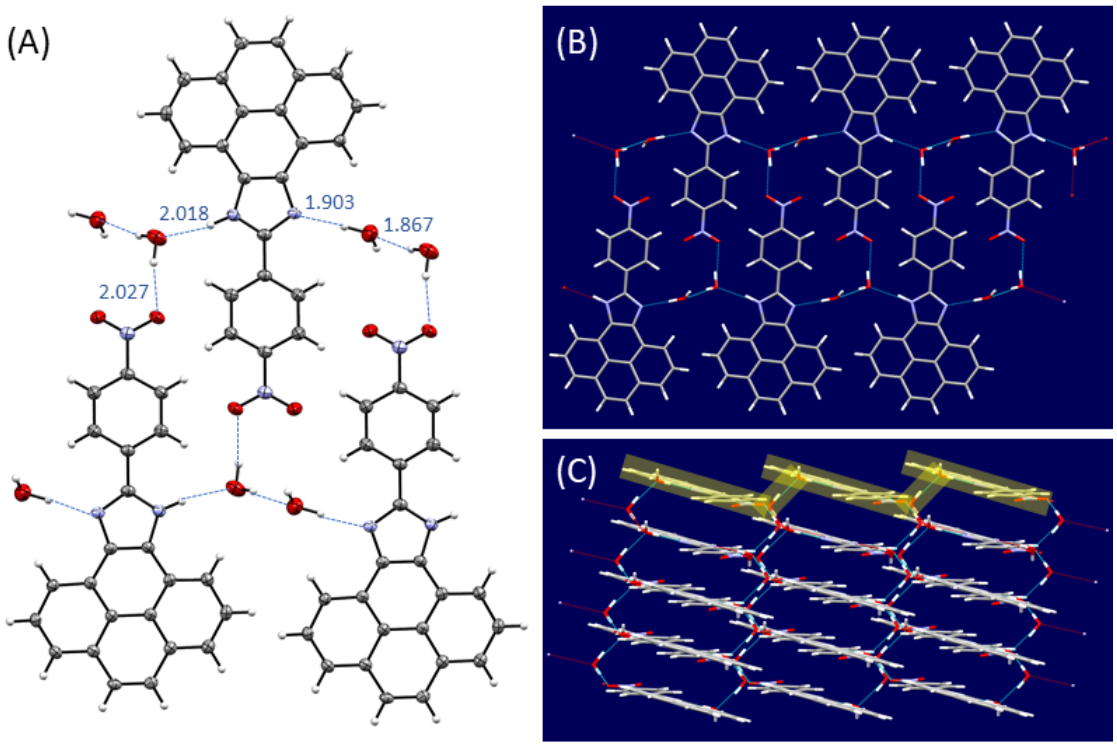

Figure 3.14: (A) ORTEP diagram of compound **3h** co-crystalized with water molecules (50% ellipsoid probability, hydrogen bonds highlighted in Å). (B) Hydrogen bonded networks of **3h** and water molecules in the crystal structure of **3h-II**. (C) π-Stacking motif of **3h-II** in the crystal structure. CCDC 1957899.

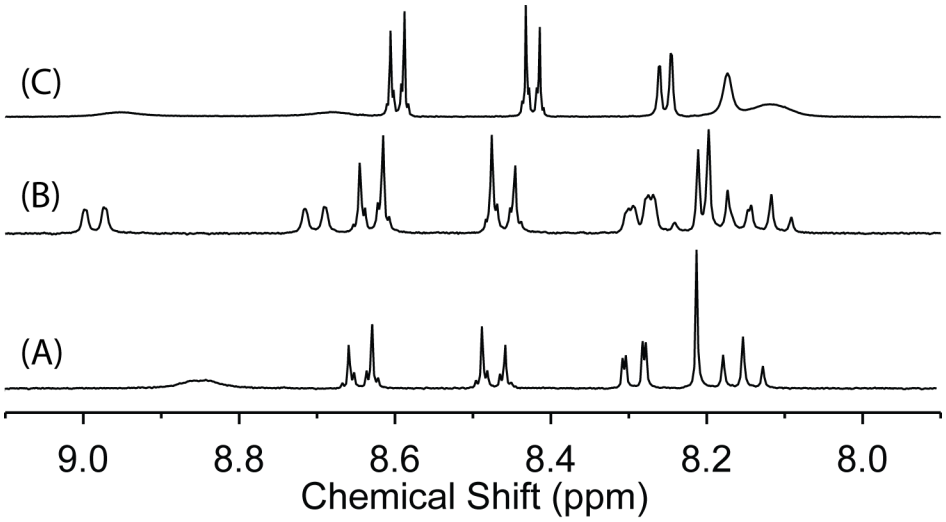

Figure 3.15: Expanded ^{1}H NMR (300 MHz) spectra of (A) crystals of **3h-II** dissolved in acetone-d_6, (B) crystals of **3h-I** dissolved in acetone-d_6, and (C) crystals of **3h-I** dissolved in acetone-d_6 after addition of 5.6 equiv of CD_3OD.

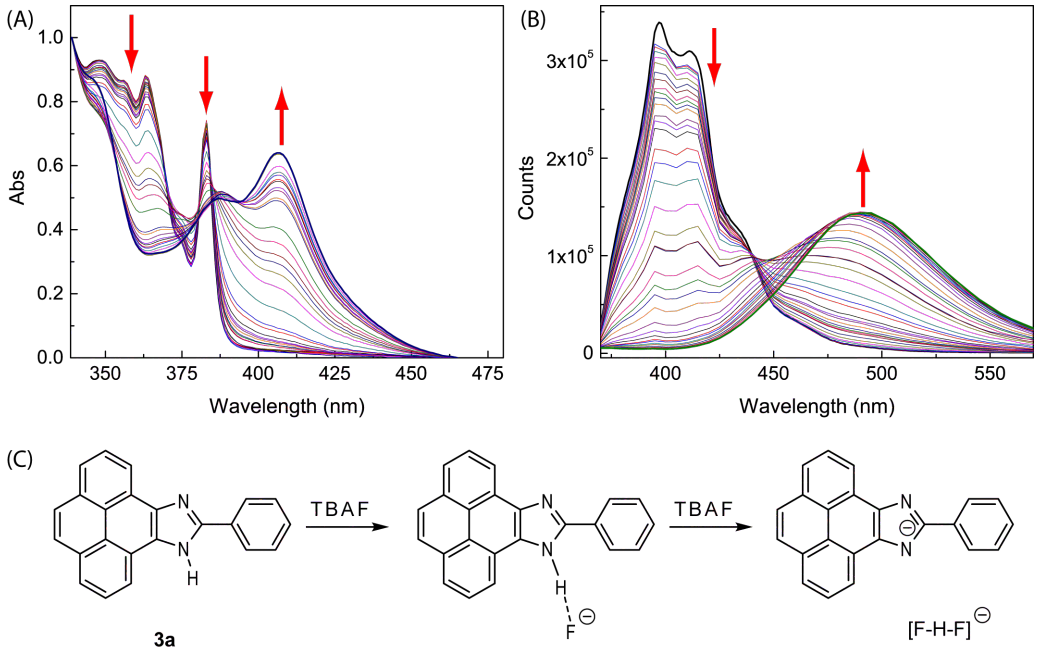

Figure 3.16: (A) UV-Vis absorption and (B) fluorescence spectra monitoring the titration of **3a** (56.5 μM) with TBAF (0–20.0 molar equiv) in acetone. (C) Hydrogen bonding interactions of **3a** and fluoride anion and subsequent deprotonation reaction.

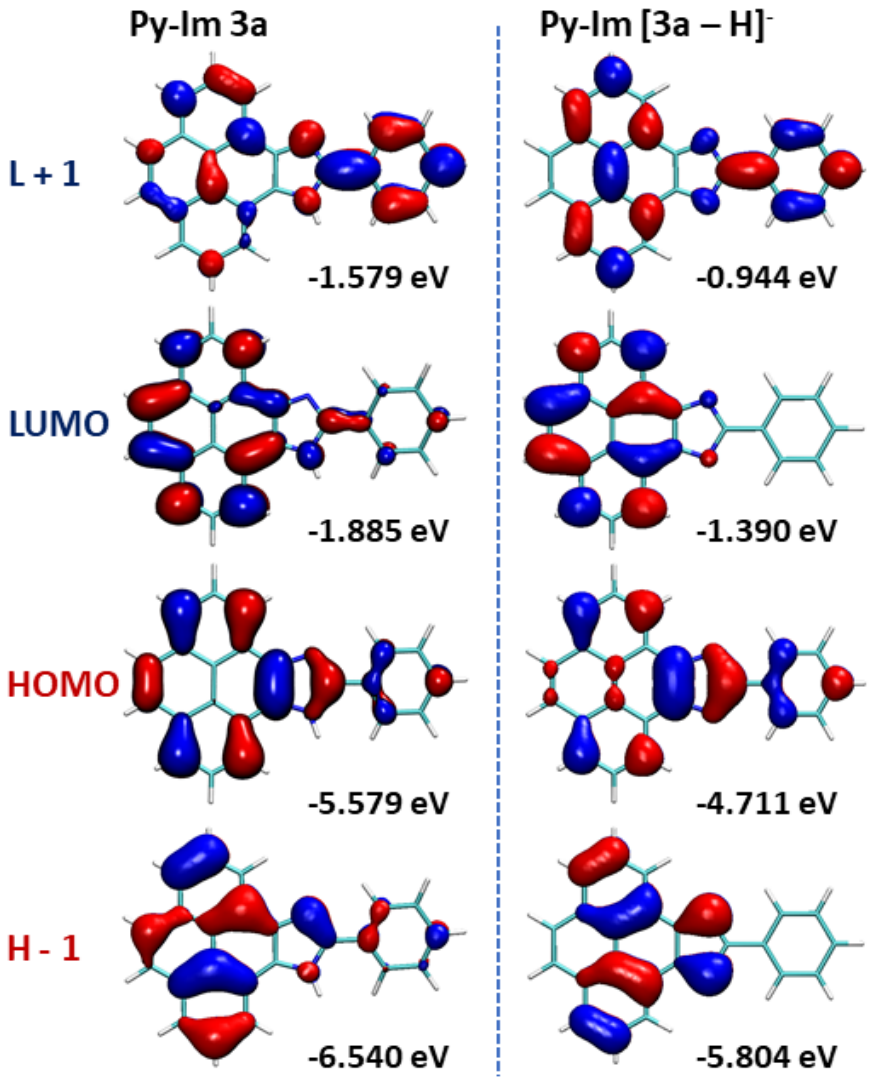

Figure 3.17: Contours (isovalue = 0.03 au) and eigenvalues (in eV) of FMOs of **3a** (left) and deprotonated **3a** anion (right) calculated at TD-B3LYP/6-311+G(d,p) level.

3.4 Conclusions

In conclusion, we have synthesized a series of phenyl-substituted **Py-Im** systems (**3a**–**h**) through a one-pot condensation reaction. X-ray single crystallographic analysis disclosed that the substituent groups attached to the phenyl ring exert significant effects on the intermolecular interactions between the **Py-Im** and various solvent molecules. Hydrogen bonding and π-π interactions are two dominant cohesive forces that govern the packing of **Py-Im** molecules in the solid state, while the MEP analysis serves as a useful tool for interpretation and assessment of the intermolecular interactions in their crystal structures. Weak-to-moderate electron-donating and withdrawing substituents have little influence on the UV-Vis absorption and fluorescence behavior of **Py-Im** systems. Strong electron-withdrawing groups (e.g., *para*-CHO and *para*-nitro) give substantially changed photophysical properties, and this effect arises from the facile proton exchange at the imidazolyl group, which leads to deprotonation of the imidazolyl N–H. We have also demonstrated that crystal engineering can be achieved by using **Py-Im** as a tunable supramolecular synthon. Overall, this work has accomplished a systematic examination on the solid-state and photophysical properties of **Py-Im** systems and our findings should provide useful guidance to the application of **Py-Im** derivatives in materials science and technology.

Chapter 4

Designed Synthesis and Crystallization of Pyrenoimidazole-based Supramolecular Synthons

The contents of this chapter are under peer review as a research article sent to *CrystEngComm*. Contributions of authors are described below:

Zahra A. Tabasi is the first author, who conducted the synthesis of all the pyrenoimidazole compounds, growth of all the single crystals and co-crystals, and relevant spectroscopic characterizations. She also contributed to the manuscript preparation and editing.

Joshua C. Walsh and Prof. Graham J. Bodwell are collaborators of this project, who synthesized pyrene-4,5-dione and assisted in manuscript editing.

Profs. David W. Thompson and Yuming Zhao are the supervisors of Z. A. Tabasi, and they helped develop the concepts and design of this project. Prof. Y. Zhao is the corresponding author of this paper.

4.1 Introduction

Organic crystal engineering has become an important frontier in the field of crystal engineering.[166,167] Ever since the concept of supramolecular synthons was introduced by Desiraju in 1995,[168], a large number of rationally designed organic molecules have been investigated as synthons for the assembly of crystalline materials with desirable properties and functions (e.g., nonlinear optical properties, electrical conductivity, microporosity, and pharmaceutical activities).[169–174] According to Dunitz,[175] the crystal structure can be viewed as a supramolecule *par excellence*, the high degree of order of which results from complementary disposition of shape features and interactions of functional groups among neighboring molecules in the solid state. In this sense, functional groups that introduce directional interactions such as hydrogen bonding, halogen bonding, and π–π stacking are commonly utilized to control the packing and inter-connectivity of molecules in the crystal structure with pre-programmed order and precision.[176–180]

We have recently investigated the single-crystal structural properties of a class of phenyl-substituted pyrenoimidazole (**PyIm**) derivatives, with a range of substituents (*p*-Me, *p*-OMe, *p*-Cl, *p*-Br, *p*-CHO, *m*-CHO, and *p*-NO_2) attached to the phenyl group.[181] Our studies showed that the substituents exert important effects on their photophysical properties as well as crystal packing behaviors. Especially, the

hydrogen bonding interactions arising from the imidazole moiety could allow complex supramolecular networks (*e.g.*, linear, helical, and layered) to be assembled through crystallization or co-crystallization with solvent molecules that are hydrogen bond donors/acceptors. Our previous findings thus motivated us to further pursue the potential of developing pyrenoimidazoles as versatile supramolecular synthons for the assembly of defined network structures in the solid state. To this end, the development of a deeper understanding of how to manipulate the solid-state structure would be of great value for promoting their application in solid-state optoelectronic materials and devices.

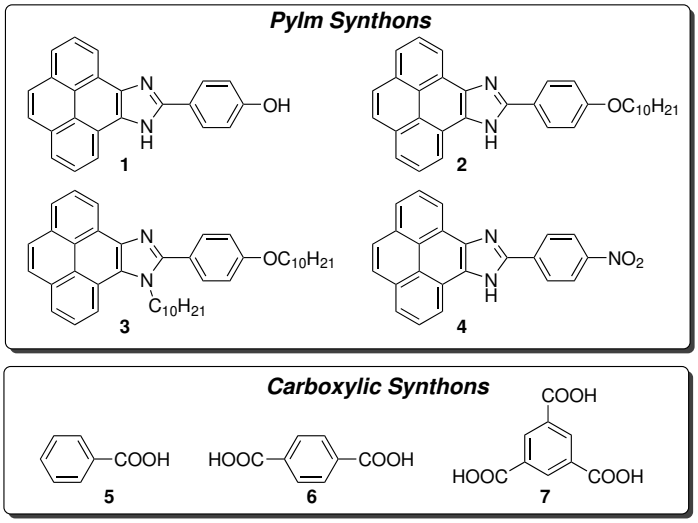

Figure 4.1: Supramolecular synthons investigated in this work.

In this work, we prepared and investigated four phenyl-pyrenoimidazoles (**1**–**4**, Figure 4.1) as supramolecular synthons for the construction of organic crystalline materials with different solid-state structures. In terms of functionality, compounds **1**–**4** can be divided into two groups; *para*-OH/OR substituted (**1**–**3**) and *para*-NO_2 substituted (**4**). In the first group, compound **1**, which has a hydroxy (OH) group at

the *para*-position of the phenyl ring, was chosen as a new supramolecular synthon with multiple hydrogen bond donor and acceptor sites existing in its molecular structure. For comparative studies, two analogous compounds (**2** and **3**) were also synthesized and analyzed. In the structures of these two compounds, one and two hydrophobic *n*-decyl groups are respectively attached to the *O* and *N* sites of the phenyl-pyrenoimidazole core. The intention here was to gradually alter their intermolecular hydrogen bonding and π–π stacking properties as well as add alkyl–π interactions in the crystalline packing. The interplay of these intermolecular forces should be conducive to generating different supramolecular assemblies,[182–185] and allow comparative studies to better understand the effects of weak non-covalent attractions on crystal packing behavior.

Previously, we examined the crystallographic properties of a series of phenyl-pyrenoimidazoles.[181] Among them, compound **4** exhibited the strongest Lewis acidity at the imidazolyl NH site and most pronounced intramolecular charge-transfer (ICT) properties. In the literature, the interactions of imidazoles with carboxylic acids have been known to yield imidazolium carboxylate salts, which readily co-crystallized to form organized supramolecular layers and networks.[186–191] Therefore, for the second group of pyrenoimidazole supramolecular synthons investigated in this work, compound **4** was subjected to co-crystallization with three aromatic carboxylic acids, namely benzoic acid (**5**), terephthalic acid (**6**), and trimesic acid (**7**). Our studies herein were focused on exploring the crystal form diversity of **4** resulting from co-crystallization with different carboxylic acid supramolecular synthons.

4.2 Experimental

4.2.1 Synthesis and Characterization

Compound **1** was prepared using the previously-reported synthetic method.[148,181] Alkylation of **1** resulted in the formation of compounds **2** and **3**, which were separated by silica flash column chromatography. The synthesis of compound **4** was reported previously.[181] All the compounds were subjected to NMR, IR, and MS analyses to confirm their structures and purity. ^{1}H and ^{13}C NMR spectra were measured on a Bruker 300 MHz AVANCE III spectrometer. Infrared (IR) spectra were recorded on a Bruker Alfa spectrometer. High-resolution mass spectrometric (HRMS) analyses were performed on a GCT premier Micromass Technologies instrument.

4-(9*H*-Pyreno[4,5-*d*]imidazol-10-yl)phenol (1)

Pyrene-4,5-dione (0.20 g, 0.86 mmol), *p*-hydroxybenzaldehyde (0.32 g, 2.6 mmol), ammonium acetate (1.3 g, 17 mmol), and glacial acetic acid (99.7%, 7 mL) were mixed in a round-bottom flask equipped with a condenser. The reaction was heated at 110 °C for 5 h, and then slowly cooled down to rt. The resulting precipitate was collected by vacuum filtration and then sequentially washed with glacial acetic acid, saturated $NaHCO_3$ solution (aq), and water to yield crude product **1**, which was subjected to silica flash column chromatography using EtOAc/hexanes (10:90, v/v) as eluent to afford pure compound **1** (0.15 g, 0.45 mmol, 52%, $R_f = 0.22$) as a black solid. IR (neat): 3612, 3458, 3221, 2920, 2852, 1728, 1605, 1541, 1248, 1175, 889, 762, 716 cm^{-1}; ^{1}H NMR (300 MHz, CD_3OD): δ 8.66 (d, J = 7.5 Hz, 2H), 8.05 (t, J = 7.8 Hz, 2H), 7.99 (s, 2H), 7.95 (d, J = 7.7 Hz, 2H), 7.23 (s, 1H, *NH*), 6.93 (d, J =

8.8 Hz, 2H) ppm; A meaningful ^{13}C NMR spectrum was not obtained due to limited solubility; HRMS (MALDI-TOF):*m/z* calcd for $C_{23}H_{15}N_2O$ $[M + H]^+$ 335.1184 found 355.1171.

10-(4-(Decyloxy)phenyl)-9*H*-pyreno[4,5-*d*]imidazole (2)

To a solution of compound **1** (0.10 g, 0.30 mmol) in absolute ethanol (7 mL) were added 1-bromodecane (0.066 g, 0.30 mmol) and potassium carbonate (0.041 g, 0.30 mmol). The reaction mixture was heated at reflux for 4 h, and then another portion of potassium carbonate (0.020 g, 0.15 mmol) was added. After keeping reflux for another 6 h, the reaction mixture was slowly cooled down to rt. The solvent was removed by rotary evaporation and the crude mixture of alkylated products was collected purified by silica flash column chromatography using EtOAc/hexanes (5:95, v/v) as eluent. Compound **2** (0.064 g, 0.13 mmol, 43%, $R_f = 0.59$) was obtained as a white crystalline solid. IR (neat): 3498, 3359, 2946, 2852, 1632, 1613, 1468, 1248, 1185, 998, 716, 666 cm^{-1}; ^{1}H NMR (300 MHz, acetone-d_6): δ 13.54 (s, 1H, *NH*), 8.91–8.71 (m, 2H), 8.31 (d, J = 8.9 Hz, 2H), 8.24 (d, J = 6.5 Hz, 2H), 8.22–8.09 (m, 4H), 7.18 (d, J = 8.9 Hz, 2H), 4.09 (t, J = 6.5 Hz, 2H), 1.85–1.66 (m, 2H), 1.52–1.18 (m, 14 H), 0.86 (t, J = 6.9 Hz, 3H) ppm; ^{13}C NMR (75 MHz, acetone-d_6): δ 160.2, 150.1, 137.9, 132.1, 131.9, 128.3, 128.2, 127.9, 126.8, 126.6, 124.06, 123.3, 122.2, 122.0, 119.5, 119.3, 119.2, 115.3, 68.1, 31.8, 29.5, 29.4, 29.3, 29.2, 26.0, 22.6, 14.4 ppm (three aromatic and one aliphatic carbon signals not observed due to coincidental overlap); HRMS (MALDI-TOF): *m/z* calcd for $C_{33}H_{35}N_2O$ $[M + H]^+$ 475.2749 found 475.2752.

9-Decyl-10-(4-(decyloxy)phenyl)-9*H*-pyreno[4,5-*d*]imidazole (3)

In the above alkylation reaction, compound **3** (0.046 g, 0.075 mmol, 25%, R_f = 0.76) was obtained as a white crystalline solid after silica column chromatographic separation. IR (neat): 2918, 2848, 1591, 1426, 1242, 1180, 1016, 824, 715, 657, 630, 540 cm^{-1}; $^{-1}$H NMR (300 MHz, acetone-d_6): δ 8.96 (dd, J = 7.6, 1.3 Hz, 1H), 8.70 (d, J = 7.9 Hz, 1H), 8.26–8.22 (m, 2H), 8.19 (d, J = 1.9 Hz, 2H), 8.16–8.08 (m, 2H), 7.81 (d, J = 8.8 Hz, 2H), 7.18 (d, J = 8.8 Hz, 2H), 4.88 (t, J = 7.5 Hz, 2H), 4.14 (t, J = 6.5 Hz, 2H), 1.94–1.78 (m, 2H), 1.60–1.49 (m, 2H), 1.49–11.5 (m, 28H), 0.90 (t, J = 7.0 Hz, 3H), 0.84 (t, J = 6.9 Hz, 3H) ppm; ^{13}C NMR (75 MHz, acetone-d_6): δ 160.2, 153.2, 138.5, 132.4, 131.8, 131.4, 127.8, 127.7, 126.9, 126.2, 126.0, 124.1, 124.0, 123.6, 123.0, 119.3, 118.2, 114.5, 67.9, 46.6, 31.75, 31.68, 29.2, 29.0, 25.93, 25.86, 22.44, 22.38, 13.5, 13.4 ppm (two aromatic carbon signals not observed due to coincidental overlap, and eight aliphatic carbon signals not observed due to overlap with solvent signals); HRMS (MALDI-TOF): m/z calcd for $C_{43}H_{55}N_2O$ $[M + H]^+$ 615.4314 found 615.4290.

4.2.2 Crystallization Conditions and X-ray Crystallographic Analysis

Single crystals of compounds **1**–**3** suitable for X-ray diffraction analysis were grown from mixture of solvents (1:1 hexanes/methanol for **1**, and 5:95 ethyl acetate/hexanes for **2** and **3**) by slow evaporation at room temperature. Co-crystallization of compound **4** with carboxylic acids **5**–**7** was conducted in 1:1 hexanes/acetone (wet) through slow evaporation at room temperature as well. The molar ratio of **4** and

carboxylic acid was kept at 1:1.

Single crystal X-ray diffraction (XRD) analysis was performed on a Bruker PLATFORM/APEX II CCD diffractometer, and the crystal structures were solved by direct methods using the SHELXD program[151] and refined by full-matrix least-squares methods with SHELXL–2014.[152]

4.3 Results and Discussion

4.3.1 Crystallization Behavior of Pyrenoimidazoles 1–3

The X-ray structure of **1** was elucidated and detailed structural features are illustrated in Figure 4.2. In the crystal structure, compound **1** co-crystallizes with methanol in a 1:1 ratio, where hydrogen bonding interactions appear to be the dominant attracting forces among the molecules. Figure 4.2A and B show the structure of **1** and methanol molecules packing in a monoclinic $P2_1/n$ space group in the crystalline state. Herein four molecules of **1** and four molecules of methanol are linked together *via* three types of intermolecular hydrogen bonds. The imidazolyl NH group (donor) forms a hydrogen bond with the O atom (acceptor) of methanol at a distance of 2.01 Å, which is the longest one among the hydrogen bonds. The imidazolyl N=C acts as a hydrogen bond acceptor to interact with the O atom of the phenolic OH group in an adjacent molecule **1**, and the hydrogen bond distance is 1.68 Å, which is the shortest hydrogen bond in the crystal structure. Additionally, the methanol OH group forms a hydrogen bond with the phenolic O atom in an adjacent molecule **1** at a distance of 1.96 Å. Collectively, the hydrogen bonds lead to an infinite 3-

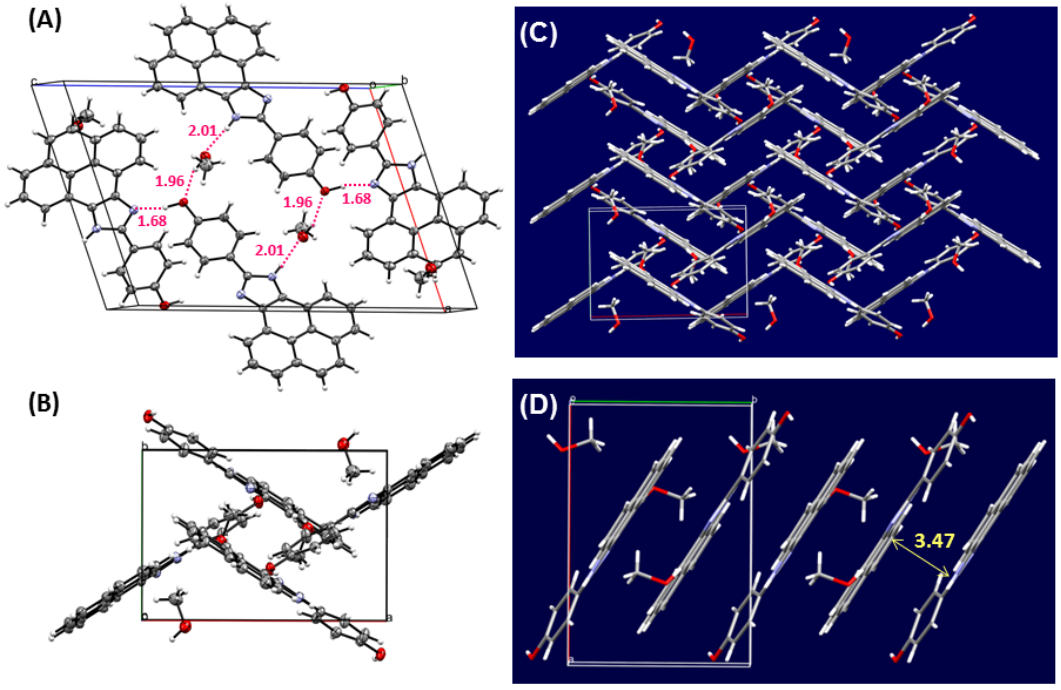

Figure 4.2: (A) ORTEP drawing of molecules of **1** and methanol packed in the unit cell (30% ellipsoid probability, hydrogen bonds highlighted in Å). (B) ORTEP drawing of **1** and methanol molecules in the unit cell viewed along the *c*-axis. (C) Packing diagram of **1** and methanol molecules. (D) Alignment of **1** and methanol molecules showing the π–stacking motif (interplanar distance highlighted in Å). CCDC 1949991.

dimensional network structure, the details of which can be better viewed from Figure 4.3. In addition to the hydrogen bonding interactions, significant π–π interactions are also observed in the crystal structure. As shown in Figure 4.2D, the pyrenoimidazolyl moieties of molecules **1** show an intimate slip-stacked packing motif with an average interfacial distance of 3.47 Å between adjacent molecules. Overall, the hydrogen bonding interaction and π-stacking forces work together to drive the co-crystal of **1** and methanol into a tightly packed solid-state structure that features an ordered grid-like pattern (see Figure 4.2C).

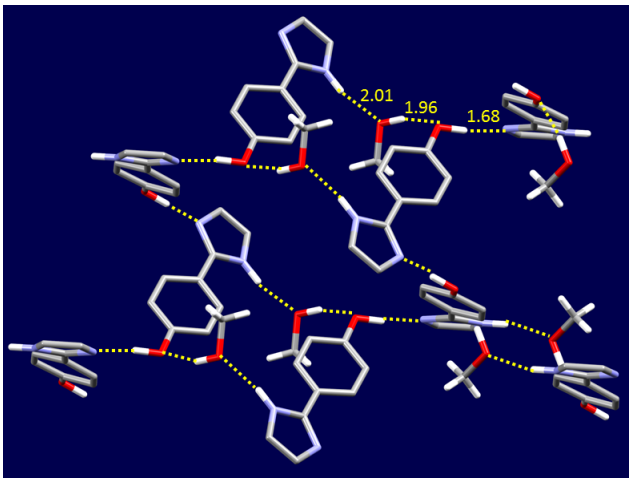

Figure 4.3: Hydrogen bonds among **1** and methanol molecules in the crystal structure. The pyrenyl group of **1** is hidden for clarity and the hydrogen bond distances are highlighted in Å.

Compound **2** was found to co-crystallize with water molecules in the single crystal structure. As shown in Figure 4.4A, two adjacent molecules of **2** are linked together through four intermolecular hydrogen bonds in the unit cell. Two of the hydrogen bonds are H$\cdots$N bonds (1.92 Å) between water H atoms and imidazolyl N=C groups, while another two hydrogen bonds are H$\cdots$O bonds (2.03 Å) between water H and the phenolic ether O atoms. These hydrogen bonds draw the two molecules of **2** in close proximity, and they are nearly co-planar and aligned in an anti-parallel orientation. To maximize the packing efficiency, the decyl chain of the phenolic ether group adopts a curved conformation that matches the circumference of the pyrenyl unit of the adjacent molecule. As shown in Figure 4.4C, the complementary pair of molecules **2** in the unit cell are closely packed in the crystal structure, forming an organized 3-dimensional supramolecular network. It is worth noting that alkyl CH$\cdots\pi$ interactions occur significantly between the decyl and pyrenyl moieties (see

Figure 4.4C), which plays an important role in the solid-state packing structure. Moreover, hydrogen bonds between adjacent water molecules are also involved in the formation of supramolecular assembly. Detailed connectivity of the hydrogen bonds that constitute the 3-dimensional supramolecular network of **2** and water molecules is illustrated in Figure 4.4D. Herein, a cluster of four water molecules are assembled via hydrogen bonding interactions. Six molecules of **2** are connected to this cluster through hydrogen bonding interactions.

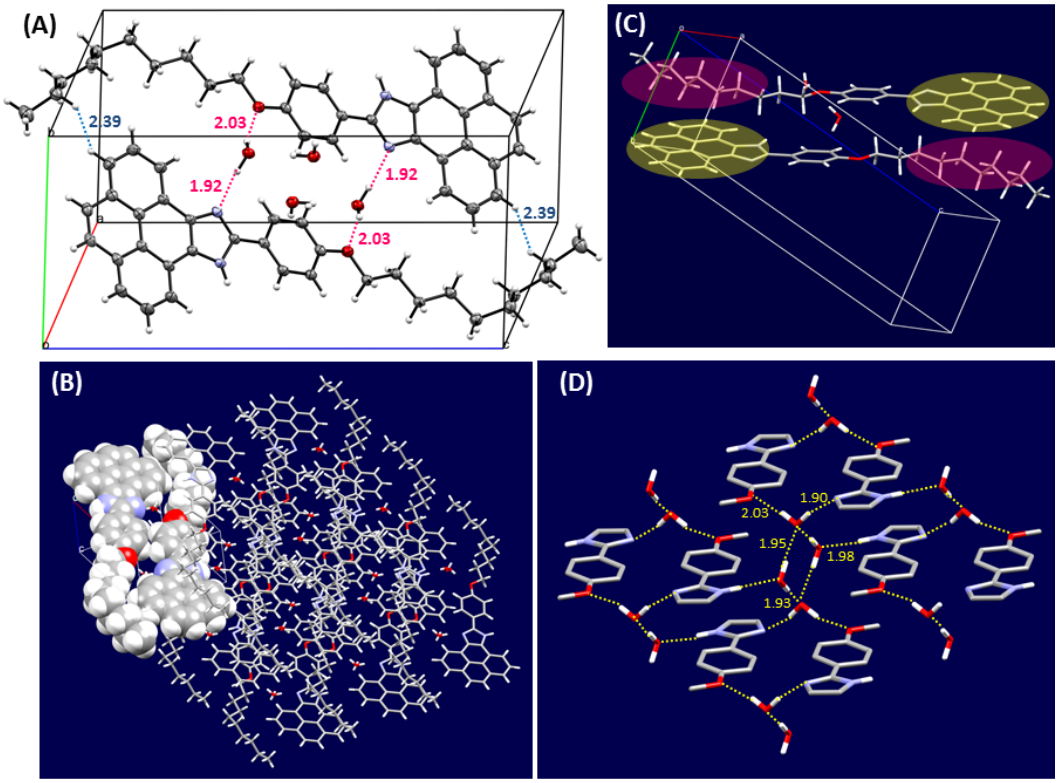

Figure 4.4: (A) ORTEP drawing of molecules of **2** and water packed in the unit cell (30% ellipsoid probability, hydrogen bonds highlighted in Å). (B) Packing diagram of **2** and water molecules, with a complementary molecular pair of **2** in the unit cell highlighted by space filling model. (C) Alignment of two adjacent molecules of **2** showing C-H$\cdots\pi$ interactions. (D) Hydrogen bonds among **2** and water molecules in the crystal structure. The pyrenyl group of **2** is hidden for clarity and the hydrogen bond distances are highlighted in Å. CCDC 1972848.

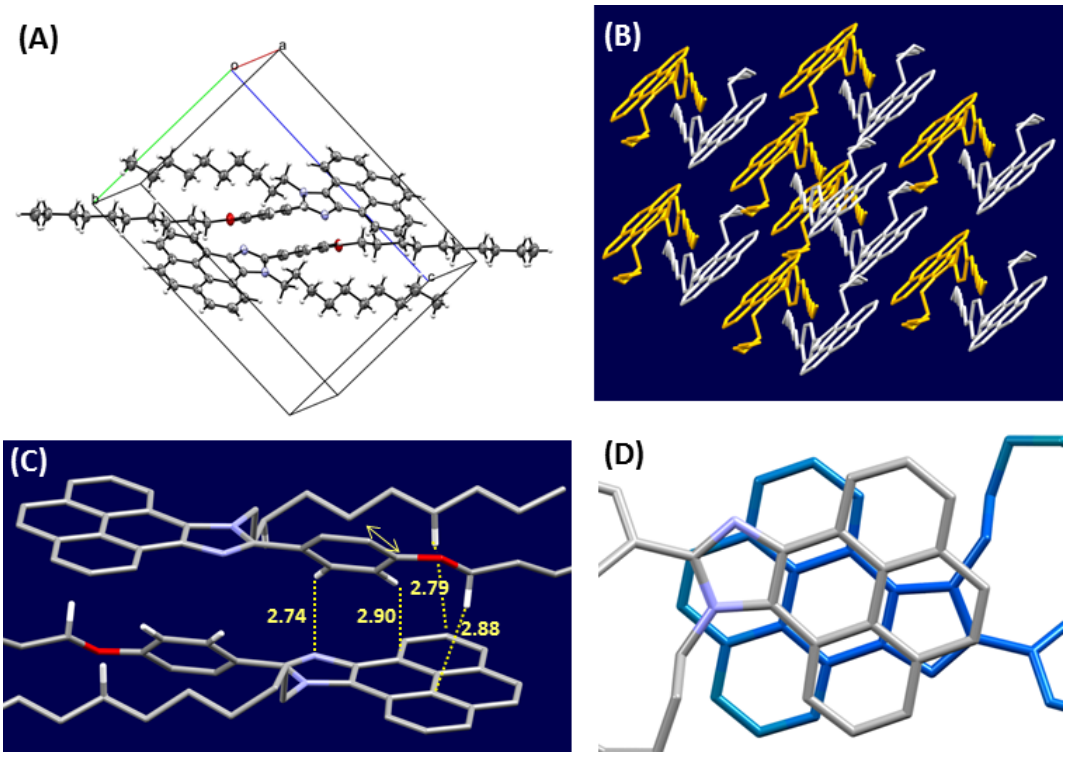

Figure 4.5: (A) ORTEP drawing of molecules of **3** packed in the unit cell (30% ellipsoid probability). (B) Packing diagram of **3** where molecules are colored by symmetry operation (hydrogen atoms are hidden for clarity). (C) Alignment of two adjacent molecules of **3** showing C-H$\cdots\pi$ interactions (distances highlighted in Å). (D) Top view of a pair of **3** showing the geometry of pyrenoimidazole π-stacking (hydrogen atoms omitted). CCDC 1972837.

The single crystal structure of compound **3** is illustrated in Figure 4.5. In contrast to compounds **1** and **2**, the lack of hydrogen bond donors in compound **3** dramatically alters the solid-state packing properties. As shown in Figure 4.5A, the unit cell contains two molecules of **3**, which are oriented in an anti-parallel fashion to form a complementary pair. The attachment of two decyl groups to the imidazolyl N and phenolic O sites in the molecular structure of **3** increases the hydrophobicity of the

molecule, and hence excludes solvents molecules from the single crystal structure. The two molecules in the unit cell are assembled through multiple CH$\cdots\pi$ interactions as indicated in Figure 4.5C. In the packing diagram, the complementary pairs of **3** in the unit cell (highlighted by different colors in Figure 4.5B) are organized through intermolecular π–π stacking. The detailed π–π stacking geometry is depicted in Figure 4.5D, where the two adjacent pyenoimidazolyl moieties are face-to-face stacked in an anti-parallel fashion with slight slipping between the π-surfaces. Overall, the supramolecular assemblies in the single crystal structure of **3** are dictated by two types of attractive forces, π–π stacking and CH$\cdots\pi$ interactions, which assemble the molecules into organized layers.

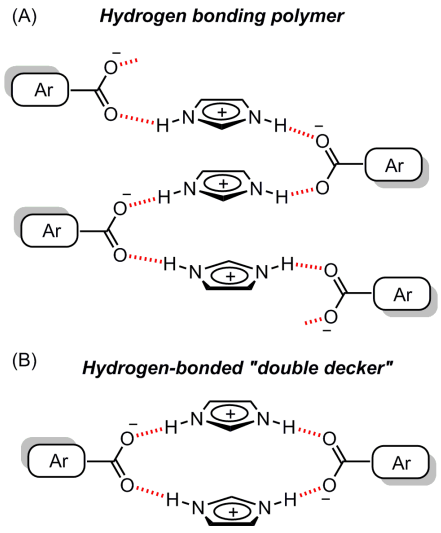

Figure 4.6: Proposed hydrogen-bonded assemblies between imidazolium and carboxylate ions. (A) Hydrogen bonding polymer, and (B) hydrogen-bonded "double-decker" assembly.

4.3.2 Co-crystallization of Pyrenoimidazole 4 with Aromatic Carboxylic Acids

The conjugate acid of imidazole shows a pK_a value of 6.95 (in water)[192] and hence allows imidazole to readily undergo proton transfer with an organic carboxylic acid to form a salt of imidazolium and carboxylate ions. In an imidazolium ion, the two NH groups are strong hydrogen bond donors, while the oxygen atoms of a carboxylate anion are hydrogen bond acceptors. The combined use of imidazolium and carboxylate ions as supramolecular synthons has been reported in the literature to generate designed organic crystal structures, ranging from self-assembled layers to various supramolecular frameworks through charge-assisted hydrogen bonds.[186,188,193–197] To shed light on the possibility of using pyrenoimidazoles as a class of controllable supramolecular synthons to form designed organic crystals, we investigated the co-crystallization of pyrenoimidazole **4** and three aromatic carboxylic acids (**5**–**7**). Our choice of pyrenoimidazole **4** was made primarily for the following reasons. First, the *para*-NO_2 substitution in the structure of **4** should facilitate the hydrogen bonding donor ability of the imidazolyl group through the resonance effect. Second, the strong-electron withdrawing effect of NO_2 group induces a large molecular dipole moment that may work together with the hydrogen bonding and π–π stacking interactions to enhance crystal packing and formation of highly ordered supramolecular assemblies. Third, in our previous work, pyrenoimidazole **4** was found to yield various crystal forms, which are sensitive to crystallization conditions.[181] Such features suggest the versatility of **4** in building complex supramolecular structures, particularly, 2D- and 3D-supramolecular

frameworks.

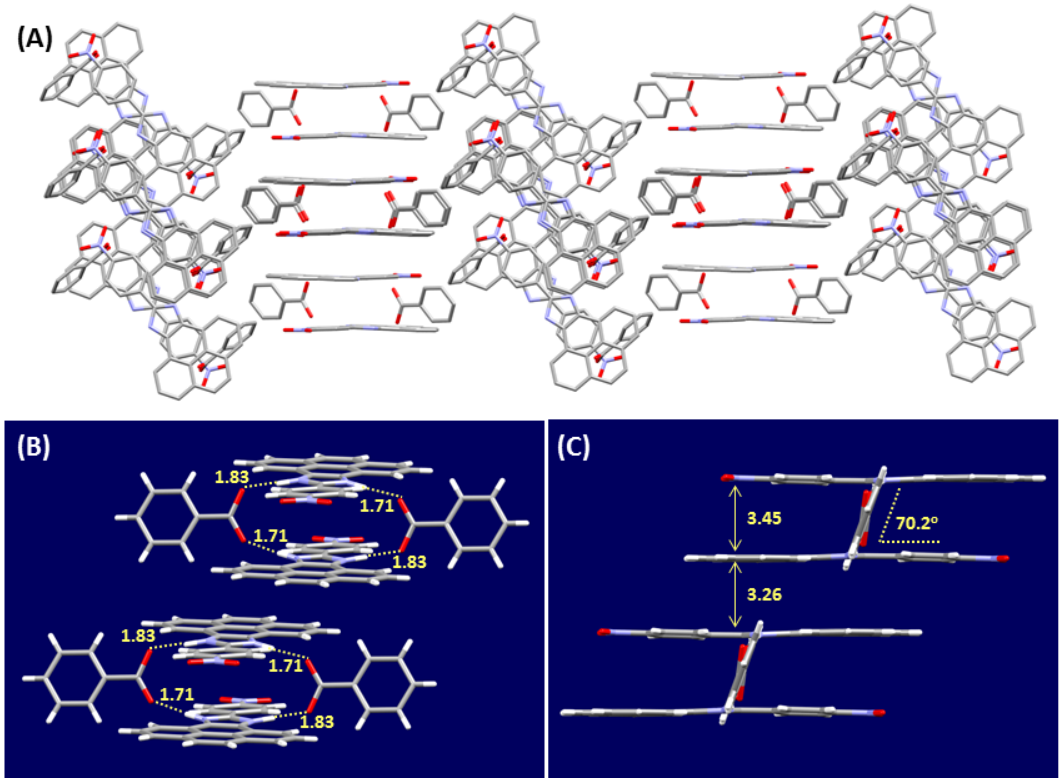

Figure 4.7: (A) Packing diagram of the co-crystal of **4** and benzoic acid (hydrogen atoms are hidden for clarity). (B) Hydrogen-bonded "double-decker" assemblies of **4** and benzoic acid molecules in the crystal structure (hydrogen bonds highlighted in Å). (C) Side view of the hydrogen-bonded "double-decker" assemblies of **4** and benzoic acid molecules, with interplanar distances (in Å) and tilt angle highlighted. CCDC 1972771.

At the outset of our studies, two types of straightforward imidazolium–carboxylate interacting motifs were envisioned for the co-crystallization of pyrenoimidazole **4** and aromatic carboxylic acid synthons, which are (A) hydrogen bonding polymer wires and (B) a hydrogen-bonded "double-decker" shaped assembly (Figure 4.6). The first

motif was observed in some reported imidazolium–carboxylate co-crystals,[186,189] while the second motif is generally deemed less favored than the first one due to the repulsive face-to-face imidazolium stacking. Nevertheless, compound **4** and benzoic acid (**5**) yielded co-crystals that actually contain the"double-decker" assemblies in the crystal structure (see Figure 4.7). Two pairs of NH$\cdots$O hydrogen bonds are involved in each of the "double-decker" structures, which show bond lengths of 1.83 Å and 1.71 Å, respectively (see Figure 4.7B). The two molecules of **4** are oriented in an anti-parallel slipped face-to-face stacking fashion. Such a geometry allows the molecular dipole moments of the pair to align oppositely, hence giving rise to attractive dipole–dipole interactions. The interplanar distance between the two anti-parallel molecules of **4** is 3.45 Å, and each benzoic acid molecule adopts an angle of 70.2° with respect to the plane of associated pyrenoimidazole **4** (see Figure 4.7C). In addition to hydrogen bonding interactions, close intermolecular π–π stacking can also be observed between adjacent "double-decker" assemblies, resulting in the formation of repeating parallel layers in the crystal structure.

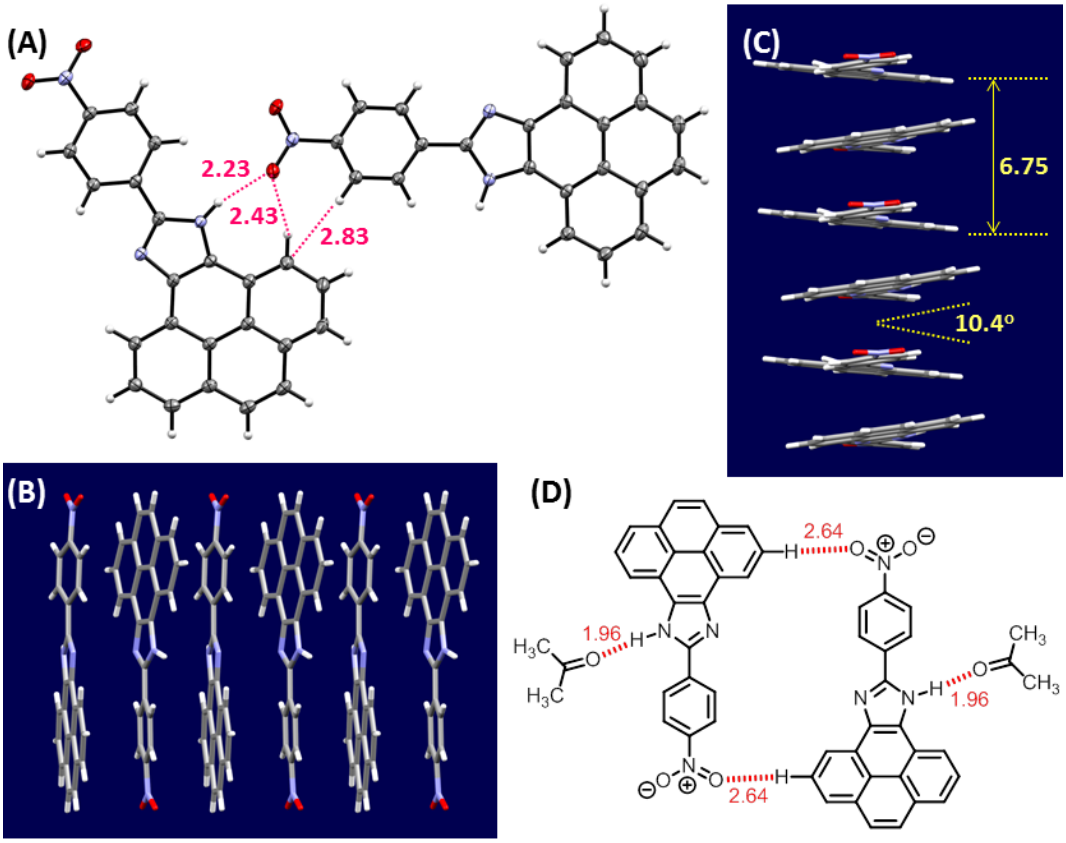

Figure 4.8: (A) ORTEP drawing of two molecules of **4** in the unit cell (30% probability, close intermolecular contacts highlighted in Å, CCDC 1981368). (B) π–Stacking motif of compound **4** showing anti-parallel orientation between adjacent molecules. (C) Side view of π–stacking of **4** with interplanar distance (in Å) and angle highlighted. (D) Topology of a dimeric assembly of **4**/acetone reported in our previous paper.

Attempts to co-crystallize compound **4** with terephthalic acid (**6**) did not yield co-crystals. Instead, single crystals of **4** were formed under the co-crystallization conditions, and the result can be attributed to the unsuited of the shapes of **4** and terephthalic acid. Nevertheless, the solid-state structure of the resulting single crystals of **4** is still worth some remarks here. Previously, we determined the X-ray structure of **4** co-crystallized with acetone, which features a square-shaped hydrogen-bonded dimeric assembly (see Figure 4.8D). In that structure, the imidazolyl NH groups form hydrogen bonds with acetone O atoms (1.96 Å), while the nitro O atoms interact with the pyrenyl CH groups (2.64 Å). For the single crystal structure determined in this work (Figure 4.8A), two molecules of **4** are also bonded together through intermolecular hydrogen bonds but in a different geometry; the nitro O atom of each molecule interacts with the imidazolyl NH and the pyrenyl CH groups of the adjacent molecule, forming double hydrogen bonds at distances of 2.23 Å and 2.43 Å, respectively. In addition, the phenyl and pyrenyl edges also show close contact as a result of electrostatic attraction (see Figure 4.8A). The different hydrogen bonding geometries attest to the versatility of compound **4** as a molecular building block for construction of diverse crystalline forms. The single crystal structure of **4** also shows interesting π–π stacking features. As shown in Figure 4.8B, each pair of adjacent molecules of **4** are oriented in the opposite direction. As such, the electron-deficient *para*-nitrophenyl groups interact with the relatively electron-rich pyrenyl units through a face-to-face stacking motif. Viewing from the side of this π-stack, the adjacent molecules of **4** show an angle of 10.4° between their pyrenoimidazolyl planes. This angle is consistent with the torsion angle between the phenyl and pyrenoimidazolyl group (10.8°) in the molecular structure of **4**.

Compound **4** co-crystallized with trimesic acid (**7**), water, and acetone together to yield good-quality four-component molecular crystals. In the crystal structure, molecules of **4** form arrays of herringbone-shaped stacks, which are intercalated with trimesic acid, water, and acetone molecules (see Figure 4.9A). The detailed hydrogen bonding interactions among the molecules of **4**, **7**, water, and acetone are illustrated in Figure 4.9B. For the trimesic acid, two of the three carboxylic groups are deprotonated to form carboxylate anions, whereas the third carboxylic group remains intact. Hydrogen bonds are thus formed between imidazolyl NH groups and carboxylate O atoms, water OH and carboxylate O atoms, carboxylic COOH groups and water O atoms, and water OH and acetone O atoms, respectively. The multiple hydrogen bonds assemble the molecules into a complex 3-dimensional hydrogen bonding networks. Of particular note is that two molecules of trimesic acid are linked together to form a dimeric cluster through two $COOH\cdots OH_2$ hydrogen bonds and two $COO^{-}\cdots H–OH$ bonds (see Figure 4.9B). Another carboxylate (COO^{-}) group of each trimesic acid forms double hydrogen bonds with the imidazolyl NH groups nearby, leading to the formation of hydrogen-bonded "double-decker" shaped assemblies as subunits in the crystal structure (see Figure 4.9C). The "double-decker" structure here is similar to that observed in the co-crystal structure of **4** and benzoic acid. Overall, hydrogen bonding and π–π stacking constitute the dominant cohesive forces to steer the architecture of complex network structures in the co-crystal. The topology of hydrogen-bonded networks containing imidazole and trimesic acid molecules can be better viewed in Figure 4.10A, where ordered grid-like supramolecular frameworks is clearly revealed. The arrangement of solvent molecules (water and acetone) also show organized topology as depicted in Figure 4.10B. Through hydrogen bonds,

the solvent molecules are associated with the **4**–trimesic acid frameworks, forming column-shaped assemblies along a direction that is nearly perpendicular to the π-surfaces of pyrenoimidazole molecules. Such complex underlying topologies in the co-crystal structure demonstrate the applicability of pyrenoimidazoles as versatile supramolecular synthons in organic crystal design and engineering.

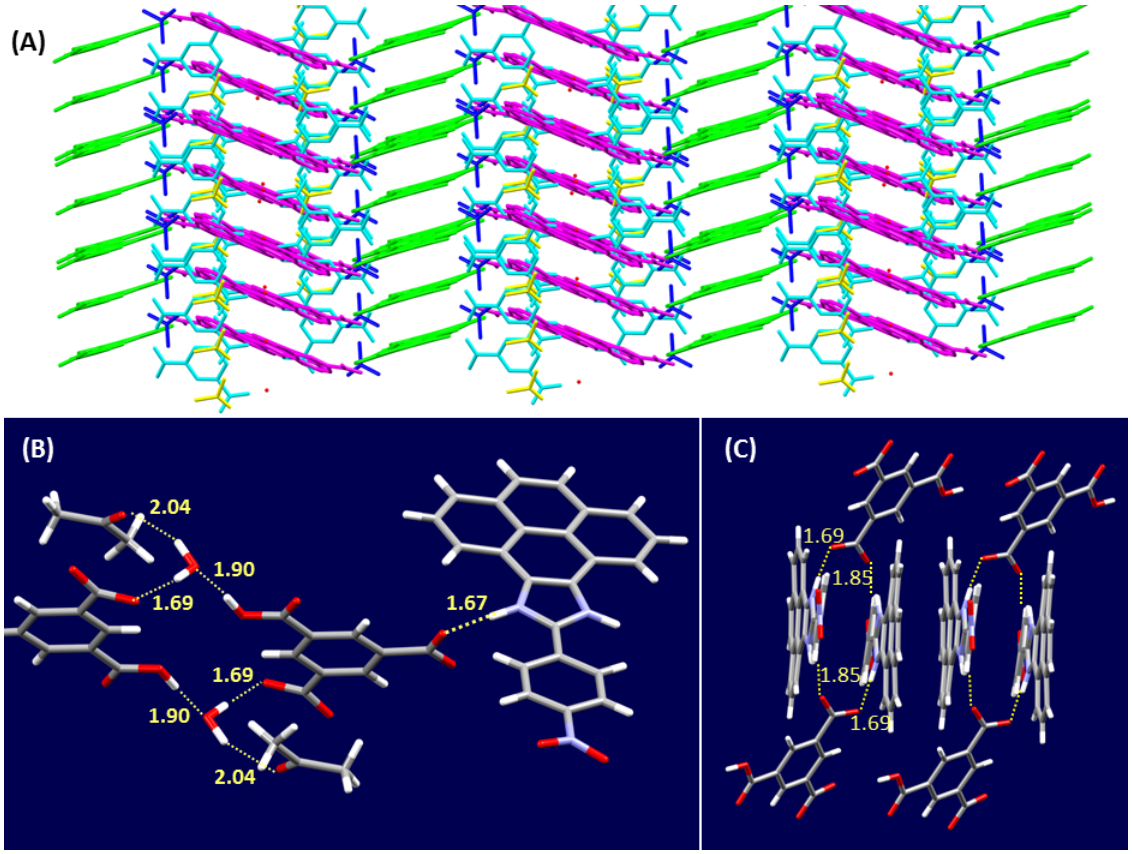

Figure 4.9: (A) Packing diagram of the co-crystal of **4**, trimesic acid, water, and acetone (hydrogen atoms molecules colored by operation symmetry). (B) Hydrogen bonds among **4**, trimesic acid, water, and acetone (distances highlighted in Å). (C) Hydrogen-bonded "double-decker" assemblies of **4** and trimesic acid molecules in the crystal structure (hydrogen bonds highlighted in Å). CCDC 1972772.

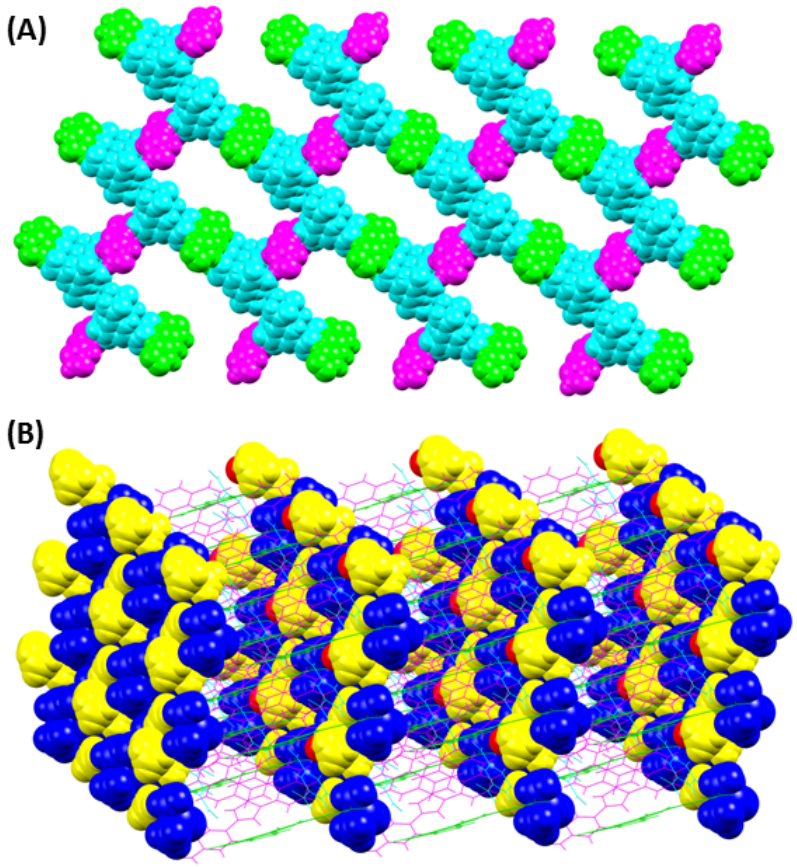

Figure 4.10: (A) Topology of hydrogen-bonded trimesic acid–imidazole frameworks, and (B) arrangement of solvent molecules in the co-crystal of **4**, trimesic acid, water, and acetone (highlighted by space filling model and colored by symmetry operation).

4.4 Conclusions

In conclusion, we have synthesized a series of pyrenoimidazole derivatives **1**–**4** and investigated their crystallization behavior in order to demonstrate the feasibility of using them as supramolecular synthons to construct designed organic crystals. Our crystallographic studies disclosed the effects of hydrogen bonding, π–π interactions, and CH$\cdots$-π stacking on the crystal packing properties of pyrenoimidazoles. Moreover, co-crystallization of pyrenoimidazole **4** with various aromatic carboxylic

acids has been proven a feasible approach to achieve organized 3D supramolecular frameworks, in which hydrogen bonding interactions between imidazolium and carboxylate ions play a dictating role. On the other hand, the influence of other weak non-covalent forces is also significant in the crystal packing structure. The failure to co-crystallize **4** with terephthalic acid points out that size and shape complementarity warrants careful consideration in the design of pyrenoimidazole/carboxylic acid co-crystals. Finally, it is worth remarking that pyrenoimidazoles have been known as an important class of organic chromo-/fluorophores with tunable electronic properties and versatile acidity/basicity.[68,84,98,100,101,148,181] Our findings in this work open a promising avenue for the development of functional pyrenoimidazole-based crystalline materials with potential application in the fields of organic optoelectronics, supramolecular guest-host chemistry, and catalysis.

Chapter 5

Hirshfeld Surfaces Analysis of Pyrenoimidazole Crystal Structures

The contents of this chapter form the basis of a manuscript under preparation, which is intended to be submitted to a Physical (Organic) Chemistry journal soon. The Hirshfeld surface analysis was independently carried out by Z. A. Tabasi, while density functional theory (DFT) calculations and analyses through the quantum theory of atoms in molecules (QTAIM) approach were performed by Prof. Y. Zhao (supervisor, co-author).

5.1 Introduction to Hirshfeld Surfaces Analysis

The major topics of crystal engineering in recent years can all be found in Desiraju's 1989 monograph, entitled *Crystal Engineering-The Design of Organic Solids.*[198] The first discussion about using visualization tools for crystal engineering was made in 1999 by Seddon, who identified synthetic vectors (hydrogen bonding, inter-ring interactions, non-covalent bonds, Coulombic forces, etc.) through computational chemistry and Cambridge Structural Database (CSD).[199] One popular way to comprehensively examine the intermolecular interactions in the crystal packing is by means of the Hirshfeld surfaces analysis and two-dimensional fingerprint plots.[200,201] Hirshfeld surfaces were named after F. L. Hirshfeld, whose "stockholder partitioning" scheme for defining atoms in molecules suggested an extension to defining a molecule in a crystal.[202] The concept of Hirshfeld surface analysis was first introduced in 1997 by Spackman and Byrom.[203,204] In 1998 McKinnon *et al.* devised grayscale three-dimensional isosurfaces for illustration of a variety of molecular crystals and their relationships with fused vdW spheres and molecular electron density isosurfaces in the crystals of naphthalene and terephthalic.[205] In the present research, a software package, *CrystalExplorer*, is available for performing the calculations of Hishfeld surfaces of molecules within a crystal structure and determination of the intermolecular interactions between particular molecules in the crystal structure.[206] Furthermore, in order to make meaningful comparisons between crystal structures it is essential that bond distances to hydrogen atoms are standardized to realistic values. For this purpose, *CrystalExplorer* uses average bond distances derived from neutron diffraction experiments, and a value of 1.190 Å for B—H. Molecular Hirshfeld surfaces

divide the crystal into regions due to the electron distribution of atoms in a molecule and reflect intermolecular interactions in a visual manner. Intermolecular interactions can be identified by color coding distances from the surface to the nearest atom exterior or interior to the surface. Various intermolecular forces, weak and strong, can create an energetic system. Both qualitative and quantitative information of a crystal can be measured through the space occupied of a molecule in the crystal. Hirshfeld surfaces show tight packing in the crystal without overlapping and with small intermolecular voids.[202]

Hirshfeld defined a weight function ($0 \leq W_A(r) \leq 1$) for crystal through partitioning space of crystal into regions which are related to the electron density of each atom and the proximity of neighboring atoms. The detailed expression of this function is given below.[201]

$$W_A(r) = \sum_{i \in moleculeA} {\rho_i}^{at}(r) / \sum_{i \in crystal} {\rho_i}^{at}(r) = \rho_{promolecule}(r)/\rho_{procrystal}(r) \qquad (5.1)$$

This simple scalar function is highly localized to the molecule of interest, flat across the molecule itself with $W_A(r) > 0.9$, and decays rapidly to values less than 0.1, with contours closely spaced around the molecule in the vicinity of the van der Waals (vdW) surface. On the particular isosurface, where $W_A(r) = 0.5$, the electron density of a sum of spherical atoms for the molecule (i.e., the promolecule) exceeds the corresponding sum over the crystal (i.e., the procrystal). The maximum proximity of neighboring molecular volumes without overlapping of them is observed. The "promolecule" and the "procrystal" are ideal reference systems made up by non-interacting atoms located at the same positions of the corresponding real molecule

and crystal. Hirshfeld surfaces of molecules fill about 95% of the crystal volume that is much larger than conventional ones (0.65–0.80%). Their packing is very tight in the crystal with small intermolecular voids that is similar to the growth of pomegranate seeds as described by Kepler.[207]

5.1.1 Surface Properties

In 1998, Spackman *et al.* reported the computational measurement of two descriptors of shape globularity (G) and asphericity (Ω) for some compounds through molecular volume (V_H), surface area (S_H), and packing ratio (P_H). The P_H is defined by the following equation.[202]

$$P_H = \sum_{cell} V_H / V_{cell} \tag{5.2}$$

Globularity (G) is measured through difference degrees of a sphere of the same volume that will be 1.0 for a sphere, and will be more structured in less than one. Asphericity (Ω) is a measure of anisotropy with values of zero for an isotropic object (e.g., asphere, tetrahedron or octahedron, where all principal values are identical), 1.0 for a prolate object, and 0.25 for an oblate object. The combination of G and Ω along with surface area and volume can provide shape information of molecules in crystals, but quantities derived directly from these measures are not informative as much as weight function. By using the weight function, unusual properties of Hirshfeld surfaces can be found for examining anomalies in crystal structures.[208]

5.1.2 Properties Encoded on the Hirshfeld Surface

In contrast to a vdW surface or an outer surface of the electron density, the Hirshfeld surface is defined by the molecule and the proximity of its nearest neighbors. The surface can be encoded differently to show information about various types of intermolecular interactions. Close intermolecular contacts are reflected on the Hirshfeld surfaces that are defined as different functions mapped in colors, including d_e, d_i, d_{norm}, **shape index**, **curvedness** and **fragment patches**.[201,207] Each function is observed as an example on the pyrene-4,5-dione molecule (see Figure 5.1).

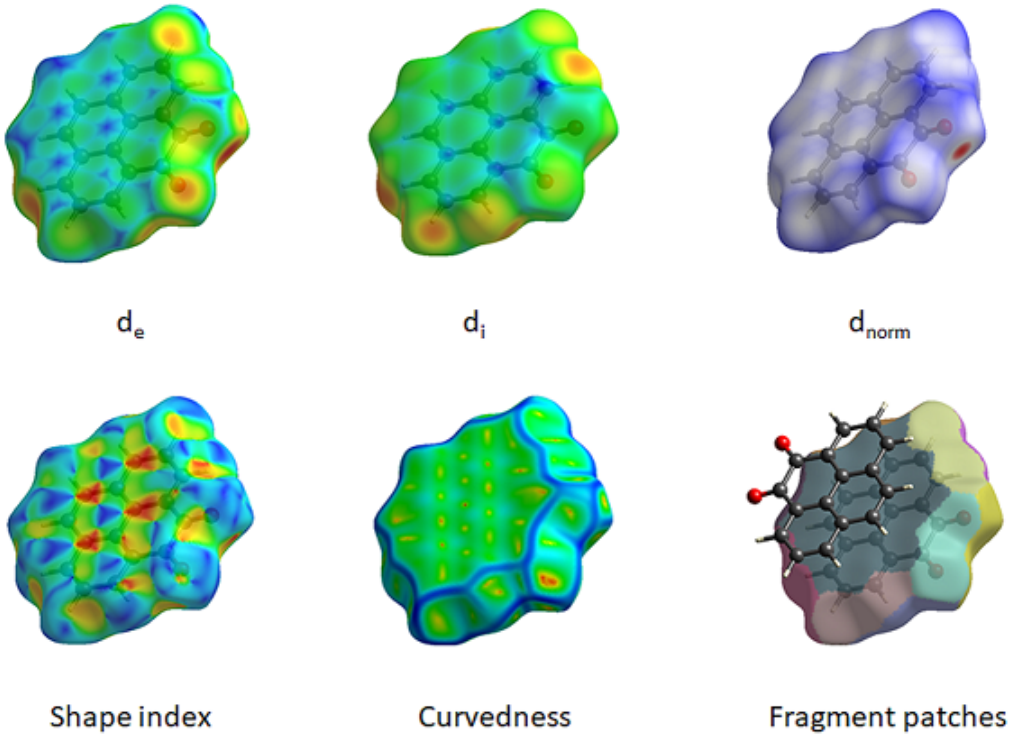

Figure 5.1: Hirshfeld surfaces of pyrene-4,5-dione.

As illustrated in Figure 5.1, the d_e mapped surface reflects the distance from the surface to the nearest nucleus in another molecule. Close contacts, especially

hydrogen-bond donor and acceptor regions, are observed on the surface as nearly flat regions in different colors. Proximity of the two 6-rings of closely stacked molecules gives rise to small blue hexagons on the Hirshfeld surface. The d_i map measures distance from the surface to the nearest atom in the molecule itself and reveals close contacts. The d_{norm} is the sum and symmetric function of normalized contact distances of d_i and d_e that are normalized by the vdW radii of the atoms involved, using a color scale of red (shorter than vdW separation), white (equal to vdW separation), and blue (longer than vdW separation). The **shape index** map depicts the shape index on the Hirshfeld surface, with complementary red and blue regions (hollow and bump) through touching of surfaces of molecules. This pattern is observed in red and blue triangles with stacking of 6-rings or π–π stacking. The **curvedness** map shows large regions of green, which are separated by dark blue edges. Sometimes the yellow or red spots are observed on the surface that is related to hydrogen bonds. Finally, the **fragment patches** map is colored to show patches on the Hirshfeld surface, indicating closeness of adjacent molecules and hence coordination number.

5.1.3 Two-Dimensional Fingerprint Plots

In any crystal structure with different intermolecular contacts, it is always helpful to condense all the information into a single picture or plot. For instance, non-bonded interaction pattern matrix (NIPMAT) scheme has been used during the years of 1995 to 2003 for visualizing intermolecular interactions. Such a scheme uses grayscale squares of varying darkness, in which darker squares are related to closer contacts and exhibited the sum of vdW radii of the contacting atoms in diagonally mirrored

pictures as close contacts of two atoms. The NIPMAT scheme is a useful application for explanation of intermolecular interactions, but it is not a good choice for relatively large molecules, due to increasing number of squares as the number of atoms increases. For instance, an N-atomic molecule can be represented by an N × N matrix of grayscale pixels.[208–210]

In 2002, Spackman & McKinnon introduced a different but more efficient method for summarizing information of crystal structures through two-dimensional (2D) histogram fingerprint plots related to the frequencies of different distances from the Hirshfeld surface to the nearest nucleus both inside (internal = d_i) and outside (external = d_e) the surface. In a 2D fingerprint plot, bins are created with 0.01 Å width that its color represents the fraction of points of surface in this bin. The range on this graph is usually between 0.4–2.6 Å, in which blue color represents few, green moderate and red many points of interactions.[201,202]

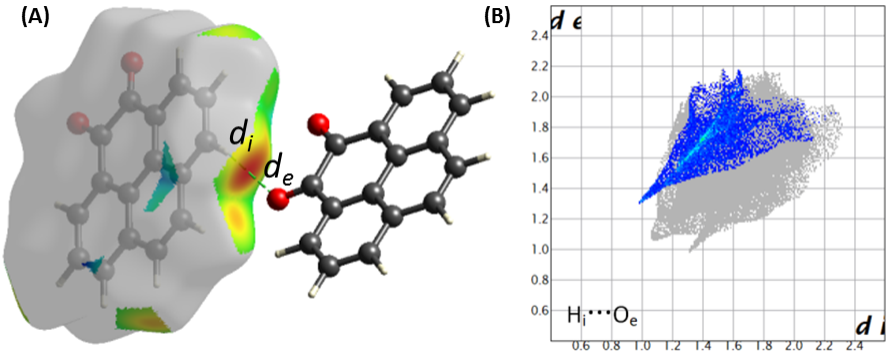

Figure 5.2: (A) Hirshfeld surface mapping the O···H contacts in the crystal of pyrene-4,5-dione. (B) Fingerprint plot with the O···H contacts of pyrene-4,5-dione highlighted.

As illustrated in Figure 5.2A, the Hirshfeld surface gives two distances, d_i and

d_e. Herein, the d_i map of pyrene-4,5-dione shows a red spot that is due to close intermolecular contacts between hydrogen and oxygen atoms of pyrene. The type of interactions can be viewed as hydrogen-bonding interactions, where the pyrenyl hydrogen atoms act as hydrogen bond donors. Also in this diagram, d_e denotes the distance of the oxygen on another molecule (hydrogen bond acceptor) to the surface.

The O$\cdots$H contacts are reflected on a 2D fingerprint plot (Figure 5.2B), where each point corresponds to a unique (d_e, d_i) pair, and the color of each point corresponds to the relative area of the surface associated with that (d_e, d_i) pair. Points on the plot with no contribution on the surface are left uncolored, while points with a contribution to the surface are colored blue for a small contribution, and through green to red for points with the large contribution. In this particular 2D fingerprint plot, the majority of the O$\cdots$H interactions in the crystal of pyrene-4,5-dione gives a blue colored spike with green color in the middle. It is also worth mentioning that Figure 5.2B is partially colored to highlight a special type of intermolecular contacts. The fingerprint plot can also be fully colored show information about all interamolecular interactions. Because Hirshfeld surfaces nearly fill the available space, the void volume is very small. The 2D fingerprint plots are usually pseudo-mirrored along the $d_e = d_i$ diagonal. Features along the diagonal are generally due to like$\cdots$like contacts (e.g., H$\cdots$H and C$\cdots$C contacts), while the "wings" on the plot are due to O$\cdots$H, N$\cdots$H, and C–H$\cdots\pi$ interactions.

5.2 Hirshfeld Surface Analysis of Pyrenoimidazole Crystals

5.2.1 Phenyl-Substituted Pyrenoimidazole

The results of Hirshfeld surface analysis of the crystal structure of phenyl-substituted pyrenoimidazole are shown in Figure 5.3. In Figure 5.3B, the d_{norm} mapped surface shows a number of red spots, with the most significant one appearing at the imidazolyl N–H and C=N positions. These spots correspond to the hydrogen bond donor and acceptor groups in the molecule, which afford intermolecular N–H$\cdots$N=C bonds in the crystal packing. In the fingerprint plot, the intermolecular N$\cdots$H contacts are reflected by two distinct sharp spikes with symmetric distribution of points at the sum of $d_i + d_e \approx 1.9$ Å, which constitute 6.6% of the total Hirshfeld surfaces.

The intermolecular C$\cdots$H interactions in the crystal structure are depicted as two wings ($d_i + d_e \approx 2.4$ Å) in the fingerprint plot, which make 38.2% contribution in the two-dimensional fingerprint plot. In the crystal structure, the phenyl C–H edge shows a T-shaped stacking motif with the pyrenyl unit of an adjacent molecule. So, a significant portion of the C$\cdots$H interactions arises from intermolecular C–H$\cdots\pi$ stacking.

The H$\cdots$H interactions are dominant intermolecular interactions with a contribution of 44.9% to the total Hirshfeld surfaces ($d_i + d_e \approx 2.2$ Å). Additionally, $\pi\cdots\pi$ (C$\cdots$C) interactions make a relatively significant contribution (9.2%). In the crystal structure, pyrenyl units are found to stack intermolecularly in a face-to-face fashion. The Hirshfeld surface mapped with shape index reveals such $\pi - \pi$

stacking features by showing similar adjacent red and blue rhomboid-like shapes (highlighted within the red circle of Figure 5.3C). Apart from the above-mentioned intermolecular interactions, C$\cdots$N contacts are also identified on the finger print plot, which contribute 1.1% to the Hirshfeld surface.

5.2.2 Tolyl-Substituted Pyrenoimidazole

The results of Hirshfeld surface analysis of the crystal structure of tolyl-substituted pyrenoimidazole are shown in Figure 5.4. Compared with phenyl-substituted pyrenoimidazole, the intermolecular H$\cdots$H interactions make a larger contribution (49.7%), which can be linked to the presence of methyl group in the molecular structure. The intermolecular N$\cdots$H hydrogen bonds give two sharp symmetrical spikes in the two-dimensional fingerprint plots with $d_i + d_e \approx 2.2$ Å and make a contribution of 5.6% of the total Hirshfeld surface. Significant red-colored spots on the Hirshfeld surface due to the strong and short N$\cdots$H interactions can be observed in the d_{norm} mapped surface (Figure 5.4B). The C$\cdots$H interactions make 30.9% contribution on the Hirshfeld surface and show two distinct spikes with scattered points in the middle of the fingerprint plot with $d_i + d_e \approx 2.4$ Å. Furthermore, $\pi - \pi$ interactions give a contribution of 7.7%, while the shape index mapped surface (Figure 5.4C) shows complementary red and blue triangles (highlighted within the red circle), which are characteristic of $\pi - \pi$ stacking. The C$\cdots$N contacts amount to 2.0% contribution to the intermolecular interactions in the crystal structure of tolyl-substituted pyrenoimidazole.

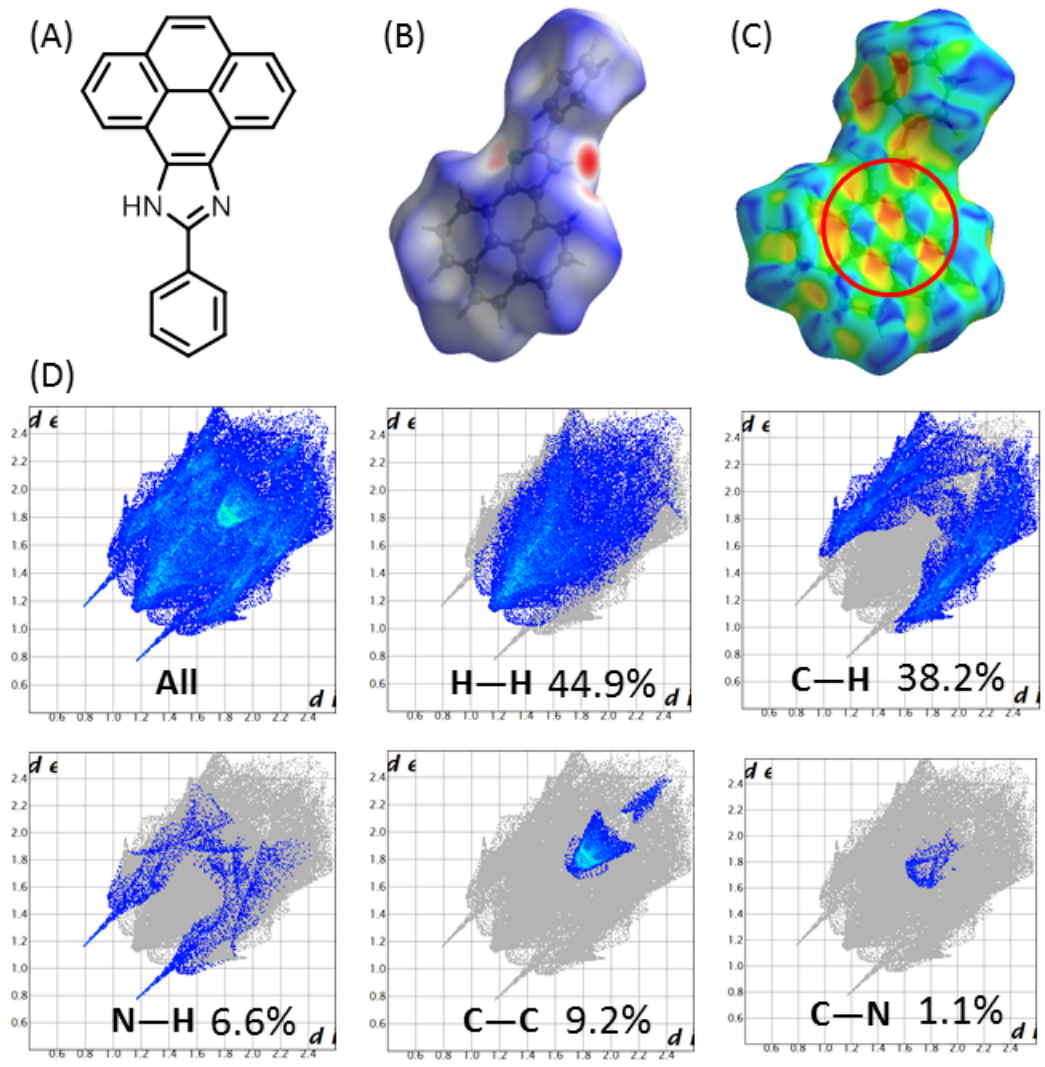

Figure 5.3: (A) Molecular structure of phenyl-pyrenoimidazole. (B) Hirshfeld surface mapped with d_{norm}. (C) Hirshfeld surface mapped with shape index. (D) Fingerprint plots with different intermolecular contacts highlighted.

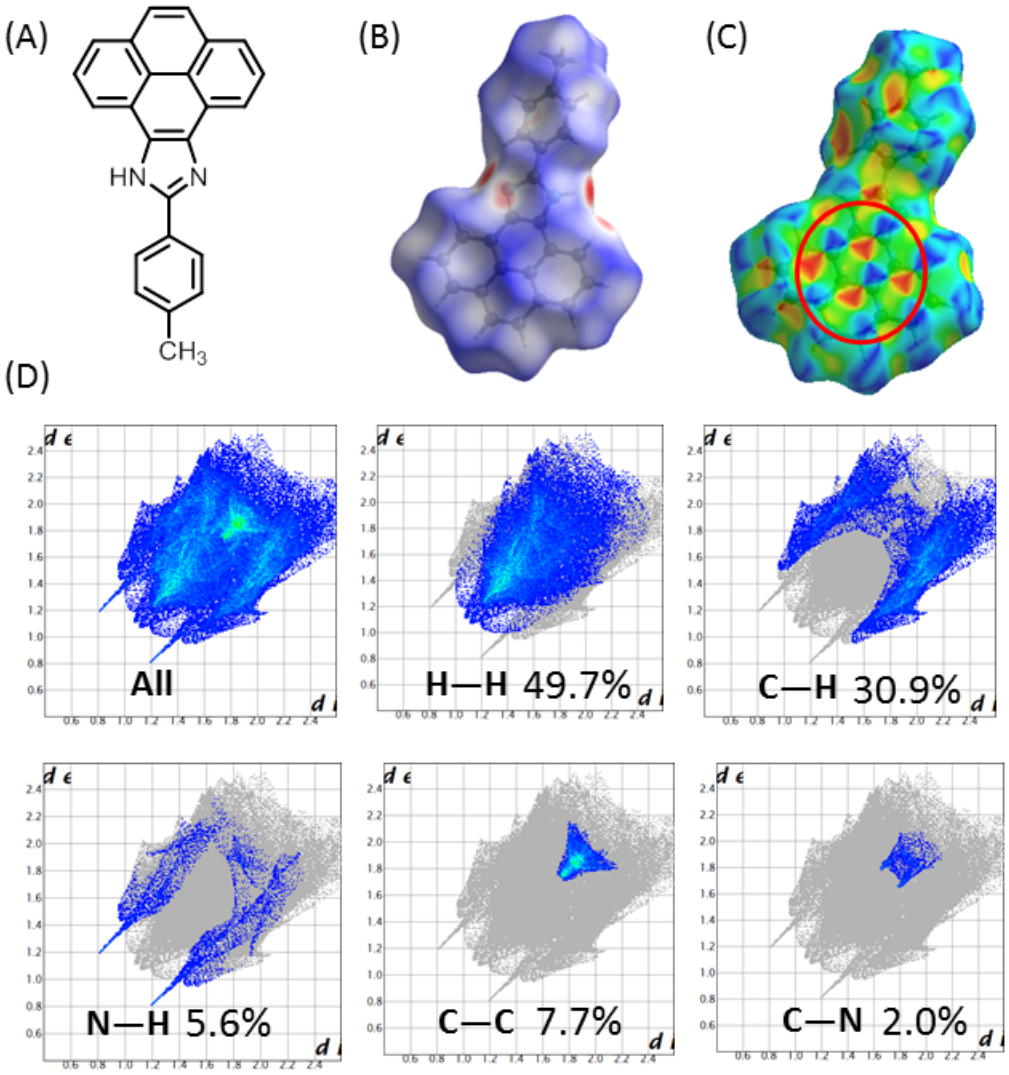

Figure 5.4: (A) Molecular structure of tolyl-pyrenoimidazole. (B) Hirshfeld surface mapped with d_{norm}. (C) Hirshfeld surface mapped with shape index. (D) Fingerprint plots with different intermolecular contacts highlighted.

5.2.3 *p*-Methoxyphenyl-Substituted Pyrenoimidazole

The results of Hirshfeld surface analysis of the crystal structure of *p*-methoxyphenyl-substituted pyrenoimidazole are shown in Figure 5.5. The co-crystallization of this compound with methanol results in intermolecular O$\cdots$H and N$\cdots$H hydrogen bonds, which are reflected as red spots on the Hirshfeld surface mapped with d_{norm} (Figure 5.5B). In the 2D fingerprint plot, N$\cdots$H hydrogen bonds give rise to two spikes in an asymmetric shape with a contribution of 5.3%. The sharp spike appears at d_i = 1.1 Å and d_e = 0.7 Å. Intermolecular O$\cdots$H hydrogen bonds account for 4.6% on the total Hirshfeld surfaces. In the fingerprint plot, there are two asymmetric spikes that can be attributed to these interactions. The sharp spike appears at d_i = 0.7 Å and d_e = 1.1 Å. The C$\cdots$H interactions make a 39% contribution and show a symmetric pair of wings in the 2D fingerprint plot ($d_i + d_e \approx 2.56$ Å). The H$\cdots$H interactions account for 43.4% on the Hirshfeld surface with $d_i + d_e$ = 2.1 Å. The C$\cdots$C interactions make 3.2% contribution, which is smaller than those in the crystals of phenyl- and tolyl-substituted pyrenoimidazoles. Also, there are no complementary adjacent triangle-shaped red and blue spots observable on the Hirshfeld surface mapped with shape index (Figure 5.5C), indicating relatively weak $\pi - \pi$ stacking in the crystal structure of *p*-methoxyphenyl-substituted pyrenoimidazole.

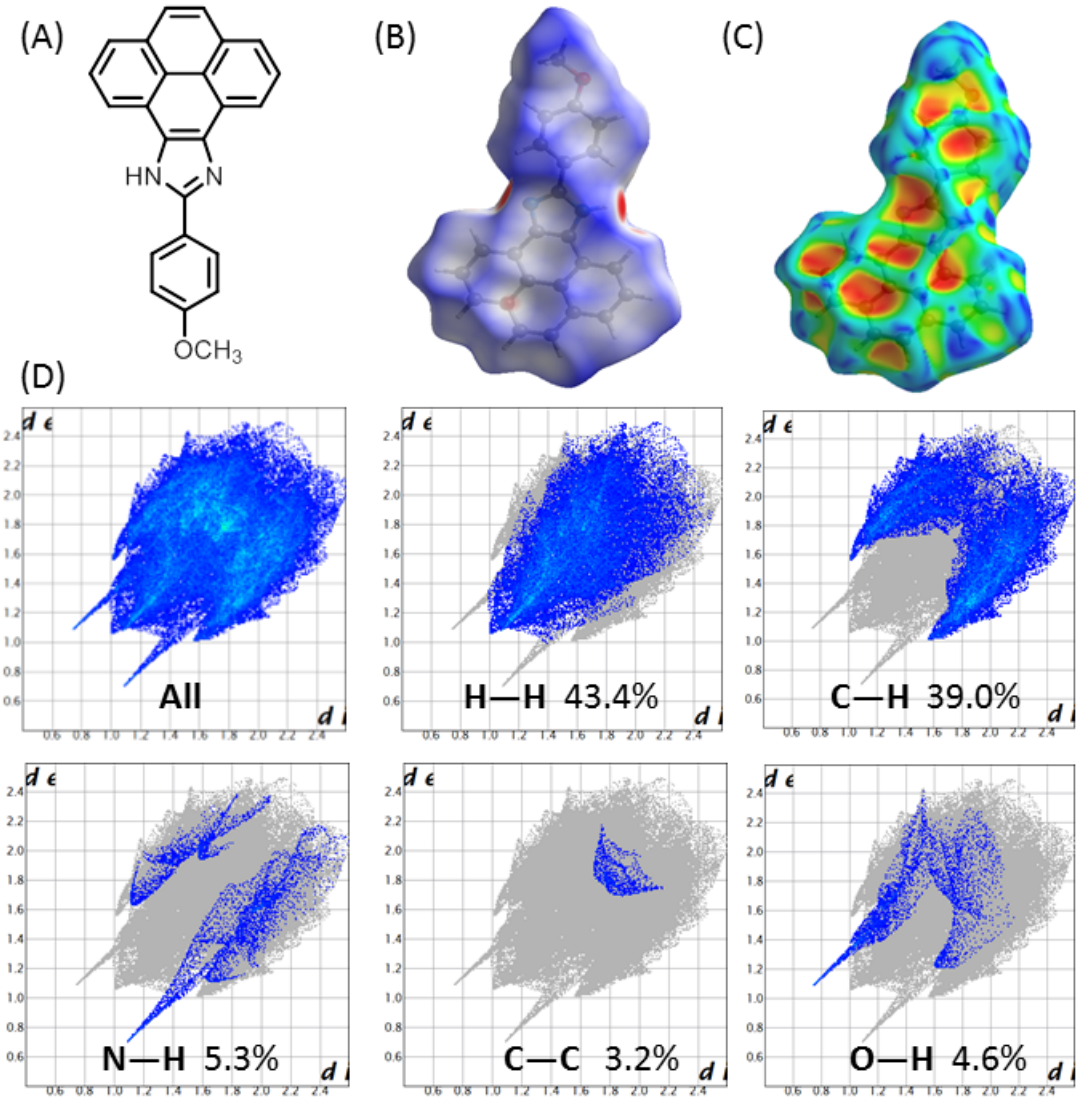

Figure 5.5: (A) Molecular structure of *p*-methoxyphenyl-pyrenoimidazole. (B) Hirshfeld surface mapped with d_{norm}. (C) Hirshfeld surface mapped with shape index. (D) Fingerprint plots with different intermolecular contacts highlighted.

5.2.4 *p*-Chlorophenyl-Substituted Pyrenoimidazole

The results of Hirshfeld surface analysis of the crystal structure of *p*-chlorophenyl-substituted pyrenoimidazole are shown in Figure 5.6. Because of the electron withdrawing effect of the *para*-Cl group, the electron density around the C=N site of imidazolyl moiety is decreased. As a result, only one bright red spot at the N–H region can be seen on the d_{norm} mapped surface (Figure 5.6B). The N$\cdots$H intermolecular interactions are reflected by two asymmetrical broaden regions in the 2D fingerprint plots with $d_i + d_e = 2.8$ Å, which is at a longer distance than those in the previously discussed pyrenoimidazole crystals. The contribution of N$\cdots$H contacts is 4.6%. The C$\cdots$H interactions give 33.9% contribution on the Hirshfeld surface and show two distinct spikes on the fingerprint plot with $d_e = 1.05$ and 1.65 Å, and $d_i = 1.54$ and 1.07 Å. The H$\cdots$H interactions constitute the greatest contribution (35.1%) among other intermolecular interactions, with a significantly sharp spike on the fingerprint plot at a very close contact $d_i + d_e = 2$ Å. $\pi - \pi$ Stacking (C$\cdots$C) is determined to give a contribution of 6.2%. Complementary blue and red triangles on the shape index surface can be observed (Figure 5.6C). Moreover, C$\cdots$N interactions give 3.8% contribution on the Hirschfeld surface. The C$\cdots$Cl interactions are significant with a contribution of 14.6%. On the fingerprint plot, the C$\cdots$Cl are reflected by two symmetrical sharp spikes with $d_i + d_e = 2.8$ Å.

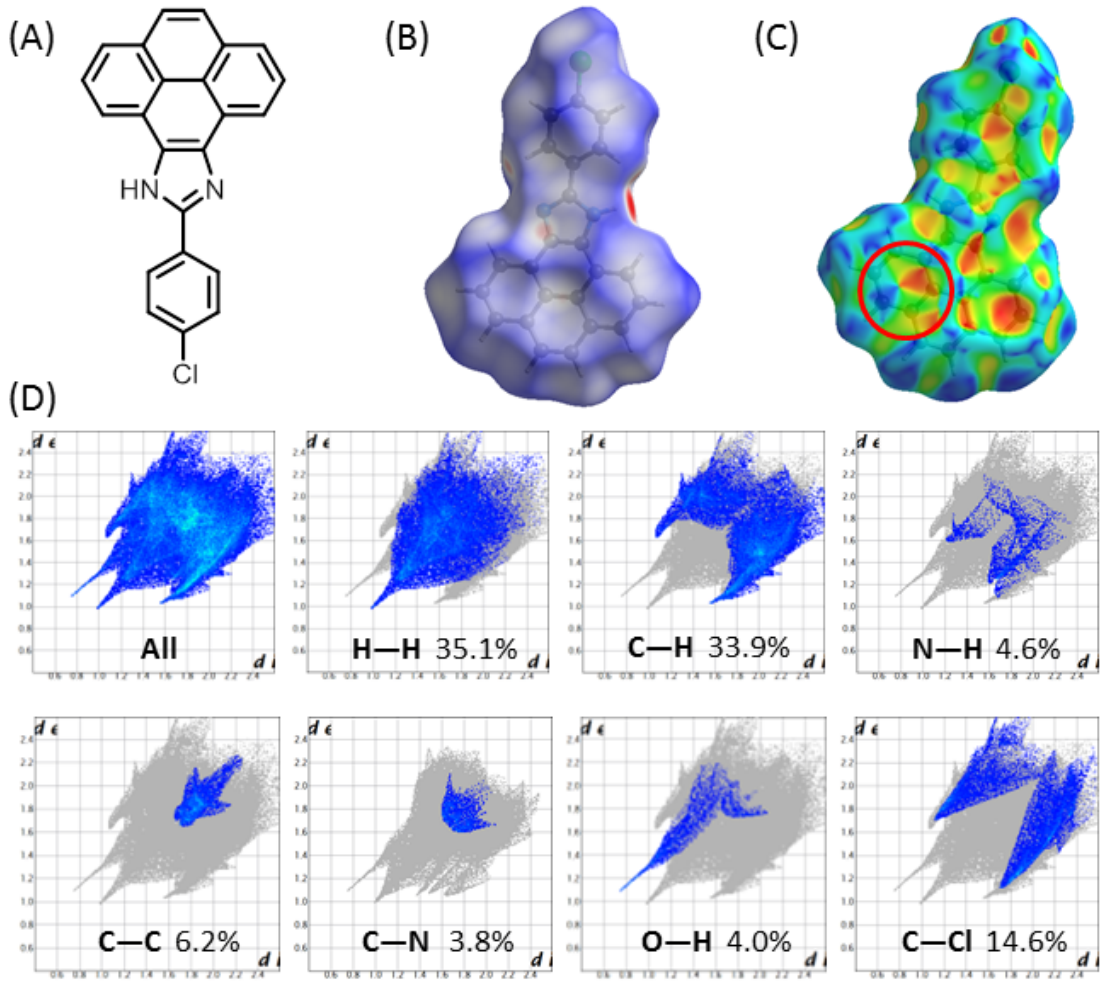

Figure 5.6: (A) Molecular structure of *p*-chlorophenyl-pyrenoimidazole. (B) Hirshfeld surface mapped with d_{norm}. (C) Hirshfeld surface mapped with shape index. (D) Fingerprint plots with different intermolecular contacts highlighted.

5.2.5 *p*-Nitrophenyl-Substituted Pyrenoimidazole

The results of Hirshfeld surface analysis of the crystal structure of *p*-nitrophenyl-substituted pyrenoimidazole (co-crystallized with acetone) are shown in Figure 5.7. Herein, the contribution of N$\cdots$H interactions is decreased to 4.1% and they appear as widely scattered points in the middle and lower region of the fingerprint plot. However, the O$\cdots$H contribution is increased to 18% and can be observed as two asymmetric sharp spikes on the 2D fingerprint plot at the sums of $d_i + d_e \approx 1.8$ Å and 2.4 Å, respectively. The C$\cdots$H interactions in the crystal structure make 24.5% contribution and are reflected on the fingerprint plot with dominating C_i and H_e ($d_i + d_e \approx 2.8$ Å). The H$\cdots$H interactions are dominant interactions in the crystal packing, with a contribution of 35.2% to the total Hirshfeld surface and showing a sharp spike at $d_i + d_e \approx 2.0$ Åon the fingerprint plot. The $\pi - \pi$ (C$\cdots$C) interactions also give a significant contribution to the total Hirshfeld surface, which is of 7.5% contribution. The C$\cdots$N interactions are 3.8% contribution. The bumps and hollows on the edge of the shape index map with distinctive blue crosses and yellow spots illustrate the H$\cdots$H interactions (Figure 5.7C).

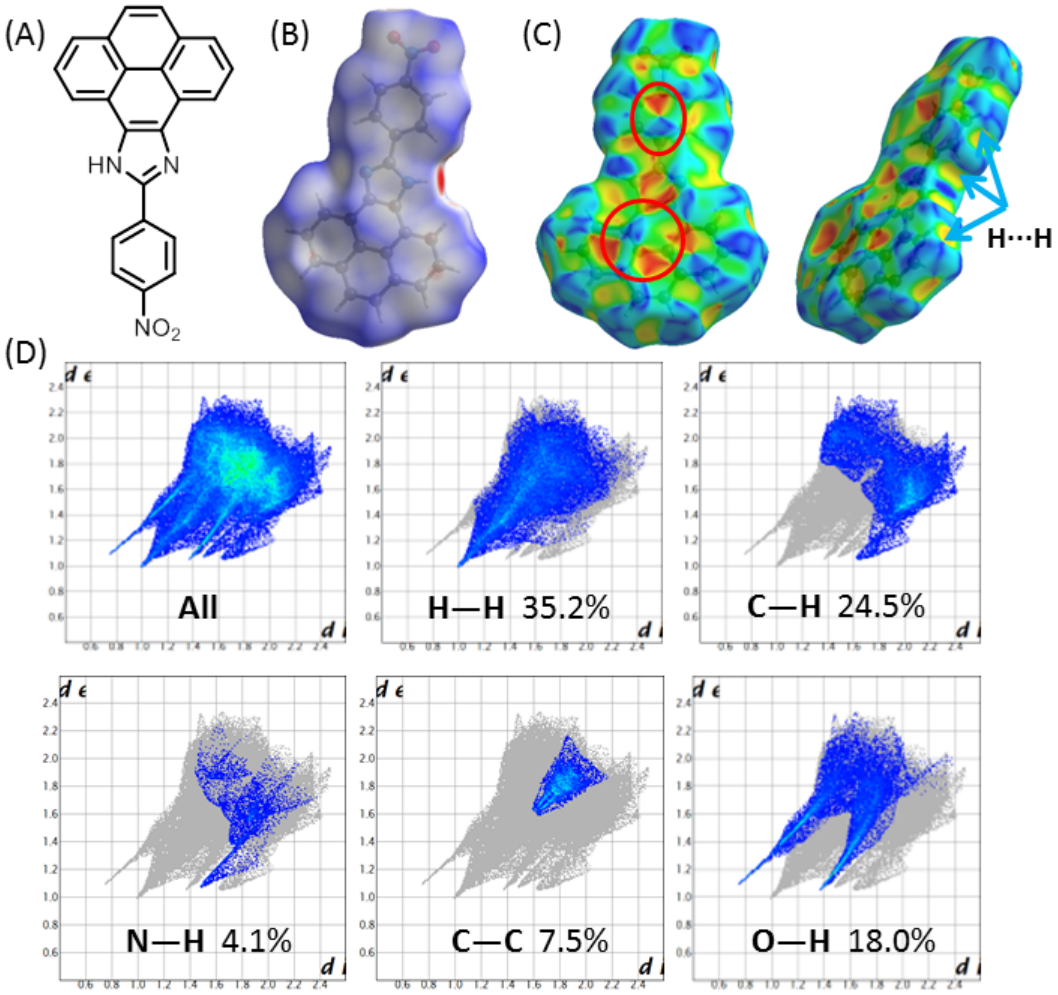

Figure 5.7: (A) Molecular structure of *p*-nitrophenyl-pyrenoimidazole (co-crystallized with acetone). (B) Hirshfeld surface mapped with d_{norm}. (C) Hirshfeld surface mapped with shape index. (D) Fingerprint plots with different intermolecular contacts highlighted.

The results of Hirshfeld surface analysis of the crystal structure of *p*-nitrophenyl-substituted pyrenoimidazole (co-crystallized with water) are shown in Figure 5.8. The Hirshfeld surface mapped with d_{norm} exhibits more red spots compared with the previous co-crystal with acetone, due to the interactions of nitro oxygen atoms with water and phenyl protons. The proportions of C$\cdots$H and C$\cdots$C intermolecular interactions are greatly changed as well; the contribution of C$\cdots$H interactions is decreased to 11%, with two very tiny spikes at $d_i + d_e \approx 2.7$ Å appearing on the fingerprint plot. The contribution of C$\cdots$C contacts is increased to 20.4%. On the fingerprint plot, these contacts are visualized as a bird-like shaped, green colored spike with a tip at $d_i + d_e \approx 3.35$ Å. The contribution of O$\cdots$H interactions is 19.2% and they can be seen on the fingerprint plot as two distinct almost symmetric spikes at $d_i + d_e \approx 1.9$ Å for the upper spike and $d_i + d_e \approx 2.0$ Å for the lower spike. The contribution of N$\cdots$H interactions is 2.5%, with just one sharp spike at very close contact ($d_i + d_e \approx 1.83$ Å) on the fingerprint plot. Like other pyrenoimidazole derivatives, the greatest proportion is contributed by the H$\cdots$H contacts (39.6%). These interactions give a fish-like shaped distribution on the fingerprint plot, with a close contact of $d_i + d_e \approx 2.1$ Å. The shape index mapped surface (Figure 5.8C) reveals characteristic features of $\pi - \pi$ stacking (blue and red colored triangles) on both pyrene and phenyl regions.

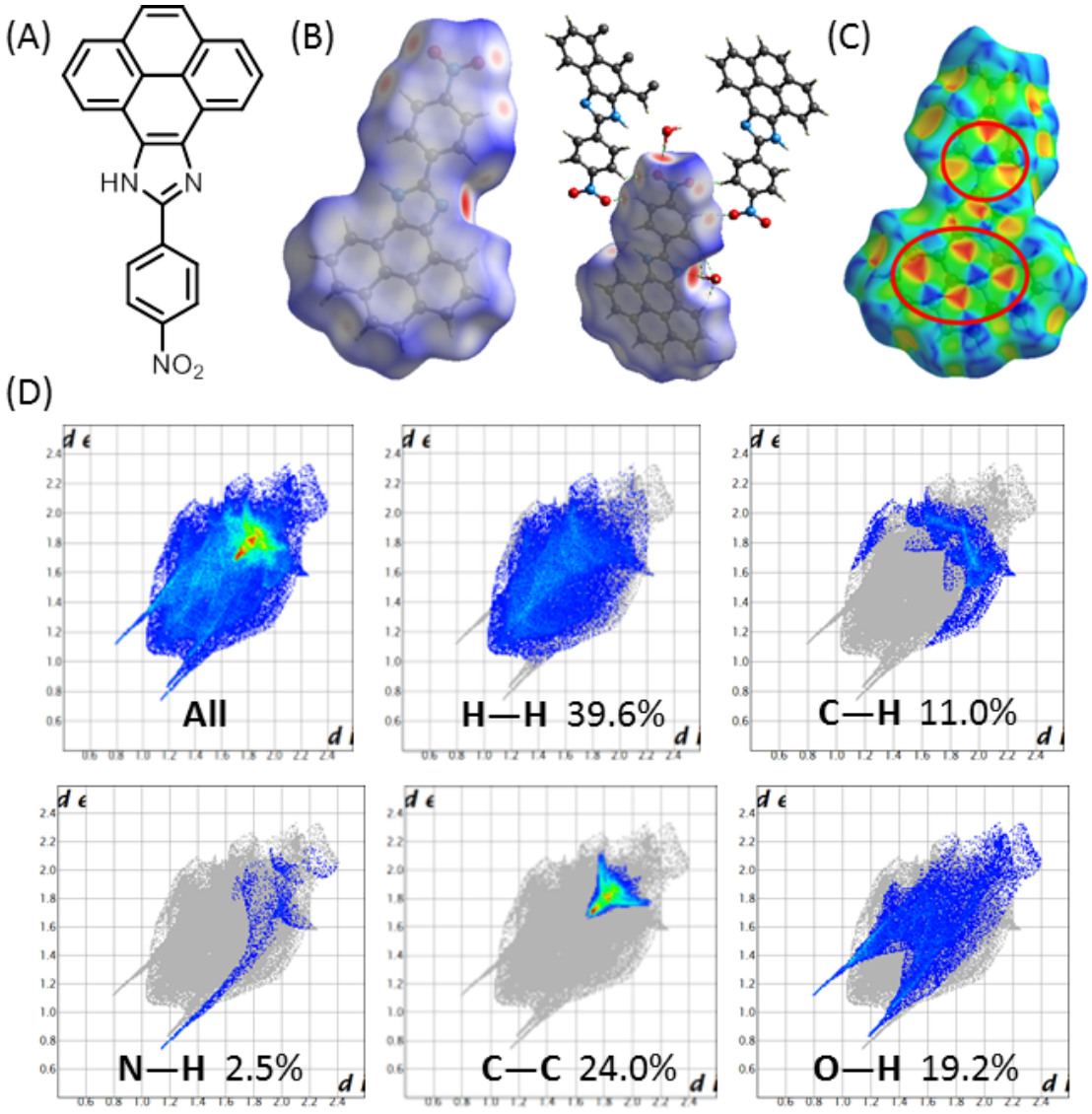

Figure 5.8: (A) Molecular structure of *p*-nitrophenyl-pyrenoimidazole (co-crystallized with water). (B) Hirshfeld surface mapped with d_{norm}. (C) Hirshfeld surface mapped with shape index. (D) Fingerprint plots with different intermolecular contacts highlighted.

The results of Hirshfeld surface analysis of the crystal structure of *p*-nitrophenyl-substituted pyrenoimidazole (co-crystallized with benzoic acid) are shown in Figure 5.9. In this co-crystal, the O$\cdots$H interactions make a contribution of 21.9% to the Hirshfeld surface, and they are reflected on the fingerprint plot as two asymmetric spikes, in which the upper one is in a very sharp shape and at a very close distance of $d_i + d_e \approx 1.65$ Å. The lower spike also shows a sharp shape but appears at a longer distance of $d_i + d_e \approx 2.3$ Å on the fingerprint plot. The N$\cdots$H interactions make a small contribution of 1.7% to the Hirshfeld surface, and their distribution on the fingerprint plot appears to be weak and featureless. The C–H$\cdots\pi$ interactions account for 26.7% contribution on the Hirshfeld surface, and they can be observed as two asymmetric wings on the fingerprint plot at $d_i + d_e \approx 2.8$ Å and 3.0 Å, respectively. The C$\cdots$C contacts are mainly due to the $\pi - \pi$ stacking within the "double-decker" shaped assemblies of pyrenoimidazole and benzoic acid molecules. These interactions are clearly reflected by a number of red and blue colored triangles on the shape index mapped surface (Figure 5.9C). On the fingerprint plot, the C$\cdots$C contacts are visualized as an arrow shape with a green-colored central region appearing at $d_i = d_e \approx 1.6$ Å, and these interactions give 9.7% contribution. The H$\cdots$H contacts make 30.6% on the Hirsfeld surface, which is the highest contribution among others. On the fingerprint plot, the H$\cdots$H contacts encompass the largest area with a tip at $d_i + d_e \approx 2.1$ Å.

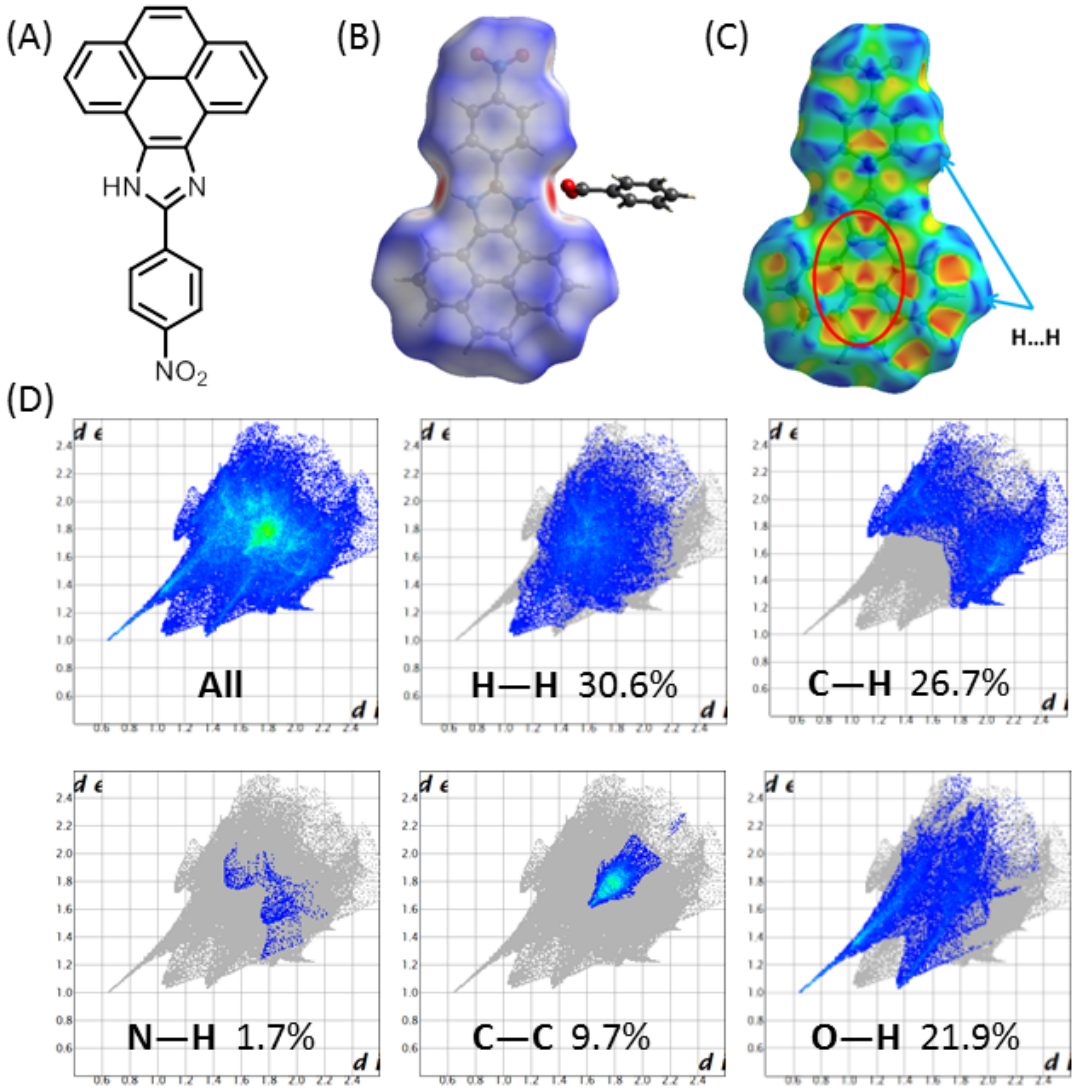

Figure 5.9: (A) Molecular structure of *p*-nitrophenyl-pyrenoimidazole (co-crystallized with benzoic acid). (B) Hirshfeld surface mapped with d_{norm}. (C) Hirshfeld surface mapped with shape index. (D) Fingerprint plots with different intermolecular contacts highlighted.

The results of Hirshfeld surface analysis of the crystal structure of *p*-nitrophenyl-substituted pyrenoimidazole (co-crystallized with trimesic acid) are shown in Figure 5.10. The co-crystallization of *p*-nitrophenyl-substituted pyrenoimidazole with trimesic acid also involved the participation of water and acetone molecules. As such, the O$\cdots$H hydrogen bonding takes a large portion (22%) of the non-covalent interactions in the crystal packing. On the fingerprint plot, the O$\cdots$H contacts appear as two asymmetric spikes, with the upper spike at $d_i + d_e \approx 1.52$ Å and the lower spike at a relatively long distance of $d_i + d_e \approx 2.5$ Å. Of particular note is that the upper spike shows a uniquely sharp shape and appears at a very short distance. This feature can be attributed to the close contacts between imidazolium N–H and adjacent carboxylate groups. On the d_{norm} mapped surface, these contacts are clearly visualized as two very significant red spots near the imidazolium N–H sites (Figure 5.10B). The N$\cdots$H contacts are weak and show somewhat featureless distribution on the fingerprint plot. There are two characteristic symmetric spikes at $d_i + d_e \approx 2.7$ Å, which correspond to the C–H$\cdots\pi$ interactions (18.8% contribution). Again, H$\cdots$H contacts make the largest contribution on the Hirshfeld surface (34.5%), which give a distinct pattern with a minimum value of $d_i = d_e \approx 1.1$ Å. The C$\cdots$C interactions are reflected by a very small region on the fingerprint plot, in the middle of which there is a highly concentrated and green color spot. The distribution of C$\cdots$C interactions on the fingerprint plot shows a tip at $d_i + d_e \approx 3.3$ Å, which is shorter than the sum of van der Waal radii of two carbon atoms. This feature can be attributed to the close $\pi - \pi$ stacking in the "double-decker" assemblies in the crystal structure. On the shape index mapped surface (Figure 5.10)C, blue and red colored triangles can be observed, which are characteristic of the close $\pi - \pi$ stacking. The contribution of

C$\cdots$C contacts constitutes 14.3% of the total Hirshfeld surface.

The results of Hirshfeld surface analysis of the crystal structure of *p*-nitrophenyl-substituted pyrenoimidazole (without any solvents) are shown in Figure 5.11. On the d_{norm} mapped Hirshfeld surface (Figure 5.11B), significant red spots can be visualized to account for the intermolecular O$\cdots$H hydrogen bonds between the nitro oxygen atom and the imidazolyl N–H and pyrenyl protons. On the fingerprint plot, there are two sharp spikes at $d_i + d_e \approx 2.15$ /AA due to the O$\cdots$H contacts (17.7%). On the other hand, the N$\cdots$H contacts in the crystal packing are weak and somewhat randomly scattered on the fingerprint plot. The C$\cdots$H interactions give 17.3% contribution, and show two broad wings with tips at $d_i + d_e \approx 3.1$ Å on the fingerprint plot. The C$\cdots$C contacts make a contribution of 16.8% to the total surface, and they can be visualized by a concentrated, green color shape on the fingerprint plot ($d_i + d_e \approx$ 3.35 Å). On the shape index mapped surface (Figure 5.11C), blue and red colored triangles are observable for $\pi - \pi$ stacking. Like the previous crystal structures, the H$\cdots$H contacts constitute the largest region on the fingerprint plot (38.2%), with a tip at $d_i + d_e \approx 1.9$ Å that reflects very close H$\cdots$H contacts.

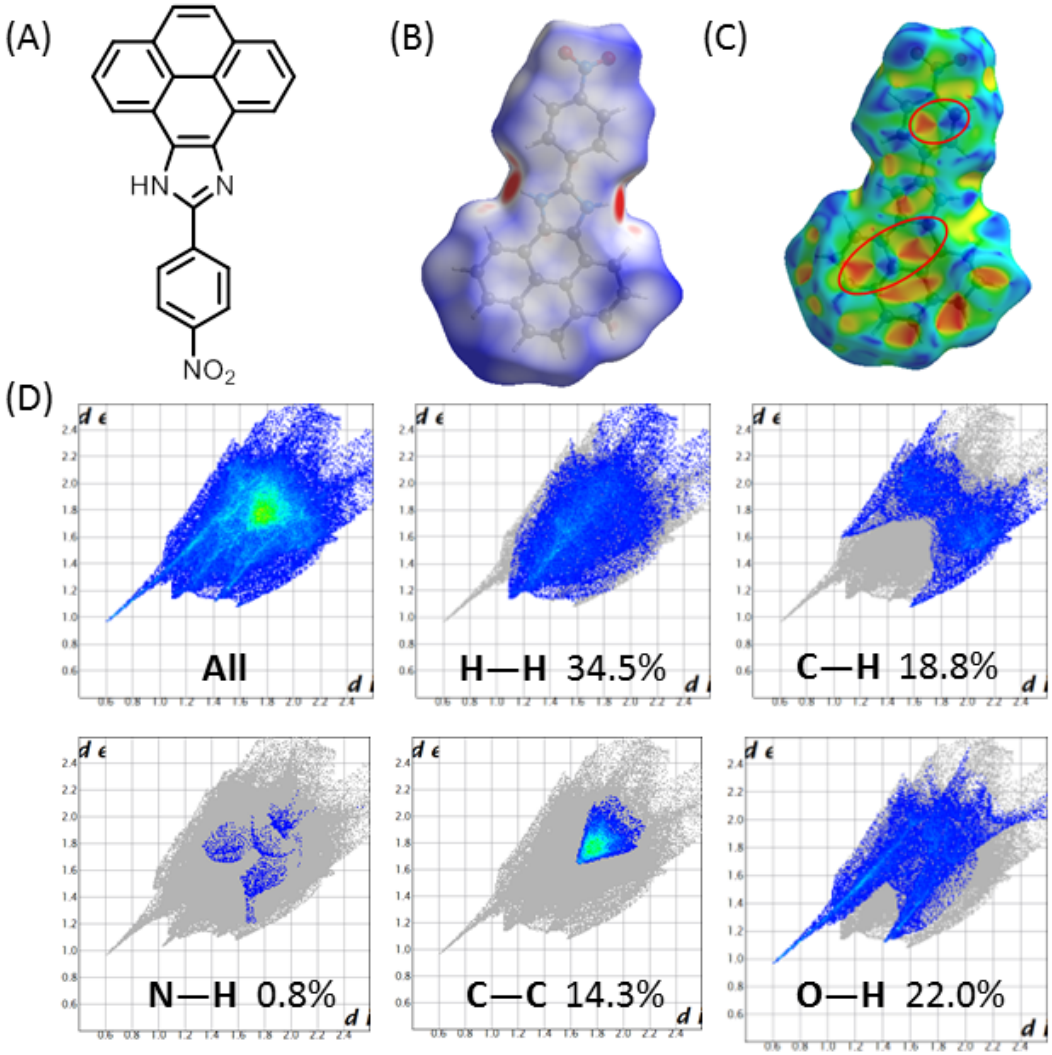

Figure 5.10: (A) Molecular structure of *p*-nitrophenyl-pyrenoimidazole (co-crystallized with trimesic acid). (B) Hirshfeld surface mapped with d_{norm}. (C) Hirshfeld surface mapped with shape index. (D) Fingerprint plots with different intermolecular contacts highlighted.

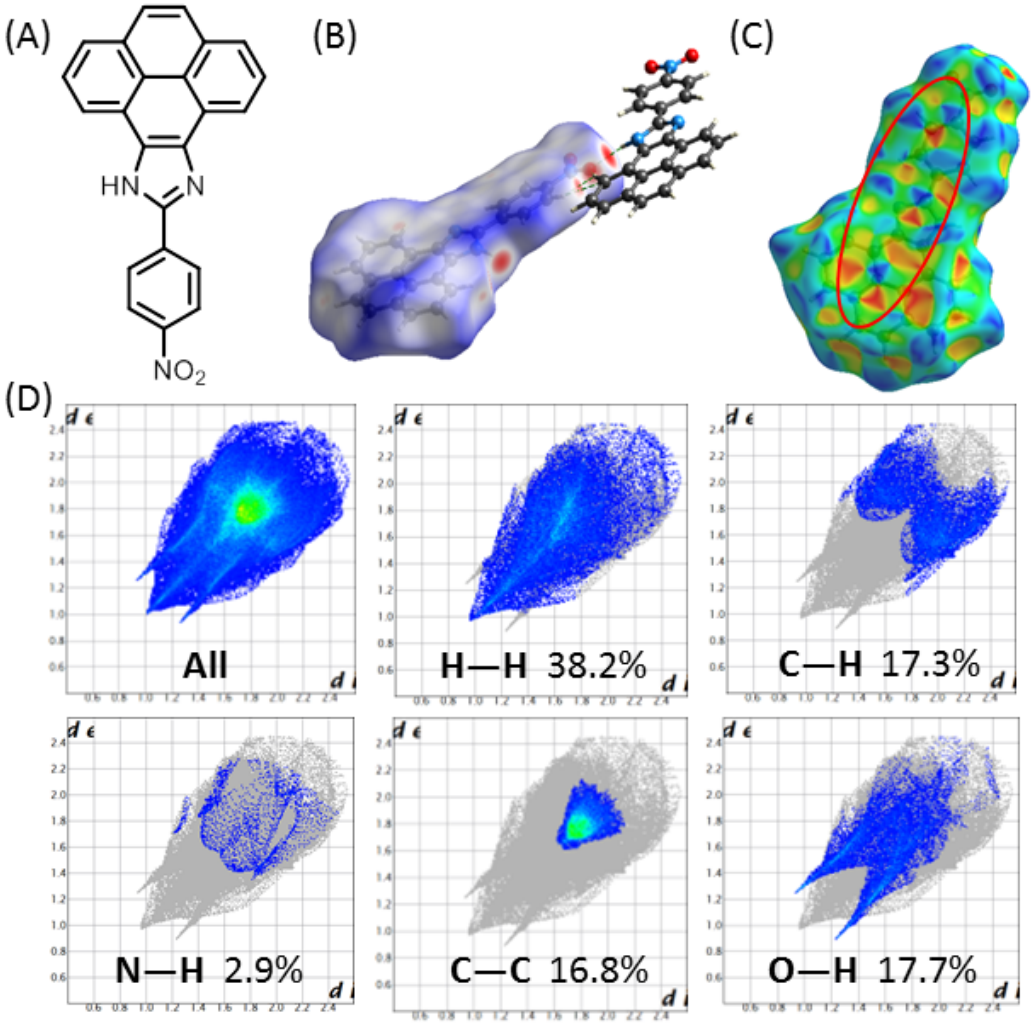

Figure 5.11: (A) Molecular structure of *p*-nitrophenyl-pyrenoimidazole (without solvents). (B) Hirshfeld surface mapped with d_{norm}. (C) Hirshfeld surface mapped with shape index. (D) Fingerprint plots with different intermolecular contacts highlighted.

5.2.6 *p*-Formylphenyl-Substituted Pyrenoimidazole

The results of Hirshfeld surface analysis of the crystal structure of *p*-formylphenyl-substituted pyrenoimidazole are shown in Figure 5.12. With a formyl group substituted, the contribution of N$\cdots$H interaction is 5.4%, which is a little bit greater than that of nitro substituted one. On the fingerprint plot, these interactions appear as two symmetric wide spikes at $d_i + d_e \approx 2.8$ Å. The proportion of O$\cdots$H interactions is 9.3% of the total interactions and give by two sharp symmetric spikes at a sum of $d_i + d_e \approx 2.2$ Å, which is smaller compare to that of N$\cdots$H interactions in terms of contribution. The C$\cdots$H interactions make 35.3% contribution and give two wide spikes in the fingerprint plot, with very sharp tips at $d_i + d_e \approx 2.6$ Å. Like the previous pyrenoimidazole derivatives, the dominant contribution arise from H$\cdots$H contacts, which make a contribution of 35.2% to the total Hirshfeld surface. The H$\cdots$H interactions give a sharp spike at the lowest of $d_i + d_e \approx 1.8$ Å. The $\pi - \pi$ (C$\cdots$C) interactions give 9.3% contribution. On the Hirshfeld surface mapped with shape index, similar blue and red shapes are observable as highlighted in the red circle of Figure 5.12C. The C$\cdots$N contacts make a small contribution of 2.3%.

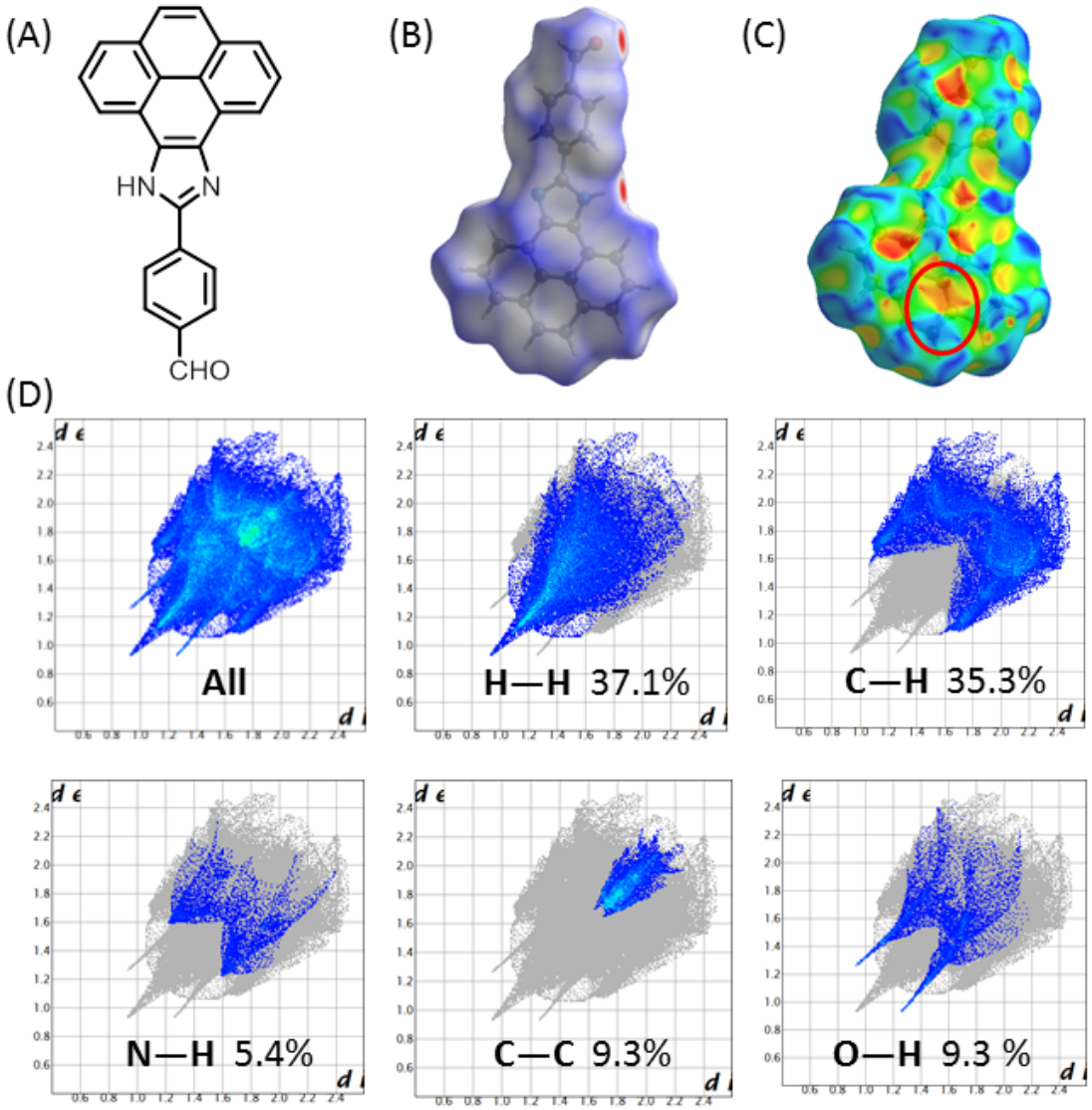

Figure 5.12: (A) Molecular structure of *p*-nitrophenyl-pyrenoimidazole. (B) Hirshfeld surface mapped with d_{norm}. (C) Hirshfeld surface mapped with shape index. (D) Fingerprint plots with different intermolecular contacts highlighted.

5.2.7 *p*-Hydroxyphenyl-Substituted Pyrenoimidazole

The results of Hirshfeld surface analysis of the crystal structure of *p*-hydroxyphenyl-substituted pyrenoimidazole are shown in Figure 5.13. In the presence of two hydrogen bond donor groups, O–H and N–H, multiple hydrogen bonds are formed in the crystal structure. On the d_{norm} mapped Hirshfeld surface, two significant red spots can be observed around the OH and imidazolyl NH sites (Figure 5.13B). On the fingerprint plot, there are two symmetric spikes at $d_i + d_e \approx 1.7$ Å, corresponding to the N$\cdots$H interactions. Another two sharp spikes at $d_i + d_e \approx 1.85$ Å are due to the intermolecular O$\cdots$H contacts. The contribution of N$\cdots$H contacts is 5.2% and the contribution of O$\cdots$H contacts is 7.6%. The C$\cdots$H interactions make 26.1% contribution to the Hirshfeld surface, and show two wings on the fingerprint plot which are more condensed on C_i and H_e ($d_i + d_e \approx 2.8$ Å). Like other pyrenoimidazole derivatives, the dominant interactions in this crystal structure are the H$\cdots$H contacts that give a contribution of 46.5%. On the fingerprint plot, there is a tip at $d_i + d_e \approx$ 2.1 Å corresponding to the H$\cdots$H contacts. Significant $\pi - \pi$ interactions also exit in the crystal packing, and their contribution is 11.9%. In the fingerprint plot, the $\pi - \pi$ stacking is reflected by a prominent green-colored region. The complementary blue and red triangles on the shape index surface also illustrate the characteristic features of $\pi - \pi$ interactions in the crystal structure (Figure 5.13C). The H$\cdots$H interactions can be visualized through bumps and hollows, including blue crosses and yellow spots, on the edge of the shape index mapped Hirshfeld surface.

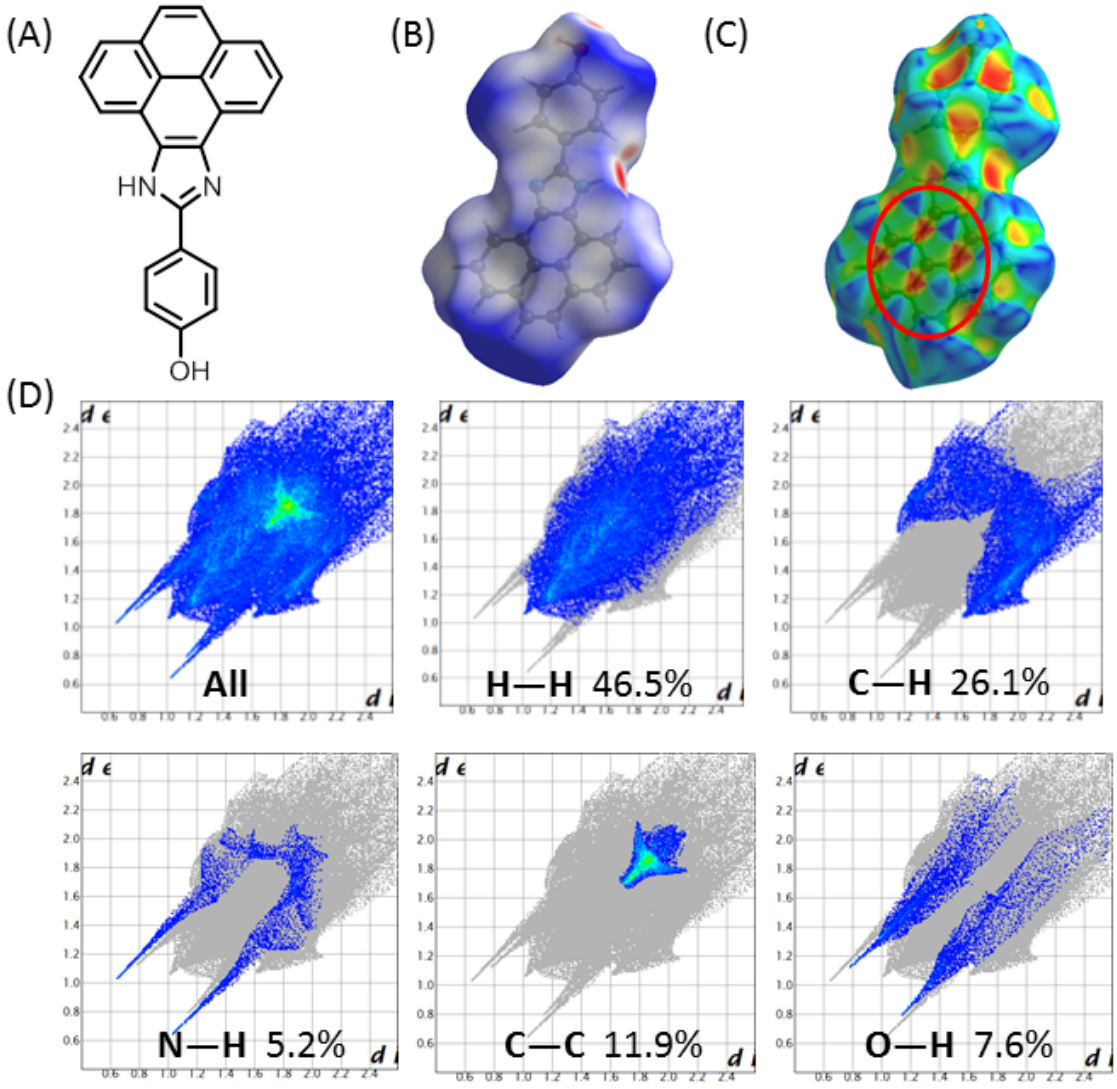

Figure 5.13: (A) Molecular structure of *p*-hydroxyphenyl-pyrenoimidazole. (B) Hirshfeld surface mapped with d_{norm}. (C) Hirshfeld surface mapped with shape index. (D) Fingerprint plots with different intermolecular contacts highlighted.

5.2.8 *p*-Decyloxyphenyl-Substituted Pyrenoimidazole

The results of Hirshfeld surface analysis of the crystal structure of *p*-decyloxyphenyl-substituted pyrenoimidazole are shown in Figure 5.14. Compared with its analogue, p-hydroxyphenyl-substituted pyrenoimidazole, attachment of a decyloxy chain to the *para*-position of the phenyl group removes the hydrogen bond donor O–H. On the Hirshfeld surface mapped with d_{norm} (Figure 5.14B), significant red spots are observed near the imidazolyl N and decyloxy O sites, which are related to the hydrogen bonding interactions between water molecules and these sites. On the fingerprint plot, the N$\cdots$H interactions are shown as two asymmetric spikes with a wing-shaped distribution of scattered points. One of the spikes has a larger contribution (2.1%) than the other (0.9%), and the total contribution of N$\cdots$H interactions is 3%. The larger spike shows a tip at $d_i + d_e \approx 1.8$ Å, which is due to the close contact of water O–H with the imidazolyl N=C group. The O$\cdots$H contacts contain two type of intermolecular hydrogen bonds, water–water and decyloxy–water interactions. On the fingerprint plot the O$\cdots$H interactions give two sharp spikes at $d_i + d_e \approx 1.8$ /AA, which are symmetrical in distribution. The total contribution of O$\cdots$H interactions is 3.5%.

In the crystal structure, decyl and pyrenyl protons show H$\cdots$H, C–H$\cdots$H and C–H$\cdots\pi$ interactions. Compared with *p*-hydroxyphenyl-substituted pyrenoimidazole, the incorporation of decyl group leads to a higher contribution of H$\cdots$H interactions (60.3%) in the crystal packing. These interactions appear as two slightly separated wing-shaped distributions of scattered points at a minimum value of $d_i + d_e \approx 2.15$ Å. on the shape index mapped surface (Figure 5.14C), the H$\cdots$H interactions are

observed as blue crosses. The C–H$\cdots\pi$ interactions make a 28.9% contribution to the overall crystal packing, and they show two distinct wing-shaped distribution of points at three levels with tips at $d_i + d_e \approx 2.65$ Å, which is much smaller than that of *p*-hydroxylphenyl substituted pyrenoimidazole. The concave red and convex blue spots on the shape index mapped surface (Figure 5.14C) represent C–H$\cdots\pi$ interactions. Close intermolecular C$\cdots$C contacts give 2.4% contribution to the Hirshfeld surface. On the fingerprint plot, they are reflected by an arrow-shaped distribution of points, with the vertex at $d_i = d_e \approx 1.6$ Å. There are no significant $\pi - \pi$ interactions in this crystal packing, because of the absence of adjacent red and blue triangles on the shape index mapped surface. Additionally, the N$\cdots$C contacts give a 0.9% contribution to the overall crystal packing.

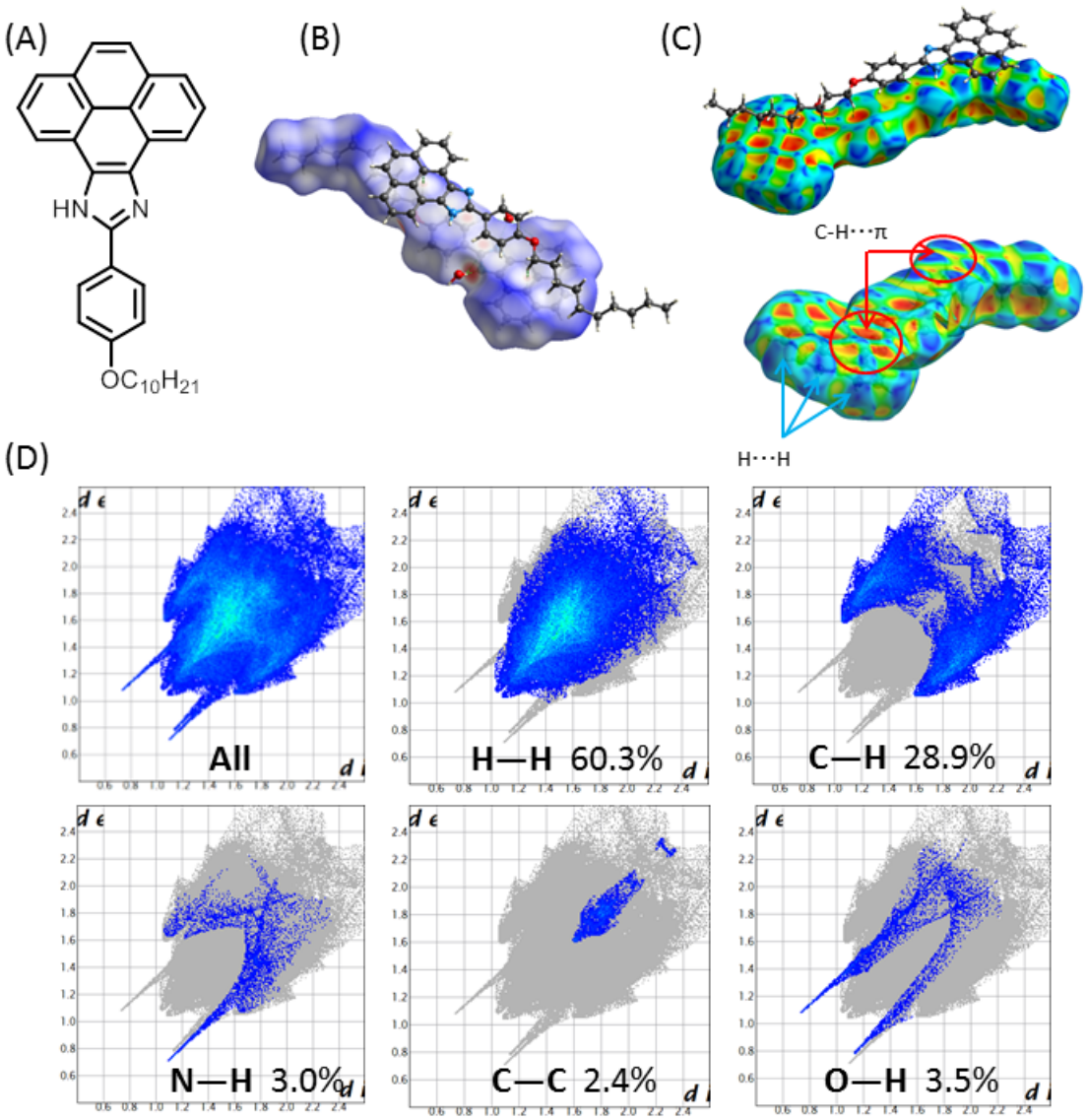

Figure 5.14: (A) Molecular structure of *p*-decyloxyphenyl-pyrenoimidazole. (B) Hirshfeld surface mapped with d_{norm}. (C) Hirshfeld surface mapped with shape index. (D) Fingerprint plots with different intermolecular contacts highlighted.

5.2.9 *N*-decyl-*p*-decyloxyphenyl-Substituted Pyrenoimidazole

The results of Hirshfeld surface analysis of the crystal structure of *N*-decyl-*p*-decyloxyphenyl-substituted pyrenoimidazole are shown in Figure 5.15. The presence of two decyl groups in the molecular structure makes the H$\cdots$H interactions more pronounced (73.1%) than the *para*-hydroxyphenyl and *para*-decyloxyphenyl-substituted pyrenoimidazoles. On the fingerprint plot the H$\cdots$H interactions show a significant sharp tip at $d_i + d_e \approx 1.95$ Å. The high density of the widely scattered points is shown as green color region on the fingerprint plot, which are consistent with the blue crosses on the edges of shape index mapped surface (Figre 5.15C). Intermolecular C–H$\cdots\pi$ contacts make a 18.8% contribution to the Hirshfeld surface, which is about 10% less than that of *p*-decyloxyphenyl-substituted pyrenoimidazole. On the fingerprint plot, there are two symmetric distinct wings at two levels with minimum distance of $d_i + d_e \approx 2.7$ Å, corresponding to the C$\cdots$H interactions. The red concave and blue convex shapes on the shape index mapped surface (Figure 5.15C) reflect the C–H$\cdots\pi$ interactions as well. Significant $\pi - \pi$ stacking is present in the crystal structure with a 3.9% contribution. There are complementary red and blue triangles observed on the shape index mapped surface (Figure 5.15C). The N$\cdots$H and O$\cdots$H interactions give two sets of distinct pairs of spikes with a vertex ($d_i + d_e \approx 2.6$ Å) and rocket-shaped ($d_i + d_e \approx 2.53$ Å) distributions of scattered points, respectively, on the fingerprint plot. The contributions of O$\cdots$H and N$\cdots$H contacts are 2.3% and 0.8%, respectively.

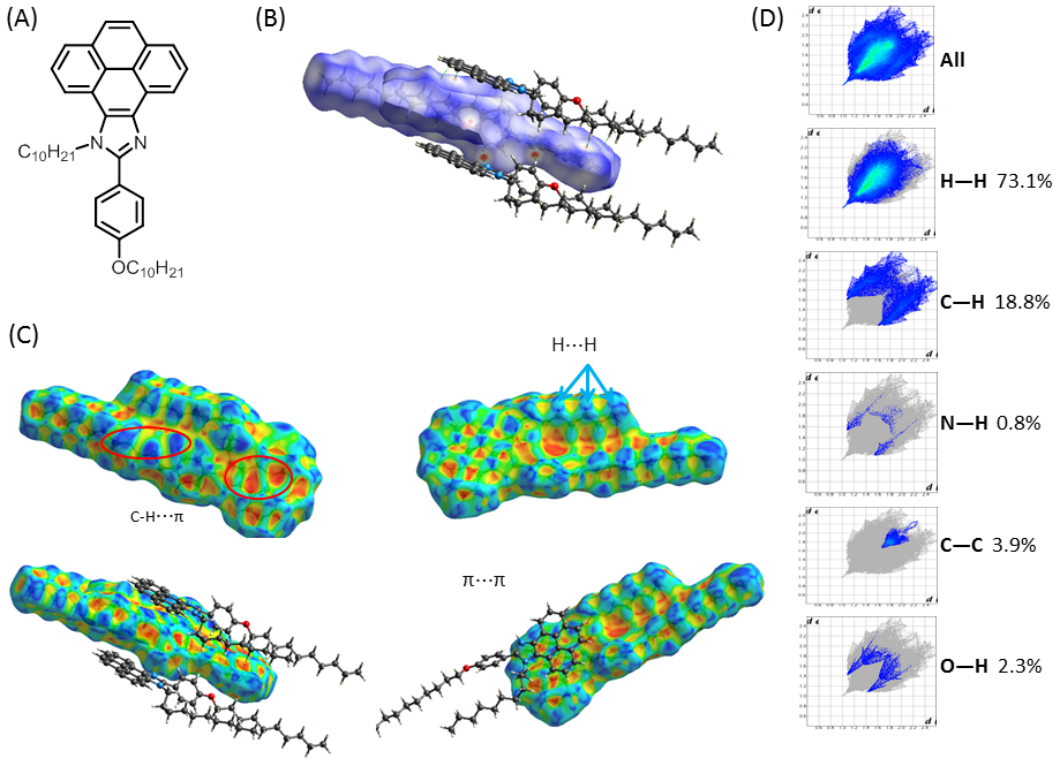

Figure 5.15: (A) Molecular structure of *p*-decyloxyphenyl-pyrenoimidazole. (B) Hirshfeld surface mapped with d_{norm}. (C) Hirshfeld surface mapped with shape index. (D) Fingerprint plots with different intermolecular contacts highlighted.

5.3 On the Close H···H Contacts Observed in the Crystal Structures of Pyrenoimidazoles

Hydrogen bonding is an important concept in modern chemistry, owing to its fundamentally important role in supramolecular chemistry and biology.[211,212] Typical hydrogen bonding interactions occur between the positively charged hydrogen of a proton donor (e.g., A–H, where A = O, N, halogen, C, etc.) and a proton acceptor such as the lone pair of an electronegative element, the π electrons of a multiple bond or aromatic ring, or a transition metal center. On the other hand, some unusual types of hydrogen bonding have also been known. A very interesting type of hydrogen bonding is the so-called hydridic-to-protonic interaction, which has also often referred to as many other terms, including dihydrogen bonding, proton-hydride bonding, H···H hydrogen bonding, or hydrogenhydrogen bonding.[213] This type of bonding has strength and directionality comparable with those found in conventional hydrogen bonding, and hence can influence structural properties and chemical reactivities in the solution and solid state. Figure 5.16 illustrates a number of examples for dihydrogen bonding, where σ-bonding electron pairs are formed between an electron-rich metal–hydride bond or non-metal–hydride bond with a traditional A–H proton donor bond. Geometrically, the dihydrogen bonding is characterized by short H···H contact distances (1.7–2.2 Å) and strongly bent M–H···H–A angles (90–135°). The interaction energies are generally between 1 to 7 kcal/mol. As such, dihydrogen bonds are comparable with moderately strong conventional hydrogen bonds. The nature of dihydrogen bonds is mostly electrostatic, although a weak covalent contribution may be found sometimes.

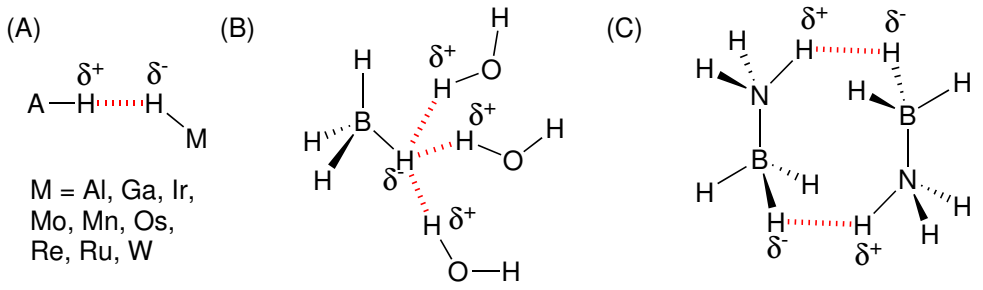

Figure 5.16: Examples of dihydrogen bonding.

In 2003, Bader and co-workers carried out a computational study on another type of hydrogen bonding interactions, which involve hydrogen pairs with identical or similar charges.[214] Using the approach of the quantum theory of atoms in molecules (QTAIM), which was pioneered by Richard F. W. Bader,[215] the authors found bond paths linking such hydrogen pairs and examined the physics underlying such interactions. This interesting paper pointed out that "the H$\cdots$H interactions must be ubiquitous, their stabilization energies contributing to the sublimation energies of hydrocarbon molecular crystals, as well as solid hydrogen." They therefore termed this type of interactions "hydrogen–hydrogen bonding" to be distinct from the "dihydrogen bonding" interactions.

The claim by Bader *et al.* that the new type of "hydrogen–hydrogen bonding"causes a stabilizing effect rather than the classical view of "non-bonded steric repulsions" soon incurred severe criticisms from others.[216–218] In 2009, Bader wrote an account article to address those criticisms and defended the use of bond path as a valid theoretical tool for understanding chemical bonds.[219] In 2011, an article entitled "Definition of the Hydrogen Bond (IUPAC Recommendations 2011)*" was published on *Pure Appl. Chem.*, which was aimed to recommend criteria that could be used as evidence for the presence of a hydrogen bond.[220] In this article, one of the

characteristics of hydrogen bonds is stipulated as follows: "**analysis of the electron density topology of hydrogen-bonded systems usually shows a bond path connecting H and Y and a (3,–1) bond critical point between H and Y**". In the meantime, the article raised a caution that "**if an interaction is primarily due to dispersion forces, then it would not be characterized as a hydrogen bond**". So, the debates over the nature of hydrogen–hydrogen bonding proposed by Bader are not conclusively resolved and still waiting for more experimental evidence and fundamental analysis. Nonetheless, the combination of X-ray crystallographic data and QTAIM analysis has offered a valuable approach for casting light on various weak non-covalent interactions, particularly hydrogen bonding interactions.[221]

The Hirshfeld surface analysis described in the previous section has allowed the various non-covalent interactions in the crystal structures of pyrenoimidazole derivatives to be clearly identified and assessed. For example, intermolecular N$\cdots$H and O$\cdots$H hydrogen bonds can be easily visualized as characteristic sharp spikes on their 2-D fingerprint plots. In some of crystal structures, a unique sharp spike corresponding to close H$\cdots$H contacts is also observable with the $(d_i + d_e)$ value less than the sum of van der Waals radii of dihydrogen (2.4 Å). Such a feature indicates very close H$\cdots$H contacts that deserve a closer examination. Following the QTAIM analysis approach first utilized by Bader *et al.*, these hydrogen–hydrogen interactions were subjected to DFT-based QTAIM analysis (at the M06-2X/def2SVP level of theory) to investigate the electron density topology and related characteristics in these systems.

Figure 5.17 illustrates the molecular graph of the dimer of *p*-chlorophenyl-substituted pyrenoimidazole calculated based on the geometry obtained from the

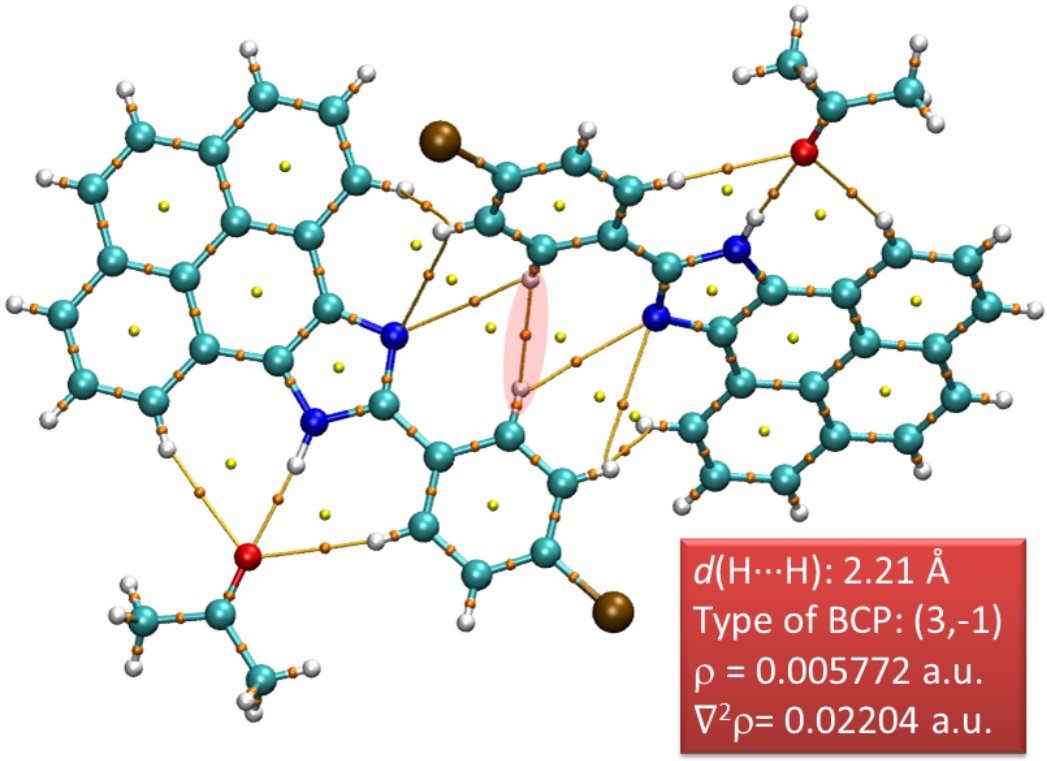

Figure 5.17: Molecular graph of the dimer of *p*-chlorophenyl-substituted pyrenoimidazole obtained from QTAIM analysis. The closest intermolecular H···H is highlighted by a oblong red shade, and related characteristics are indicated.

crystal structure. As highlighted, a bond path connects two adjacent phenyl hydrogen atoms with a (3,-1) bond critical point (BCP) located between them. In principle, The presence of a (3,-1) BCP and related bond path indicates that electronic charge density is accumulated between the two closely positioned hydrogen atoms. The topological features are in line with the hydrogen–hydrogen bonding interactions discussed in Bader's paper; that is, a small electronic density (ρ), a small positive $\nabla^2\rho$, very small but positive energy density (H_r).[215] Following a linear regression equation by Matta,[221] E_{H-H} (kcal/mol) $= 22.662 - 2934.74 \times \rho$ (a.u.), the H···H bond stabilization energy (E_{H-H}) was calculated as +5.72 kcal/mol, which is actually

a destabilizing effect. In addition to the H···H contact, bond paths and (3,-1) BCPs are also found among the phenyl hydrogen atoms (partially positive in charge) and the imidazyloy nitrogen atoms (partially negative in charge) in the nearby molecule. Obviously, the Ar–H···N interactions are electrostatic attraction, which is a contributing force for the formation of close H···H contact between these two molecules.

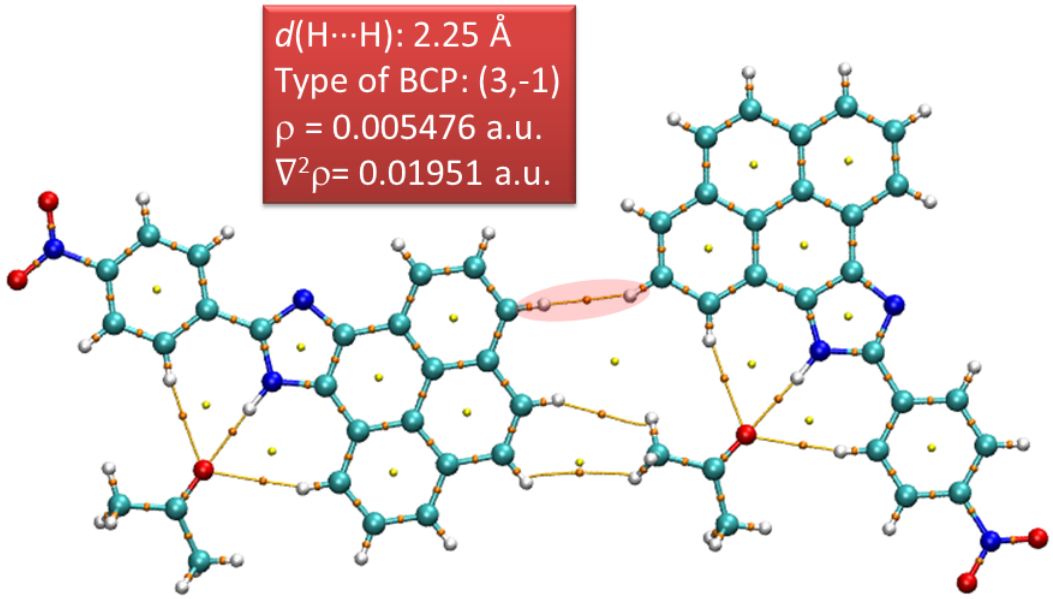

Figure 5.18: Molecular graph of the dimer of *p*-nitrophenyl-substituted pyrenoimidazole (co-crystallized with acetone) obtained from QTAIM analysis. The closest intermolecular H···H is highlighted by a oblong red shade, and related characteristics are indicated.

Figure 5.18 illustrates the molecular graph of the dimer of *p*-nitrophenyl-substituted pyrenoimidazole calculated based on the geometry obtained from the crystal structure (co-crystallized with acetone). Herein, a close H···H distance (2.25

Å) between two pyrenyl hydrogen atoms is observed and the topological features related to this H$\cdots$H system reveals a clear bond path and a (3,-1) BCP in between, with the H$\cdots$H bond stabilization energy (E_{H-H}) being +6.59 kcal/mol. On the other side, an acetone molecule bridges the two pyrenoimidazole molecules through various intermolecular attractive forces, including a typical hydrogen bond between the acetone oxygen atom (donor) and imidazolyl N–H (acceptor) group, as well as C–H$\cdots\pi$ interactions between one of the acetone CH_3 groups and the adjacent pyrenyl edge.

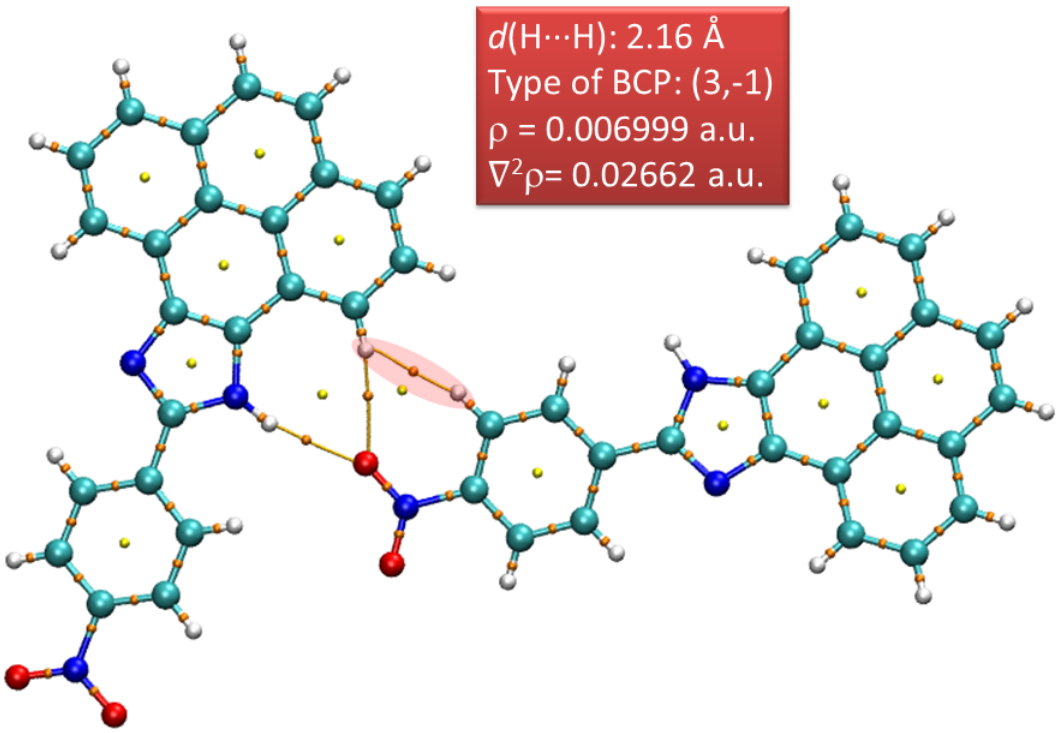

Figure 5.19: Molecular graph of the dimer of *p*-nitrophenyl-substituted pyrenoimidazole (without solvents) obtained from QTAIM analysis. The closest intermolecular H$\cdots$H is highlighted by a oblong red shade, and related characteristics are indicated.

In the crystal structure of *p*-nitrophenyl-substituted pyrenoimidazole without the presence of any solvent molecules, very close H$\cdots$H contacts are still observable; however, they occur between one of the hydrogens *ortho* to the nitro group and an adjacent pyrenyl proton (see Figure 5.19). The H$\cdots$H distance is much shorter (2.16 Å) than the previous examples, indicating relatively strong interactions. In the molecular graph, a (3,-1) BCP and a bond path can be clearly seem in this H$\cdots$H interaction. The H$\cdots$H bond stabilization energy (E_{H-H}) was calculated as +2.12 kcal/mol. Along with this, a Y-shaped double-hydrogen bonding is formed between one of the nitro oxygen atom and adjacent imidazolyl N–H and pyrenyl C–H. Again, these attractive forces are electrostatic in origin and can account for the very close intermolecular H$\cdots$H contacts observed in this crystal structure.

In the crystal structure of *N*-decyl-*p*-decyloxyphenyl-substituted pyrenoimidazole, two types of close H$\cdots$H contacts are observable. The first one (highlighted by red oblong shades in Figure 5.20) is a H$\cdots$H bonding between the C–H located at the β-position of the phenol ether chain and an adjacent pyrenyl C(sp^2)–H, and the second one is between two closely positioned alkyl C(sp^3)–H groups. Again, these H$\cdots$H systems feature (3,-1) BCPs and bond paths connecting the hydrogen pairs. It is worth noting that the close H$\cdots$H contacts are relatively longer than those observed in the previously discussed crystal structures, indicating that they are relatively weak interactions. The calculated H$\cdots$H bond stabilization energies (E_{H-H}) are 5.60 and 7.38 kcal/mol, respectively. The DFT calculated molecular graph also discloses multiple non-covalent interactions, including O$\cdots$H, N$\cdots$H, and C–H$\cdots\pi$ interactions, the presence of which (attractive electrostatic forces) can be viewed as a key contributor to the formation of these short H$\cdots$H contacts.

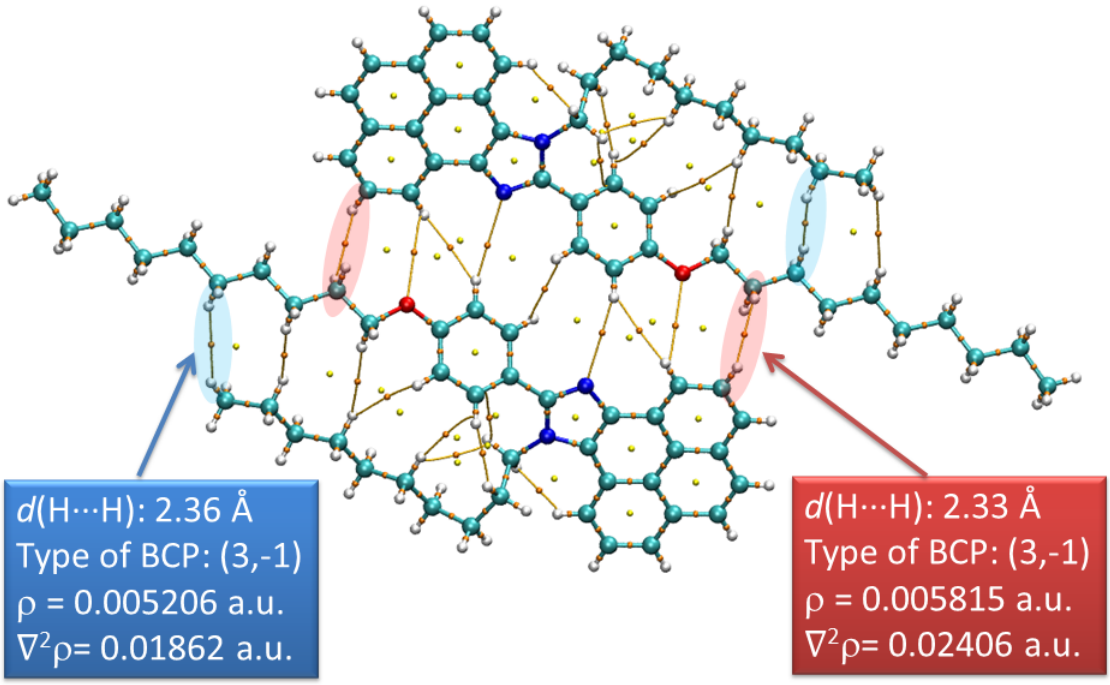

Figure 5.20: Molecular graph of the dimer of didecyl-substituted pyrenoimidazole obtained from QTAIM analysis. The closest intermolecular H···H contacts are highlighted by oblong red and blue shades, respectively. Related characteristics are indicated.

Finally, close H···H contacts in the crystal structure of *p*-formylphenyl-substituted pyrenoimidazole are examined. Figure 5.21 shows the geometry and DFT-calculated molecular graph for a dimer of the pyrenoimidazole in the crystal, in which a very close intermolecular H···H distance (2.11 Å) is observed between two adjacent pyrenyl protons. QTAIM analysis shows a (3,-1) BCP and a bond path between these two hydrogen atoms. Interestingly, there are two more bond paths and BCPs found between the pyrenyl protons nearby; however, the corresponding H···H distances (2.59 Å) are slightly longer than the sum of van der Waals radii of dihydrogen (2.4 Å) and thus disregarded as close H···H contacts. Compared with the examples

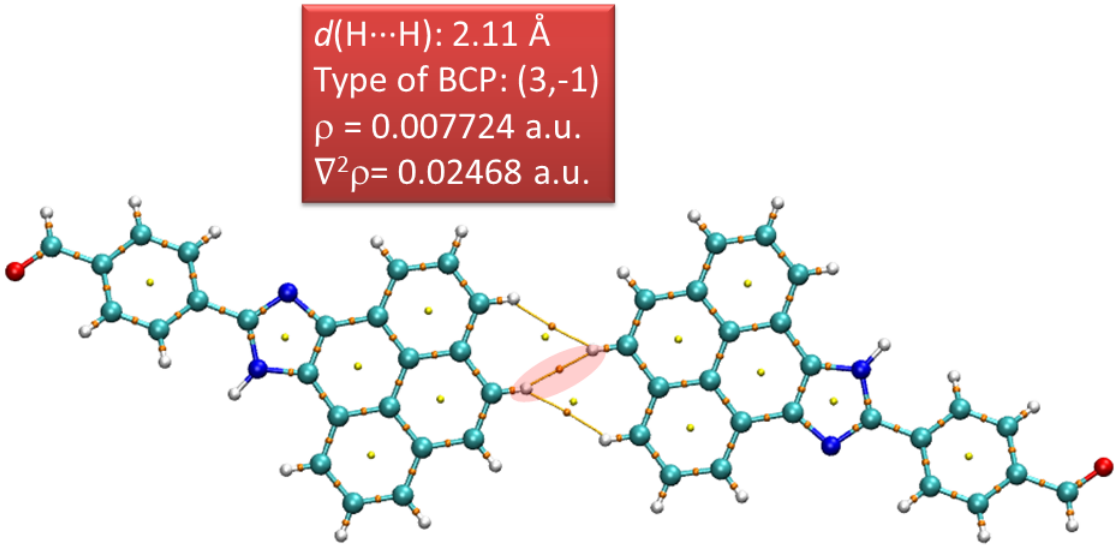

Figure 5.21: Molecular graph of the dimer of *p*-formylphenyl-substituted pyrenoimidazole obtained from QTAIM analysis. The closest intermolecular H···H is highlighted by a oblong red shade, and related characteristics are indicated.

discussed above, the close H···H contact in this crystal structure shows the shortest distance. Unlike the previous examples, there are no other non-covalent attractive forces (e.g., O···H, N···H, and C–H···π) contributing to drawing the two molecules together to form such a short H···H. The calculated H···H bond stabilization energy (E_{H-H}) is -5.93 kcal/mol, which is similar to the H–H bonding stabilization energy in 9,10-dihydrophenanthrene (-5.5 kcal/mol).[221] Therefore, the crystallographic and QTAIM results herein concur with Bader's notion of the hydrogen–hydrogen bonding interaction.[214]

Furthermore, the non-covalent interactions in the dimer of *p*-formylphenyl-substituted pyrenoimidazole were subjected to the analysis of non-covalent interactions (NCI) index proposed by the Yang group.[222,223] This NCI analysis examines the electron densities (ρ) and their reduced gradients (RDG), the results of

which can be straightforwardly visualized by an isosurface plot as shown in Figure 5.22A and a 2-D plot of RDG versus the electron density multiplied by the sign of the second Hessian eigenvalue (sign(λ_2)$\times\rho$) as shown in Figure 5.22B. The NCI analysis is a useful tool complementary to the QTAIM analysis for understanding weak non-covalent interactions. Simply put, the green colored isosurfaces between the edges of the dimer (indicated by the green arrow in Figure 5.22A) reflect the van der Waals contacts between the two molecules, which are consistent with BCPs and bond paths revealed in the QTAIM analysis. On the 2-D plot of RDG versus sign(λ_2)$\times\rho$, a green colored spike appears at a small negative value of sign(λ_2)$\times\rho$, which is indicative of weak attractive interactions. Overall, the NCI analysis also points to that the H$\cdots$H contacts in the dimer of *p*-formylphenyl-substituted pyrenoimidazole are weakly attractive in nature. Nevertheless, fundamental interpretation of the H$\cdots$H bond still needs in-depth and more cautious studies.

5.4 Conclusions

In this chapter, the X-ray crystallographic data of the group of phenyl-substituted pyrenoimidazole derivatives, which were prepared and investigated in the previous chapters (particularly in Chapter 3), were subjected to the Hirshfeld surface analysis. These substituted pyrenoimidazole systems constitute ideal models for examining the roles of various non-covalent forces (e.g., hydrogen bonding, $\pi - \pi$, and C–H$\cdots\pi$ interactions) in crystal packing. The occurrence and interplay of these forces are usually very complicated. However, the Hirshfeld surface analysis presents a powerful tool to quantitatively assess and comprehensively visualize them. Through

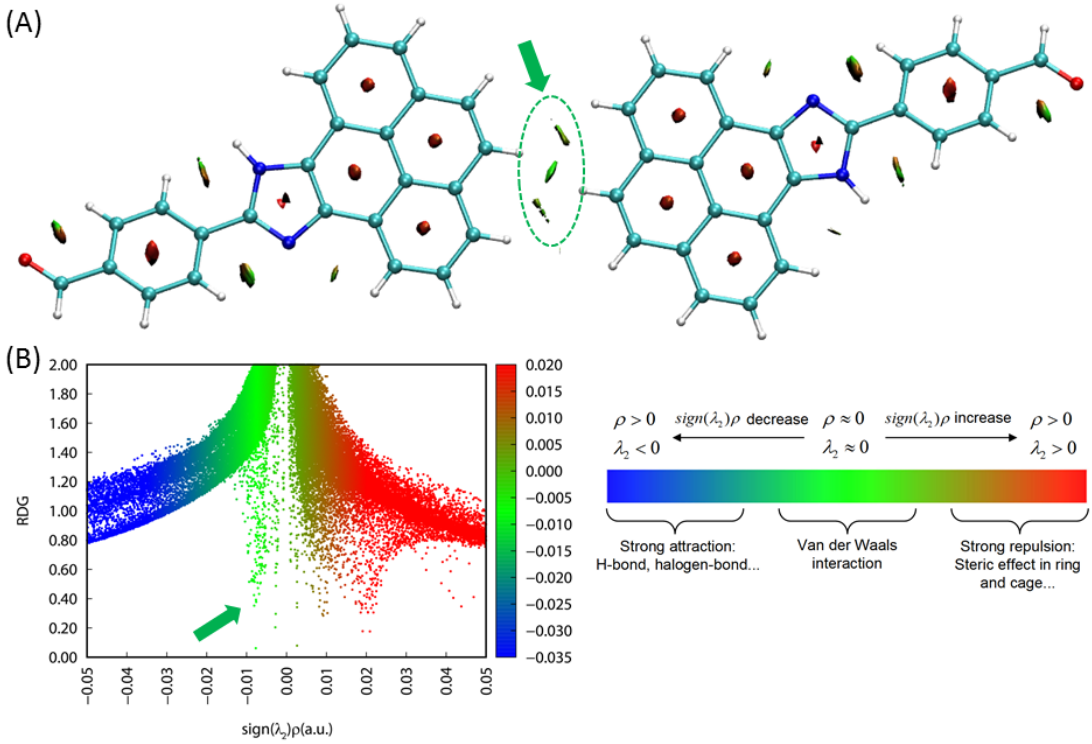

Figure 5.22: (A) NCI isosurfaces and (B) 2-D plot of RDG versus sign(λ_2)$\times\rho$ of the dimer of *p*-formylphenyl-substituted pyrenoimidazole.

the Hirshfeld surface analysis, the contributions of diverse non-covalent forces in the crystal structures could be readily summarized on 2-D fingerprint plots and visualized from the Hirshfeld surfaces mapped with different properties (d_i, d_e, d_{norm}, shape index, curvedness, etc.). It is particularly interesting to note that very close intermolecular H$\cdots$H contacts ($<$ 2.4 Å) were found with the assistance of the Hirshfeld surface analysis, and these interactions are in line with the hydrogen–hydrogen interaction proposed by Bader and co-workers. Although the fundamental concept of hydrogen–hydrogen bonding is still controversial, the crystallographic data shown in the structure of *p*-formylphenyl-substituted pyrenoimidazole casts a point of view that is supportive to Bader's notion.

Chapter 6

Conclusions and Future Work

In this PhD thesis, three projects were successfully accomplished, in which novel π-conjugated phenyl-pyrenoimidazole systems were prepared through a one-pot condensation reaction between pyrene-4,5-dione and various benzaldehyde derivatives in the presence of ammonium acetate. These compounds were characterized by various spectroscopic and single-crystal X-ray diffraction techniques to elucidate their structural, solid-state packing, photophysical, and electronic properties. Pyrenoimidazole derivatives are heterocycle-fused pyrene systems that can serve as useful materials for chemical sensing, light-emitting devices, dye sensitized solar cells, and electroluminescent materials. The imidazole unit in the pyrenoimidazole system provides an effective binding site for capturing anions and/or metal cations in a selective manner. The binding of these compounds with fluoride anion involved hydrogen bonding interactions as the dominant attractive forces, while the fluoride binding could resulted in significant colorimetric responses for certain pyrenoimidazole systems, especially *para*-benzaldehyde substituted pyrenoimidazole responded to

fluoride anion by showing a substantial shift in emission wavelength, allowing effective colorimetric sensing function to be achieved. The findings disclosed in Chapter 2 thus point to a great potential in developing highly sensitive and selective fluorescence turn-on sensors for biologically and environmentally important anions using pyrenoimidazole as a versatile design platform.

Besides the sensory properties, this thesis work has revealed that substituent groups attached to the phenyl-pyrenomidazole systems can introduce and enhance directional non-covalent forces, such as hydrogen bonding, C–H$\cdots\pi$, and $\pi - \pi$ interactions, to control and modify the supramolecular assemblies (e.g., linear, helical, and layered structures) in the solid state. Co-crystallization with various hydrogen bond donors/acceptors (e.g., protic solvents and carboxylic acids) has been found to result in various organic crystal structures. The versatility of crystal packing motifs observed in the X-ray structural analysis opens a new avenue for the design of functional organic crystals using pyrenoimidazoles as controllable and tunable supramolecular synthons.

Finally, this thesis work demonstrated that comprehensive theoretical tools, such as the Hirshfeld surface analysis and DFT calculations are of great value in terms of gaining deeper understanding the physical origins of various spectroscopic and crystallographic properties. Acquisition of such knowledge allows the detailed structure-property relationships to be established and offer insightful guidance to the future research on pyrenoimidazole-based materials.

On the basis of the current thesis work, a number of future research directions are suggested as follows.

- Synthesis of new phenyl-pyrenoimidazole derivatives is suggested, particularly the design of molecular structures with more π-extended 2-dimensional frameworks. A challenging but highly intriguing class of synthetic targets is represented by the macrocyclic structure **6-1** depicted in Figure 6.1. Herein, pyrenoimidazole is a key sub-unit of this shape-persistent macrocycle. The inner cavity of the macocycle is expected to show binding properties with acids and/or metal cations, while the edge functionality (R) can be modified to show supramolecular self-assembling properties. These compounds should show interesting photophysical properties and are predicted as ideal molecular building blocks for fluorescence sensors and functional organic crystals (e.g., hydrogen-bonded supramolecular frameworks). The synthesis of these compounds is certainly not easy, especially acquisition of the essential pyrene-4,5-dione precursor (**6-2**) requires extensive studies to establish a selective, high-yielding, and cost-effective synthetic method.

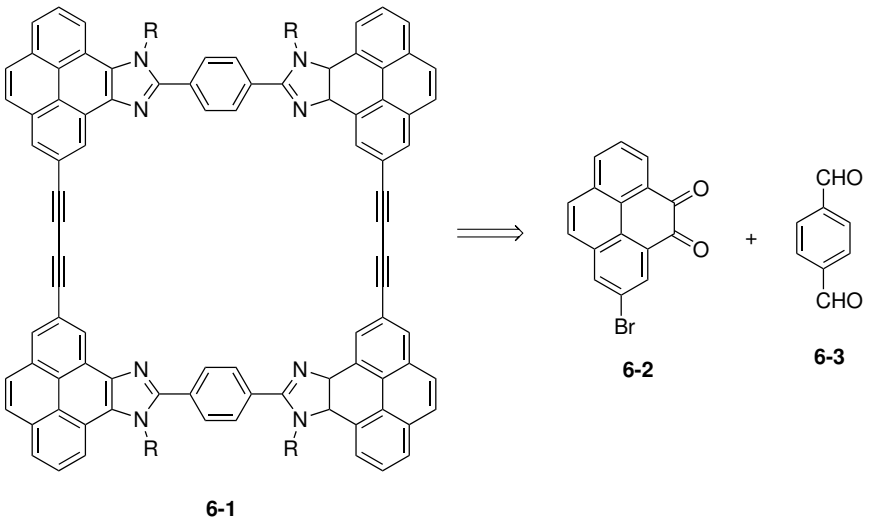

Figure 6.1: A targeted pyrenoimidazole macrocycle in the future work.

- Exploration of other optoelectronic properties of the pyrenoimidazole derivatives. It is envisioned that the phenyl-pyrenoimidazole derivatives described in this thesis work would give interesting nonlinear optical (NLO), photovoltaic, and electroluminescence properties. In this respect, their application in advanced optoelectronic devices such as waveguides, dye-sensitized solar cells, and organic light emitting devices (OLEDs) is predicted to yield fruitful outcomes. However, studies in these fields require expertise beyond the scope of the Zhao group. Therefore, extensive collaboration with other research groups specializing in device fabrication and characterization should be established in the future.

- Design and synthesis of microporous organic crystals using pyrenoimidazoles as supramolecular synthons. As demonstrated in Chapters 3 and 4, the crystal structures of pyrenoimidazole derivatives show dependence on their molecular structures and crystallization conditions (e.g., solvents and co-crystallizing agents). In recent years, microporous crystalline materials such as metal-organic frameworks (MOFs) and covalent organic framewoks (COFs) have taken the central stage of materials science and engineering. The development of other advanced microporous materials is also appealing, owing to the great potential in chemical sensing, drug delivery, CO_2 capture, energy storage, and catalysis. Recently, supramolecular organic frameworks (SOFs)[224–226] have been introduced to the field, but their examples are rare and the development demands more efficient supramolecular synthons to be available. In this light, the co-crystallization strategy demonstrated in Chapter 4 is a promising

approach to generate new SOFs with novel fluorescence and catalytic properties. It is anticipated that co-crystallization of pyrenoimidazole derivatives with various organic carboxylic acids should deliver novel organic crystals and eventually lead to the discovery of useful SOFs.

Bibliography

[1] Keefe, T. The nature of light. *Community College of Rhode Island* **2007**,

[2] Valeur, B.; Berberan-Santos, M. N. A Brief History of Fluorescence and Phosphorescence Before the Emergence of Quantum Theory. *J. Chem. Educ.* **2011**, *88*, 731–738.

[3] Acuña, A.; Amat-Guerri, F. *Fluorescence of supermolecules, polymers, and nanosystems*; Springer, 2007; pp 3–20.

[4] Acuña, A. U.; Amat-Guerri, F.; Morcillo, P.; Liras, M.; Rodriguez, B. Structure and Formation of the Fluorescent Compound of Lignum Nephriticum. *Org. Lett.* **2009**, *11*, 3020–3023.

[5] (Washington), S. I. P. *Annual Report of the Board of Regents of the Smithsonian Institution: Showing the Operations, Expenditures, and Condition of the Institution; for the Year Ended*; US Government Printing Office, 1869; Vol. 22.

[6] Muyskens, M. The Fluorescence of Lignum Nephriticum: a Flash Back to the Past and a Simple Demonstration of Natural Substance Fluorescence. *J. Chem. Educ.* **2006**, *83*, 765.

[7] Nesse, W. D. *Introduction to mineralogy*; 2012.

[8] Manutchehr-Danai, M. *Dictionary of gems and gemology*; Springer Science & Business Media, 2013.

[9] Jameson, J. L. *Harrison's principles of internal medicine.*; McGraw-Hill Education,, 2018.

[10] Sahoo, H. Fluorescent labeling techniques in biomolecules: a flashback. *Rsc Advances* **2012**, *2*, 7017–7029.

[11] Zollinger, H. *Color chemistry: syntheses, properties, and applications of organic dyes and pigments*; John Wiley & Sons, 2003.

[12] Steinthal, G.; Sunshine, S.; Burch, T.; Plotkin, N.; Hsiung, C.-M. Chemical and biological agent sensor array detectors. 2007; US Patent 7,171,312.

[13] Bunner, A. N. Cosmic ray detection by atmospheric fluorescence. Ph.D. thesis, Cornell University Ithaca, New York, 1967.

[14] Louis, R. Fluorescent electric lamp. 1950; US Patent 2,505,993.

[15] Harris, D. C.; Bertolucci, M. D. *Symmetry and spectroscopy: an introduction to vibrational and electronic spectroscopy*; Courier Corporation, 1989.

[16] Berlman, I. *Handbook of Florescence Spectra of Aromatic Molecules, chapter 1*; Elsevier, 2012.

[17] orević, J.; Maćej, O. Atomska apsorpcijska spektrofotometrija i njena primjena u odreivanju mineralnog sastava mlijeka. *Mljekarstvo: časopis za unaprjeenje proizvodnje i prerade mlijeka* **1982**, *32*, 233–243.

[18] Szudy, J. *Born 100 Years Ago: Aleksander Jabłonski, 1898-1980*; Uniwersytet Mikołaja Kopernika, 1998.

[19] Coolidge, A. S.; James, H. M.; Present, R. D. A Study of the Franck-Condon Principle. *The Journal of Chemical Physics* **1936**, *4*, 193–211.

[20] Stokes, G. G. XXX. On the change of refrangibility of light. *Philosophical transactions of the Royal Society of London* **1852**, 463–562.

[21] del Valle, J. C.; Catalán, J. Kasha's rule: a reappraisal. *Physical Chemistry Chemical Physics* **2019**, *21*, 10061–10069.

[22] Kasha, M. Characterization of Electronic Transitions in Complex Molecules. *Discuss. Faraday Soc.* **1950**, *9*, 14–19.

[23] Ishikawa-Ankerhold, H. C.; Ankerhold, R.; Drummen, G. P. Advanced fluorescence microscopy techniques—Frap, Flip, Flap, Fret and flim. *Molecules* **2012**, *17*, 4047–4132.

[24] Lakowicz, J. R.; Balter, A. Analysis of Excited-State Processes by Phase-Modulation Fluorescence Spectroscopy. *Biophys. Chem.* **1982**, *16*, 117–132.

[25] Williams, A. T. R.; Winfield, S. A.; Miller, J. N. Relative fluorescence quantum yields using a computer-controlled luminescence spectrometer. *Analyst* **1983**, *108*, 1067–1071.

[26] Condon, E. U. Nuclear Motions Associated with Electron Transitions in Diatomic Molecules. *Phys. Rev.* **1928**, *32*, 858.

[27] Feng, X.; Hu, J.-Y.; Redshaw, C.; Yamato, T. Functionalization of Pyrene to Prepare Luminescent Materials—Typical Examples of Synthetic Methodology. *Chem. Eur. J.* **2016**, *22*, 11898–11916.

[28] Berenblum, I. 3: 4-Benzpyrene from coal tar. *Nature* **1945**, *156*, 601–601.

[29] Laurent, A. Pyrene from Coal Tar. *Ann. Chim. Phys.* **1837**, *66*, 136–137.

[30] Förster, T.; Kasper, K. Ein Konzentrationsumschlag der Fluoreszenz des Pyrens. *Zeitsch. Elektrochem., Berich. Bunseng. Physik. Chem.* **1955**, *59*, 976–980.

[31] Birks, J. Photophysics of Aromatic Molecules Wiley. *New York* **1970**, 1294–1340.

[32] Kalyanasundaram, K.; Thomas, J. Environmental Effects on Vibronic Band Intensities in Pyrene Monomer Fluorescence and Their Application in Studies of Micellar Systems. *J. Am. Chem. Soc.* **1977**, *99*, 2039–2044.

[33] Pokhrel, M. R.; Bossmann, S. H. Synthesis, Characterization, and First Application of High Molecular Weight Polyacrylic Acid Derivatives Possessing Perfluorinated Side Chains and Chemically Linked Pyrene Labels. *J. Phys. Chem. B* **2000**, *104*, 2215–2223.

[34] Yang, J.-S.; Lin, C.-S.; Hwang, C.-Y. Cu^{2+}-Induced Blue Shift of the Pyrene Excimer Emission: A New Signal Transduction Mode of Pyrene Probes. *Org. Lett.* **2001**, *3*, 889–892.

[35] Bodenant, B.; Weil, T.; Businelli-Pourcel, M.; Fages, F.; Barbe, B.; Pianet, I.; Laguerre, M. Synthesis and Solution Structure Analysis of a Bispyrenyl Bishydroxamate Calix[4]arene-based Receptor, a Fluorescent Chemosensor for Cu^{2+} and Ni^{2+} Metal Oons. *J. Org. Chem.* **1999**, *64*, 7034–7039.

[36] Anthony, J. E. The Larger Acenes: Versatile Organic Semiconductors. *Angew. Chem. Int. Ed.* **2008**, *47*, 452–483.

[37] Birks, J.; Christophorou, L. Excimer fluorescence spectra of pyrene derivatives. *Spectrochimica Acta* **1963**, *19*, 401–410.

[38] Figueira-Duarte, T. M.; Mullen, K. Pyrene-based Materials for Organic Electronics. *Chem. Rev.* **2011**, *111*, 7260–7314.

[39] Shi, Y.-R.; Wei, H.-l.; Shi, Y.-t.; Liu, Y.-F. Theoretical Study of Pyrene Derivatives as High Performance Organic Semiconductor Materials. *Synth. Met.* **2017**, *223*, 218–225.

[40] Casas-Solvas, J. M.; Howgego, J. D.; Davis, A. P. Synthesis of Substituted Pyrenes by Indirect Methods. *Org. Biomol. Chem.* **2014**, *12*, 212–232.

[41] Suzuki, K.; Seno, A.; Tanabe, H.; Ueno, K. New Host Materials for Blue Emitters. *Synth. Met.* **2004**, *143*, 89–96.

[42] Karthik, S.; Ajantha, J.; Nagaraja, C.; Easwaramoorthi, S.; Gandhi, T. Synthesis and Photophysics of Extended π-Conjugated Systems of Substituted 10-Aryl-pyrenoimidazoles. *Org. Biomol. Chem.* **2016**, *14*, 10255–10266.

[43] Harvey, R. G. *Polycyclic Aromatic Hydrocarbons: Chemistry and Carcinogenicity*; CUP Archive, 1991.

[44] Hu, J.; Zhang, D.; Harris, F. W. Ruthenium (III) Chloride Catalyzed Oxidation of Pyrene and 2,7-Disubstitued Pyrenes: An Efficient, One-Step Synthesis of Pyrene-4,5-diones and Pyrene-4,5,9,10-Tetraones. *J. Org. Chem.* **2005**, *70*, 707–708.

[45] Kawano, S.-i.; Baumgarten, M.; Chercka, D.; Enkelmann, V.; Müllen, K. Electron donors and acceptors based on 2, 7-functionalized pyrene-4, 5, 9, 10-tetraone. *Chemical Communications* **2013**, *49*, 5058–5060.

[46] Vollmann, H.; Becker, H.; Corell, M.; Streeck, H. Beiträge zur Kenntnis des Pyrens und seiner Derivate. *Justus Liebigs Annalen der Chemie* **1937**, *531*, 1–159.

[47] Dewar, M. A Molecular Orbital Theory of Organic Chemistry. VI. 1 Aromatic Substitution and Addition. *J. Am. Chem. Soc.* **1952**, *74*, 3357–3363.

[48] Harvey, R. G.; Goh, S. H.; Cortez, C. K-region Oxides and Related Oxidized Metabolites of Carcinogenic Aromatic Hydrocarbons. *J. Am. Chem. Soc.* **1975**, *97*, 3468–3479.

[49] Venkataramana, G.; Dongare, P.; Dawe, L. N.; Thompson, D. W.; Zhao, Y.; Bodwell, G. J. 1,8-Pyrenylene-Ethynylene Macrocycles. *Org. Lett.* **2011**, *13*, 2240–2243.

[50] Walsh, J. C.; Williams, K.-L. M.; Lungerich, D.; Bodwell, G. J. Synthesis of Pyrene-4,5-dione on a 15 g Scale. *Eur. J. Org. Chem.* **2016**, *2016*, 5933–5936.

[51] Bramley, S. E.; Dupplin, V.; Goberdhan, D. G.; Meakins, G. D. The Hantzsch Thiazole Synthesis under Acidic Conditions: Change of Regioselectivity. *J. Chem. Soc, Perkin Trans. 1* **1987**, 639–643.

[52] Chawla, A.; Sharma, A.; kumar Sharma, A. A Convenient Approach for the Synthesis of Imidazole Derivatives using Microwaves. *Synthesis* **2012**, *5*, 7.

[53] Matuszak, C.; Matuszak, A. Imidazole-versatile today, prominent tomorrow. *Journal of Chemical Education* **1976**, *53*, 280.

[54] Wu, C.; Alqahtani, A.; Sangtarash, S.; Vezzoli, A.; Sadeghi, H.; Robertson, C. M.; Cai, C.; Lambert, C. J.; Higgins, S. J.; Nichols, R. J. In situ formation of H-bonding imidazole chains in break-junction experiments. *Nanoscale* **2020**, *12*, 7914–7920.

[55] Debus, H. Ueber die Einwirkung des Ammoniaks auf Glyoxal. *Justus Liebigs Ann. Chem.* **1858**, *107*, 199–208.

[56] Pifferi, G.; Parravicini, F.; Carpi, C.; Dorigotti, L. Synthesis and antihypertensive properties of new 3-hydrazinopyridazine derivatives. *Journal of Medicinal Chemistry* **1975**, *18*, 741–746.

[57] Ebel, K.; Koehler, H.; Gamer, A. O.; Jäckh, R. Imidazole and derivatives. *Ullmann's Encyclopedia of Industrial Chemistry* **2000**,

[58] Debus, H.; Liebigs, S. Synthesis of 2, 2'-imidazole. *Liebigs Ann Chem* **1858**, *107*, 199–208.

[59] Radziszewski, B. Ueber die Constitution des Lophins und verwandter Verbindungen. *Berich. Deutsch. Chemisch. Gesellsch.* **1882**, *15*, 1493–1496.

[60] Weidenhagen, R.; Herrmann, R. Eine neue Synthese von Imidazol-Derivaten. *Berich. Deutsch. Chemisch. Gesellsch.* **1935**, *68*, 1953–1961.

[61] Zhao, N.; Wang, Y.-L.; Wang, J.-Y. A Rapid and Convenient Synthesis of Derivatives of Imidazoles under Microwave Irradiation. *J. Chin. Chem. Soc.* **2005**, *52*, 535–538.

[62] Qasim, S. S.; Ali, S. S. Microwave assisted a novel synthesis for new substituted imidazoles. *Der Pharma Chemica* **2011**, *3*, 518–522.

[63] Wu, D.; Sedgwick, A. C.; Gunnlaugsson, T.; Akkaya, E. U.; Yoon, J.; James, T. D. Fluorescent Chemosensors: the Past, Present and Future. *Chem. Soc. Rev.* **2017**, *46*, 7105–7123.

[64] Raj, T.; Saluja, P.; Singh, N. A New Class of Pyrene Based Multifunctional Chemosensors for Differential Sensing of Metals in Different Media: Selective Recognition of Zn_{2+} in Organic and Fe*3+* in Aqueous Medium. *Sensors Actuators B* **2015**, *206*, 98–106.

[65] Sahoo, S. K.; Kim, G.-D.; Choi, H.-J. Optical sensing of anions using C3v-symmetric tripodal receptors. *Journal of Photochemistry and Photobiology C: Photochemistry Reviews* **2016**, *27*, 30–53.

[66] Kang, J.; Kim, H. S.; Jang, D. O. Fluorescent Anion Chemosensors using 2-Aminobenzimidazole Receptors. *Tetrahedron Lett.* **2005**, *46*, 6079–6082.

[67] Lee, S.-C.; Heo, J.; Woo, H. C.; Lee, J.-A.; Seo, Y. H.; Lee, C.-L.; Kim, S.; Kwon, O.-P. Fluorescent molecular rotors for viscosity sensors. *Chemistry–A European Journal* **2018**, *24*, 13706–13718.

[68] Mardanya, S.; Karmakar, S.; Mondal, D.; Baitalik, S. An Imidazolyl-Pyreno-Imidazole Conjugate as a Cyanide Sensor and a Set–Reset Memorized Sequential Logic Device. *Dalton Trans.* **2015**, *44*, 15994–16012.

[69] Lee, M. H.; Kim, J. S.; Sessler, J. L. Small Molecule-based Ratiometric Fluorescence Probes for Cations, Anions, and Biomolecules. *Chem. Soc. Rev.* **2015**, *44*, 4185–4191.

[70] Ahmad, M. W.; Kim, B.-Y.; Kim, H.-S. Selective Fluorescence Sensing of Salicylic Acid using a Simple Pyrene Appended Imidazole Receptor. *New J. Chem.* **2014**, *38*, 1711–1716.

[71] Das, S.; Sahana, A.; Lohar, S.; Sarkar, B.; Mukhopadhya, S. K.; Banerjee, A.; Das, D. A Visible Light Excitable Pyrene–Naphthalene Conjugate for ON Fluorescence Sensing of Histidine in Living Cells. *RSC Adv.* **2014**, *4*, 7495–7499.

[72] Shree, G. J.; Sivaraman, G.; Siva, A.; Chellappa, D. Anthracene and Pyrene-bearing Imidazoles as Turn-On Fluorescent Chemosensor for Aluminum Ion in Living Cells. *Dyes Pigm.* **2019**, *163*, 204–212.

[73] Kushwaha, A.; Patil, S. K.; Das, D. A Pyrene-Benzimidazole Composed Effective Fluoride Sensor: Potential Mimicking of a Boolean Logic Gate. *New J. Chem.* **2018**, *42*, 9200–9208.

[74] Bhat, M. P.; Kigga, M.; Govindappa, H.; Patil, P.; Jung, H.-Y.; Yu, J.; Kurkuri, M. A reversible fluoride chemosensor for the development of multi-input molecular logic gates. *New Journal of Chemistry* **2019**, *43*, 12734–12743.

[75] Jadhav, T.; Dhokale, B.; Mobin, S. M.; Misra, R. Aggregation induced emission and mechanochromism in pyrenoimidazoles. *J. Mater. Chem. C* **2015**, *3*, 9981–9988.

[76] Hong, Y.; Lam, J. W.; Tang, B. Z. Aggregation-induced Emission. *Chem. Soc. Rev.* **2011**, *40*, 5361–5388.

[77] Mei, J.; Hong, Y.; Lam, J. W.; Qin, A.; Tang, Y.; Tang, B. Z. Aggregation-induced Emission: the Whole is More Brilliant than the Parts. *Adv. Mater.* **2014**, *26*, 5429–5479.

[78] Wang, Y.-F.; Zhang, T.; Liang, X.-J. Aggregation-induced Emission: Lighting up Cells, Revealing Life! *Small* **2016**, *12*, 6451–6477.

[79] Peng, Y.-X.; Dai, Y.; Wang, N.; Huang, W. Symmetrical Fluorescent Oligothiophene and Benzene Centered Bispyrenoimidazole Derivatives with Double *n*-Dodecyl Chains Showing High Thermal Stability. *Tetrahedron Lett.* **2014**, *55*, 5984–5987.

[80] Shan, T.; Liu, Y.; Tang, X.; Bai, Q.; Gao, Y.; Gao, Z.; Li, J.; Deng, J.; Yang, B.;

Lu, P., et al. Highly Efficient Deep Blue Organic Light-Emitting Diodes Based on Imidazole: Significantly Enhanced Performance by Effective Energy Transfer with Negligible Efficiency Roll-Off. *ACS Appl. Mater. Interf.* **2016**, *8*, 28771–28779.

[81] Mishra, A.; Fischer, M. K.; Bäuerle, P. Metal-free Organic Dyes for Dye-sensitized Solar Cells: From Structure: Property Relationships to Design Rules. *Angew. Chem. Int. Ed.* **2009**, *48*, 2474–2499.

[82] Yum, J.-H.; Jang, S.-R.; Walter, P.; Geiger, T.; Nüesch, F.; Kim, S.; Ko, J.; Grätzel, M.; Nazeeruddin, M. K. Efficient Co-Sensitization of Nanocrystalline TiO_2 Films by Organic Sensitizers. *Chem. Commun.* **2007**, 4680–4682.

[83] Ogomi, Y.; Pandey, S. S.; Kimura, S.; Hayase, S. Probing Mechanism of Dye Double Layer Formation from Dye-Cocktail Solution for Dye-sensitized Solar Cells. *Thin Solid Films* **2010**, *519*, 1087–1092.

[84] Chang, J.; Lee, C.-P.; Kumar, D.; Chen, P.-W.; Lin, L.-Y.; Thomas, K. J.; Ho, K.-C. Co-Sensitization Promoted Light Harvesting for Organic Dye-sensitized Solar Cells using Unsymmetrical Squaraine Dye and Novel Pyrenoimidazole-based Dye. *J. Power Sources* **2013**, *240*, 779–785.

[85] Liu, Y.-L.; Yang, L.; Guo, Y.-Q.; Xu, G.-Q.; Qu, B.; Fu, Y. Synthesis and Configurational Character Study of Novel Structural Isomers Based on Pyrene–Imidazole. *Molecules* **2019**, *24*, 2293.

[86] Cicoira, F.; Santato, C. *Organic Electronics: Emerging Concepts and Technologies*; Wiley-VCH, 2013.

[87] Sun, S.-S.; Dalton, L. R. *Introduction to Organic Electronic and Optoelectronic Materials and Devices*; CRC Press, 2016.

[88] Facchetti, A. π-Conjugated Polymers for Organic Electronics and Photovoltaic Cell Applications. *Chem. Mater.* **2011**, *23*, 733–758.

[89] Wang, C.; Dong, H.; Hu, W.; Liu, Y.; Zhu, D. Semiconducting Ï-Conjugated Systems in Field-Effect Transistors: A Material Odyssey of Organic Electronics. *Chem. Rev.* **2012**, *112*, 2208–2267, PMID: 22111507.

[90] Ostroverkhova, O. Organic Optoelectronic Materials: Mechanisms and Applications. *Chem. Rev.* **2016**, *116*, 13279–13412, PMID: 27723323.

[91] Li, Y. *Organic Optoelectronic Materials*; Springer, 2016.

[92] Figueira-Duarte, T. M.; Müllen, K. Pyrene-based Materials for Organic Electronics. *Chem. Rev.* **2011**, *111*, 7260–7314.

[93] Mateo-Alonso, A. Pyrene-fused Pyrazaacenes: from Small Molecules to Nanoribbons. *Chem. Soc. Rev.* **2014**, *43*, 6311–6324.

[94] Ghasemabadi, P. G.; Yao, T.; Bodwell, G. J. Cyclophanes Containing Large Polycyclic Aromatic Hydrocarbons. *Chem. Soc. Rev.* **2015**, *44*, 6494–6518.

[95] Valdés, H.; Poyatos, M.; Peris, E. A Pyrene-Based N-Heterocyclic Carbene: Study of Its Coordination Chemistry and Stereoelectronic Properties. *Organometallics* **2013**, *33*, 394–401.

[96] Therrien, J. A.; Wolf, M. O.; Patrick, B. O. Polyannulated Bis(N-heterocyclic

carbene) palladium Pincer Complexes for Electrocatalytic CO2 Reduction. *Inorg. Chem.* **2015**, *54*, 11721–11732.

[97] Liu, B.; Lystrom, L.; Kilina, S.; Sun, W. Tuning the Ground State and Excited State Properties of Monocationic Iridium (III) Complexes by Varying the Site of Benzannulation on Diimine Ligand. *Inorg. Chem.* **2017**, *56*, 5361–5370.

[98] Kumar, D.; Thomas, K.; Lin, C.-C.; Jou, J.-H. Pyrenoimidazole-Based Deep-Blue-Emitting Materials: Optical, Electrochemical, and Electroluminescent Characteristics. *Chem.–Asian J.* **2013**, *8*, 2111–2124.

[99] Peng, Y.-X.; Dai, Y.; Wang, N.; Huang, W. Symmetrical Fluorescent Oligothiophene and Benzene Centered Bispyrenoimidazole Derivatives with Double *n*-Dodecyl Chains Showing High Thermal Stability. *Tetrahedron Lett.* **2014**, *55*, 5984–5987.

[100] Jadhav, T.; Dhokale, B.; Mobin, S. M.; Misra, R. Aggregation Induced Emission and Mechanochromism in Pyrenoimidazoles. *J. Mater. Chem. C* **2015**, *3*, 9981–9988.

[101] Karthik, S.; Ajantha, J.; Nagaraja, C.; Easwaramoorthi, S.; Gandhi, T. Synthesis and Photophysics of Extended π-Conjugated Systems of Substituted 10-Aryl-pyrenoimidazoles. *Org. Biomol. Chem.* **2016**, *14*, 10255–10266.

[102] Zapata, F.; Caballero, A.; Espinosa, A.; Tárraga, A.; Molina, P. Cation Coordination Induced Modulation of the Anion Sensing Properties of a Ferrocene-Imidazophenanthroline Dyad: Multichannel Recognition from Phosphate-related to Chloride Anions. *J. Org. Chem.* **2008**, *73*, 4034–4044.

[103] Saha, D.; Das, S.; Maity, D.; Dutta, S.; Baitalik, S. Synthesis, Structural Characterization, and Photophysical, Electrochemical, Intercomponent Energy-Transfer, and Anion-sensing Studies of Imidazole 4, 5-Bis(benzimidazole)-bridged OsIIOsII and RuIIOsII Bipyridine Complexes. *Inorg. Chem.* **2010**, *50*, 46–61.

[104] Bhaumik, C.; Maity, D.; Das, S.; Baitalik, S. Anion Sensing Studies of Luminescent Bis-tridentate Ruthenium(II) and Osmium(II) Complexes Based on Terpyridyl-Imidazole Ligand through Different Channels. *Polyhedron* **2013**, *52*, 890–899.

[105] Das, S.; Karmakar, S.; Mardanya, S.; Baitalik, S. Synthesis, Structural Characterization, and Multichannel Anion and Cation Sensing Studies of a Bifunctional Ru(II) Polypyridyl–Imidazole Based Receptor. *Dalton Trans.* **2014**, *43*, 3767–3782.

[106] Maity, D.; Bhaumik, C.; Mondal, D.; Baitalik, S. Ru(II) and Os(II) Complexes Based on Terpyridyl-Imidazole Ligand Rigidly Linked to Pyrene: synthesis, Structure, Photophysics, Electrochemistry, and Anion-sensing Studies. *Inorg. Chem.* **2013**, *52*, 13941–13955.

[107] Mardanya, S.; Karmakar, S.; Maity, D.; Baitalik, S. Ruthenium(II) and Osmium(II) Mixed Chelates Based on Pyrenyl–Pyridylimidazole and 2,2-Bipyridine Ligands as Efficient DNA Intercalators and Anion Sensors. *Inorg. Chem.* **2014**, *54*, 513–526.

[108] Mardanya, S.; Karmakar, S.; Mondal, D.; Baitalik, S. An Imidazolyl-pyreno-

imidazole Conjugate as a Cyanide Sensor and a Set–Reset Memorized Sequential Logic Device. *Dalton Trans.* **2015**, *44*, 15994–16012.

[109] Causey, C. P.; Allen, W. E. Anion Binding by Fluorescent Biimidazole Diamides. *J. Org. Chem.* **2002**, *67*, 5963–5968.

[110] Zhang, M.; Li, M.; Li, F.; Cheng, Y.; Zhang, J.; Yi, T.; Huang, C. A Novel Y-Type, Two-Photon Active Fluorophore: Synthesis and Application in Ratiometric Fluorescent Sensor for Fluoride Anion. *Dyes Pigm.* **2008**, *77*, 408–414.

[111] Mo, H.-J.; Shen, Y.; Ye, B.-H. Selective Recognition of Cyanide Anion via Formation of Multipoint NH and Phenyl CH Hydrogen Bonding with Acyclic Ruthenium Bipyridine Imidazole Receptors in Water. *Inorg. Chem.* **2012**, *51*, 7174–7184.

[112] Molina, P.; Tárraga, A.; Otón, F. Imidazole Derivatives: A Comprehensive Survey of Their Recognition Properties. *Org. Biomol. Chem.* **2012**, *10*, 1711–1724.

[113] Esteves, C. I.; Raposo, M. M. M.; Costa, S. P. New 2,4,5-Triarylimidazoles Based on a Phenylalanine Core: Synthesis, Photophysical Characterization and Evaluation as Fluorimetric Chemosensors for Ion Recognition. *Dyes and Pigments* **2016**, *134*, 258–268.

[114] Lin, W.; Long, L.; Yuan, L.; Cao, Z.; Chen, B.; Tan, W. A Ratiometric Fluorescent Probe for Cysteine and Homocysteine Displaying a Large Emission Shift. *Org. Lett.* **2008**, *10*, 5577–5580.

[115] Long, L.; Zhou, L.; Wang, L.; Meng, S.; Gong, A.; Zhang, C. A Ratiometric Fluorescent Probe for Iron(III) and Its Application for Detection of Iron(III) in Human Blood Serum. *Anal. Chim. Acta* **2014**, *812*, 145–151.

[116] Kubo, Y.; Yamamoto, M.; Ikeda, M.; Takeuchi, M.; Shinkai, S.; Yamaguchi, S.; Tamao, K. A Colorimetric and Ratiometric Fluorescent Chemosensor with Three Emission Changes: Fluoride Ion Sensing by a Triarylborane–Porphyrin Conjugate. *Angew. Chem. Int. Ed.* **2003**, *42*, 2036–2040.

[117] Peng, X.; Wu, Y.; Fan, J.; Tian, M.; Han, K. Colorimetric and Ratiometric Fluorescence Sensing of Fluoride: Tuning Selectivity in Proton Transfer. *J. Org. Chem.* **2005**, *70*, 10524–10531.

[118] Xu, Z.; Xiao, Y.; Qian, X.; Cui, J.; Cui, D. Ratiometric and Selective Fluorescent Sensor for Cu(II) Based on Internal Charge Transfer (ICT). *Org. Lett.* **2005**, *7*, 889–892.

[119] Liu, B.; Tian, H. A Ratiometric Fluorescent Chemosensor for Fluoride Ions Based on a Proton Transfer Signaling Mechanism. *J. Mater. Chem.* **2005**, *15*, 2681–2686.

[120] Zhang, J. F.; Lim, C. S.; Bhuniya, S.; Cho, B. R.; Kim, J. S. A Highly Selective Colorimetric and Ratiometric Two-Photon Fluorescent Probe for Fluoride Ion Detection. *Org. Lett.* **2011**, *13*, 1190–1193.

[121] Chen, S.; Hong, Y.; Liu, Y.; Liu, J.; Leung, C. W.; Li, M.; Kwok, R. T.; Zhao, E.; Lam, J. W.; Yu, Y., et al. Full-Range Intracellular pH Sensing by an

Aggregation-induced Emission-active Two-Channel Ratiometric Fluorogen. *J. Am. Chem. Soc.* **2013**, *135*, 4926–4929.

[122] Walsh, J. C.; Williams, K.-L. M.; Lungerich, D.; Bodwell, G. J. Synthesis of Pyrene-4,5-dione on a 15 g Scale. *Eur. J. Org. Chem.* **2016**, 5933–5936.

[123] Bräuer, M.; Mosquera, M.; Pérez-Lustres, J. L.; Rodríguez-Prieto, F. Ground-State Tautomerism and Excited-State Proton-Transfer Processes in 4,5-Dimethyl-2-(2-hydroxyphenyl)imidazole in Solution: Fluorescence Spectroscopy and Quantum Mechanical Calculations. *J. Phys. Chem. A* **1998**, *102*, 10736–10745.

[124] Park, S.; Kwon, O.-H.; Kim, S.; Park, S.; Choi, M.-G.; Cha, M.; Park, S. Y.; Jang, D.-J. Imidazole-based excited-state intramolecular proton-transfer materials: synthesis and amplified spontaneous emission from a large single crystal. *J. Am. Chem. Soc.* **2005**, *127*, 10070–10074.

[125] Park, S.; Kwon, O.-H.; Lee, Y.-S.; Jang, D.-J.; Park, S. Y. Imidazole-based Excited-State Intramolecular Proton-Transfer (ESIPT) Materials: Observation of Thermally Activated Delayed Fluorescence (TDF). *J. Phys. Chem. A* **2007**, *111*, 9649–9653.

[126] Li, G.-Y.; Zhao, G.-J.; Liu, Y.-H.; Han, K.-L.; He, G.-Z. TD-DFT Study on the Sensing Mechanism of a Fluorescent Chemosensor for Fluoride: Excited-State Proton Transfer. *J. Comput. Chem.* **2010**, *31*, 1759–1765.

[127] Bader, R. F. *Atoms in Molecules*; Oxford University Press: New York, USA, 1994.

[128] Koch, U.; Popelier, P. L. Characterization of CHO Hydrogen Bonds on the Basis of the Charge Density. *J. Phys. Chem.* **1995**, *99*, 9747–9754.

[129] Grabowski, S. J. Hydrogen Bonding Strength–Measures Based on Geometric and Topological Parameters. *J. Phys. Org. Chem.* **2004**, *17*, 18–31.

[130] Becke, A. D. Density-functional Exchange-Energy Approximation with Correct Asymptotic Behavior. *Phys. Rev. A* **1988**, *38*, 3098–3100.

[131] Lee, C.; Yang, W.; Parr, R. G. Development of the Colle-Salvetti Correlation-Energy Formula into a Functional of the Electron Density. *Phys. Rev. B* **1988**, *37*, 785–789.

[132] Frisch, M. J. et al. Gaussian09 Revision E.01. Gaussian Inc. Wallingford CT 2009.

[133] Miertuš, S.; Scrocco, E.; Tomasi, J. Electrostatic Interaction of a Solute with a Continuum. A Direct Utilizaion of Ab Initio Molecular Potentials for the Prevision of Solvent Effects. *Chem. Phys.* **1981**, *55*, 117–129.

[134] Legault, C. Y. CYLview, 1.0b. 2009; Université de Sherbrooke (http://www.cylview.org).

[135] Dennington, R.; Keith, T.; Millam, J. GaussView Version 5. Semichem Inc. Shawnee Mission KS 2009.

[136] Lu, T.; Chen, F. Multiwfn: a Multifunctional Wavefunction Analyzer. *J. Comput. Chem.* **2012**, *33*, 580–592.

[137] Zhao, Y. S.; Fu, H.; Peng, A.; Ma, Y.; Xiao, D.; Yao, J. Low-dimensional Nanomaterials Based on Small Organic Molecules: Preparation and Optoelectronic Properties. *Adv. Mater.* **2008**, *20*, 2859–2876.

[138] Zheng, Q.; Juette, M. F.; Jockusch, S.; Wasserman, M. R.; Zhou, Z.; Altman, R. B.; Blanchard, S. C. Ultra-stable Organic Fluorophores for Single-Molecule Research. *Chem. Soc. Rev.* **2014**, *43*, 1044–1056.

[139] Kalyani, N. T.; Dhoble, S. Organic Light Emitting Diodes: Energy Saving Lighting Technology-—A Review. *Renew. Sust. Energ. Rev.* **2012**, *16*, 2696–2723.

[140] Tsai, M.-S.; Hsu, Y.-C.; Lin, J. T.; Chen, H.-C.; Hsu, C.-P. Organic Dyes Containing 1*H*-phenanthro[9,10-*d*]imidazole Conjugation for Solar Cells. *J. Phys. Chem. C* **2007**, *111*, 18785–18793.

[141] Wang, Z.; Lu, P.; Chen, S.; Gao, Z.; Shen, F.; Zhang, W.; Xu, Y.; Kwok, H. S.; Ma, Y. Phenanthro[9,10-*d*]imidazole as a New Building Block for Blue Light Emitting Materials. *J. Mater. Chem.* **2011**, *21*, 5451–5456.

[142] Gao, Z.; Liu, Y.; Wang, Z.; Shen, F.; Liu, H.; Sun, G.; Yao, L.; Lv, Y.; Lu, P.; Ma, Y. High-Efficiency Violet-Light-Emitting Materials Based on Phenanthro[9,10-*d*]imidazole. *Chem.–Eur. J.* **2013**, *19*, 2602–2605.

[143] Li, W.; Lin, W.; Wang, J.; Guan, X. Phenanthro[9,10-*d*]imidazole-Quinoline Boron Difluoride Dyes with Solid-State Red Fluorescence. *Org. lett.* **2013**, *15*, 1768–1771.

[144] Gao, Z.; Wang, Z.; Shan, T.; Liu, Y.; Shen, F.; Pan, Y.; Zhang, H.; He, X.; Lu, P.; Yang, B.; Ma, Y. High-Efficiency Deep Blue Fluorescent Emitters Based on Phenanthro[9,10-*d*]imidazole Substituted Carbazole and Their Applications in Organic Light Emitting Diodes. *Org. Electron.* **2014**, *15*, 2667–2676.

[145] Zhao, B.; Liu, T.; Fang, Y.; Wang, L.; Song, B.; Deng, Q. Two 'turn-off' Schiff Base Fluorescence Sensors Based on Phenanthro[9,10-*d*]imidazole-Coumarin Derivatives for Fe^{3+} in Aqueous Solution. *Tetrahedron Lett.* **2016**, *57*, 4417–4423.

[146] Bhaumik, C.; Maity, D.; Das, S.; Baitalik, S. Synthesis, Structural Characterization, Solvatochromism, and Ion-binding Studies of a Ditopic Receptor Based on 2-(4-[2,2:6',2"]terpyridin-4'-yl-phenyl)-1*H*-phenanthro[9, 10-*d*]imidazole (tpy-HImzphen) Unit. *RSC Adv.* **2012**, *2*, 2581–2594.

[147] Kumar, D.; Thomas, K. J.; Lee, C.-P.; Ho, K.-C. Triarylamine-Free Pyrenoimidazole-Containing Organic Dyes with Different π-Linkers for Dye-Sensitized Solar Cells. *Asian J. Org. Chem.* **2015**, *4*, 164–172.

[148] Tabasi, Z. A.; Younes, E. A.; Walsh, J. C.; Thompson, D. W.; Bodwell, G. J.; Zhao, Y. Pyrenoimidazolyl-Benzaldehyde Fluorophores: Synthesis, Properties, and Sensing Function for Fluoride Anions. *ACS Omega* **2018**, *3*, 16387–16397.

[149] Williams, A. T. R.; Winfield, S. A.; Miller, J. N. Relative Fluorescence Quantum Yields using a Computer-controlled Luminescence Spectrometer. *Analyst* **1983**, *108*, 1067–1071.

[150] Miller, J. N. In *Standards in Flourescence Spectrometry. Techniques in Visible and Ultraviolet Spectometry, vol 2.*; Miller, J. N., Ed.; Springer: Dordrecht, 1981; pp 68–78.

[151] Schneider, T. R.; Sheldrick, G. M. Substructure Solution with SHELXD. *Acta Cryst.* **2002**, *D58*, 1772–1779.

[152] Sheldrick, G. M. Crystal Structure Refinement with SHELXL. *Acta Cryst.* **2015**, *C71*, 3–8.

[153] Zhao, Y.; Truhlar, D. G. The M06 Suite of Density Functionals for Main Group Thermochemistry, Thermochemical Kinetics, Noncovalent Interactions, Excited States, and Transition Elements: Two New Functionals and Systematic Testing of Four M06-Class Functionals and 12 Other Functionals. *Theor. Chem. Acc.* **2008**, *120*, 215–241.

[154] Weigend, F.; Ahlrichs, R. Balanced Basis Sets of Split Valence, Triple Zeta Valence and Quadruple Zeta Valence Quality for H to Rn: Design and Assessment of Accuracy. *Phys. Chem. Chem. Phys.* **2005**, *7*, 3297–3305.

[155] Spartan'18 Parallel Suite. Wavefunction, Inc., Irvine, CA, USA.

[156] Gaussian 16, Revision B.01, Frisch, M. J.; Trucks, G. W.; Schlegel, H. B.; Scuseria, G. E.; Robb, M. A.; Cheeseman, J. R.; Scalmani, G.; Barone, V.; Petersson, G. A.; Nakatsuji, H.; Li, X.; Caricato, M.; Marenich, A. V.; Bloino, J.; Janesko, B. G.; Gomperts, R.; Mennucci, B.; Hratchian, H. P.; Ortiz, J. V.; Izmaylov, A. F.; Sonnenberg, J. L.; Williams-Young, D.; Ding, F.; Lipparini, F.; Egidi, F.; Goings, J.; Peng, B.; Petrone, A.; Henderson, T.; Ranasinghe,

D.; Zakrzewski, V. G.; Gao, J.; Rega, N.; Zheng, G.; Liang, W.; Hada, M.; Ehara, M.; Toyota, K.; Fukuda, R.; Hasegawa, J.; Ishida, M.; Nakajima, T.; Honda, Y.; Kitao, O.; Nakai, H.; Vreven, T.; Throssell, K.; Montgomery, J. A., Jr.; Peralta, J. E.; Ogliaro, F.; Bearpark, M. J.; Heyd, J. J.; Brothers, E. N.; Kudin, K. N.; Staroverov, V. N.; Keith, T. A.; Kobayashi, R.; Normand, J.; Raghavachari, K.; Rendell, A. P.; Burant, J. C.; Iyengar, S. S.; Tomasi, J.; Cossi, M.; Millam, J. M.; Klene, M.; Adamo, C.; Cammi, R.; Ochterski, J. W.; Martin, R. L.; Morokuma, K.; Farkas, O.; Foresman, J. B.; Fox, D. J. Gaussian, Inc., Wallingford CT, 2016.

[157] Humphrey, W.; Dalke, A.; Schulten, K. VMD: Visual Molecular Dynamics. *J. Mol. Graph.* **1996**, *14*, 33–38.

[158] Faizi, M. S. H.; Dege, N.; Malinkin, S. Crystal Structure and DFT Study of 2-(Pyren-1-yl)-1*H*-benzimidazole. *Acta Cryst.* **2017**, *E73*, 1180–1183.

[159] Stibrany, R. T.; Potenza, J. A. Structures of 1-Hydrophenanthroimidazoles: Building Blocks in the Synthesis of Expanded-Ring Bis(imidazoles). *Acta Cryst.* **2009**, *C65*, o406–o409.

[160] Sureshbabu, B.; Venkatachalam, R.; Sankararaman, S. Substituent Effect on the Formation of Helical to Layered Hydrogen Bond Networks in Hydroxyl and Carboxyl Substituted 1-Aryl-1H-1,2,3-triazoles. *CrystEngComm* **2014**, *16*, 6098–6106.

[161] Saha, S.; Desiraju, G. R. A Hand-twisted Helical Crystal Based Solely on Hydrogen Bonding. *Chem. Commun.* **2017**, *53*, 6371–6374.

[162] Gavezzotti, A. Are Crystal Structures Predictable? *Acc. Chem. Res.* **1994**, *27*, 309–314.

[163] Coombes, D. S.; Price, S. L.; Willock, D. J.; Leslie, M. Role of Electrostatic Interactions in Determining the Crystal Structures of Polar Organic Molecules. A Distributed Multipole Study. *J. Phys. Chem.* **1996**, *100*, 7352–7360.

[164] Spackman, M. A.; McKinnon, J. J.; Jayatilaka, D. Electrostatic Potentials Mapped on Hirshfeld Surfaces Provide Direct Insight into Intermolecular Interactions in Crystals. *CrystEngComm* **2008**, *10*, 377–388.

[165] Corpinot, M. K.; Bučar, D.-K. A Practical Guide to the Design of Molecular Crystals. *Cryst. Growth Des.* **2018**, *19*, 1426–1453.

[166] Hollingsworth, M. D. Crystal Engineering: from Structure to Function. *Science* **2002**, *295*, 2410–2413.

[167] Tiekink, E. R.; Vittal, J.; Zaworotko, M. *Organic Crystal Engineering: Frontiers in Crystal Engineering*; John Wiley & Sons: Chichester, UK, 2010.

[168] Desiraju, G. R. Supramolecular Synthons in Crystal Engineering–A New Organic Synthesis. *Angew. Chem. Int. Ed. Engl.* **1995**, *34*, 2311–2327.

[169] Braga, D.; Grepioni, F. Organometallic Crystal Engineering: Prospects for a Systematic Design. *Coord. Chem. Rev.* **1999**, *183*, 19–41.

[170] Evans, O. R.; Lin, W. Crystal Engineering of NLO Materials Based on Metal-Organic Coordination Networks. *Acc. Chem. Res.* **2002**, *35*, 511–522.

[171] Desiraju, G. R. Crystal Engineering. From Molecules to Materials. *J. Mol. Struct.* **2003**, *656*, 5–15.

[172] Almarsson, Ö.; Zaworotko, M. J. Crystal Engineering of the Composition of Pharmaceutical Phases. Do Pharmaceutical Co-crystals Represent a New Path to Improved Medicines? *Chem. Commun.* **2004**, 1889–1896.

[173] Suponitsky, K. Y.; Timofeeva, T. V.; Antipin, M. Y. Molecular and Crystal Design of Nonlinear Optical Organic Materials. *Russ. Chem. Rev.* **2006**, *75*, 457.

[174] Desiraju, G. R. Crystal Engineering: A Brief Overview. *J. Chem. Sci.* **2010**, *122*, 667–675.

[175] Dunitz, J. D. In *The Crystal as a Supramolecular Entity*; Desiraju, G. R., Ed.; John Wiley & Sons: Chichester, 1996; Chapter Thoughts on Crystals as Supermolecules, pp 1–30.

[176] Aakeröy, C. B.; Seddon, K. R. The Hydrogen Bond and Crystal Engineering. *Chem. Soc. Rev.* **1993**, *22*, 397–407.

[177] Burrows, A. D.; Chan, C.-W.; Chowdhry, M. M.; McGrady, J. E.; Mingos, D. M. P. Multidimensional Crystal Engineering of Bifunctional Metal Complexes Containing Complementary Triple Hydrogen Bonds. *Chem. Soc. Rev.* **1995**, *24*, 329–339.

[178] Walsh, R. B.; Bradner, M.; Fleischman, S.; Morales, L.; Moulton, B.; Rodriguez-

Hornedo, N.; Zaworotko, M. Crystal Engineering of the Composition of Pharmaceutical Phases. *Chem. Commun.* **2003**, 186–187.

[179] Roesky, H. W.; Andruh, M. The Interplay of Coordinative, Hydrogen Bonding and π–π Stacking Interactions in Sustaining Supramolecular Solid-State Architectures.: A Study Case of Bis(4-pyridyl)-and Bis(4-pyridyl-N-oxide) Tectons. *Coord. Chem. Rev.* **2003**, *236*, 91–119.

[180] Priimagi, A.; Cavallo, G.; Metrangolo, P.; Resnati, G. The Halogen Bond in the Design of Functional Supramolecular Materials: Recent Advances. *Acc. Chem. Res.* **2013**, *46*, 2686–2695.

[181] Tabasi, Z. A.; Walsh, J. C.; Bodwell, G. J.; Thompson, D. W.; Zhao, Y. Crystal Engineering and Photophysical Properties of Phenyl-Pyrenoimidazole Systems. *Cryst. Growth Des.* **2020**, *20*, 1681–1693.

[182] Nishio, M. CH/π Hydrogen Bonds in Crystals. *CrystEngComm* **2004**, *6*, 130–158.

[183] Nishio, M.; Umezawa, Y.; Honda, K.; Tsuboyama, S.; Suezawa, H. CH/π Hydrogen Bonds in Organic and Organometallic Chemistry. *CrystEngComm* **2009**, *11*, 1757–1788.

[184] Bishop, R. Organic Crystal Engineering beyond the Pauling Hydrogen Bond. *CrystEngComm* **2015**, *17*, 7448–7460.

[185] Gospodinova, N.; Tomšík, E. Hydrogen-bonding versus π–π Stacking in the

Design of Organic Semiconductors: From Dyes to Oligomers. *Prog. Polym. Sci.* **2015**, *43*, 33–47.

[186] MacDonald, J. C.; Dorrestein, P. C.; Pilley, M. M. Design of Supramolecular Layers via Self-Assembly of Imidazole and Carboxylic Acids. *Cryst. Growth Des.* **2001**, *1*, 29–38.

[187] Trivedi, D. R.; Ballabh, A.; Dastidar, P. Supramolecular Assemblies in Salts and Co-crystals of Imidazoles with Dicarboxylic Acids. *CrystEngComm* **2003**, *5*, 358–367.

[188] Aakeröy, C. B.; Desper, J.; Leonard, B.; Urbina, J. F. Toward High-Yielding Supramolecular Synthesis: Directed Assembly of Ditopic Imidazoles/Benzimidazoles and Dicarboxylic Acids into Cocrystals via Selective O–H Hydrogen Bonds. *Cryst. Growth Des.* **2005**, *5*, 865–873.

[189] Jin, S.; Zhang, W.; Wang, D.; Gao, H.; Zhou, J. Z.; Chen, R.; Xu, X. Crystal and Molecular Structure of the 1:2 Adduct Formed between *N*,*N*-butylenebis(imidazole) and Carboxylic Acid Derivatives. *J. Chem. Crystallogr.* **2010**, *40*, 87–92.

[190] Mahapatra, A. K.; Sahoo, P.; Goswami, S.; Fun, H.-K. Model Pharmaceutical Co-crystallization: Guest-directed Assembly of Caffeine and Aromatic Trihydroxy and Dicarboxylic Acids into Different Heteromolecular Hydrogen Bonding Networks in Solid State. *J. Mol. Struct.* **2010**, *963*, 63–70.

[191] Kakkar, S.; Bhattacharya, B.; Reddy, C. M.; Ghosh, S. Tuning Mechanical

Behaviour by Controlling the Structure of a Series of Theophylline Co-crystals. *CrystEngComm* **2018**, *20*, 1101–1109.

[192] Oszczapowicz, J.; Czuryłowska, M. The pKa, Values of the Conjugate Acid of Imidazole in Water–Ethanol Mixtures. *Talanta* **1984**, *31*, 559–560.

[193] Baures, P. W.; Rush, J. R.; Wiznycia, A. V.; Desper, J.; Helfrich, B. A.; Beatty, A. M. Intramolecular Hydrogen Bonding and Intermolecular Dimerization in the Crystal Structures of Imidazole-4,5-dicarboxylic Acid Derivatives. *Cryst. Growth Des.* **2002**, *2*, 653–664.

[194] Trivedi, D. R.; Ballabh, A.; Dastidar, P. Supramolecular Assemblies in Salts and Co-crystals of Imidazoles with Dicarboxylic Acids. *CrystEngComm* **2003**, *5*, 358–367.

[195] Ward, M. D. Design of Crystalline Molecular Networks with Charge-assisted Hydrogen Bonds. *Chem. Commun.* **2005**, 5838–5842.

[196] Yigit, M. V.; Biyikli, K.; Moulton, B.; MacDonald, J. C. Bis(imidazolium 2,4,6-tricarboxypyridine) Metal(II) Complexes: Molecular Building Blocks that Generate Isomorphous Hydrogen-bonded Frameworks. *Cryst. Growth Des.* **2006**, *6*, 63–69.

[197] Wang, W.-H.; Xi, P.-H.; Su, X.-Y.; Lan, J.-B.; Mao, Z.-H.; You, J.-S.; Xie, R.-G. Supramolecular Assemblies of Multifunctional Diimidazole and Dicarboxylic Acids via Various Hydrogen Bonds and X$\cdots\pi$ (X= π, CH) Interactions. *Cryst. Growth Des.* **2007**, *7*, 741–746.

[198] Desiraju, G. R.; Parshall, G. W. Crystal Engineering: the Design of Organic Solids. *Materials science monographs* **1989**, *54*.

[199] Seddon, K. R.; Zaworotko, M. *Crystal Engineering: the Design and Application of Functional Solids*; Springer Science & Business Media, 1999; Vol. 539.

[200] Mackenzie, C. F.; Spackman, P. R.; Jayatilaka, D.; Spackman, M. A. CrystalExplorer Model Energies and Energy Frameworks: Extension to Metal Coordination Compounds, Organic Salts, Solvates and Open-Shell Systems. *IUCrJ* **2017**, *4*, 575–587.

[201] Spackman, M. A.; Jayatilaka, D. Hirshfeld Surface Analysis. *CrystEngComm* **2009**, *11*, 19–32.

[202] CrystalExplorer (Version 3.1), Wolff, S. K.; Grimwood, D. J.; McKinnon, J. J.; Turner, M. J.; Jayatilaka, D.; Spackman, M. A., University of Western Australia, 2012.

[203] Spackman, M. A.; Byrom, P. G. A Novel Definition of a Molecule in a Crystal. *Chem. Phys. Lett.* **1997**, *267*, 215–220.

[204] McKinnon, J. J.; Spackman, M. A.; Mitchell, A. S. Novel Tools for Visualizing and Exploring Intermolecular Interactions in Molecular Crystals. *Acta Cryst.* **2004**, *B60*, 627–668.

[205] Aakeröy, C. B. Crystal Engineering: Strategies and Architectures. *Acta Crystallographica Section B: Structural Science* **1997**, *53*, 569–586.

[206] Atwood, J. L. *Comprehensive Supramolecular Chemistry II*; Elsevier, 2017.

[207] Spackman, M. A. Molecules in Crystals. *Phys. Scrip.* **2013**, *87*, 048103.

[208] McKinnon, J. J.; Mitchell, A. S.; Spackman, M. A. Hirshfeld Surfaces: A New tool for Visualising and Exploring Molecular Crystals. *Chem. Eur. J.* **1998**, *4*, 2136–2141.

[209] Chattopadhyay, B.; Mukherjee, A. K.; Narendra, N.; Hemantha, H.; Sureshbabu, V. V.; Helliwell, M.; Mukherjee, M. Supramolecular architectures in 5, 5-substituted hydantoins: crystal structures and hirshfeld surface analyses. *Crystal growth & design* **2010**, *10*, 4476–4484.

[210] Tan, S. L.; Jotani, M. M.; Tiekink, E. R. Utilizing Hirshfeld surface calculations, non-covalent interaction (NCI) plots and the calculation of interaction energies in the analysis of molecular packing. *Acta Crystallographica Section E: Crystallographic Communications* **2019**, *75*, 308–318.

[211] Scheiner, S., et al. *Hydrogen Bonding: A Theoretical Perspective*; Oxford University Press on Demand, 1997.

[212] Jeffrey, G. A.; Saenger, W. *Hydrogen Bonding in Biological Structures*; Springer Science & Business Media, 2012.

[213] Custelcean, R.; Jackson, J. E. Dihydrogen Bonding: Structures, Energetics, and Dynamics. *Chem. Rev.* **2001**, *101*, 1963–1980.

[214] Matta, C. F.; Hernández-Trujillo, J.; Tang, T.-H.; Bader, R. F. Hydrogen–Hydrogen Bonding: A Stabilizing Interaction in Molecules and Crystals. *Chem. Eur. J.* **2003**, *9*, 1940–1951.

[215] Bader, R. Principle of Stationary Action and the Definition of a Proper Ppen System. *Phys. Rev. B* **1994**, *49*, 13348.

[216] Grimme, S.; Mück-Lichtenfeld, C.; Erker, G.; Kehr, G.; Wang, H.; Beckers, H.; Willner, H. When Do Interacting Atoms form a Chemical Bond? Spectroscopic Measurements and Theoretical Analyses of Dideuteriophenanthrene. *Angew. Chem. Int. Ed.* **2009**, *48*, 2592–2595.

[217] Cerpa, E.; Krapp, A.; Vela, A.; Merino, G. The Implications of Symmetry of the External Potential on Bond Paths. *Chem. Eur. J.* **2008**, *14*, 10232–10234.

[218] Cerpa, E.; Krapp, A.; Flores-Moreno, R.; Donald, K. J.; Merino, G. Influence of Endohedral Confinement on the Electronic Interaction between He Atoms: A He2@ C20H20 Case Study. *Chem. Eur. J.* **2009**, *15*, 1985–1990.

[219] Bader, R. F. Bond Paths Are Not Chemical Bonds. *J. Phys. Chem. A* **2009**, *113*, 10391–10396.

[220] Arunan, E.; Desiraju, G. R.; Klein, R. A.; Sadlej, J.; Scheiner, S.; Alkorta, I.; Clary, D. C.; Crabtree, R. H.; Dannenberg, J. J.; Hobza, P., et al. Definition of the Hydrogen Bond (IUPAC Recommendations 2011). *Pure Appl. Chem.* **2011**, *83*, 1637–1641.

[221] Matta, C. F. *Hydrogen Bonding—-New Insights*; Springer, 2006; pp 337–375.

[222] Johnson, E. R.; Keinan, S.; Mori-Sánchez, P.; Contreras-García, J.; Cohen, A. J.; Yang, W. Revealing Noncovalent Interactions. *J. Am. Chem. Soc.* **2010**, *132*, 6498–6506.

[223] Contreras-García, J.; Johnson, E. R.; Keinan, S.; Chaudret, R.; Piquemal, J.-P.; Beratan, D. N.; Yang, W. NCIPLOT: a Program for Plotting Noncovalent Interaction Regions. *J. Chem. Theor. Comput.* **2011**, *7*, 625–632.

[224] Tan, L.-L.; Li, H.; Tao, Y.; Zhang, S. X.-A.; Wang, B.; Yang, Y.-W. Pillar[5]arene-based Supramolecular Organic Frameworks for Highly Selective CO_2–Capture at Ambient Conditions. *Adv. Mater.* **2014**, *26*, 7027–7031.

[225] Tian, J.; Chen, L.; Zhang, D.-W.; Liu, Y.; Li, Z.-T. Supramolecular Organic Frameworks: Engineering Periodicity in Water Through Host–Guest Chemistry. *Chem Commun.* **2016**, *52*, 6351–6362.

[226] Li, Y.; Dong, Y.; Miao, X.; Ren, Y.; Zhang, B.; Wang, P.; Yu, Y.; Li, B.; Isaacs, L.; Cao, L. Shape-Controllable and Fluorescent Supramolecular Organic Frameworks Through Aqueous Host–Guest Complexation. *Angew. Chem.* **2018**, *130*, 737–741.

Supporting Information

Pyrenoimidazolyl-Benzaldehyde Fluorophores: Synthesis, Properties, and Sensing Function for Fluoride Anion

Zahra A. Tabasi,[a] *Eyad A. Younes,*[b] *Joshua C. Walsh,*[a] *David W. Thompson,*[a] *Graham J. Bodwell,*[a] *and Yuming Zhao**[a]

[a]Department of Chemistry, Memorial University, St. John's, Newfoundland and Labrador, CANADA A1B 3X7; yuming@mun.ca

[b]Department of Chemistry, The Hashemite University, P.O. Box 150459, Zarqa 13115, Jordan

Table of Content

1. NMR Spectra of Compounds 4 and 5 S2

2. X-ray Crystallographic Data for Compounds 4 and 5 S8

3. Detailed Results of UV-Vis and Fluorescence Spectral Analysis S10

4. Detailed ^{1}H NMR Titration Data S14

5. Detailed Results of DTF and TD-DFT Studies S18

1. NMR Spectra of Compounds 4 and 5

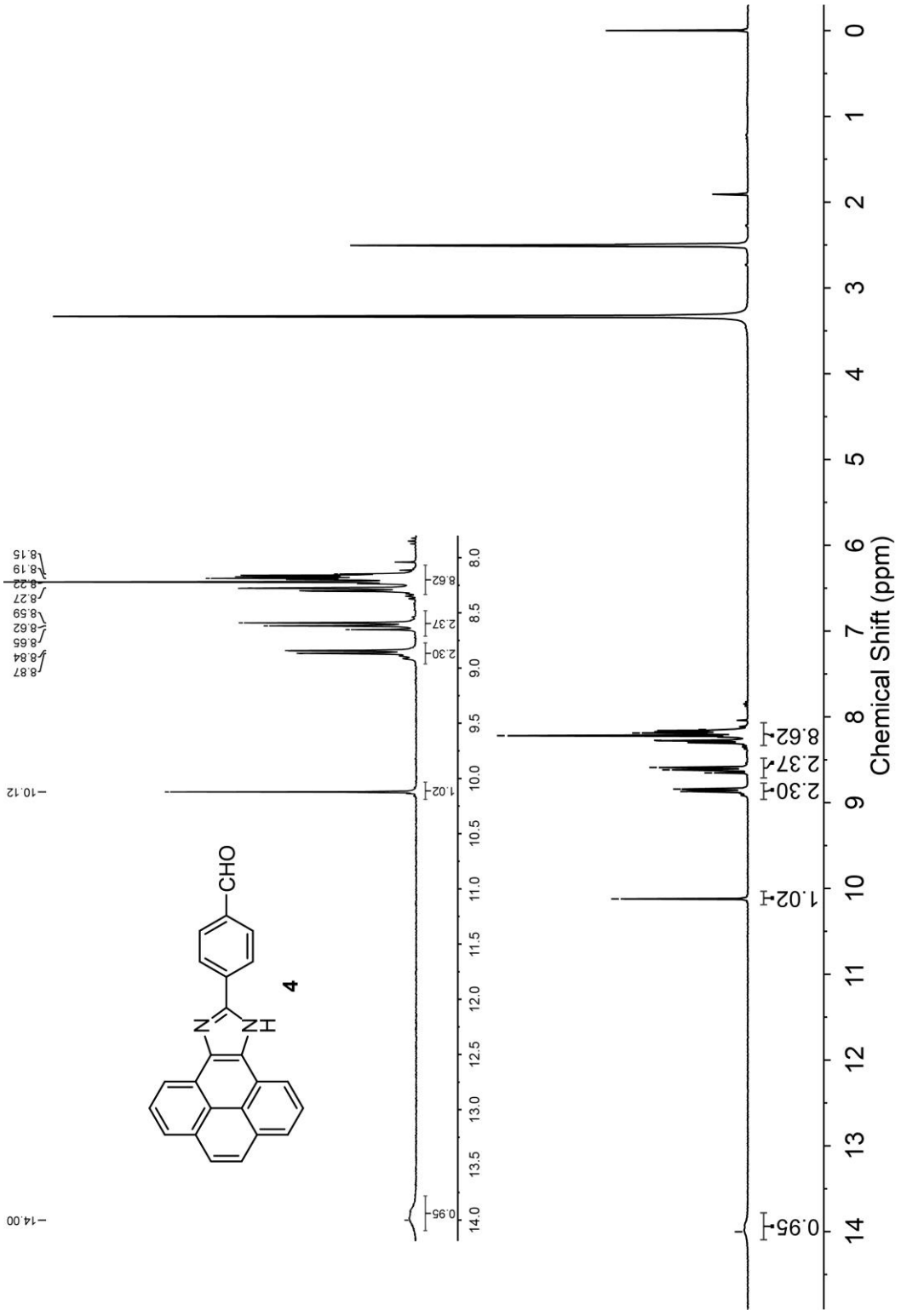

Fig. S-1 ^{1}H NMR (300 MHz, acetone-d_6) spectrum of compound **4**.

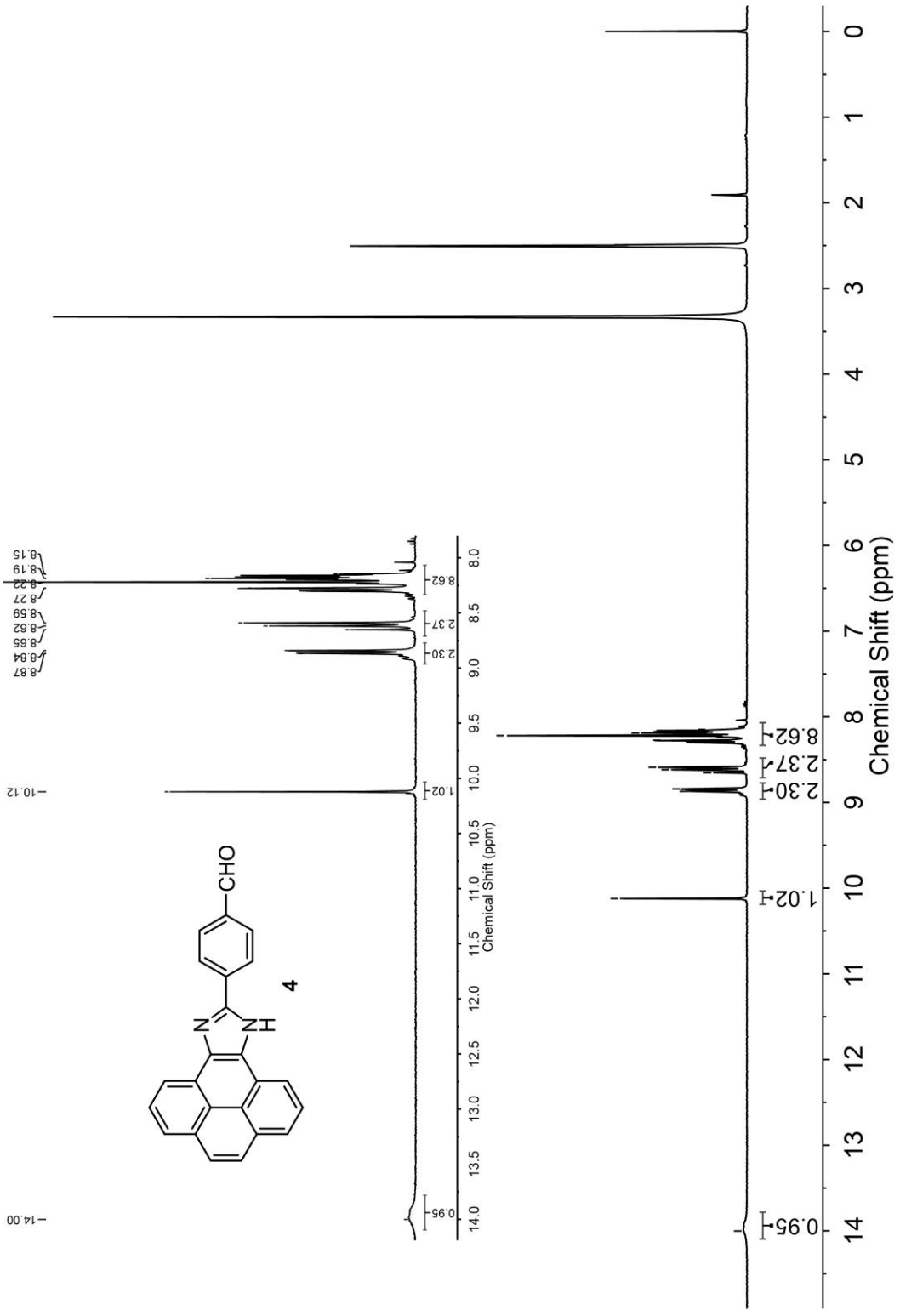

Fig. S-2 ^{1}H NMR (300 MHz, DMSO-d_6) spectrum of compound **4**.

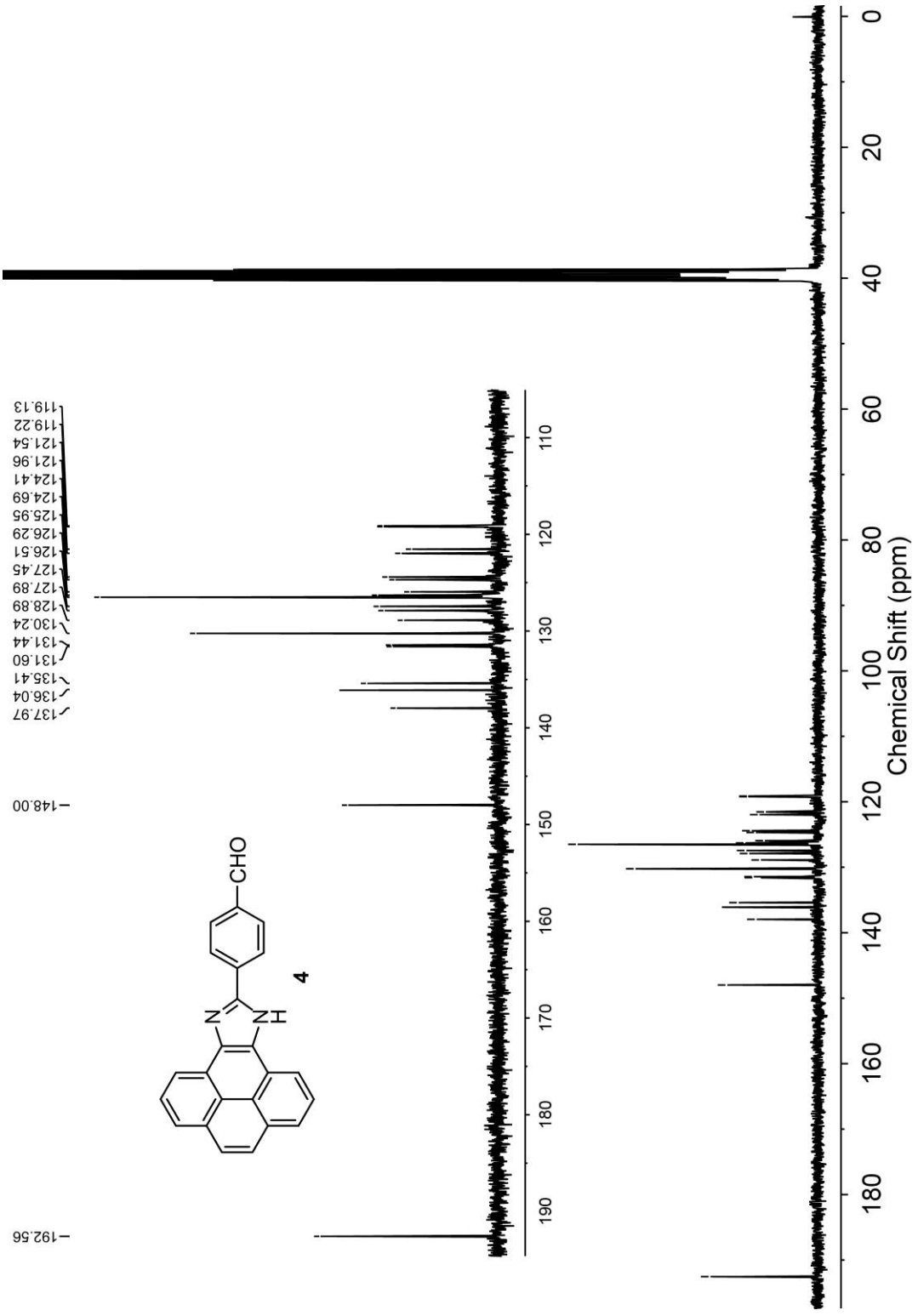

Fig. S-3 ^{13}C NMR (75 MHz, DMSO-d_6) spectrum of compound **4**.

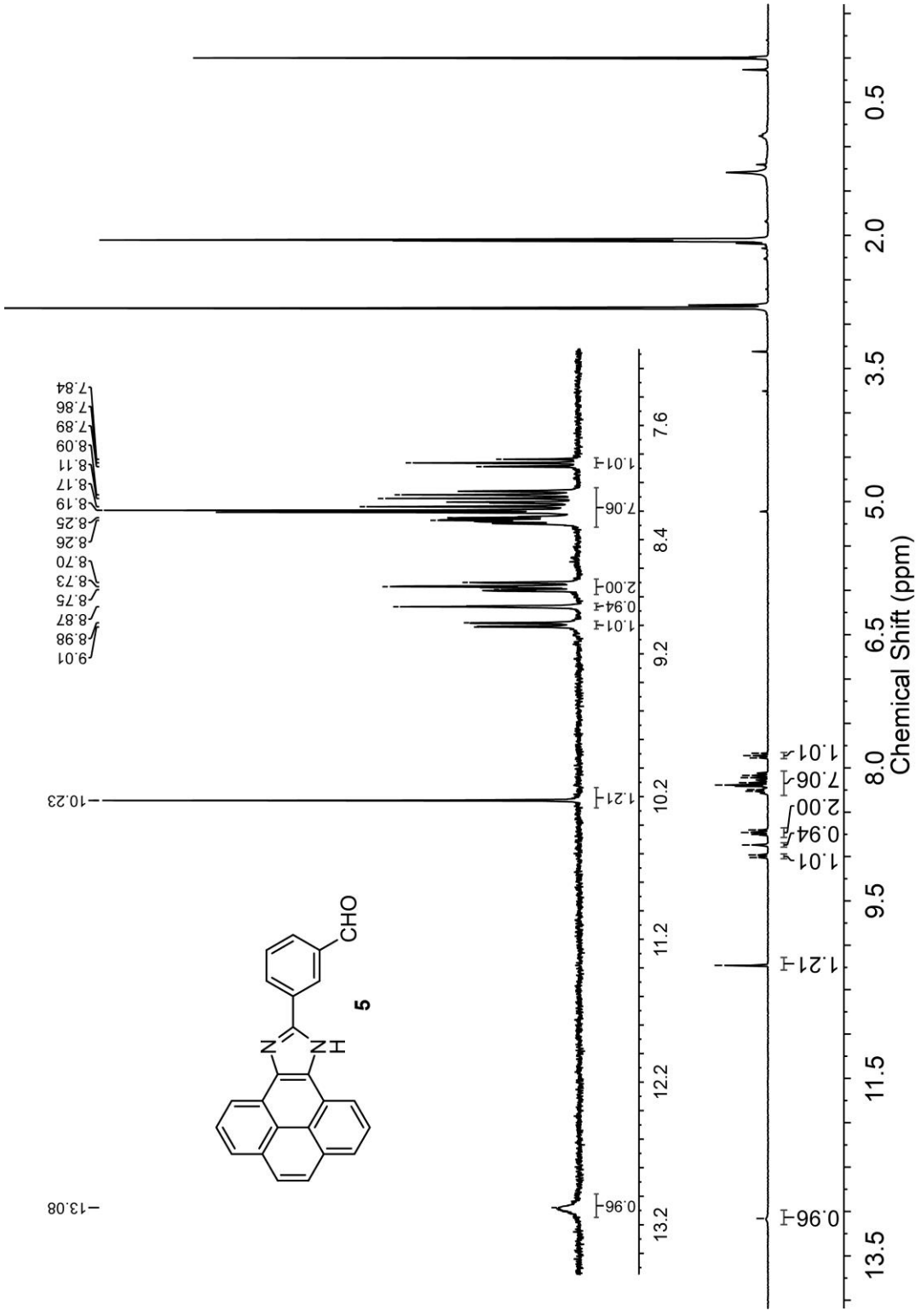

Fig. S-4 ^{1}H NMR (300 MHz, acetone-d_6) spectrum of compound **5**.

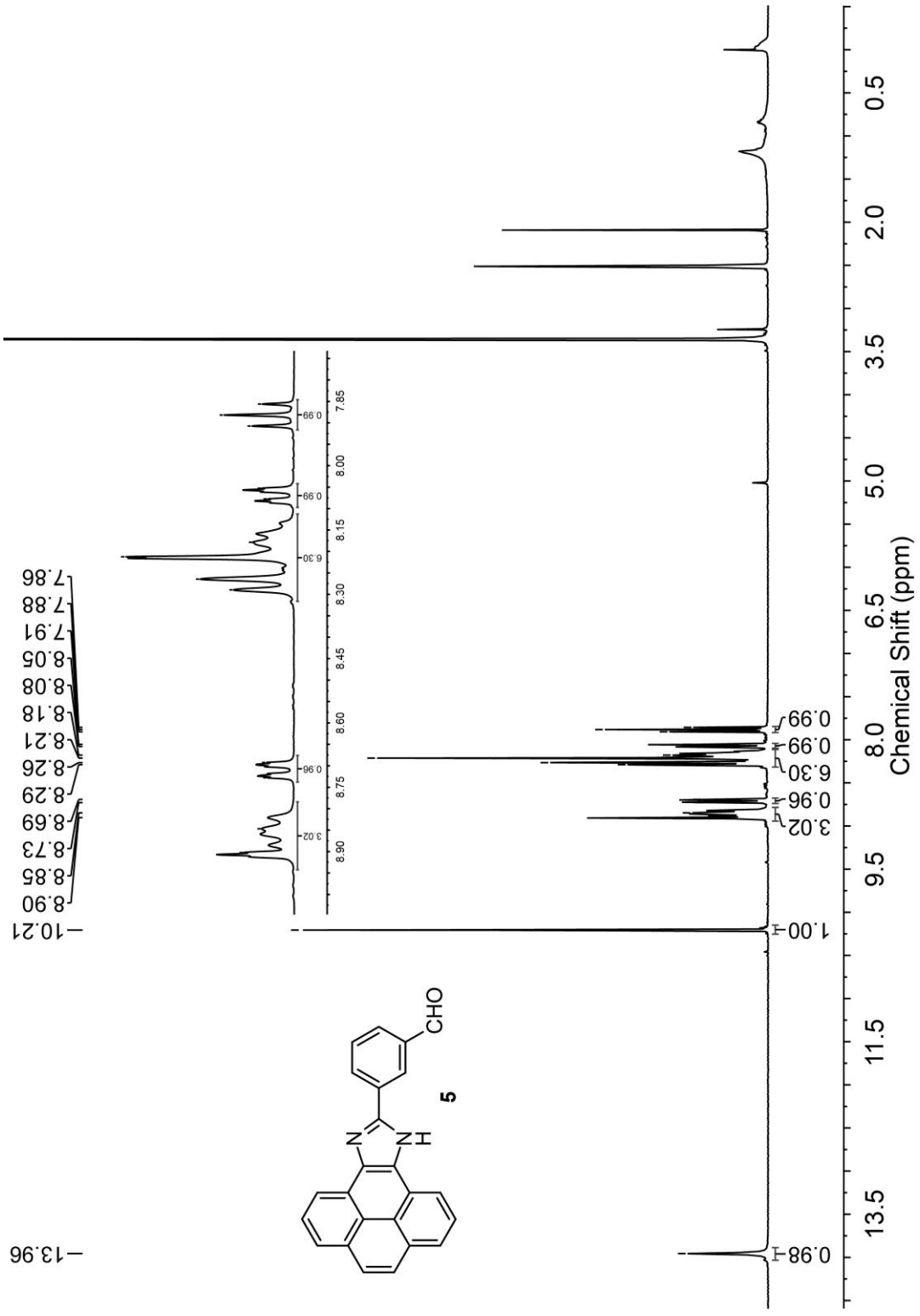

Fig. S-5 ^{1}H NMR (300 MHz, DMSO-d_6) spectrum of compound **5**.

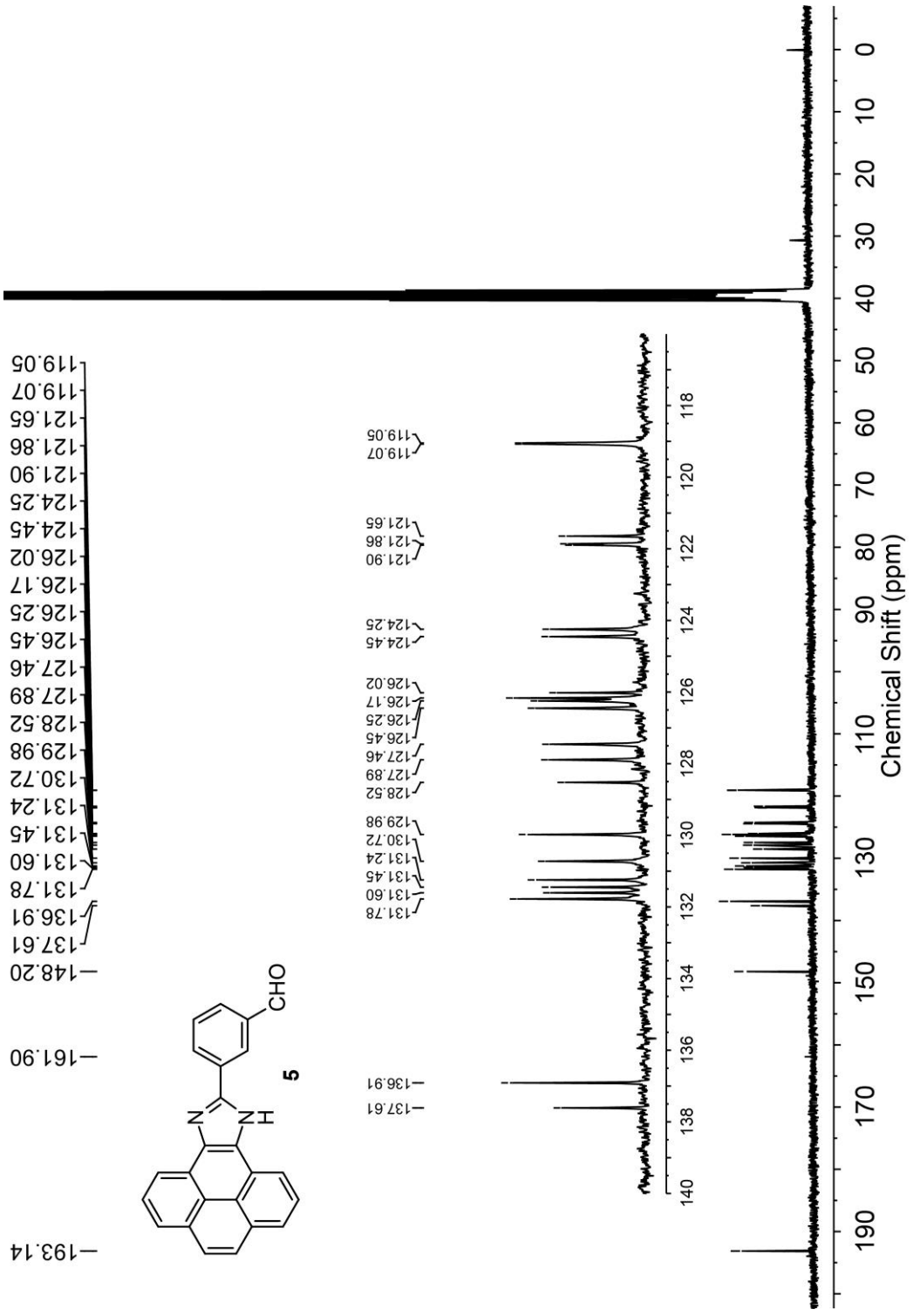

Fig. S-6 ^{13}C NMR (75 MHz, DMSO-d_6) spectrum of compound **5**.

2. X-ray Crystallographic Data for Compounds 4 and 5

Table S-1. Crystallographic Experimental Details for Compound **4**

A. Crystal Data	
formula	$C_{24}H_{14}N_2O$
formula weight	346.37
crystal dimensions (mm)	0.34 × 0.34 × 0.08
crystal system	monoclinic
space group	$P2_1/c$ (No. 14)
unit cell parameters[a]	
a (Å)	15.8330 (5)
b (Å)	6.44809 (19)
c (Å)	15.5345 (5)
β (deg)	90.5223 (15)
V (Å^3)	1585.89 (9)
Z	4
ρ_{calcd} (g cm^{-3})	1.451
μ (mm^{-1})	0.710
B. Data Collection and Refinement Conditions	
diffractometer	Bruker D8/APEX II CCD[b]
radiation (λ [Å])	graphite-monochromated Mo Kα (0.71073)
temperature (°C)	–100
scan type	ω and ϕ scans (1.0°) (5 s exposures)
data collection 2θ limit (deg)	147.75
total data collected	10660 (-19 ≤ h ≤ 19, -8 ≤ k ≤ 8, -18 ≤ l ≤ 17)
independent reflections	3109 Rint 0.0482)
number of observed reflections (*NO*)	2807 [$F_o^2 \geq 2\sigma(F_o^2)$]
structure solution method	direct methods/dual space (*SHELXD*[c])
refinement method	full-matrix least-squares on F^2 (*SHELXL–2014*[d])
absorption correction method	Gaussian integration (face-indexed)
range of transmission factors	1.0000–0.6287
data/restraints/parameters	3109 / 0 / 248
goodness-of-fit (S)[e] [all data]	1.107
final R indices[f]	
R_1 [$F_o^2 \geq 2\sigma(F_o^2)$]	0.0521
wR_2 [all data]	0.1617
largest difference peak and hole	0.284 and –0.343 e Å^{-3}

[a]Obtained from least-squares refinement of 9234 reflections with 5.58° < 2θ < 147.76°.
[b]Programs for diffractometer operation, data collection, data reduction and absorption correction were those supplied by Bruker.

Table S-2. Crystallographic Experimental Details for Compound **5**

A. Crystal Data	
formula	$C_{28}H_{26}N_2O_3S_2$
formula weight	502.63
crystal dimensions (mm)	0.30 × 0.19 × 0.05
crystal system	monoclinic
space group	$P2_1/n$ (an alternate setting of $P2_1/c$ [No. 14])
unit cell parameters[a]	
a (Å)	13.7747(2)
b (Å)	8.16130(10)
c (Å)	22.0303(3)
β (deg)	102.2491(7)
V (Å^3)	2420.25(6)
Z	4
ρ_{calcd} (g cm^{-3})	1.379
μ (mm^{-1})	2.270
B. Data Collection and Refinement Conditions	
diffractometer	Bruker D8/APEX II CCD[b]
radiation (λ [Å])	Cu Kα (1.54178) (microfocus source)
temperature (°C)	–100
scan type	ω and ϕ scans (1.0°) (5 s exposures)
data collection 2θ limit (deg)	144.69
total data collected	16192 (-17 ≤ h ≤ 17, -9 ≤ k ≤ 9, -27 ≤ l ≤ 27)
independent reflections	4765 (R_{int} = 0.0221)
number of observed reflections (*NO*)	4219 [$F_o^2 \geq 2\sigma(F_o^2)$]
structure solution method	intrinsic phasing (*SHELXT-2014*[c])
refinement method	full-matrix least-squares on F^2 (*SHELXL–2016*[d])
absorption correction method	Gaussian integration (face-indexed)
range of transmission factors	0.9035–0.656
data/restraints/parameters	4765 / 0 / 324
goodness-of-fit (S)[e] [all data]	1.072
final R indices[f]	
R_1 [$F_o^2 \geq 2\sigma(F_o^2)$]	0.0402
wR_2 [all data]	0.1191
largest difference peak and hole	0.804 and –0.491 e Å^{-3}

[a]Obtained from least-squares refinement of 9861 reflections with 6.96° < 2θ < 144.44°.
[b]Programs for diffractometer operation, data collection, data reduction and absorption correction were those supplied by Bruker.

3. Detailed Results of UV-Vis and Fluorescence Spectral Analysis

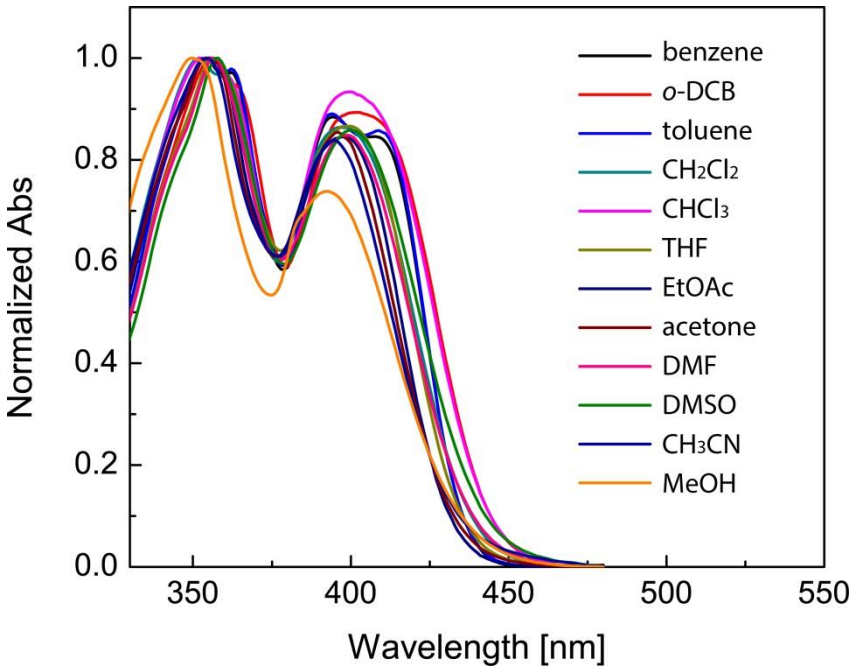

Fig. S-7 UV-Vis absorption spectra of compound **4** measured in various organic solvents.

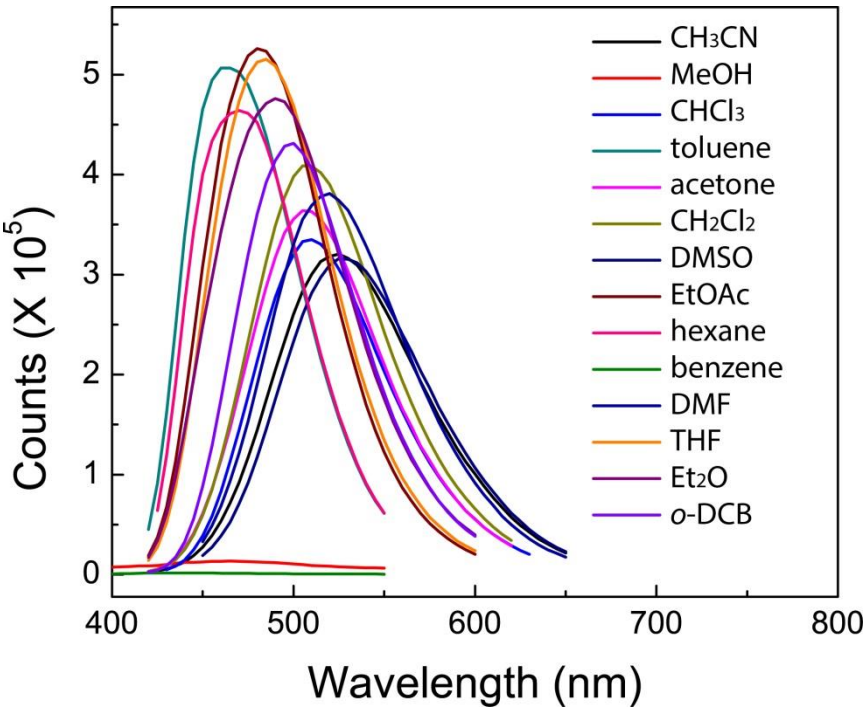

Fig. S-8 Fluorescence spectra of compound **4** measured in various organic solvents.

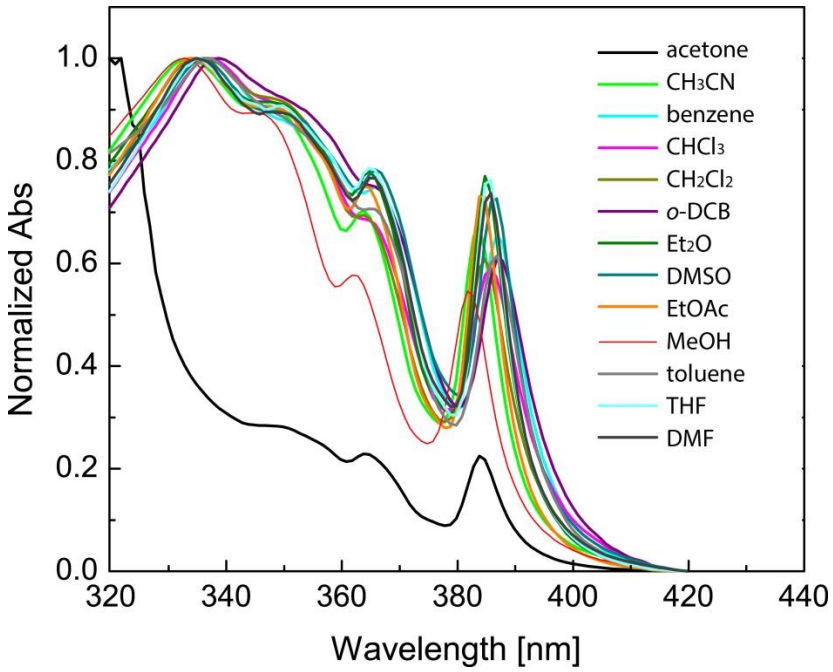

Fig. S-9 UV-Vis absorption spectra of compound **5** measured in various organic solvents.

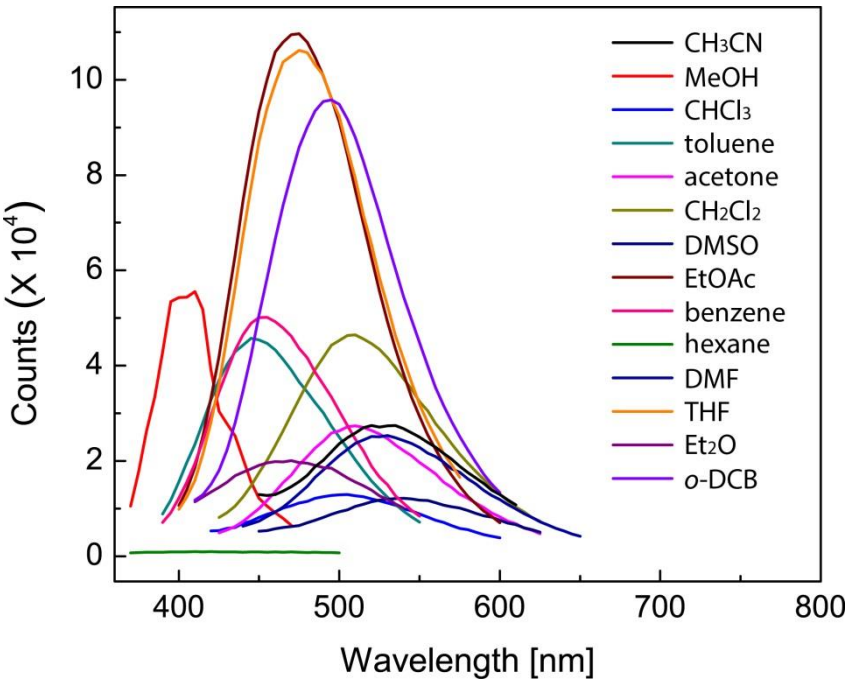

Fig. S-10 Fluorescence spectra of compound **5** measured in various organic solvents.

Table S-1 Summary of maximum UV-Vis absorption wavelengths (λ_{max}) and fluorescence emission wavelength (λ_{em}) of compounds **4** and **5** in various organic solvents

	4		**5**	
Solvents	λ_{abs} (nm)	λ_{em} (nm)	λ_{abs} (nm)	λ_{em} (nm)
CH_3CN	394, 354	524	383, 364, 348(sh), 333	559
MeOH	392, 350	464	381, 362, 346(sh), 333	403
$CHCl_3$	399, 352	508	386, 336, 355(sh), 351	503
toluene	410, 394, 362, 355	464	386, 365(sh), 349(sh), 337	445
acetone	395, 354	506	384, 364, 349	509
CH_2Cl_2	397, 359(sh), 352	507	385, 363(sh), 350(sh), 336	507
DMSO	400, 357	529	386, 366, 349(sh), 335	542
EtOAc	397, 358(sh), 354	480	384, 364, 349(sh), 334	474
benzene	409, 394, 353	469	387, 366, 351(sh), 337	451
DMF	398, 356	518	385, 365, 349(sh), 335	526
THF	399, 361(sh), 355	482	385, 365, 349(sh), 335	475
Et_2O	401, 362(sh) 355	489	385, 364, 348(sh), 334	470
ortho-diclorobenzene	402, 364(sh), 355	497	387, 338, 365(sh), 353	492

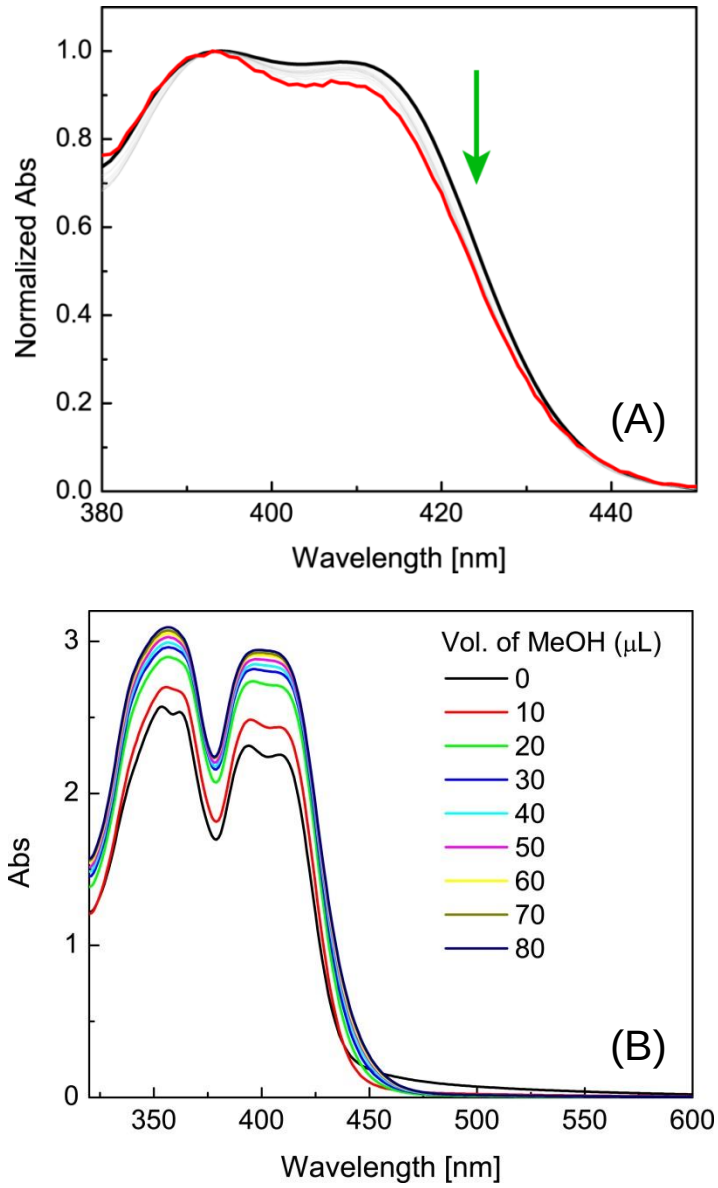

Fig. S-11 (A) Normalized UV-Vis absorption spectra of compound **4** measured in toluene. The arrow indicates the trend of spectral changes associated with the concentration of **4** varying from 4.00×10^{-3} to 1.20×10^{-5} M. (B) UV-Vis spectra monitoring the titration of **4** (3.50×10^{-3} M) in toluene (2.00 mL) with varied amounts of methanol.

4. Detailed ^{1}H NMR Titration Data

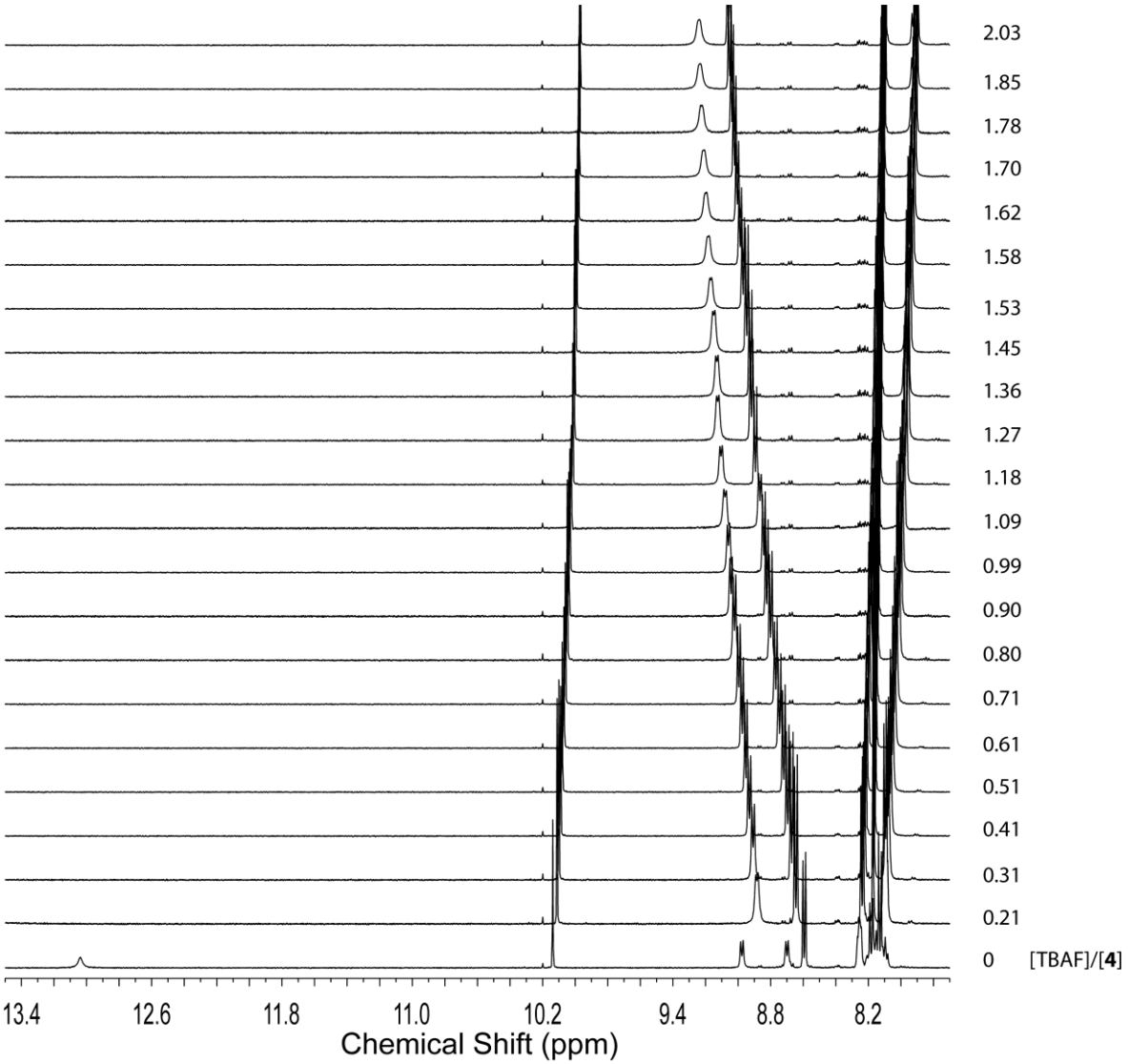

Fig. S-12 ^{1}H NMR (300 MHz, acetone-d_6) spectra monitoring the titration of **4** with TBAF.

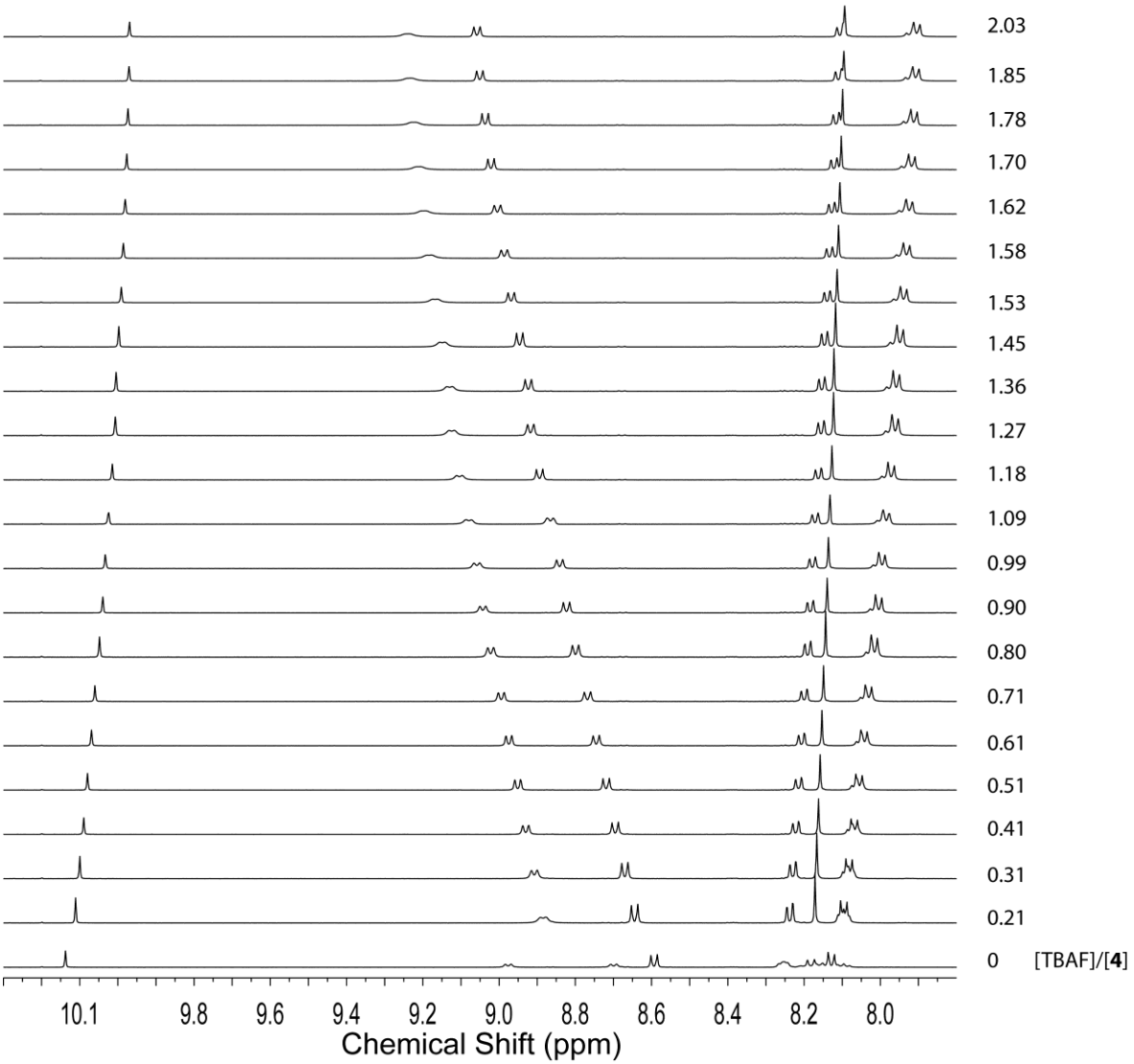

Fig. S-13 Expanded ^{1}H NMR (300 MHz, acetone-d_6) spectra monitoring the titration of **4** with TBAF.

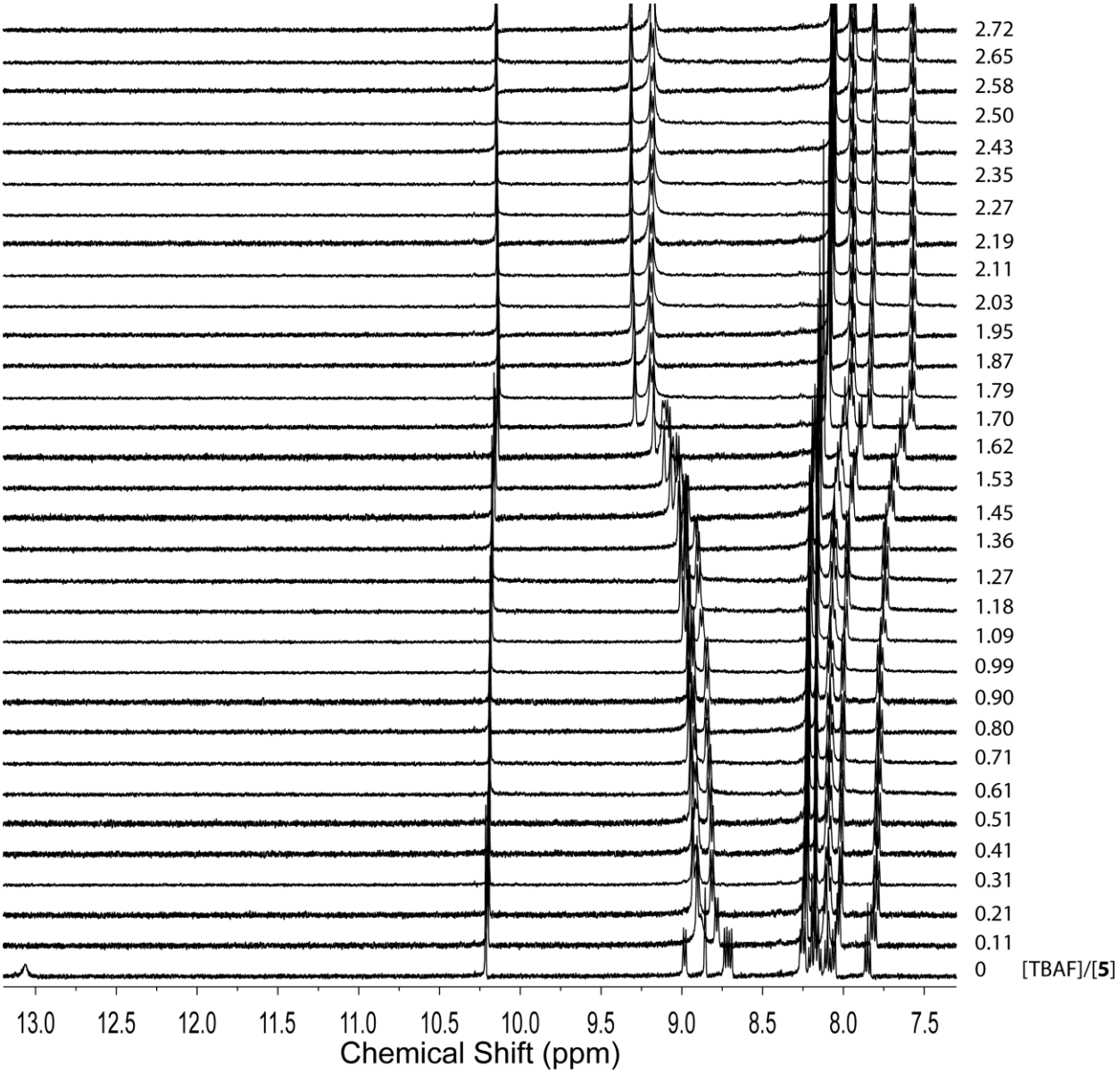

Fig. S-14 ^{1}H NMR (300 MHz, acetone-d_6) spectra monitoring the titration of **5** with TBAF.

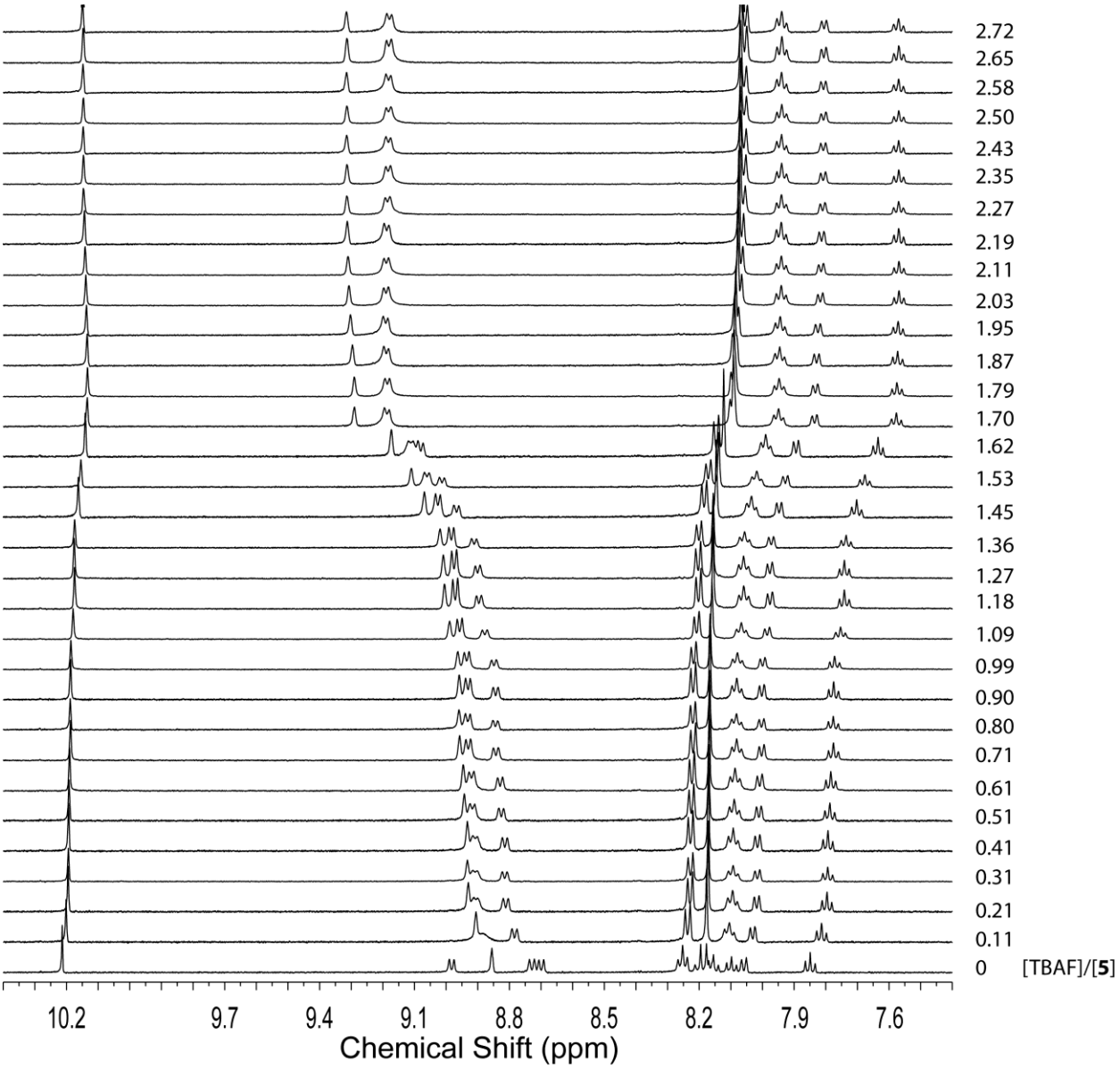

Fig. S-15 Expanded ^{1}H NMR (300 MHz, acetone-d_6) spectra monitoring the titration of **5** with TBAF.

5. Detailed Results of DFT and TD-DFT Studies

5.1 Optimized Geometries of Compounds 4 and 5 and Related Anions

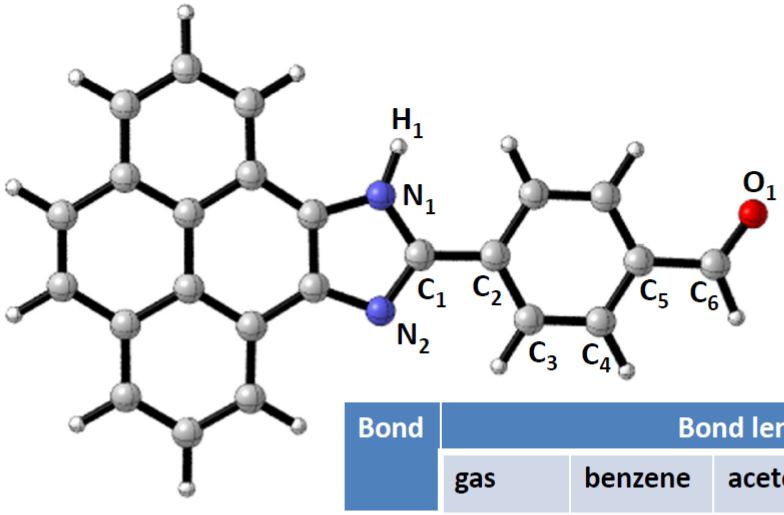

Bond	Bond length (Å)				
	gas	benzene	acetone	DMSO	MeOH
H_1-N_1	1.008	1.009	1.009	1.009	1.009
N_1-C_1	1.382	1.380	1.378	1.377	1.377
C_1-N_2	1.326	1.327	1.329	1.330	1.330
C_1-C_2	1.462	1.463	1.463	1.464	1.463
C_2-C_3	1.408	1.408	1.409	1.409	1.409
C_3-C_4	1.390	1.390	1.390	1.390	1.390
C_4-C_5	1.404	1.405	1.406	1.406	1.406
C_5-C_6	1.478	1.475	1.473	1.472	1.472
C_6-O_1	1.220	1.223	1.227	1.227	1.227

Fig. S-16 Optimized geometry of compound **4** in the gas phase and selected bond lengths optimized in the gas phase as well as in different organic solvents. Optimization was conducted at the B3LYP/6-31++G(d,p) level and the PCM method was used to account for solvent effects.

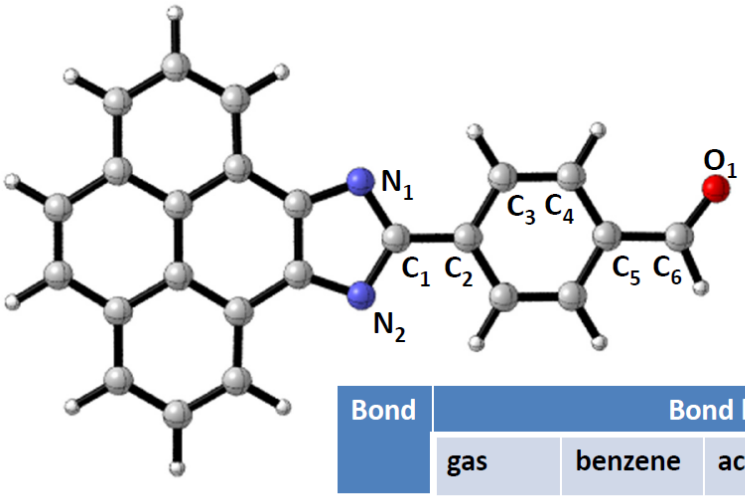

Bond	Bond length (Å)				
	gas	benzene	acetone	DMSO	MeOH
N_1-C_1	1.363	1.363	1.362	1.362	1.362
C_1-N_2	1.363	1.362	1.362	1.362	1.362
C_1-C_2	1.456	1.458	1.461	1.461	1.461
C_2-C_3	1.418	1.418	1.417	1.417	1.417
C_3-C_4	1.384	1.385	1.385	1.385	1.385
C_4-C_5	1.412	1.412	1.411	1.411	1.411
C_5-C_6	1.459	1.459	1.461	1.462	1.461
C_6-O_1	1.230	1.231	1.232	1.232	1.232

Fig. S-17 Optimized geometry of the anion of **4** in the gas phase and selected bond lengths optimized in the gas phase as well as in different organic solvents. Optimization was conducted at the B3LYP/6-31++G(d,p) level and the PCM method was used to account for solvent effects.

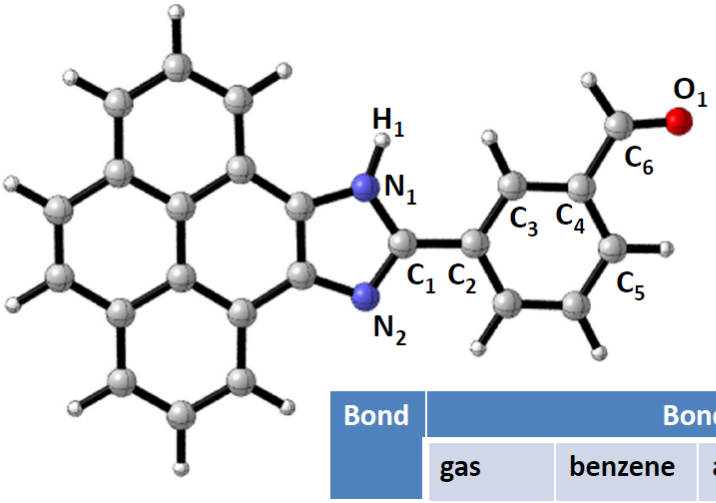

Bond	Bond length (Å)				
	gas	benzene	acetone	DMSO	MeOH
H_1-N_1	1.008	1.009	1.010	1.010	1.010
N_1-C_1	1.381	1.380	1.377	1.376	1.377
C_1-N_2	1.324	1.325	1.328	1.328	1.328
C_1-C_2	1.466	1.466	1.467	1.467	1.467
C_2-C_3	1.403	1.403	1.403	1.403	1.403
C_3-C_4	1.400	1.401	1.402	1.402	1.402
C_4-C_5	1.403	1.404	1.405	1.405	1.405
C_5-C_6	1.481	1.479	1.477	1.472	1.477
C_6-O_1	1.218	1.221	1.224	1.227	1.225

Fig. S-18 Optimized geometry of compound **5** in the gas phase and selected bond lengths optimized in the gas phase as well as in different organic solvents. Optimization was conducted at the B3LYP/6-31++G(d,p) level and the PCM method was used to account for solvent effects.

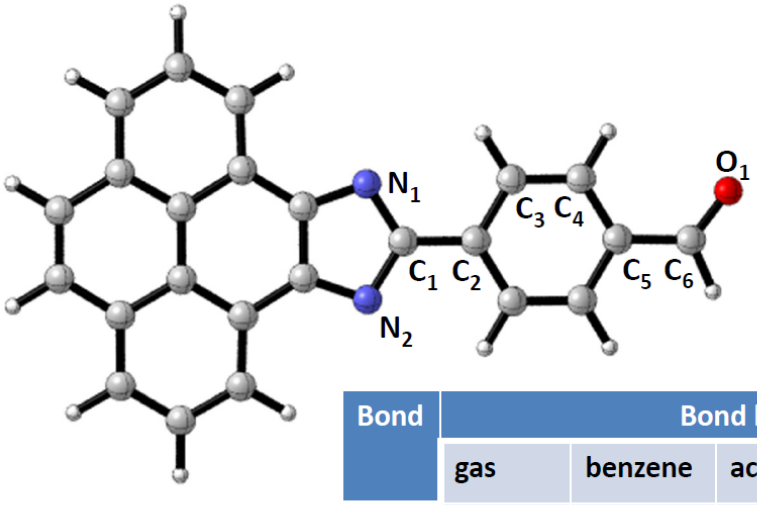

Bond	Bond length (Å)				
	gas	benzene	acetone	DMSO	MeOH
N_1-C_1	1.363	1.363	1.362	1.362	1.362
C_1-N_2	1.363	1.362	1.362	1.362	1.362
C_1-C_2	1.456	1.458	1.461	1.461	1.461
C_2-C_3	1.418	1.418	1.417	1.417	1.417
C_3-C_4	1.384	1.385	1.385	1.385	1.385
C_4-C_5	1.412	1.412	1.411	1.411	1.411
C_5-C_6	1.459	1.459	1.461	1.462	1.461
C_6-O_1	1.230	1.231	1.232	1.232	1.232

Fig. S-19 Optimized geometry of the anion of **5** in the gas phase and selected bond lengths optimized in the gas phase as well as in different organic solvents. Optimization was conducted at the B3LYP/6-31++G(d,p) level and the PCM method was used to account for solvent effects.

5.2 Summary of UV-Vis Absorption Data Obtained from TD-DFT Calculations

Table S-2 Calculated UV-Vis absorption properties for compound **4** in the gas phase and various solvents at the TD-B3LYP/6-31++G(d,p) level

Medium	**λ_{max} (nm)[a]**	***f*[b]**	**MO composition**
Gas	442	0.430	H → L (98.5%)
Benzene	458	0.582	H → L (99.2%)
Acetone	458	0.561	H → L (99.2%)
DMSO	460	0.576	H → L (99.2%)
MeOH	458	0.554	H → L (99.2%)

[a]Maximum absorption wavelength; [b]Oscillator strength

Table S-3 Calculated UV-Vis absorption properties for compound **5** in the gas phase and various solvents at the TD-B3LYP/6-31++G(d,p) level

Medium	**λ_{max} (nm)[a]**	***f*[b]**	**MO composition**
Gas	434	0.073	H → L (98.6%)
Benzene	441	0.105	H → L (99.1%)
Acetone	440	0.096	H → L (99.1%)
DMSO	440	0.100	H → L (99.1%)
MeOH	440	0.094	H → L (99.1%)

[a]Maximum absorption wavelength; [b]Oscillator strength

Table S-4 Calculated UV-Vis absorption properties for the 1:1 complex of **4** and fluoride anion in the gas phase and various solvents at the TD-B3LYP/6-31++G(d,p) level

Medium	**λ_{max} (nm)[a]**	***f*[b]**	**MO composition**
Gas	466	0.728	H → L (99.0%)
Benzene	481	0.854	H → L (99.3%)
Acetone	465	0.679	H → L (99.3%)
DMSO	466	0.685	H → L (99.3%)
MeOH	464	0.664	H → L (99.3%)

[a]Maximum absorption wavelength; [b]Oscillator strength

Table S-5 Calculated UV-Vis absorption properties for 1:1 complex of **5** and fluoride anion in the gas phase and various solvents at the TD-B3LYP/6-31++G(d,p) level

Medium	**λ_{max} (nm)[a]**	***f*[b]**	**MO composition**
Gas	498	0.079	H → L (98.6%)
Benzene	479	0.116	H → L (99.2%)
Acetone	459	0.101	H → L (99.1%)
DMSO	458	0.103	H → L (99.1%)
MeOH	458	0.098	H → L (99.1%)

[a]Maximum absorption wavelength; [b]Oscillator strength

Table S-6 Calculated UV-Vis absorption properties for the anion of **4** in the gas phase and various solvents at the TD-B3LYP/6-31++G(d,p) level

Medium	**λ_{max} (nm)[a]**	***f*[b]**	**MO composition**
Gas	481	0.835	H → L (99.0%)
Benzene	503	0.995	H → L (99.4%)
Acetone	489	0.875	H → L (99.3%)
DMSO	490	0.883	H → L (99.4%)
MeOH	488	0.860	H → L (99.4%)

[a]Maximum absorption wavelength; [b]Oscillator strength

Table S-7 Calculated UV-Vis absorption properties for anion of **5** in the gas phase and various solvents at the TD-B3LYP/6-31++G(d,p) level

Medium	**λ_{max} (nm)[a]**	***f*[b]**	**MO composition**
Gas	576	0.069	H → L (99.1%)
Benzene	557	0.095	H → L (99.4%)
Acetone	524	0.084	H → L (99.3%)
DMSO	521	0.087	H → L (99.3%)
MeOH	521	0.083	H → L (99.3%)

[a]Maximum absorption wavelength; [b]Oscillator strength

5.3 Summary of QTAIM Analysis

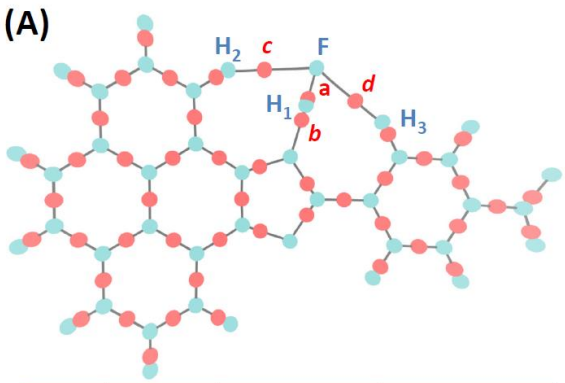

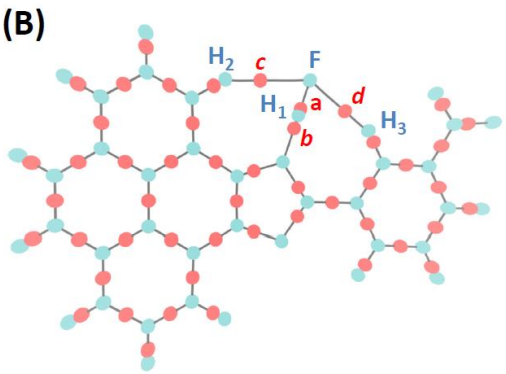

CP	Type	ρ(BCP)	$\nabla^2\rho$(BCP)
a	(3,-1)	0.240	-0.879
b	(3,-1)	0.106	-0.006
c	(3,-1)	0.011	0.041
d	(3,-1)	0.013	0.046

CP	Type	ρ(BCP)	$\nabla^2\rho$(BCP)
a	(3,-1)	0.229	-0.757
b	(3,-1)	0.115	-0.056
c	(3,-1)	0.014	0.050
d	(3,-1)	0.010	0.038

Fig. S-20 Molecular graphs of the 1:1 complexes of (A) **4** and fluoride anion, and (B) **5** and fluoride anion calculated at the B3LYP/6-31++G(d,p) level of theory in the gas phase. The electron density ρ(BCP) and the Laplacian of ρ(BCP) at the highlighted bond critical points are listed.

Table S-7 Results of QTAIM analysis showing the highlighted bond critical points in the 1:1 complexes of **4** and fluoride anion in different organic solvents (B3LYP/6-31++G(d,p) level)

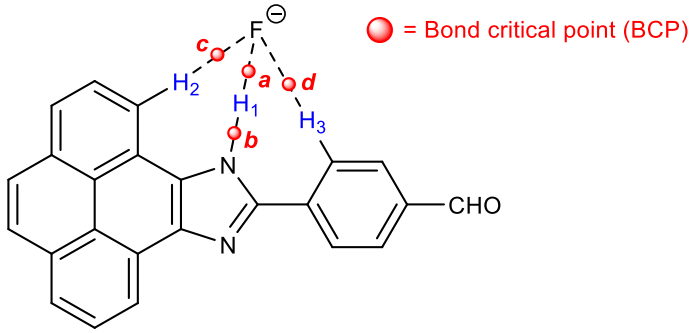

BCP	Solvents							
	Benzene		Acetone		DMSO		MeOH	
	ρ(BCP)	∇^2ρ(BCP)	ρ(BCP)	∇^2ρ(BCP)	ρ(BCP)	∇^2ρ(BCP)	ρ(BCP)	∇^2ρ(BCP)
a	0.199	-0.503	0.096	0.177	0.093	0.184	0.094	0.183
b	0.142	-0.239	0.251	-0.119	0.255	-0.122	0.254	-0.122
c	0.011	0.041	0.016	0.051	0.011	0.039	0.011	0.039
d	0.014	0.049	0.011	0.039	0.016	0.051	0.016	0.051

Table S-8 Results of QTAIM analysis showing the highlighted bond critical points in the 1:1 complexes of **4** and fluoride anion in different organic solvents (B3LYP/6-31++G(d,p) level)

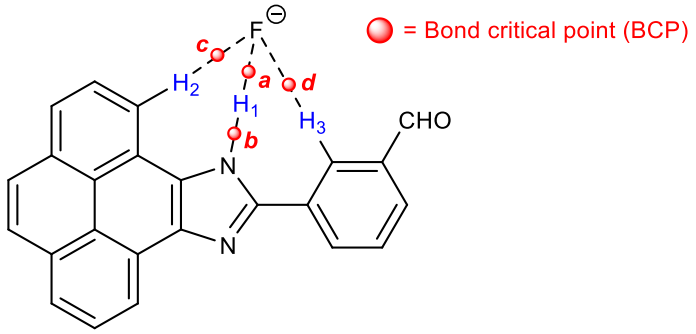

BCP	Solvents							
	Benzene		Acetone		DMSO		MeOH	
	ρ(BCP)	∇^2ρ(BCP)	ρ(BCP)	∇^2ρ(BCP)	ρ(BCP)	∇^2ρ(BCP)	ρ(BCP)	∇^2ρ(BCP)
a	0.155	-0.165	0.092	0.188	0.089	0.192	0.090	0.190
b	0.186	-0.622	0.257	-0.124	0.260	-0.126	0.259	-0.126
c	0.011	0.040	0.010	0.037	0.010	0.037	0.010	0.037
d	0.016	0.052	0.017	0.053	0.017	0.053	0.017	0.053

5.4 Cartesian Coordinates and Energies of Compounds 4/5 and Related Structures

Compound 4 (*in vacuo*)

#N B3LYP/6-31++G(d,p) OPT FREQ

0 1

C	-5.41294400	-0.67493600	-0.00000800
C	-5.41666500	0.68711700	-0.00001600
C	-4.18929400	1.43684200	-0.00001500
C	-2.94741900	0.73036500	-0.00000700
C	-2.94324400	-0.70901600	0.00000100
C	-4.18312300	-1.41982000	0.00000000
C	-4.17197600	-2.82755000	0.00000900
C	-2.97089900	-3.53226200	0.00001700
C	-1.74989800	-2.85246300	0.00001700
C	-1.72071800	-1.45346800	0.00001000
C	-0.49994900	-0.69063200	0.00000900
C	-0.52566100	0.70292000	0.00000300
C	-1.72583600	1.48283500	-0.00000500
C	-1.76685100	2.88435200	-0.00001200
C	-2.99081300	3.55786300	-0.00002100
C	-4.18644600	2.84525300	-0.00002300
H	-5.13550500	3.37419600	-0.00002900
H	-3.00691600	4.64358100	-0.00002600
H	-0.84352600	3.45754400	-0.00001100
N	0.79873500	1.08163600	0.00000900
C	1.56030800	-0.07141300	0.00001500
N	0.79219300	-1.15167000	0.00001200
C	3.02237900	-0.08253100	0.00002000
C	3.69271000	-1.32069600	-0.00004800
C	5.08193100	-1.36400000	-0.00005000
C	5.83696500	-0.18006800	0.00001700
C	5.17254900	1.05771300	0.00008500
C	3.78512400	1.10467600	0.00008900
H	3.29945900	2.07640900	0.00015300
H	5.76307100	1.96835000	0.00013800
C	7.31339400	-0.24782700	0.00001900
O	8.05565800	0.72021100	-0.00007300
H	7.73327400	-1.27653600	-0.00021100
H	5.59186300	-2.32455300	-0.00010400
H	3.10322100	-2.23037400	-0.00010100
H	1.14702600	2.02721700	-0.00001900
H	-0.81066500	-3.39551100	0.00002400
H	-2.98192900	-4.61825000	0.00002300
H	-5.11834500	-3.36171000	0.00000800
H	-6.35508100	1.23505300	-0.00002300
H	-6.34944700	-1.22640700	-0.00000900

E(RB3LYP) = --1107.843984 Hartree; Dipole moment = 3.688745 Debye

Compound 4 (*in benzene*)

#N B3LYP/6-31++G(d,p) OPT FREQ SCRF=(PCM,Solvent=Benzene)

0 1

C	-5.41489400	-0.67254400	0.00001500
C	-5.41701300	0.68985400	0.00000100
C	-4.18839300	1.43830000	-0.00001300
C	-2.94672600	0.73086900	-0.00001300
C	-2.94408800	-0.70889000	0.00000200
C	-4.18514400	-1.41846500	0.00001600
C	-4.17625400	-2.82664500	0.00003100
C	-2.97575000	-3.53295500	0.00003300
C	-1.75360200	-2.85435000	0.00001900
C	-1.72184900	-1.45478500	0.00000400
C	-0.50033800	-0.69225100	-0.00000800
C	-0.52405500	0.70178000	-0.00001800
C	-1.72452300	1.48260500	-0.00002400
C	-1.76401500	2.88436700	-0.00003500
C	-2.98806100	3.55859900	-0.00003700
C	-4.18476600	2.84701000	-0.00002600
H	-5.13326400	3.37678200	-0.00002700
H	-3.00315800	4.64423700	-0.00004700
H	-0.84057500	3.45638300	-0.00004300
N	0.79946500	1.07960900	-0.00001300
C	1.56055900	-0.07180400	-0.00000600
N	0.79195700	-1.15365200	-0.00000800
C	3.02313800	-0.08310700	0.00001100
C	3.69538700	-1.32072400	-0.00010400
C	5.08458900	-1.36320000	-0.00008700
C	5.83778100	-0.17731600	0.00005300
C	5.17105400	1.06009700	0.00016100
C	3.78364900	1.10607400	0.00014500
H	3.29745000	2.07680100	0.00025300
H	5.75611200	1.97392200	0.00026700
C	7.31130800	-0.25021200	0.00009400
O	8.06111100	0.71621500	-0.00010700
H	7.72751700	-1.27853300	-0.00037700
H	5.59503400	-2.32309300	-0.00017700
H	3.11069800	-2.23334200	-0.00020700
H	1.14795600	2.02600200	-0.00004600
H	-0.81671500	-3.40158600	0.00002100
H	-2.98794800	-4.61887200	0.00004600
H	-5.12313300	-3.35966800	0.00004300
H	-6.35485600	1.23861700	0.00000000
H	-6.35191700	-1.22292700	0.00002600

E(RB3LYP) = -1107.850933Hartree; Dipole moment = 4.217157 Debye

Compound 4 (*in acetone*)

#N B3LYP/6-31++G(d,p) OPT FREQ SCRF=(PCM,Solvent=Acetone)

0 1

C	-5.41695300	-0.67157700	0.00005200
C	-5.41782000	0.69107500	0.00002400
C	-4.18829300	1.43873100	-0.00001100
C	-2.94634000	0.73118200	-0.00001600
C	-2.94496500	-0.70899100	0.00001400
C	-4.18691200	-1.41790900	0.00004800
C	-4.17995200	-2.82658900	0.00007800
C	-2.97977900	-3.53389800	0.00007500

C	-1.75683200	-2.85584100	0.00004300
C	-1.72260200	-1.45576200	0.00001300
C	-0.50070300	-0.69306400	-0.00001600
C	-0.52253100	0.70145800	-0.00004100
C	-1.72380800	1.48282000	-0.00004700
C	-1.76263800	2.88472600	-0.00007400
C	-2.98730200	3.55852300	-0.00007000
C	-4.18476500	2.84762900	-0.00003800
H	-5.13312500	3.37757500	-0.00003400
H	-3.00165300	4.64411200	-0.00009000
H	-0.84007800	3.45710400	-0.00009600
N	0.79971800	1.07833200	-0.00005100
C	1.56108100	-0.06981600	-0.00003000
N	0.79215700	-1.15437100	-0.00001400
C	3.02446300	-0.08109000	-0.00001700
C	3.69760200	-1.31854000	-0.00022400
C	5.08662900	-1.36237300	-0.00022300
C	5.83942900	-0.17543200	-0.00001100
C	5.17133000	1.06199700	0.00020600
C	3.78399800	1.10918400	0.00020700
H	3.29984100	2.08023700	0.00041000
H	5.75118600	1.97903700	0.00038000
C	7.30983300	-0.25470600	-0.00001600
O	8.06697300	0.71041000	0.00014000
H	7.72225900	-1.28254800	-0.00022500
H	5.59616600	-2.32234600	-0.00039100
H	3.11714300	-2.23367100	-0.00039400
H	1.14779600	2.02579700	-0.00011400
H	-0.82233700	-3.40738300	0.00004200
H	-2.99261800	-4.61979000	0.00009900
H	-5.12726900	-3.35866100	0.00010400
H	-6.35513000	1.24062600	0.00002800
H	-6.35412900	-1.22151200	0.00007800

E(RB3LYP) = -1107.859831 Hartree; Dipole moment = 4.844379 Debye

Compound 4 (*in DMSO*)

#N B3LYP/6-31++G(d,p) OPT FREQ SCRF=(PCM,Solvent=DMSO)

0 1

C	-5.41721100	-0.67143600	0.00004500
C	-5.41792500	0.69125400	0.00001800
C	-4.18828800	1.43881800	-0.00001300
C	-2.94630200	0.73123600	-0.00001600
C	-2.94507600	-0.70898300	0.00001300
C	-4.18714000	-1.41782900	0.00004300
C	-4.18041200	-2.82657200	0.00007200
C	-2.98027400	-3.53401200	0.00007100
C	-1.75723100	-2.85601200	0.00004300
C	-1.72269700	-1.45586900	0.00001400
C	-0.50073400	-0.69319000	-0.00001200
C	-0.52237200	0.70138200	-0.00003700
C	-1.72371400	1.48283800	-0.00004400
C	-1.76245400	2.88476800	-0.00007100
C	-2.98718400	3.55854000	-0.00006800
C	-4.18475600	2.84774300	-0.00004000

H	-5.13310000	3.37770200	-0.00003700
H	-3.00142500	4.64411900	-0.00008800
H	-0.84000100	3.45719300	-0.00009100
N	0.79972500	1.07815600	-0.00004500
C	1.56112600	-0.06964600	-0.00002300
N	0.79220300	-1.15452300	-0.00000800
C	3.02460700	-0.08087300	-0.00000900
C	3.69783900	-1.31830800	-0.00021300
C	5.08685900	-1.36233000	-0.00021500
C	5.83962900	-0.17529400	-0.00001100
C	5.17139800	1.06216000	0.00020400
C	3.78406000	1.10950100	0.00020900
H	3.30020200	2.08061400	0.00041000
H	5.75072100	1.97953900	0.00037400
C	7.30980400	-0.25514800	-0.00002500
O	8.06758400	0.70987500	0.00012000
H	7.72193600	-1.28291300	-0.00022600
H	5.59624300	-2.32233900	-0.00037900
H	3.11778600	-2.23367700	-0.00037700
H	1.14770500	2.02574100	-0.00010800
H	-0.82300100	-3.40800400	0.00004400
H	-2.99320000	-4.61989500	0.00009400
H	-5.12778800	-3.35851400	0.00009600
H	-6.35515700	1.24091500	0.00002100
H	-6.35439500	-1.22132500	0.00006900

E(RB3LYP) = -1107.860704 Hartree; Dipole moment = 4.907951 Debye

Compound 4 (*in methanol*)

#N B3LYP/6-31++G(d,p) OPT FREQ SCRF=(PCM,Solvent=Methanol)

0 1

C	-5.41712100	-0.67148700	0.00004800
C	-5.41788900	0.69119000	0.00002000
C	-4.18829100	1.43878600	-0.00001200
C	-2.94631500	0.73121700	-0.00001600
C	-2.94503700	-0.70898700	0.00001300
C	-4.18706000	-1.41785800	0.00004500
C	-4.18025000	-2.82657900	0.00007400
C	-2.98009900	-3.53397300	0.00007300
C	-1.75709000	-2.85595300	0.00004300
C	-1.72266300	-1.45583200	0.00001300
C	-0.50072300	-0.69314500	-0.00001400
C	-0.52242700	0.70141000	-0.00003800
C	-1.72374700	1.48283300	-0.00004500
C	-1.76252000	2.88475400	-0.00007200
C	-2.98722800	3.55853400	-0.00006900
C	-4.18476100	2.84770300	-0.00003900
H	-5.13311100	3.37765700	-0.00003600
H	-3.00150800	4.64411700	-0.00008900
H	-0.84003000	3.45716300	-0.00009300
N	0.79972300	1.07821800	-0.00004800
C	1.56111000	-0.06970300	-0.00002500
N	0.79218600	-1.15446900	-0.00001000
C	3.02455700	-0.08094800	-0.00001200
C	3.69775700	-1.31838800	-0.00021800

C	5.08677900	-1.36234400	-0.00021800
C	5.83955900	-0.17534000	-0.00001100
C	5.17137400	1.06210500	0.00020500
C	3.78403800	1.10939300	0.00020800
H	3.30007500	2.08048400	0.00041100
H	5.75088100	1.97936600	0.00037700
C	7.30981200	-0.25499600	-0.00002200
O	8.06737400	0.71005700	0.00012800
H	7.72204200	-1.28278900	-0.00022500
H	5.59621700	-2.32233900	-0.00038400
H	3.11756400	-2.23367500	-0.00038400
H	1.14773800	2.02576200	-0.00011100
H	-0.82276800	-3.40779000	0.00004300
H	-2.99299500	-4.61985900	0.00009600
H	-5.12760500	-3.35856700	0.00009900
H	-6.35514900	1.24081100	0.00002300
H	-6.35430200	-1.22139200	0.00007300

E(RB3LYP) = -1107.860403 Hartree; Dipole moment = 4.885954 Debye

Compound 5 (*in vacuo*)

#N B3LYP/6-31++G(d,p) OPT FREQ

0 1

C	-5.37979100	-0.34532700	-0.00004000
C	-5.25814900	1.01118100	-0.00000700
C	-3.96707200	1.64494500	0.00002000
C	-2.79552100	0.82713100	0.00001200
C	-2.92387800	-0.60615000	-0.00002200
C	-4.22384600	-1.20022700	-0.00004900
C	-4.34215300	-2.60280800	-0.00008300
C	-3.21069300	-3.41471800	-0.00009000
C	-1.93256000	-2.85006500	-0.00006400
C	-1.77479400	-1.45958400	-0.00003000
C	-0.48973600	-0.81214400	-0.00000200
C	-0.38661900	0.57589000	0.00002700
C	-1.50933700	1.46348400	0.00003700
C	-1.42179000	2.86288600	0.00007000
C	-2.57857800	3.64601900	0.00007800
C	-3.83491100	3.04688800	0.00005300
H	-4.73134000	3.66086900	0.00005900
H	-2.49451600	4.72869000	0.00010300
H	-0.44973200	3.34913300	0.00008800
N	0.96947100	0.83078900	0.00004100
C	1.61942600	-0.38796900	0.00002800
N	0.75626900	-1.39147200	-0.00000100
C	3.07721200	-0.53938000	0.00004300
C	3.62690000	-1.83520700	0.00018100
C	5.00957600	-2.02605100	0.00020300
C	5.87439900	-0.93309400	0.00008900
C	5.34187700	0.36538700	-0.00005300
C	3.95447800	0.55551100	-0.00007700
H	3.57835500	1.57647300	-0.00020400
C	6.23052200	1.55055600	-0.00018400
O	7.44754800	1.50962200	-0.00016500
H	5.70247000	2.52937200	-0.00029200

H	6.95215300	-1.05888700	0.00010500
H	5.40928100	-3.03559400	0.00031100
H	2.94871400	-2.68136200	0.00027000
H	1.40182700	1.74101400	0.00009600
H	-1.04709400	-3.47706900	-0.00007100
H	-3.32132400	-4.49518900	-0.00011700
H	-5.33370700	-3.04757900	-0.00010300
H	-6.14225300	1.64312700	-0.00000100
H	-6.36318100	-0.80811600	-0.00006000

E(RB3LYP) = -1107.842472 Hartree; Dipole moment = 3.082464 Debye

Compound 5 (*in benzene*)

#N B3LYP/6-31++G(d,p) OPT FREQ SCRF=(PCM,Solvent=Benzene)

0 1

C	-5.38134900	-0.34154000	-0.00004300
C	-5.25765200	1.01507800	-0.00001000
C	-3.96528200	1.64697100	0.00001900
C	-2.79444200	0.82766200	0.00001300
C	-2.92482000	-0.60560900	-0.00002200
C	-4.22596900	-1.19791000	-0.00005000
C	-4.34703500	-2.60064700	-0.00008500
C	-3.21644800	-3.41424800	-0.00009200
C	-1.93721900	-2.85114300	-0.00006400
C	-1.77626000	-1.46054500	-0.00002800
C	-0.49019400	-0.81414100	0.00000200
C	-0.38467200	0.57394200	0.00003200
C	-1.50743200	1.46247100	0.00004100
C	-1.41788500	2.86179000	0.00007400
C	-2.57407800	3.64634500	0.00008000
C	-3.83168500	3.04904100	0.00005300
H	-4.72726900	3.66416100	0.00005800
H	-2.48834300	4.72884400	0.00010600
H	-0.44530900	3.34558200	0.00009400
N	0.97083300	0.82778900	0.00005000
C	1.62008000	-0.38942700	0.00003000
N	0.75596500	-1.39432600	0.00000500
C	3.07855700	-0.54149700	0.00004200
C	3.62968800	-1.83690100	0.00018900
C	5.01265900	-2.02796400	0.00020600
C	5.87635600	-0.93437800	0.00007900
C	5.34247300	0.36414900	-0.00007100
C	3.95443000	0.55463800	-0.00009100
H	3.57796100	1.57481500	-0.00022300
C	6.22494100	1.55119600	-0.00021700
O	7.44519200	1.51549000	-0.00013900
H	5.69560600	2.52702500	-0.00027200
H	6.95358600	-1.06316700	0.00009200
H	5.41257600	-3.03720400	0.00032100
H	2.95535700	-2.68597100	0.00029000
H	1.40405000	1.73859000	0.00010400
H	-1.05426500	-3.48164800	-0.00007000
H	-3.32837200	-4.49456000	-0.00011900
H	-5.33923700	-3.04384000	-0.00010600
H	-6.14080900	1.64827100	-0.00000500

H	-6.36522100	-0.80306900	-0.00006500

E(RB3LYP) = -1107.849354 Hartree; Dipole moment = 3.517528 Debye

Compound 5 (*in acetone*)

#N B3LYP/6-31++G(d,p) OPT FREQ SCRF=(PCM,Solvent=Acetone)

0 1

C	-5.38348100	-0.33490400	-0.00004000
C	-5.25624500	1.02177300	0.00000400
C	-3.96183800	1.65064200	0.00004100
C	-2.79226800	0.82883000	0.00002900
C	-2.92625500	-0.60459000	-0.00001700
C	-4.22928000	-1.19389200	-0.00005200
C	-4.35487100	-2.59681900	-0.00009600
C	-3.22601100	-3.41341600	-0.00010700
C	-1.94492400	-2.85312700	-0.00007400
C	-1.77885900	-1.46240600	-0.00003000
C	-0.49135600	-0.81789000	0.00000200
C	-0.38199400	0.57022800	0.00004000
C	-1.50388500	1.46116300	0.00006100
C	-1.41035300	2.86049200	0.00010700
C	-2.56569100	3.64703900	0.00012000
C	-3.82532400	3.05274700	0.00008700
H	-4.71933500	3.66999300	0.00009700
H	-2.47731800	4.72922300	0.00015500
H	-0.43676700	3.34121000	0.00013200
N	0.97236000	0.82196400	0.00005200
C	1.62076600	-0.39250800	0.00001500
N	0.75495800	-1.39945900	-0.00000600
C	3.08012100	-0.54534200	0.00000700
C	3.63355000	-1.83973100	0.00029200
C	5.01716200	-2.02996100	0.00029500
C	5.87851900	-0.93485500	0.00001600
C	5.34218300	0.36339300	-0.00028100
C	3.95340200	0.55315900	-0.00027900
H	3.57549100	1.57178300	-0.00053600
C	6.21747900	1.55306400	-0.00062500
O	7.44154500	1.52090500	0.00024000
H	5.68804900	2.52594200	0.00004500
H	6.95531600	-1.06650400	0.00001300
H	5.41828500	-3.03848100	0.00052000
H	2.96468900	-2.69299500	0.00051800
H	1.40544600	1.73393100	0.00012300
H	-1.06601000	-3.48947700	-0.00008400
H	-3.34037100	-4.49341600	-0.00014200
H	-5.34819600	-3.03716500	-0.00012200
H	-6.13790700	1.65691000	0.00001300
H	-6.36823300	-0.79425800	-0.00006700

E(RB3LYP) = -1107.858425 Hartree; Dipole moment = 4.219250 Debye

Compound 5 (*in DMSO*)

#N B3LYP/6-31++G(d,p) OPT FREQ SCRF=(PCM,Solvent=DMSO)

0 1

C	-5.38369200	-0.33412300	-0.00004400
C	-5.25604300	1.02255400	0.00000700
C	-3.96141000	1.65107900	0.00004800
C	-2.79198400	0.82898500	0.00003500
C	-2.92640000	-0.60446400	-0.00001800
C	-4.22963800	-1.19341600	-0.00005700
C	-4.35574700	-2.59636000	-0.00010800
C	-3.22710700	-3.41331900	-0.00012000
C	-1.94580200	-2.85338000	-0.00008200
C	-1.77916000	-1.46264400	-0.00003200
C	-0.49151500	-0.81834500	0.00000400
C	-0.38172100	0.56977500	0.00004700
C	-1.50344400	1.46104900	0.00007100
C	-1.40942100	2.86039500	0.00012300
C	-2.56468100	3.64713700	0.00013800
C	-3.82453600	3.05317800	0.00010100
H	-4.71836100	3.67067600	0.00011200
H	-2.47602700	4.72928300	0.00017900
H	-0.43572000	3.34086000	0.00015100
N	0.97249300	0.82124300	0.00005900
C	1.62082600	-0.39291300	0.00001600
N	0.75481400	-1.40006800	-0.00000600
C	3.08026100	-0.54582400	0.00000600
C	3.63395400	-1.84008000	0.00033000
C	5.01764400	-2.03014400	0.00033200
C	5.87870500	-0.93483700	0.00001200
C	5.34207700	0.36336100	-0.00032900
C	3.95322900	0.55296200	-0.00032300
H	3.57505700	1.57137600	-0.00061700
C	6.21669700	1.55332000	-0.00072600
O	7.44111700	1.52138200	0.00028500
H	5.68730200	2.52594100	0.00007300
H	6.95547100	-1.06671300	0.00000600
H	5.41896200	-3.03856600	0.00058900
H	2.96565900	-2.69378100	0.00059100
H	1.40545500	1.73335900	0.00013700
H	-1.06736400	-3.49043400	-0.00009300
H	-3.34177300	-4.49328000	-0.00015900
H	-5.34920400	-3.03636400	-0.00013700
H	-6.13753700	1.65790900	0.00001600
H	-6.36854600	-0.79323000	-0.00007500

E(RB3LYP) = -1107.859330 Hartree; Dipole moment = 4.302797 Debye

Compound 5 (*in methanol*)

#N B3LYP/6-31++G(d,p) OPT FREQ SCRF=(PCM,Solvent=Methanol)

0 1

C	-5.38361900	-0.33439600	-0.00004200
C	-5.25611500	1.02228100	0.00000600
C	-3.96156100	1.65092500	0.00004600
C	-2.79208400	0.82893100	0.00003200
C	-2.92635000	-0.60450900	-0.00001800
C	-4.22951300	-1.19358300	-0.00005500
C	-4.35544100	-2.59652100	-0.00010300
C	-3.22672400	-3.41335300	-0.00011500

C	-1.94549500	-2.85329100	-0.00007900
C	-1.77905500	-1.46256000	-0.00003100
C	-0.49145900	-0.81818500	0.00000300
C	-0.38181600	0.56993400	0.00004400
C	-1.50359900	1.46108800	0.00006700
C	-1.40974800	2.86042800	0.00011700
C	-2.56503600	3.64710200	0.00013100
C	-3.82481300	3.05302700	0.00009600
H	-4.71870300	3.67043700	0.00010700
H	-2.47647900	4.72926200	0.00017000
H	-0.43608800	3.34097900	0.00014300
N	0.97244700	0.82149700	0.00005600
C	1.62080600	-0.39276900	0.00001600
N	0.75486500	-1.39985400	-0.00000600
C	3.08021300	-0.54565400	0.00000600
C	3.63381400	-1.83995700	0.00031600
C	5.01747600	-2.03008100	0.00031800
C	5.87864100	-0.93484500	0.00001300
C	5.34211500	0.36337100	-0.00031200
C	3.95329100	0.55303200	-0.00030700
H	3.57521300	1.57152000	-0.00058700
C	6.21696900	1.55323000	-0.00068900
O	7.44126700	1.52121700	0.00027000
H	5.68756200	2.52593900	0.00006400
H	6.95541800	-1.06664400	0.00000800
H	5.41872400	-3.03853800	0.00056300
H	2.96532200	-2.69350600	0.00056300
H	1.40545500	1.73356000	0.00013100
H	-1.06689100	-3.49009900	-0.00009000
H	-3.34128300	-4.49332800	-0.00015200
H	-5.34885300	-3.03664500	-0.00013200
H	-6.13766700	1.65755900	0.00001500
H	-6.36843800	-0.79359000	-0.00007200

E(RB3LYP) = -1107.859017 Hartree; Dipole moment = 4.273671 Debye

Complex of 4 with fluoride (*in vacuo*)

#N B3LYP/6-31++G(d,p) OPT FREQ

-1 1

C	5.49246500	-0.74697400	-0.00007300
C	5.46895000	0.61556100	-0.00011200
C	4.22905700	1.34459700	-0.00009900
C	2.99881200	0.61638100	-0.00004800
C	3.02457900	-0.82420400	-0.00000500
C	4.27647200	-1.51504600	-0.00001700
C	4.29439400	-2.92383700	0.00002400
C	3.10343500	-3.64786000	0.00007900
C	1.87161400	-2.98839100	0.00009500
C	1.81007800	-1.58736200	0.00005400
C	0.57487600	-0.85192400	0.00006700
C	0.55300300	0.55811700	0.00002800
C	1.75886100	1.34278100	-0.00003300
C	1.77847700	2.74696700	-0.00006700
C	2.99262100	3.43910600	-0.00012000
C	4.20473600	2.75274200	-0.00013700

H	5.14638700	3.29732300	-0.00017600
H	2.98617400	4.52622100	-0.00014800
H	0.83756300	3.28881200	-0.00005500
N	-0.74982600	0.95642600	0.00008600
C	-1.45844300	-0.21337700	0.00002800
N	-0.69677400	-1.32963700	0.00012200
C	-2.91906400	-0.27537500	-0.00001900
C	-3.55872600	-1.53540000	-0.00000300
C	-4.94286800	-1.62486400	-0.00003300
C	-5.74290400	-0.46519400	-0.00007700
C	-5.10754600	0.79307200	-0.00008800
C	-3.72358300	0.89018400	-0.00005800
H	-3.25181300	1.86711700	-0.00006900
H	-5.72283400	1.68786700	-0.00012200
C	-7.19993000	-0.59882700	-0.00010900
O	-8.01658800	0.31715600	-0.00013600
H	-7.56027600	-1.65337200	-0.00008500
H	-5.42270300	-2.60230500	-0.00002300
H	-2.93799800	-2.42436000	0.00003300
H	-1.19312600	2.31026800	0.00010300
H	0.93975100	-3.54480300	0.00013900
H	3.13212400	-4.73490400	0.00011200
H	5.25194600	-3.43980200	0.00001300
H	6.39809200	1.18164700	-0.00015200
H	6.44012000	-1.28140800	-0.00008200
F	-1.49563400	3.31018800	0.00049800

E(RB3LYP) = -1207.807989 Hartree; Dipole moment = 8.935087 Debye

Complex of 4 with fluoride (*in benzene*)

#N B3LYP/6-31++G(d,p) OPT FREQ SCRF=(PCM,Solvent=Benzene)

-1 1

C	5.49577300	-0.73961200	0.00005900
C	5.47073500	0.62290100	0.00001800
C	4.22911900	1.34955400	-0.00001100
C	2.99961900	0.62013000	0.00000300
C	3.02664700	-0.82069200	0.00005500
C	4.28014900	-1.50878800	0.00007700
C	4.30019800	-2.91769500	0.00011700
C	3.11129900	-3.64441200	0.00013900
C	1.87749300	-2.98733500	0.00012200
C	1.81426800	-1.58652500	0.00007700
C	0.57846300	-0.84943800	0.00006900
C	0.55727400	0.55730000	0.00002700
C	1.76030000	1.34646200	-0.00002100
C	1.77758800	2.75028300	-0.00009100
C	2.99115400	3.44416600	-0.00010900
C	4.20310000	2.75798100	-0.00006400
H	5.14375900	3.30347000	-0.00010300
H	2.98434100	4.53090800	-0.00018900
H	0.83626600	3.29145100	-0.00019900
N	-0.75027800	0.94934300	0.00015000
C	-1.46273400	-0.21936400	0.00002000
N	-0.69560900	-1.32835400	-0.00000400
C	-2.92493500	-0.28044800	-0.00004000

C	-3.56778600	-1.53826600	-0.00017400
C	-4.95297300	-1.62408600	-0.00027800
C	-5.74718600	-0.46118000	-0.00023800
C	-5.10924300	0.79503600	-0.00010800
C	-3.72482600	0.88757100	-0.00002500
H	-3.25117200	1.86371700	0.00006500
H	-5.71983400	1.69275400	-0.00007700
C	-7.20577400	-0.58743900	-0.00034000
O	-8.01073500	0.34055300	-0.00041300
H	-7.57750500	-1.63503900	-0.00051800
H	-5.43436700	-2.60007800	-0.00039800
H	-2.95594400	-2.43316200	-0.00022900
H	-1.17037700	2.19896700	0.00037500
H	0.94956500	-3.55081100	0.00015400
H	3.14224200	-4.73093200	0.00017500
H	5.25816800	-3.43209500	0.00013200
H	6.39861800	1.19016200	-0.00000400
H	6.44366400	-1.27271100	0.00006800
F	-1.50074000	3.25726900	0.00081300

E(RB3LYP) = -1207.843827 Hartree; Dipole moment = 10.646705 Debye

Complex of 4 with fluoride (*in acetone*)

#N B3LYP/6-31++G(d,p) OPT FREQ SCRF=(PCM,Solvent=Acetone)

-1 1

C	5.50728100	-0.70796200	0.00016800
C	5.47161400	0.65449300	0.00014700
C	4.22280600	1.36975800	0.00006100
C	3.00006500	0.62918400	0.00000800
C	3.03727800	-0.81127500	0.00005200
C	4.29754400	-1.48737700	0.00011300
C	4.32948900	-2.89620700	0.00011500
C	3.14787100	-3.63434800	0.00002900
C	1.90742800	-2.98834100	-0.00004300
C	1.83273300	-1.58883100	-0.00000100
C	0.59054700	-0.85911200	-0.00009800
C	0.56822500	0.54106500	-0.00014800
C	1.75723200	1.34664600	-0.00011000
C	1.75610000	2.75014800	-0.00012600
C	2.96393400	3.45519300	-0.00006000
C	4.18162200	2.77835100	0.00002700
H	5.11600100	3.33330600	0.00007600
H	2.95003300	4.54140800	-0.00007900
H	0.80648100	3.27882200	-0.00019700
N	-0.75035100	0.90851900	-0.00017100
C	-1.46987900	-0.25872600	-0.00004500
N	-0.68716900	-1.34736700	-0.00041800
C	-2.93327000	-0.31056200	0.00003400
C	-3.58472900	-1.56139900	-0.00009000
C	-4.97213000	-1.63235900	-0.00006400
C	-5.74952500	-0.45948000	0.00005600
C	-5.10107300	0.79036400	0.00015600
C	-3.71503800	0.86818300	0.00014300
H	-3.22669100	1.83918300	0.00023200
H	-5.69981700	1.69590800	0.00024700

C	-7.21301200	-0.57005700	0.00007500
O	-7.99815200	0.37543000	0.00017600
H	-7.60200100	-1.60779200	-0.00000100
H	-5.46386000	-2.60210300	-0.00014500
H	-2.98747800	-2.46591600	-0.00019700
H	-1.13049500	1.95489000	-0.00000700
H	0.98786000	-3.56485700	-0.00012200
H	3.18887400	-4.71988700	0.00001300
H	5.29111300	-3.40248500	0.00015600
H	6.39455200	1.22854700	0.00018300
H	6.45900900	-1.23284900	0.00022000
F	-1.55937700	3.25424800	-0.00000800

E(RB3LYP) = -1207.876877 Hartree; Dipole moment = 14.323719 Debye

Complex of 4 with fluoride (*in DMSO*)

#N B3LYP/6-31++G(d,p) OPT FREQ SCRF=(PCM,Solvent=DMSO)

-1 1

C	5.50802500	-0.70692400	-0.00052300
C	5.47197800	0.65555700	-0.00053100
C	4.22286000	1.37036400	-0.00026300
C	3.00025100	0.62939600	-0.00005800
C	3.03789700	-0.81108600	-0.00005000
C	4.29844400	-1.48663900	-0.00025400
C	4.33099900	-2.89550400	-0.00017300
C	3.14967700	-3.63414000	0.00011300
C	1.90890800	-2.98860200	0.00029700
C	1.83359500	-1.58909400	0.00019400
C	0.59113700	-0.85960000	0.00030900
C	0.56878100	0.54022700	0.00028300
C	1.75728300	1.34643500	0.00022600
C	1.75560500	2.74994500	0.00040900
C	2.96321100	3.45553900	0.00020500
C	4.18113700	2.77906000	-0.00016200
H	5.11526400	3.33431200	-0.00037300
H	2.94916000	4.54172400	0.00030500
H	0.80576900	3.27815000	0.00070500
N	-0.75038600	0.90698700	0.00034300
C	-1.47027000	-0.26029600	0.00019900
N	-0.68686300	-1.34811800	0.00025600
C	-2.93379200	-0.31202100	0.00011900
C	-3.58547300	-1.56255300	0.00022700
C	-4.97301900	-1.63340100	0.00011000
C	-5.74993000	-0.46027400	-0.00014200
C	-5.10129900	0.78940800	-0.00023800
C	-3.71518600	0.86694000	-0.00010200
H	-3.22675700	1.83790200	-0.00014100
H	-5.69961200	1.69523900	-0.00043900
C	-7.21369800	-0.57020300	-0.00027000
O	-7.99756200	0.37651000	-0.00058900
H	-7.60389400	-1.60718400	-0.00019100
H	-5.46487200	-2.60299400	0.00021300
H	-2.98897500	-2.46747100	0.00041000
H	-1.12936900	1.94804400	0.00029500
H	0.98980700	-3.56584900	0.00052200

H	3.19110400	-4.71960600	0.00019300
H	5.29281500	-3.40127800	-0.00031400
H	6.39471700	1.22978200	-0.00073000
H	6.45982300	-1.23157100	-0.00070600
F	-1.56294100	3.25904700	0.00013500

E(RB3LYP) = -1207.879644 Hartree; Dipole moment = 14.592891 Debye

Complex of 4 with fluoride (*in methanol*)

#N B3LYP/6-31++G(d,p) OPT FREQ SCRF=(PCM,Solvent=Methanol)

-1 1

C	-5.50781300	-0.70738700	-0.00012400
C	-5.47196700	0.65506100	-0.00009300
C	-4.22297900	1.37012400	0.00003500
C	-3.00041400	0.62930700	0.00007600
C	-3.03777900	-0.81110000	0.00002400
C	-4.29819700	-1.48703200	-0.00004700
C	-4.33022100	-2.89585900	-0.00001900
C	-3.14873000	-3.63420600	0.00008800
C	-1.90817900	-2.98832600	0.00013000
C	-1.83345300	-1.58890600	0.00005800
C	-0.59117000	-0.85928000	0.00007000
C	-0.56878500	0.54069400	0.00011200
C	-1.75744500	1.34664400	0.00021200
C	-1.75601200	2.75008400	0.00036500
C	-2.96374000	3.45540600	0.00033400
C	-4.18152100	2.77869800	0.00014500
H	-5.11573100	3.33390000	0.00005900
H	-2.94972700	4.54161000	0.00043100
H	-0.80637700	3.27878600	0.00051300
N	0.75012800	0.90737400	-0.00011700
C	1.47005100	-0.25987500	0.00006600
N	0.68677200	-1.34776100	-0.00006200
C	2.93354100	-0.31145600	0.00009400
C	3.58510600	-1.56218900	0.00014400
C	4.97254600	-1.63279000	0.00011500
C	5.74964300	-0.45977400	0.00002000
C	5.10100800	0.79000500	-0.00004400
C	3.71496300	0.86748900	-0.00000600
H	3.22628100	1.83839900	-0.00003300
H	5.69949500	1.69573200	-0.00013300
C	7.21323300	-0.57041500	0.00001200
O	7.99815500	0.37527900	-0.00054700
H	7.60219900	-1.60802800	-0.00034900
H	5.46447700	-2.60240200	0.00017500
H	2.98817700	-2.46693100	0.00021300
H	1.12970800	1.94935200	-0.00029400
H	-0.98872600	-3.56496900	0.00022200
H	-3.18994400	-4.71972000	0.00013200
H	-5.29181900	-3.40216800	-0.00005500
H	-6.39480800	1.22925900	-0.00016200
H	-6.45963700	-1.23205900	-0.00020700
F	1.56364200	3.25780100	-0.00061100

E(RB3LYP) = -1207.878713 Hartree; Dipole moment = 14.519479 Debye

Complex of 5 with fluoride (*in vauo*)

#N B3LYP/6-31++G(d,p) OPT FREQ

-1 1

C	-5.48113600	-0.33518600	-0.00030400
C	-5.31222300	1.01709400	-0.00034600
C	-4.00143000	1.60957400	-0.00022900
C	-2.85669100	0.75285400	-0.00008200
C	-3.03580500	-0.67581100	-0.00003300
C	-4.35439900	-1.22929800	-0.00014100
C	-4.52311800	-2.62773500	-0.00008900
C	-3.41559600	-3.47468500	0.00007600
C	-2.12058700	-2.95103500	0.00019400
C	-1.90842300	-1.56396900	0.00013800
C	-0.60309900	-0.96467700	0.00025300
C	-0.43299400	0.43166200	0.00021900
C	-1.54536200	1.34112900	0.00004700
C	-1.41342200	2.73986600	0.00003500
C	-2.54574500	3.55831100	-0.00012500
C	-3.82552700	3.00660400	-0.00025900
H	-4.70287400	3.64973000	-0.00037600
H	-2.42264100	4.63853200	-0.00013900
H	-0.41902200	3.17609900	0.00015100
N	0.90865500	0.68864500	0.00045200
C	1.48699700	-0.54805800	0.00016300
N	0.61556800	-1.57577600	0.00044900
C	2.94110700	-0.76044100	-0.00000700
C	3.45433900	-2.07163500	-0.00006200
C	4.83204100	-2.31207300	-0.00018300
C	5.73542400	-1.25223800	-0.00024300
C	5.23954600	0.06383500	-0.00016500
C	3.85833100	0.30695900	-0.00004300
H	3.49745700	1.33251800	0.00002300
C	6.15534500	1.22026800	-0.00020400
O	7.37867500	1.15706300	-0.00049500
H	5.64953600	2.20819400	-0.00031100
H	6.80879500	-1.41376400	-0.00033700
H	5.19527200	-3.33689500	-0.00023100
H	2.74668300	-2.89389400	-0.00001200
H	1.49739500	1.95226100	0.00067600
H	-1.25369600	-3.60421100	0.00032900
H	-3.56013300	-4.55255100	0.00012100
H	-5.53040600	-3.03821200	-0.00017400
H	-6.17563700	1.67919600	-0.00046300
H	-6.48056500	-0.76524400	-0.00038800
F	1.94282600	2.91486300	0.00079200

E(RB3LYP) = -1207.806120 Hartree; Dipole moment = 7.703836 Debye

Complex of 5 with fluoride (*in benzene*)

#N B3LYP/6-31++G(d,p) OPT FREQ SCRF=(PCM,Solvent=Benzene)

-1 1

C	5.48235900	-0.32419500	-0.00001700
C	5.31000600	1.02784300	-0.00003600

C	3.99686000	1.61601600	-0.00005800
C	2.85507800	0.75576300	-0.00005300
C	3.03703900	-0.67259900	-0.00002800
C	4.35759100	-1.22143800	-0.00001800
C	4.52948100	-2.61973100	-0.00001000
C	3.42533100	-3.47051600	-0.00003200
C	2.12820500	-2.95018500	-0.00005300
C	1.91348200	-1.56455400	-0.00003400
C	0.60575200	-0.96648800	-0.00006500
C	0.43878600	0.42522800	-0.00006700
C	1.54429900	1.34169400	-0.00008100
C	1.40335200	2.73856500	-0.00009500
C	2.53330100	3.56132600	-0.00010000
C	3.81445400	3.01270900	-0.00008300
H	4.68872500	3.65924900	-0.00008700
H	2.40746600	4.64076900	-0.00011900
H	0.40463300	3.16638000	-0.00011400
N	-0.90750100	0.67006700	0.00001700
C	-1.49427800	-0.56462900	0.00002200
N	-0.61588500	-1.58086600	-0.00026000
C	-2.94991800	-0.76833700	0.00009200
C	-3.47204700	-2.07566400	0.00018600
C	-4.85160200	-2.30446100	0.00020500
C	-5.74369100	-1.23519200	0.00013400
C	-5.23779000	0.07682600	0.00004900
C	-3.85469200	0.30896400	0.00002200
H	-3.48268700	1.33168200	-0.00000100
C	-6.14419400	1.24056600	-0.00001600
O	-7.36870800	1.18134100	-0.00002300
H	-5.63596100	2.22543400	-0.00009500
H	-6.81780200	-1.39012200	0.00013900
H	-5.22439800	-3.32509400	0.00028600
H	-2.77663200	-2.90806500	0.00023700
H	-1.42915600	1.77377400	0.00021200
H	1.26456400	-3.60729100	-0.00007000
H	3.57304700	-4.54737900	-0.00003200
H	5.53726100	-3.02783100	0.00000200
H	6.17159600	1.69146300	-0.00004100
H	6.48261300	-0.75108000	-0.00000300
F	-1.92365300	2.86532400	0.00026600

E(RB3LYP) = -1207.842361 Hartree; Dipole moment = 9.990887 Debye

Complex of 5 with fluoride (*in acetone*)

#N B3LYP/6-31++G(d,p) OPT FREQ SCRF=(PCM,Solvent=Acetone)

-1 1

C	-5.48815600	-0.31111900	0.00010500
C	-5.31182900	1.04045900	-0.00000400
C	-3.99571300	1.62311500	-0.00007700
C	-2.85663100	0.75905200	-0.00004800
C	-3.04226100	-0.66920700	0.00008300
C	-4.36563500	-1.21187900	0.00015600
C	-4.54297700	-2.60964000	0.00027200
C	-3.44329900	-3.46570600	0.00030000
C	-2.14301800	-2.95122600	0.00022300

C	-1.92345300	-1.56662300	0.00013000
C	-0.61324600	-0.96946000	0.00002700
C	-0.44812000	0.41814800	-0.00006300
C	-1.54566000	1.34264400	-0.00014200
C	-1.39806700	2.73852900	-0.00023000
C	-2.52556400	3.56565200	-0.00025100
C	-3.80782700	3.01959300	-0.00017400
H	-4.67910700	3.66916100	-0.00016300
H	-2.39859900	4.64454500	-0.00028800
H	-0.39793000	3.16377100	-0.00030700
N	0.90414600	0.64781900	0.00004300
C	1.49868600	-0.58589500	-0.00013100
N	0.61122700	-1.58775900	-0.00007600
C	2.95487000	-0.78436500	-0.00022300
C	3.48170900	-2.08964700	-0.00059600
C	4.86219200	-2.31088600	-0.00061700
C	5.74699800	-1.23527700	-0.00024000
C	5.23531800	0.07450400	0.00014200
C	3.85075200	0.29925800	0.00014700
H	3.47185900	1.32057100	0.00044800
C	6.13313700	1.24469600	0.00056200
O	7.35854400	1.19286500	0.00056000
H	5.62091300	2.22640200	0.00098900
H	6.82093400	-1.38997900	-0.00022400
H	5.24121000	-3.32839500	-0.00090900
H	2.79555800	-2.92947400	-0.00088900
H	1.39192900	1.63952700	0.00002600
H	-1.28716600	-3.61863500	0.00023900
H	-3.59598100	-4.54127000	0.00038900
H	-5.55175200	-3.01377200	0.00031400
H	-6.17068700	1.70661800	-0.00003700
H	-6.48919200	-0.73458900	0.00015600
F	1.98653600	2.89265000	-0.00001000

E(RB3LYP) = -1207.875527 Hartree; Dipole moment = 13.274936 Debye

Complex of 5 with fluoride (*in DMSO*)

#N B3LYP/6-31++G(d,p) OPT FREQ SCRF=(PCM,Solvent=DMSO)

-1 1

C	-5.48853600	-0.31175400	-0.00013900
C	-5.31249100	1.03987500	-0.00010200
C	-3.99639600	1.62264600	-0.00001800
C	-2.85701700	0.75893500	0.00002300
C	-3.04237900	-0.66939700	-0.00006500
C	-4.36573600	-1.21216800	-0.00011500
C	-4.54289500	-2.61000300	-0.00014000
C	-3.44318800	-3.46594900	-0.00008000
C	-2.14283000	-2.95135600	-0.00002200
C	-1.92352000	-1.56676000	-0.00005600
C	-0.61346900	-0.96891900	0.00004900
C	-0.44867000	0.41844900	0.00014500
C	-1.54617200	1.34302600	0.00014800
C	-1.39926900	2.73894400	0.00016400
C	-2.52703500	3.56583900	0.00010600
C	-3.80903700	3.01928100	0.00002700

H	-4.68050000	3.66850900	-0.00000400
H	-2.40054700	4.64475700	0.00014000
H	-0.39953300	3.16505900	0.00026200
N	0.90411100	0.64764100	-0.00001400
C	1.49911200	-0.58605100	0.00003000
N	0.61130100	-1.58722000	0.00054300
C	2.95531000	-0.78473600	-0.00003300
C	3.48192800	-2.09019100	0.00007100
C	4.86231800	-2.31161000	0.00008500
C	5.74734600	-1.23609300	0.00001500
C	5.23601000	0.07376800	-0.00008300
C	3.85134700	0.29854900	-0.00011400
H	3.47286700	1.31995300	-0.00025000
C	6.13327600	1.24422300	-0.00016200
O	7.35875300	1.19316700	-0.00014800
H	5.62069000	2.22572300	-0.00033100
H	6.82111800	-1.39180300	0.00004000
H	5.24121500	-3.32909500	0.00015800
H	2.79611600	-2.93026400	0.00014400
H	1.39058000	1.63564600	-0.00028400
H	-1.28753700	-3.61950500	0.00002600
H	-3.59572000	-4.54148400	-0.00008200
H	-5.55157500	-3.01423800	-0.00017700
H	-6.17138300	1.70589700	-0.00011700
H	-6.48941500	-0.73544500	-0.00018500
F	1.98974100	2.89741300	-0.00002900

E(RB3LYP) = -1207.878250 Hartree; Dipole moment = 13.530224 Debye

Complex of 5 with fluoride (*in methanol*)

#N B3LYP/6-31++G(d,p) OPT FREQ SCRF=(PCM,Solvent=Methanol)

-1 1

C	5.48843200	-0.31156900	0.00040900
C	5.31232900	1.04004100	0.00032300
C	3.99624800	1.62283200	0.00010100
C	2.85693800	0.75897900	0.00000300
C	3.04236000	-0.66932300	0.00009400
C	4.36572400	-1.21211300	0.00028300
C	4.54293000	-2.60989600	0.00033100
C	3.44320900	-3.46590000	0.00018600
C	2.14293200	-2.95132700	0.00000800
C	1.92352600	-1.56667500	-0.00002000
C	0.61340600	-0.96912600	-0.00017500
C	0.44851100	0.41838300	-0.00024200
C	1.54608100	1.34289000	-0.00020000
C	1.39892700	2.73884900	-0.00034600
C	2.52659000	3.56578700	-0.00025800
C	3.80869600	3.01937700	-0.00002900
H	4.68006900	3.66875600	0.00005100
H	2.40001900	4.64470700	-0.00038300
H	0.39904200	3.16461800	-0.00053500
N	-0.90405600	0.64772200	-0.00017400
C	-1.49899700	-0.58596800	-0.00020900
N	-0.61125300	-1.58734600	-0.00023000
C	-2.95517400	-0.78456100	-0.00019300

C	-3.48188400	-2.08994000	-0.00059300
C	-4.86231000	-2.31134100	-0.00053700
C	-5.74722800	-1.23579400	-0.00008500
C	-5.23573400	0.07405300	0.00027600
C	-3.85115700	0.29888300	0.00021500
H	-3.47251700	1.32024200	0.00041900
C	-6.13335500	1.24434100	0.00074100
O	-7.35879200	1.19283900	0.00093100
H	-5.62104800	2.22598600	0.00089500
H	-6.82107800	-1.39098000	-0.00001200
H	-5.24120300	-3.32884700	-0.00086600
H	-2.79592000	-2.92990000	-0.00095400
H	-1.39100300	1.63693700	-0.00035300
H	1.28735000	-3.61910800	-0.00010400
H	3.59582600	-4.54143800	0.00021300
H	5.55162900	-3.01412000	0.00047700
H	6.17125500	1.70604800	0.00041800
H	6.48936600	-0.73517800	0.00057600
F	-1.98892100	2.89573700	-0.00055100

E(RB3LYP) = -1207.877319 Hartree; Dipole moment = 13.443132 Debye

Anion of 4 (*in vacuo*)

#N B3LYP/6-31++G(d,p) OPT FREQ

-1 1

C	5.40637700	-0.59801700	-0.00001700
C	5.37621900	0.76468600	-0.00002700
C	4.13199100	1.48668700	-0.00002800
C	2.90750700	0.74900700	-0.00001700
C	2.93934200	-0.69164700	-0.00000600
C	4.19531200	-1.37443400	-0.00000600
C	4.22402000	-2.78340800	0.00000500
C	3.03699900	-3.51451000	0.00001500
C	1.80090100	-2.86307800	0.00001500
C	1.72637500	-1.46169200	0.00000500
C	0.48623200	-0.73510600	0.00000400
C	0.45478500	0.68396000	-0.00000700
C	1.66172700	1.46468400	-0.00001800
C	1.67421100	2.86799900	-0.00002800
C	2.88030900	3.57343000	-0.00003800
C	4.09845000	2.89549900	-0.00003800
H	5.03620000	3.44684300	-0.00004600
H	2.86754100	4.66097700	-0.00004700
H	0.72217400	3.38941700	-0.00002800
N	-0.83343700	1.10159400	-0.00000300
C	-1.53010800	-0.06985300	0.00000600
N	-0.78244000	-1.20941400	0.00001200
C	-2.98549900	-0.10255500	0.00001200
C	-3.68387000	-1.33202900	0.00002200
C	-5.07064100	-1.35505900	0.00002700
C	-5.81961100	-0.15975800	0.00002300
C	-5.12475600	1.07001300	0.00001300
C	-3.74054500	1.09770800	0.00000800
H	-3.19867400	2.03737500	0.00000000
H	-5.70080300	1.99098000	0.00001000

C	-7.27716800	-0.22448400	0.00002900
O	-8.05363900	0.72898800	0.00002800
H	-7.68649600	-1.26115200	0.00003700
H	-5.59678000	-2.30873300	0.00003500
H	-3.10488900	-2.24908700	0.00002500
H	0.87277400	-3.42594900	0.00002300
H	3.07244000	-4.60158200	0.00002300
H	5.18518400	-3.29285000	0.00000500
H	6.30284100	1.33523000	-0.00003500
H	6.35736900	-1.12689800	-0.00001600

E(RB3LYP) = -1107.320311 Hartree; Dipole moment = 7.354866 Debye

Anion of 4 (*in benzene*)

#N B3LYP/6-31++G(d,p) OPT FREQ SCRF=(PCM,Solvent=Benzene)

-1 1

C	5.40827000	-0.59775800	-0.00002700
C	5.37800400	0.76488500	-0.00003700
C	4.13303100	1.48610800	-0.00003200
C	2.90767100	0.74951500	-0.00001700
C	2.93966200	-0.69179700	-0.00000700
C	4.19646200	-1.37350600	-0.00001200
C	4.22606200	-2.78264400	-0.00000100
C	3.04044800	-3.51530000	0.00001400
C	1.80319400	-2.86485000	0.00002000
C	1.72806800	-1.46329400	0.00001000
C	0.48814000	-0.73375300	0.00001400
C	0.45620400	0.68337200	0.00000200
C	1.66309400	1.46681700	-0.00001200
C	1.67681100	2.87024800	-0.00002100
C	2.88407700	3.57472100	-0.00003500
C	4.10076400	2.89511600	-0.00004100
H	5.03866000	3.44545700	-0.00005200
H	2.87232000	4.66183800	-0.00004200
H	0.72863100	3.39892500	-0.00001600
N	-0.83486100	1.09990700	0.00001200
C	-1.53278000	-0.07066100	0.00001300
N	-0.78269600	-1.20796400	0.00002700
C	-2.98989500	-0.10476900	0.00001600
C	-3.68864900	-1.33381500	0.00003000
C	-5.07591100	-1.35787900	0.00003200
C	-5.82285800	-0.16176700	0.00002100
C	-5.12889500	1.06800800	0.00000900
C	-3.74462200	1.09524200	0.00000700
H	-3.20633400	2.03655000	-0.00000300
H	-5.70252500	1.99022600	0.00000100
C	-7.28056100	-0.22453000	0.00002100
O	-8.04957200	0.73706500	-0.00000500
H	-7.69670600	-1.25545600	0.00001800
H	-5.60065000	-2.31167000	0.00004200
H	-3.11442100	-2.25370100	0.00003800
H	0.87874800	-3.43435900	0.00003300
H	3.07697000	-4.60188500	0.00002300
H	5.18719900	-3.29133300	-0.00000500
H	6.30402000	1.33553900	-0.00004800

H	6.35882600	-1.12650000	-0.00003100

E(RB3LYP) = -1107.355568 Hartree; Dipole moment = 8.272429 Debye

Anion of 4 (*in acetone*)

#N B3LYP/6-31++G(d,p) OPT FREQ SCRF=(PCM,Solvent=Acetone)

-1 1

C	5.41291000	-0.59558600	-0.00002100
C	5.38179400	0.76712500	-0.00003100
C	4.13537600	1.48685100	-0.00003000
C	2.90951800	0.75011600	-0.00001700
C	2.94243800	-0.69158300	-0.00000600
C	4.20070700	-1.37157200	-0.00000800
C	4.23220100	-2.78101200	0.00000200
C	3.04823000	-3.51590300	0.00001500
C	1.80960200	-2.86635400	0.00001700
C	1.73236400	-1.46503700	0.00000700
C	0.49138600	-0.73387600	0.00000800
C	0.45885700	0.68029700	-0.00000300
C	1.66529800	1.46748500	-0.00001600
C	1.67880800	2.87090700	-0.00002500
C	2.88647700	3.57631000	-0.00003700
C	4.10268600	2.89622800	-0.00004000
H	5.03971200	3.44696500	-0.00004900
H	2.87476700	4.66289500	-0.00004500
H	0.73350700	3.40465700	-0.00002300
N	-0.83625400	1.09578200	0.00000300
C	-1.53594200	-0.07327800	0.00000900
N	-0.78331700	-1.20866500	0.00001800
C	-2.99653600	-0.10659900	0.00001400
C	-3.69662000	-1.33400300	0.00002500
C	-5.08495200	-1.35839000	0.00003000
C	-5.82874700	-0.16143700	0.00002400
C	-5.13512900	1.06776600	0.00001300
C	-3.75004700	1.09371700	0.00000800
H	-3.21833500	2.03866100	-0.00000100
H	-5.70264000	1.99352800	0.00000800
C	-7.28851600	-0.22628400	0.00003000
O	-8.05192000	0.74109900	0.00001000
H	-7.70766100	-1.25272100	0.00002500
H	-5.60904600	-2.31158400	0.00004000
H	-3.13012900	-2.25833400	0.00003100
H	0.88922300	-3.44208900	0.00002700
H	3.08626400	-4.60189000	0.00002300
H	5.19337500	-3.28848200	0.00000100
H	6.30706500	1.33791200	-0.00004100
H	6.36327600	-1.12346800	-0.00002300

E(RB3LYP) = -1107.386306 Hartree; Dipole moment = 9.174236 Debye

Anion of 4 (*in DMSO*)

#N B3LYP/6-31++G(d,p) OPT FREQ SCRF=(PCM,Solvent=DMSO)

-1 1

C	5.41331500	-0.59598500	-0.00002000

C	5.38236200	0.76674900	-0.00003100
C	4.13594900	1.48660800	-0.00002900
C	2.90989300	0.75007900	-0.00001700
C	2.94267900	-0.69163400	-0.00000600
C	4.20092700	-1.37177100	-0.00000800
C	4.23223600	-2.78126000	0.00000300
C	3.04821900	-3.51608300	0.00001600
C	1.80964200	-2.86626400	0.00001700
C	1.73259600	-1.46498900	0.00000600
C	0.49164900	-0.73352600	0.00000700
C	0.45920700	0.68032400	-0.00000400
C	1.66577900	1.46764600	-0.00001600
C	1.67955600	2.87105400	-0.00002600
C	2.88739200	3.57635500	-0.00003800
C	4.10346100	2.89603100	-0.00004000
H	5.04048400	3.44666300	-0.00004900
H	2.87588500	4.66289100	-0.00004600
H	0.73460500	3.40538200	-0.00002400
N	-0.83632700	1.09581900	0.00000100
C	-1.53625500	-0.07306200	0.00000900
N	-0.78347500	-1.20832700	0.00001700
C	-2.99722300	-0.10637500	0.00001300
C	-3.69722100	-1.33373600	0.00002400
C	-5.08567800	-1.35836300	0.00002900
C	-5.82932500	-0.16144100	0.00002400
C	-5.13593900	1.06779700	0.00001400
C	-3.75075500	1.09386400	0.00000900
H	-3.21994400	2.03932400	0.00000100
H	-5.70297800	1.99382400	0.00001000
C	-7.28939500	-0.22665300	0.00003100
O	-8.05228500	0.74119500	0.00001400
H	-7.70869000	-1.25273100	0.00002600
H	-5.60958200	-2.31156900	0.00003700
H	-3.13131400	-2.25842100	0.00002700
H	0.88936000	-3.44208200	0.00002700
H	3.08613800	-4.60202100	0.00002400
H	5.19327900	-3.28886000	0.00000200
H	6.30767500	1.33736200	-0.00004000
H	6.36356400	-1.12395700	-0.00002100

E(RB3LYP) = -1107.388847 Hartree; Dipole moment = 9.249219 Debye

Anion of 4 (*in methanol*)

#N B3LYP/6-31++G(d,p) OPT FREQ SCRF=(PCM,Solvent=Methanol)

-1 1

C	5.41317800	-0.59582800	-0.00002100
C	5.38216100	0.76689800	-0.00003100
C	4.13574100	1.48670300	-0.00003000
C	2.90975900	0.75009500	-0.00001700
C	2.94259800	-0.69161400	-0.00000600
C	4.20085800	-1.37169000	-0.00000800
C	4.23224300	-2.78116200	0.00000300
C	3.04824800	-3.51601700	0.00001500
C	1.80964800	-2.86630200	0.00001700
C	1.73252200	-1.46501200	0.00000700

C	0.49156000	-0.73365900	0.00000700
C	0.45908400	0.68030400	-0.00000400
C	1.66560600	1.46758600	-0.00001600
C	1.67928000	2.87100000	-0.00002600
C	2.88705500	3.57634300	-0.00003800
C	4.10317600	2.89611000	-0.00004000
H	5.04019600	3.44678200	-0.00004900
H	2.87547100	4.66289600	-0.00004500
H	0.73420600	3.40512400	-0.00002400
N	-0.83630300	1.09579200	0.00000100
C	-1.53614700	-0.07315100	0.00000900
N	-0.78341800	-1.20845700	0.00001700
C	-2.99698600	-0.10646400	0.00001400
C	-3.69702000	-1.33383600	0.00002400
C	-5.08543400	-1.35837300	0.00002900
C	-5.82912700	-0.16143700	0.00002400
C	-5.13565400	1.06778500	0.00001400
C	-3.75050600	1.09380500	0.00000900
H	-3.21937700	2.03908300	0.00000100
H	-5.70285200	1.99372400	0.00001000
C	-7.28909100	-0.22652100	0.00003000
O	-8.05215800	0.74116800	0.00001200
H	-7.70833600	-1.25272200	0.00002600
H	-5.60940800	-2.31157300	0.00003800
H	-3.13091800	-2.25840200	0.00002800
H	0.88934200	-3.44210800	0.00002700
H	3.08621500	-4.60197200	0.00002400
H	5.19333500	-3.28870900	0.00000200
H	6.30745600	1.33757600	-0.00004100
H	6.36347000	-1.12376300	-0.00002200

E(RB3LYP) = -1107.387977 Hartree; Dipole moment = 9.223541 Debye

Anion of 5 (*in vacuo*)

#N B3LYP/6-31++G(d,p) OPT FREQ

-1 1

C	5.19965200	1.10403900	0.00000200
C	5.36374300	-0.24918000	-0.00000100
C	4.23502500	-1.14116900	-0.00000300
C	2.91804400	-0.58418200	-0.00000200
C	2.74471400	0.84509800	0.00000100
C	3.89045300	1.70056600	0.00000300
C	3.71832600	3.09890800	0.00000700
C	2.43822600	3.65279300	0.00000800
C	1.30787100	2.83221000	0.00000600
C	1.43294000	1.43344800	0.00000200
C	0.31089900	0.53781700	0.00000000
C	0.48126200	-0.86770700	-0.00000100
C	1.78493800	-1.46901100	-0.00000300
C	1.99792000	-2.85719000	-0.00000600
C	3.29163700	-3.38391800	-0.00000800
C	4.40219500	-2.54014700	-0.00000600
H	5.40881900	-2.95261200	-0.00000700
H	3.43326400	-4.46243900	-0.00001000
H	1.12965600	-3.50877500	-0.00000700

N	-0.73966900	-1.46574700	-0.00000400
C	-1.58998400	-0.40609200	0.00000100
N	-1.01752300	0.82642300	0.00000100
C	-3.04486000	-0.58106600	0.00000200
C	-3.90911100	0.52940400	-0.00001300
C	-5.30100400	0.36598800	-0.00001100
C	-5.86621900	-0.92422200	0.00000600
C	-5.01758700	-2.02871300	0.00002100
C	-3.62774400	-1.86327600	0.00001900
H	-2.96430500	-2.72197000	0.00003100
H	-5.43509500	-3.03289600	0.00003600
H	-3.46917000	1.52292000	-0.00002500
H	0.30901100	3.25724600	0.00000700
H	2.31814200	4.73390200	0.00001100
H	4.59697300	3.74035800	0.00000800
H	6.36230300	-0.68184800	-0.00000300
H	6.06583200	1.76286900	0.00000300
C	-6.14940200	1.56869400	-0.00002800
H	-5.58484100	2.52680000	-0.00002500
O	-7.37443900	1.58547700	0.00000300
H	-6.94634200	-1.03065200	0.00000800

E(RB3LYP) = -1107.316640 Hartree; Dipole moment = 5.398537 Debye

Anion of 5 (*in benzene*)

#N B3LYP/6-31++G(d,p) OPT FREQ SCRF=(PCM,Solvent=Benzene)

-1 1

C	5.20411100	1.10053400	-0.00003500
C	5.36678500	-0.25286300	-0.00005900
C	4.23619700	-1.14290600	-0.00004800
C	2.91945600	-0.58486300	-0.00001400
C	2.74723000	0.84475500	0.00001000
C	3.89493900	1.69799800	0.00000000
C	3.72549400	3.09680600	0.00002500
C	2.44699400	3.65333000	0.00005900
C	1.31498200	2.83410400	0.00006700
C	1.43658900	1.43518400	0.00004200
C	0.31319900	0.53832300	0.00004600
C	0.48294300	-0.86490400	0.00002800
C	1.78671300	-1.46880000	-0.00000300
C	1.99785400	-2.85675100	-0.00002500
C	3.29122100	-3.38567400	-0.00006000
C	4.40178400	-2.54230300	-0.00007100
H	5.40749400	-2.95587800	-0.00009800
H	3.43168700	-4.46383000	-0.00007800
H	1.12983100	-3.50823800	-0.00001600
N	-0.74017800	-1.46360100	0.00003900
C	-1.59286900	-0.40550900	0.00004000
N	-1.01818200	0.82616000	0.00006400
C	-3.05028000	-0.58040400	0.00003500
C	-3.91429800	0.52995900	-0.00004300
C	-5.30642600	0.36693300	-0.00004200
C	-5.87174400	-0.92295400	0.00003400
C	-5.02437700	-2.02812100	0.00010700
C	-3.63460200	-1.86217700	0.00010700

H	-2.97786800	-2.72557100	0.00016300
H	-5.44175900	-3.03170000	0.00016500
H	-3.48077900	1.52593100	-0.00010900
H	0.31985300	3.26706700	0.00009300
H	2.32848400	4.73411600	0.00007800
H	4.60476000	3.73665900	0.00001800
H	6.36444000	-0.68646300	-0.00008600
H	6.07074000	1.75796500	-0.00004300
C	-6.15200700	1.57180700	-0.00012600
H	-5.59041600	2.52952300	-0.00018100
O	-7.37824400	1.58581700	-0.00013800
H	-6.95131800	-1.03305100	0.00003400

E(RB3LYP) = -1107.352241 Hartree; Dipole moment = 6.210333 Debye

Anion of 5 (*in acetone*)

#N B3LYP/6-31++G(d,p) OPT FREQ SCRF=(PCM,Solvent=Acetone)

-1 1

C	5.20821000	1.10024400	-0.00001900
C	5.37071400	-0.25321000	-0.00005100
C	4.23904700	-1.14267400	-0.00005100
C	2.92121500	-0.58590100	-0.00002000
C	2.74922800	0.84461200	0.00001200
C	3.89820100	1.69698800	0.00001400
C	3.72956800	3.09628200	0.00004800
C	2.45223000	3.65478900	0.00008000
C	1.31881600	2.83604500	0.00007700
C	1.43984500	1.43694600	0.00004300
C	0.31664300	0.53705300	0.00003700
C	0.48542700	-0.86365400	0.00001100
C	1.78965900	-1.47126800	-0.00002000
C	2.00216800	-2.85924000	-0.00004800
C	3.29693200	-3.38708800	-0.00007900
C	4.40590000	-2.54224600	-0.00008100
H	5.41137100	-2.95500300	-0.00010400
H	3.43859000	-4.46454700	-0.00010100
H	1.14025200	-3.51911000	-0.00004600
N	-0.74184300	-1.46142600	0.00002000
C	-1.59669000	-0.40490400	0.00002900
N	-1.01792700	0.82483600	0.00005800
C	-3.05694100	-0.57934800	0.00003500
C	-3.92003900	0.53129600	-0.00008600
C	-5.31231700	0.36803700	-0.00007300
C	-5.87710100	-0.92149000	0.00005600
C	-5.03132100	-2.02796100	0.00017600
C	-3.64166700	-1.86107700	0.00016700
H	-2.99083700	-2.72872700	0.00026700
H	-5.44890200	-3.03072700	0.00028000
H	-3.49273700	1.52956000	-0.00019200
H	0.32626400	3.27541200	0.00010200
H	2.33518900	4.73520500	0.00010700
H	4.60869200	3.73543900	0.00005000
H	6.36773200	-0.68675400	-0.00007500
H	6.07437400	1.75735400	-0.00001900
C	-6.15733700	1.57433000	-0.00019800

H	-5.60107600	2.53272200	-0.00025100
O	-7.38459600	1.58139200	-0.00011900
H	-6.95610800	-1.03519100	0.00006200

E(RB3LYP) = -1107.383242 Hartree; Dipole moment = 7.267174 Debye

Anion of 5 (*in DMSO*)

#N B3LYP/6-31++G(d,p) OPT FREQ SCRF=(PCM,Solvent=DMSO)

-1 1

C	5.20850300	1.10039400	-0.00001600
C	5.37106500	-0.25305900	-0.00004800
C	4.23935900	-1.14255700	-0.00005300
C	2.92138300	-0.58599100	-0.00002400
C	2.74934200	0.84462300	0.00001100
C	3.89837900	1.69700500	0.00001600
C	3.72971100	3.09634400	0.00005200
C	2.45244400	3.65497200	0.00008300
C	1.31893500	2.83621600	0.00007800
C	1.44004700	1.43709600	0.00004100
C	0.31694100	0.53686700	0.00003400
C	0.48570900	-0.86359700	0.00000500
C	1.78998300	-1.47158100	-0.00002700
C	2.00271000	-2.85958700	-0.00005700
C	3.29766400	-3.38719900	-0.00008600
C	4.40642800	-2.54213900	-0.00008400
H	5.41190100	-2.95474700	-0.00010600
H	3.43954000	-4.46458000	-0.00011000
H	1.14152800	-3.52049600	-0.00005800
N	-0.74197600	-1.46121400	0.00001300
C	-1.59706300	-0.40493500	0.00002700
N	-1.01795000	0.82464900	0.00005800
C	-3.05755700	-0.57932500	0.00004100
C	-3.92053000	0.53135900	-0.00007100
C	-5.31283000	0.36808700	-0.00005200
C	-5.87749100	-0.92146500	0.00007600
C	-5.03188200	-2.02807700	0.00018800
C	-3.64225000	-1.86108800	0.00017400
H	-2.99187700	-2.72907800	0.00027000
H	-5.44944300	-3.03078500	0.00029300
H	-3.49371600	1.52980800	-0.00017500
H	0.32655100	3.27607800	0.00010300
H	2.33550600	4.73535000	0.00011200
H	4.60876200	3.73551300	0.00005700
H	6.36805100	-0.68652600	-0.00007200
H	6.07459600	1.75750800	-0.00001200
C	-6.15779200	1.57453900	-0.00016400
H	-5.60183300	2.53294900	-0.00030600
O	-7.38511100	1.58113400	-0.00017900
H	-6.95644300	-1.03553700	0.00008600

E(RB3LYP) = -1107.385779 Hartree; Dipole moment = 7.371577 Debye

Anion of 5 (*in methanol*)

#N B3LYP/6-31++G(d,p) OPT FREQ SCRF=(PCM,Solvent=Methanol)

-1 1

C	5.20842100	1.10031800	-0.00001000
C	5.37094900	-0.25313700	-0.00003900
C	4.23924500	-1.14260700	-0.00004400
C	2.92131700	-0.58596600	-0.00002000
C	2.74931200	0.84461600	0.00001000
C	3.89834200	1.69698200	0.00001600
C	3.72969800	3.09630700	0.00004800
C	2.45241400	3.65491000	0.00007400
C	1.31892400	2.83617200	0.00006800
C	1.44000000	1.43706000	0.00003600
C	0.31685600	0.53693800	0.00002700
C	0.48560300	-0.86361600	0.00000200
C	1.78985800	-1.47148600	-0.00002300
C	2.00250700	-2.85947300	-0.00004900
C	3.29740200	-3.38716700	-0.00007300
C	4.40623500	-2.54218700	-0.00007100
H	5.41170600	-2.95485100	-0.00008900
H	3.43920000	-4.46457500	-0.00009300
H	1.14109000	-3.52004600	-0.00005000
N	-0.74194000	-1.46130900	0.00000900
C	-1.59692800	-0.40488600	0.00001800
N	-1.01791000	0.82471700	0.00004700
C	-3.05733600	-0.57931500	0.00002700
C	-3.92033700	0.53137900	-0.00008600
C	-5.31262100	0.36811500	-0.00006800
C	-5.87737100	-0.92139000	0.00005800
C	-5.03170400	-2.02797100	0.00017200
C	-3.64206300	-1.86105200	0.00015900
H	-2.99158000	-2.72895800	0.00025600
H	-5.44932800	-3.03067600	0.00027500
H	-3.49331400	1.52974300	-0.00019000
H	0.32648700	3.27586900	0.00008900
H	2.33545900	4.73530400	0.00009900
H	4.60878100	3.73546300	0.00005300
H	6.36794000	-0.68664400	-0.00005800
H	6.07454400	1.75742400	-0.00000700
C	-6.15769300	1.57448300	-0.00018100
H	-5.60182800	2.53295600	-0.00026200
O	-7.38500400	1.58103400	-0.00009800
H	-6.95634100	-1.03530500	0.00006700

E(RB3LYP) = -1107.384911 Hartree; Dipole moment = 7.335302 Debye

Supporting Information

Crystal Engineering and Photophysical Properties of Phenyl-Pyrenoimidazole Systems

*Zahra A. Tabasi, Joshua C. Walsh, Graham J. Bodwell, David W. Thompson, and Yuming Zhao**

Department of Chemistry, Memorial University, St. John's, Newfoundland and Labrador, CANADA A1B 3X7; yuming@mun.ca

Table of Content

1. Synthetic Procedures for Compounds 3a-h S2

2. NMR Spectra of Compounds 3a-e and 3f S6

3. DFT and TD-DFT Computational Results S23

4. UV-Vis Absorption and Fluorescence Data S24

1. Synthetic and Characterization of Compounds 3a-h

The synthesis and spectroscopic characterization of compounds **3f** and **3g** were reported in our previous publication.[1] The synthesis of compounds **3a**, **3e**, and **3h** were previously reported by Karthik *et al*.[2] and their NMR and MS characterization data are consistent with our experimental results.

Compound 3a

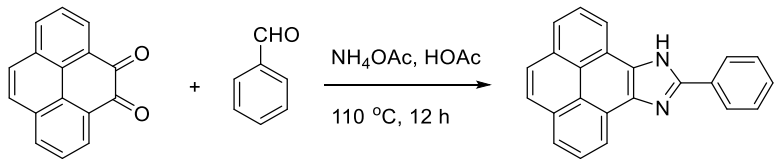

1 **2a** **3a**

Pyrene-4,5-dione (**1**) (0.200 g, 0.861 mmol), benzaldehyde (**2a**) (0.274 g, 2.58 mmol), ammonium acetate (1.33 g, 17.2 mmol), and glacial acetic acid (99.7%, 7 mL) were mixed in a round-bottom flask equipped with a condenser. The reaction was heated at 110 °C for 12 h, and then slowly cooled down to rt. The resulting precipitate was collected by vacuum filtration and the filtrate was sequentially washed with glacial acetic acid, satd $NaHCO_3$ solution (aq), and water to yield crude product **3a**. The crude product was further purified by silica flash column chromatography using ethyl acetate/hexanes (1:4, v/v) as eluent to afford pure compound **3a** (0.170 g, 0.534 mmol, 62% yield) as an off-white solid. ^{1}H NMR (300 MHz, DMSO-d_6): δ 13.75 (s, 1H), 8.85 (d, J = 7.4 Hz, 2H), 8.43–8.38 (m, 2H), 8.27 (dd, J = 7.7, 1.1 Hz, 2H), 8.22–8.13 (m, 4H), 7.66 (t, J = 7.5 Hz, 2H), 7.54 (t, J = 7.3 Hz, 1H); ^{13}C NMR (75 MHz, DMSO-d_6): δ 149.90, 131.99, 130.86, 129.81, 129.48, 128.16 (br), 126.77, 126.69, 124.62, 122.25, 119.47 (two carbon signals missing due to coincidental overlap); FTIR (neat): 3044, 3052, 2920, 2851, 1599, 1552, 1456, 1160, 825, 704, 689 cm^{-1}; HRMS (APPI−TOF, positive mode) *m/z*: calcd for $C_{23}H_{15}N_2$ $[M + H]^+$, 319.1157; found 319.1226; X-ray analysis.

Compound 3b

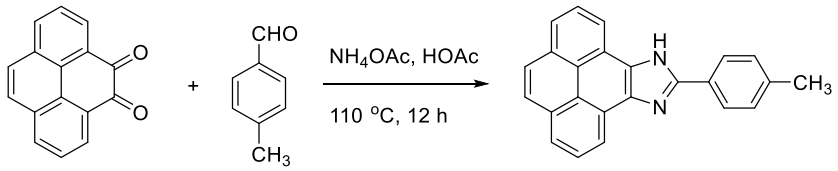

1 **2b** **3b**

[1] Tabasi, Z. A.; Younes, E. A.; Walsh, J. C.; Thompson, D. W.; Bodwell, G. J.; Zhao, Y. *ACS Omega* **2018**, *3*, 16387–6397.
[2] Karthik, S.; Ajantha, J.; Nagaraja, C. M.; Easwaramoorthi, S.; Gandhi, T. *Org. Biomol. Chem*. **2016**, *14*, 10255–10266.

Pyrene-4,5-dione (**1**) (0.200 g, 0.861 mmol), *p*-methylbenzaldehyde (**2b**) (0.310 g, 2.58 mmol), ammonium acetate (1.33 g, 17.2 mmol), and glacial acetic acid (99.7%, 7 mL) were mixed in a round-bottom flask equipped with a condenser. The reaction was heated at 110 °C for 12 h, and then slowly cooled down to rt. The resulting precipitate was collected by vacuum filtration and the filtrate was sequentially washed with glacial acetic acid, satd $NaHCO_3$ solution (aq), and water to yield crude product **3a**. The crude product was further purified by silica flash column chromatography using ethyl acetate/hexanes (2:98, v/v) as eluent to afford pure compound **3b** (0.137 g, 0.413 mmol, 48% yield) as a yellow solid. ^{1}H NMR (300 MHz, DMSO-d_6): δ 13.66 (s, 1H), 8.83 (t, *J* = 6.6 Hz, 2H), 8.36–8.08 (m, 8H), 7.46 (d, *J* = 8.0 Hz, 2H), 2.44 (s, 3H); ^{13}C NMR (75 MHz, DMSO-d_6): δ 150.07, 139.45, 132.07, 131.91, 129.99, 128.35, 128.17, 127.94, 126.84, 126.65, 124.59, 124.48, 122.26, 122.20, 122.13, 120.85, 119.49, 119.35, 21.50 (two carbon signals missing due to coincidental overlap); FTIR (neat): 3605, 3008, 2916, 1662, 1603, 1555, 1432, 1258, 823, 712,691 cm^{-1}; HRMS (APPI−TOF, positive mode) *m/z*: calcd for $C_{24}H_{17}N_2$ $[M + H]^+$, 333.1313; found 333.1379; X-ray analysis.

Compound 3c

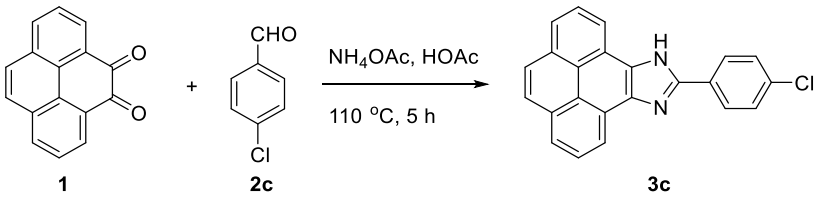

Pyrene-4,5-dione (**1**) (0.200 g, 0.861 mmol), *p*-chlorobenzaldehyde (**2c**) (0.363 g, 2.58 mmol), ammonium acetate (1.33 g, 17.2 mmol), and glacial acetic acid (99.7%, 7 mL) were mixed in a round-bottom flask equipped with a condenser. The reaction was heated at 110 °C for 5 h, and then slowly cooled down to rt. The resulting precipitate was collected by vacuum filtration and the filtrate was sequentially washed with glacial acetic acid, satd $NaHCO_3$ solution (aq), and water to yield crude product **3c**. The crude product was further purified by silica flash column chromatography using ethyl acetate/hexanes (2:98, v/v) as eluent to afford pure compound **3c** (0.173 g, 0.491 mmol, 57% yield) as an off-white solid. ^{1}H NMR (300 MHz, DMSO-d_6): δ 13.82 (s, 1H), 8.82 (d, *J* = 7.3 Hz, 2H), 8.41 (d, *J* = 8.7 Hz, 2H), 8.27 (d, *J* = 7.7 Hz, 2H), 8.22–8.13 (m, 4H), 7.73 (d, *J* = 8.7 Hz, 2H); ^{13}C NMR (75 MHz, DMSO-d_6): δ 148.76, 134.35, 132.00, 129.69, 129.59, 128.33, 126.81, 124.76, 122.30, 119.48 (three carbon signals missing due to coincidental overlap); FTIR (neat): 3627, 3043, 2920, 2851, 1682, 1633, 1551, 1433, 1179, 824, 712, 568 cm^{-1}; HRMS (APPI−TOF, positive mode) *m/z*: calcd for $C_{23}H_{14}N_2{}^{35}Cl$ $[M + H]^+$, 353.0767 found 353.0859; X-ray analysis.

Compound 3d

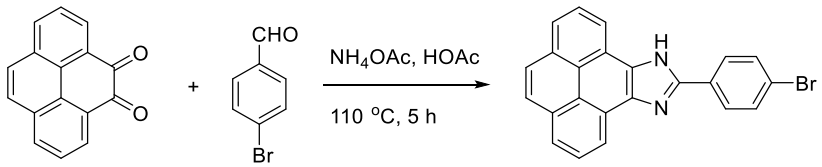

1 **2d** **3d**

Pyrene-4,5-dione (**1**) (0.200 g, 0.861 mmol), *p*-bromobenzaldehyde (**2d**) (0.477 g, 2.58 mmol), ammonium acetate (1.33 g, 17.2 mmol), and glacial acetic acid (99.7%, 7 mL) were mixed in a round-bottom flask equipped with a condenser. The reaction was heated at 110 °C for 5 h, and then slowly cooled down to rt. The resulting precipitate was collected by vacuum filtration and the filtrate was sequentially washed with glacial acetic acid, satd $NaHCO_3$ solution (aq), and water to yield crude product **3d**. The crude product was further purified by silica flash column chromatography using acetone/hexanes (1:99, v/v) as eluent to afford pure compound **3d** (0.150 g, 0.378 mmol, 44% yield) as a light brown solid. ^{1}H NMR (300 MHz, DMSO-d_6): δ 13.83 (s, 1H), 8.82 (m, 2H), 8.34 (d, J = 8.7 Hz, 2H), 8.30–8.24 (m, 2H), 8.23–8.11 (m, 4H), 7.86 (d, J = 8.7 Hz, 2H); ^{13}C NMR (75 MHz, DMSO-d_6): δ 148.81, 138.04, 132.49, 132.07, 131.91, 130.04, 128.87, 128.56, 128.36, 127.93, 126.90, 126.73, 126.47, 124.86, 124.67, 123.08, 122.34, 122.27, 122.10, 119.52, 119.46; FTIR (neat): 3484, 3042, 2919, 2849, 1703, 1630, 1529, 1430, 1259, 1007, 711, 684, 562 cm^{-1}; HRMS (APPI−TOF, positive mode) *m/z*: calcd for $C_{23}H_{13}N_2{}^{79}Br$ [M + H]$^+$, 397.0262 found 397.0407; X-ray analysis.

Compound 3e

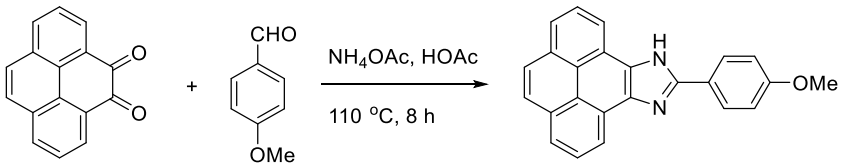

1 **2e** **3e**

Pyrene-4,5-dione (**1**) (0.200 g, 0.861 mmol), *p*-methoxybenzaldehyde (**2e**) (0.351g, 2.58 mmol), ammonium acetate (1.33 g, 17.2 mmol), and glacial acetic acid (99.7%, 7 mL) were mixed in a round-bottom flask equipped with a condenser. The reaction was heated at 110 °C for 8 h, and then slowly cooled down to rt. The resulting precipitate was collected by vacuum filtration and the filtrate was sequentially washed with glacial acetic acid, satd $NaHCO_3$ solution (aq), and water to yield crude product **3e**. The crude product was further purified by silica flash column chromatography using acetone/hexanes (5:95, v/v) as eluent to afford pure compound **3e** (0.138g, 0.396 mmol, 46% yield) as a brown solid. ^{1}H NMR (300 MHz, DMSO-d_6): δ 13.58 (s, 1H), 8.82 (dd, J = 9.9, 7.7 Hz, 2H), 8.34 (d, J = 8.9 Hz, 2H), 8.27–8.11 (m, 6H), 7.22 (d, J = 8.9 Hz, 2H), 3.89 (s, 3H); ^{13}C NMR (75 MHz, DMSO-d_6): δ 160.74, 150.07, 137.91, 132.13, 132.07, 131.91, 128.34, 128.26, 127.93, 126.80, 126.65, 126.59, 124.42, 119.47, 119.38, 119.24, 118.90, 55.84; FTIR (neat): 3308, 3000, 2957, 2851, 1697, 1604, 1517, 1356, 1176, 824, 713,702 cm^{-1};

HRMS (APPI−TOF, positive mode) *m/z*: calcd for $C_{24}H_{17}N_2O$ $[M + H]^+$, 349.1263 found 349.1340; X-ray analysis.

Compound 3h

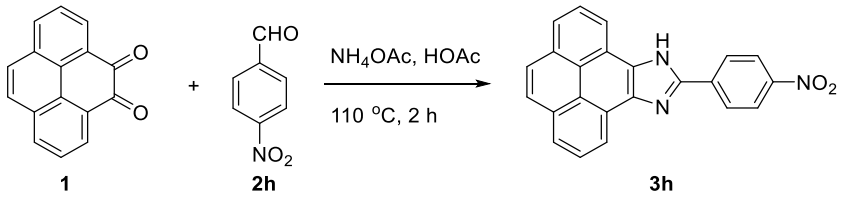

1 **2h** **3h**

Pyrene-4,5-dione (**1**) (0.200 g, 0.861 mmol), *p*-nitrobenzaldehyde (**2h**) (0.390 g, 2.58 mmol), ammonium acetate (1.33 g, 17.2 mmol), and glacial acetic acid (99.7%, 7 mL) were mixed in a round-bottom flask equipped with a condenser. The reaction was heated at 110 °C for 8 h, and then slowly cooled down to rt. The resulting precipitate was collected by vacuum filtration and the filtrate was sequentially washed with glacial acetic acid, satd $NaHCO_3$ solution (aq), and water to yield crude product **3h**. The crude product was further purified by silica flash column chromatography using acetone/hexanes (5:95, v/v) as eluent to afford pure compound **3h** (0.266 g, 0.732 mmol, 85% yield) as an orange colored solid. ^{1}H NMR (300 MHz, DMSO-d_6): δ 14.13 (s, 1H), 8.84 (d, J = 6.8 Hz, 2H), 8.62 (d, J = 9.0 Hz, 2H), 8.49 (d, J = 9.0 Hz, 2H), 8.29 (d, J = 6.7 Hz, 2H), 8.22–8.14 (m, 4H); ^{13}C NMR (75 MHz, DMSO-d_6): δ 147.72, 147.66, 136.68, 132.02, 128.15, 127.35, 126.90, 125.18, 124.90, 122.54, 119.72 (two carbon signals missing due to coincidental overlap); FTIR (neat): 2920, 2851, 1595, 1486, 1343, 852, 709 cm^{-1}; HRMS (APPI−TOF, positive mode) *m/z*: calcd for $C_{23}H_{13}N_3O_2$ $[M + H]^+$, 364.1008 found 364.1080; X-ray analysis.

2. NMR Spectra of Compounds 3a-h

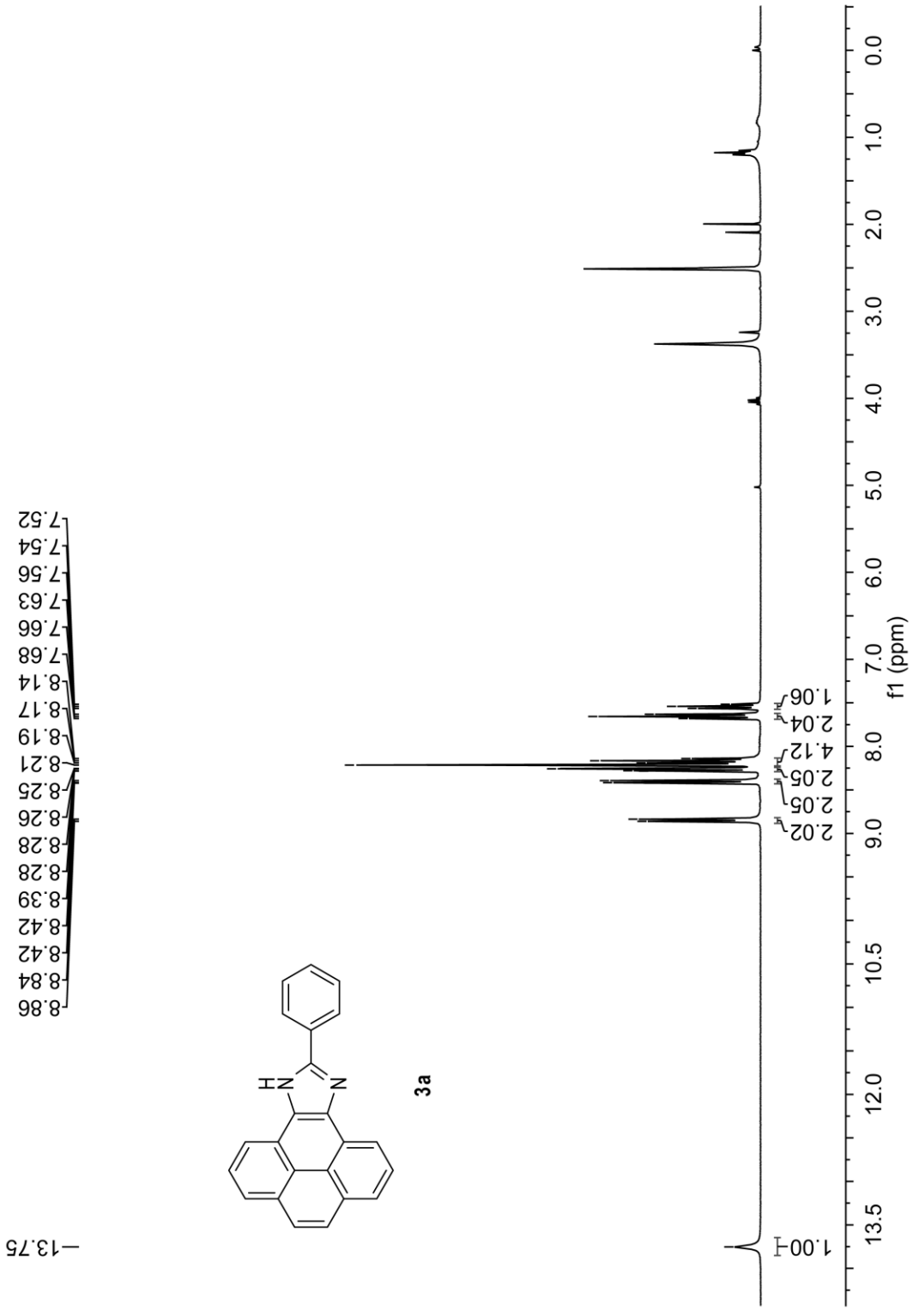

Fig. S-1 ^{1}H NMR (300 MHz, DMSO-d_6) spectrum of compound **3a**.

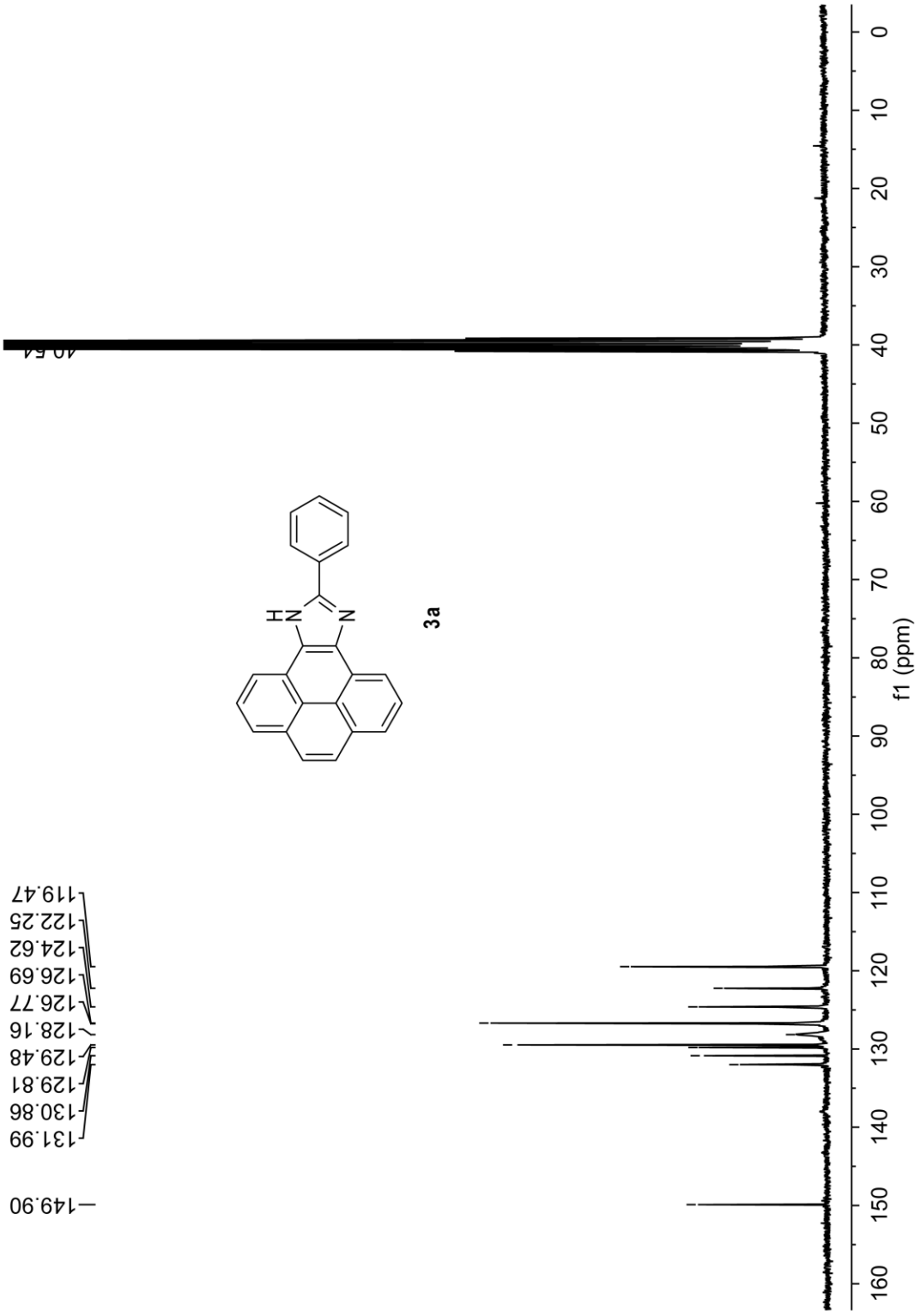

Fig. S-2 ^{13}C NMR (75 MHz, DMSO-d_6) spectrum of compound **3a**.

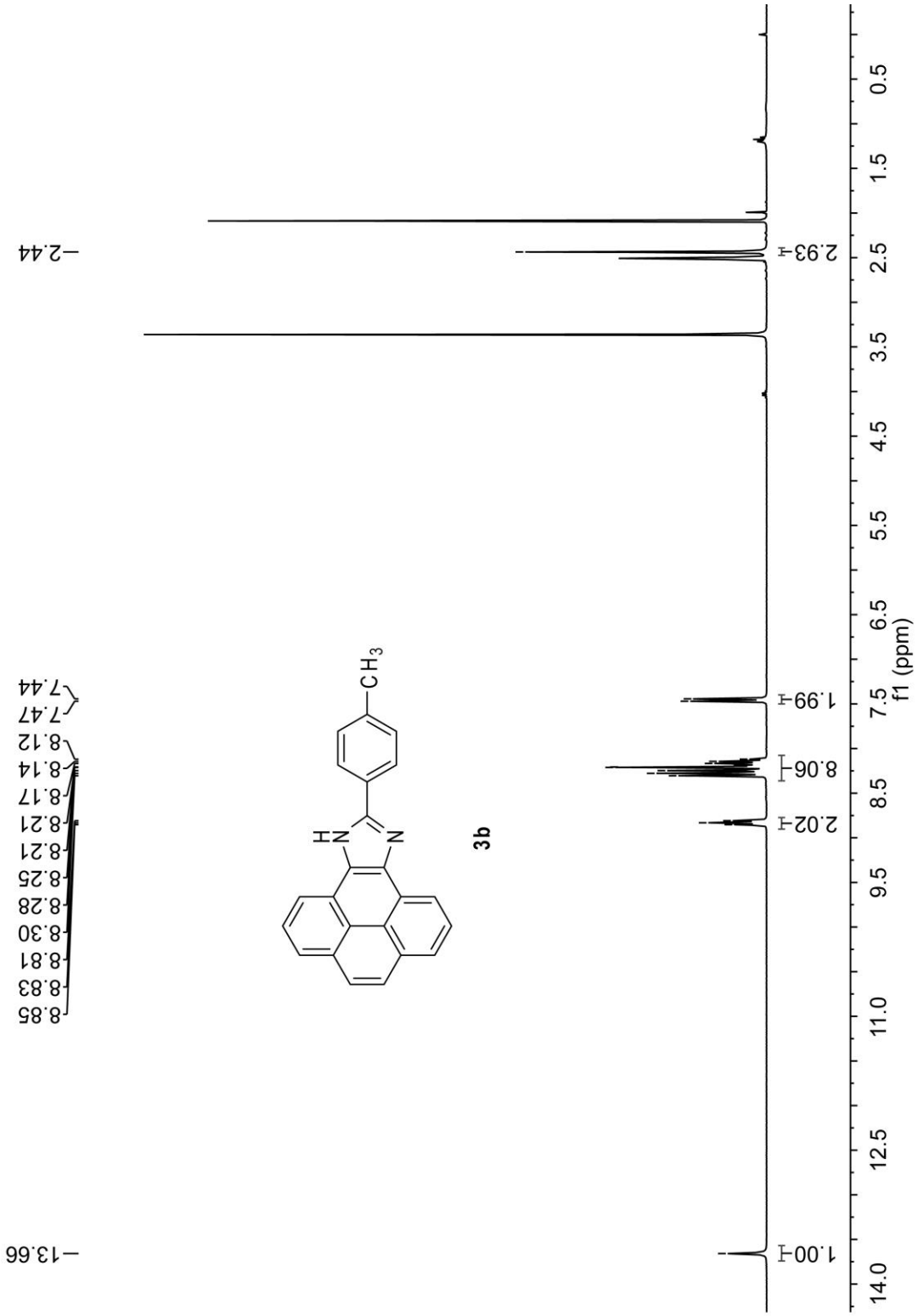

Fig. S-3 ^{1}H NMR (300 MHz, DMSO-d_6) spectrum of compound **3b**.

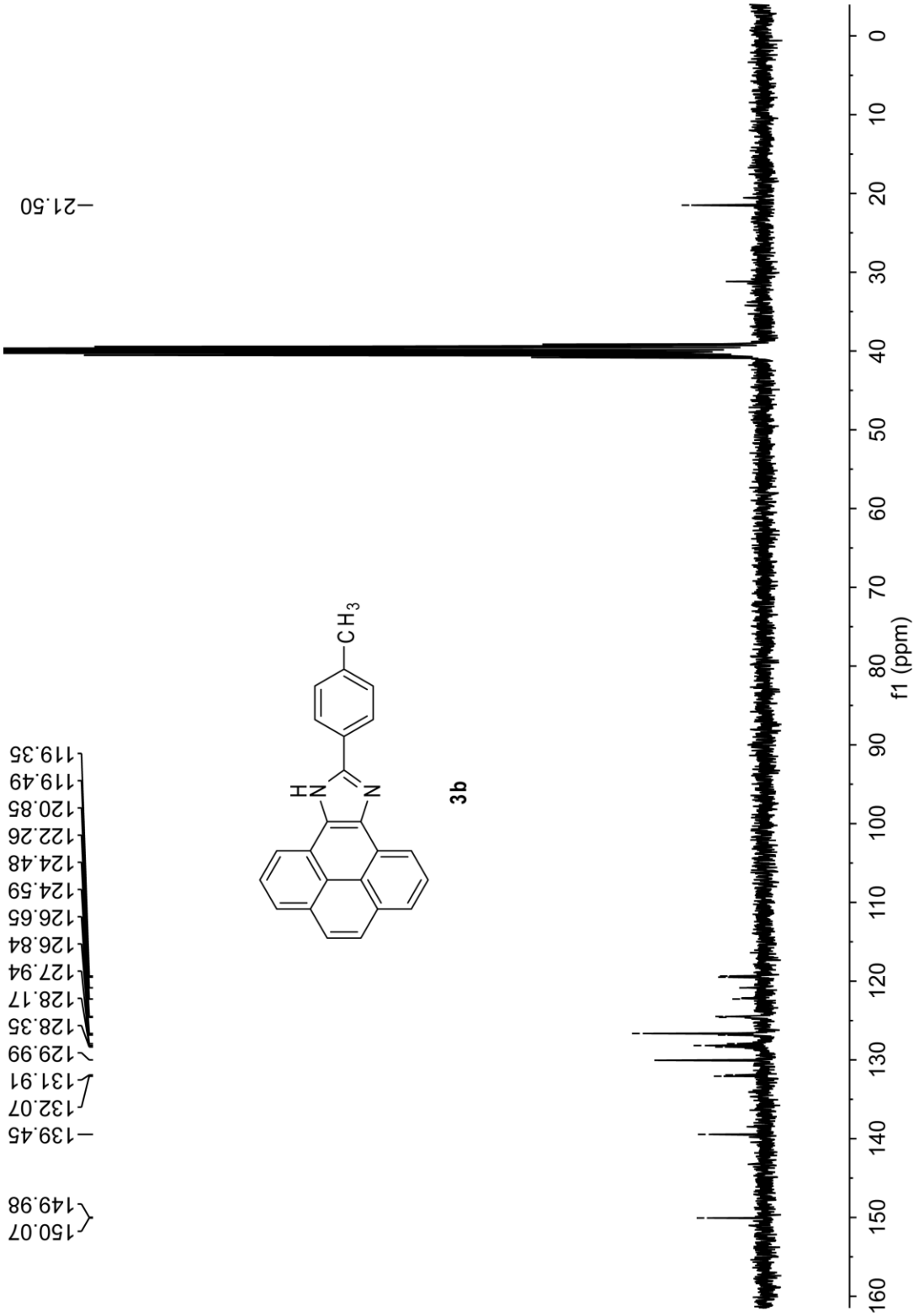

Fig. S-4 ^{13}C NMR (75 MHz, DMSO-d_6) spectrum of compound **3b**.

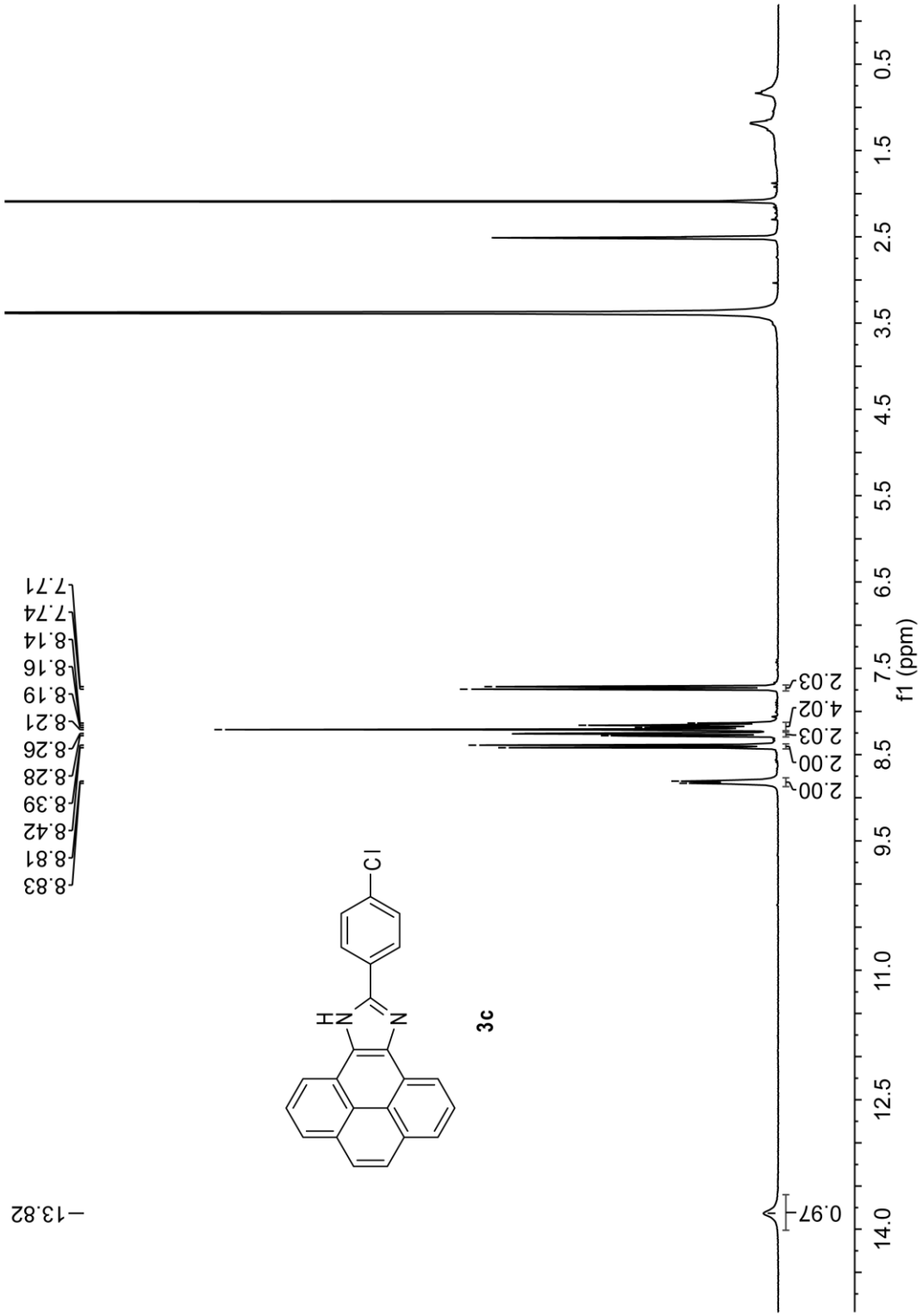

Fig. S-5 ^{1}H NMR (300 MHz, DMSO-d_6) spectrum of compound **3c**.

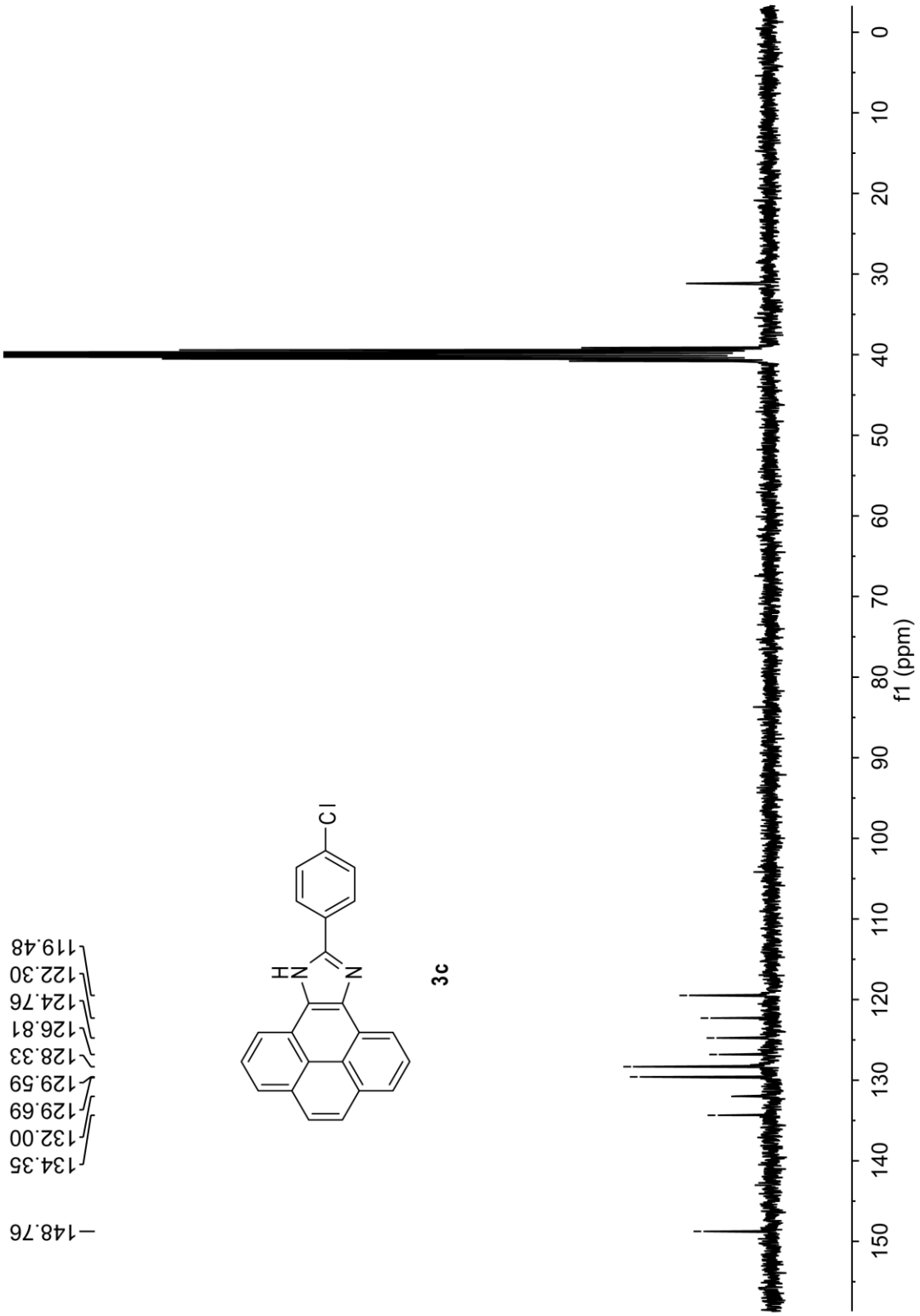

Fig. S-6 ^{13}C NMR (75 MHz, DMSO-d_6) spectrum of compound **3c**.

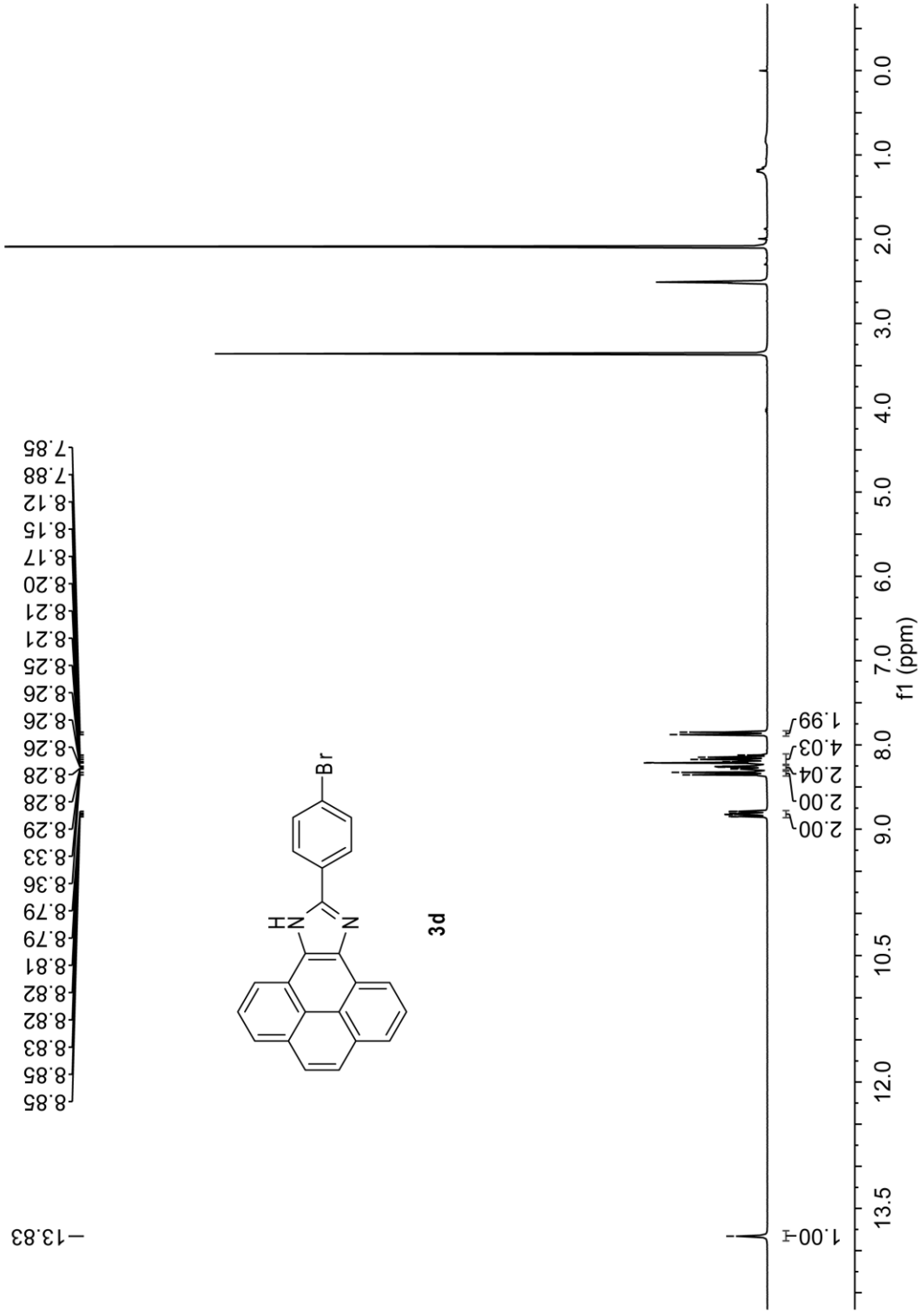

Fig. S-7 ^{1}H NMR (300 MHz, DMSO-d_6) spectrum of compound **3d**.

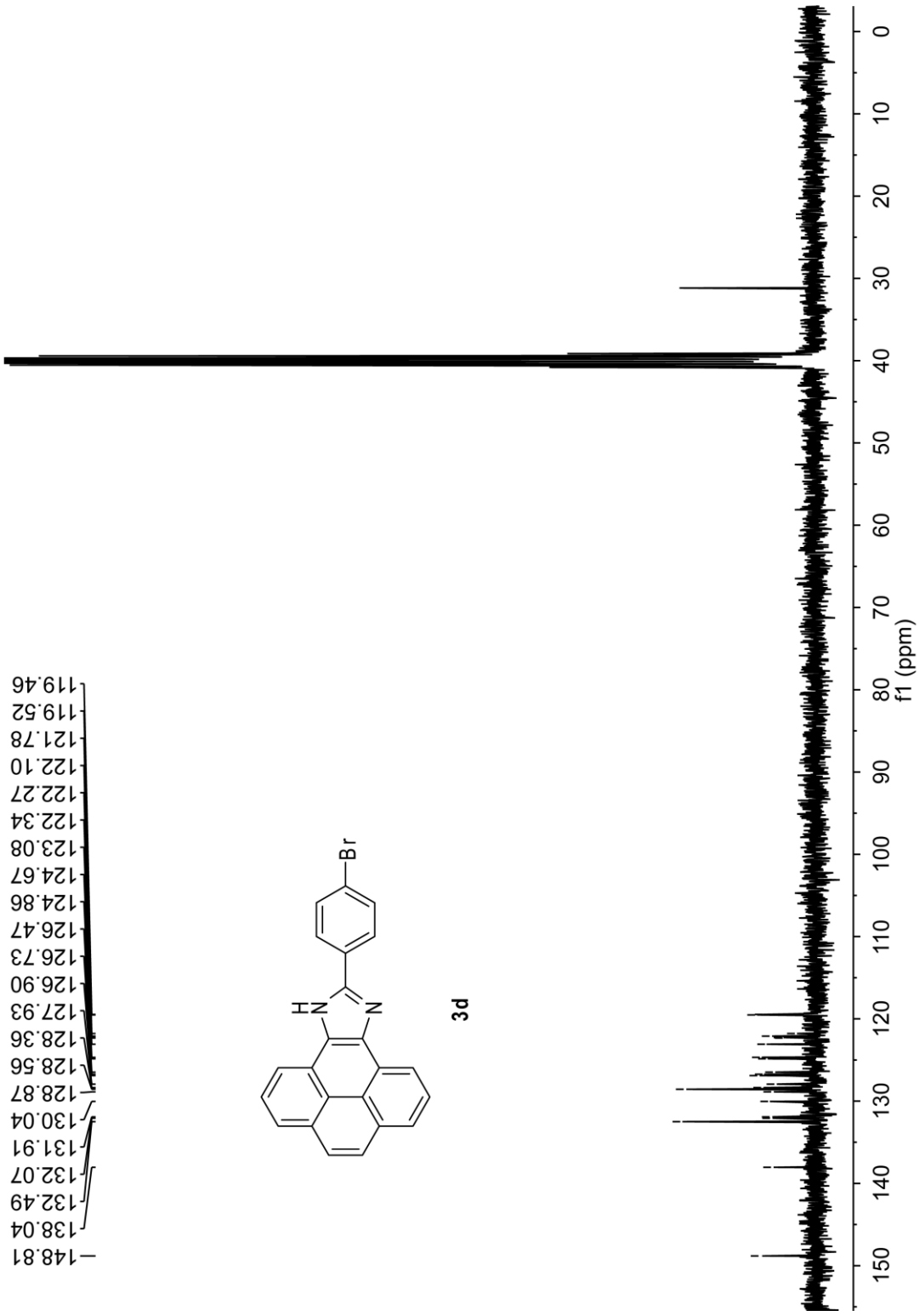

Fig. S-8 ^{13}C NMR (75 MHz, DMSO-d_6) spectrum of compound **3d**.

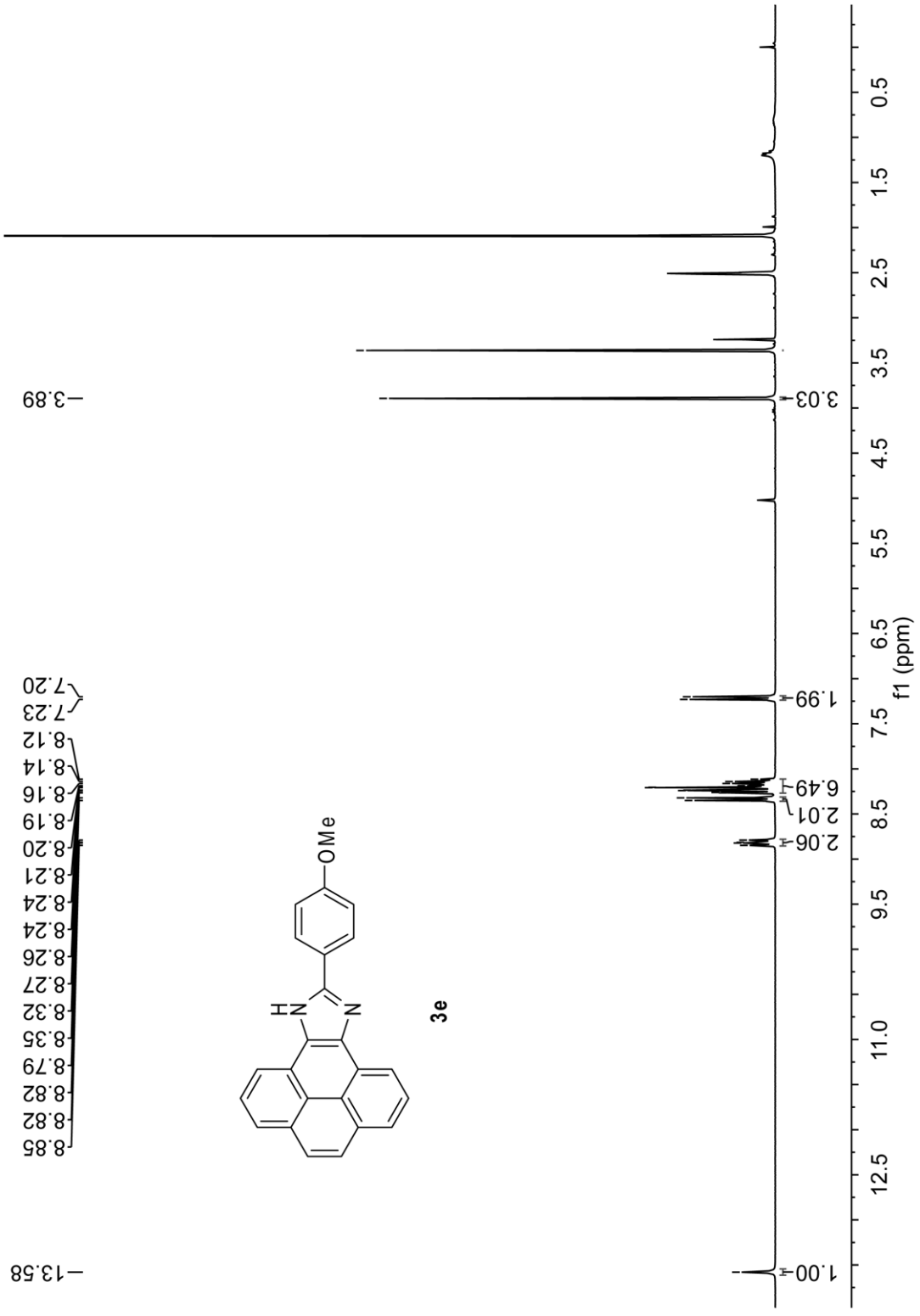

Fig. S-9 ^{1}H NMR (300 MHz, DMSO-d_6) spectrum of compound **3e**.

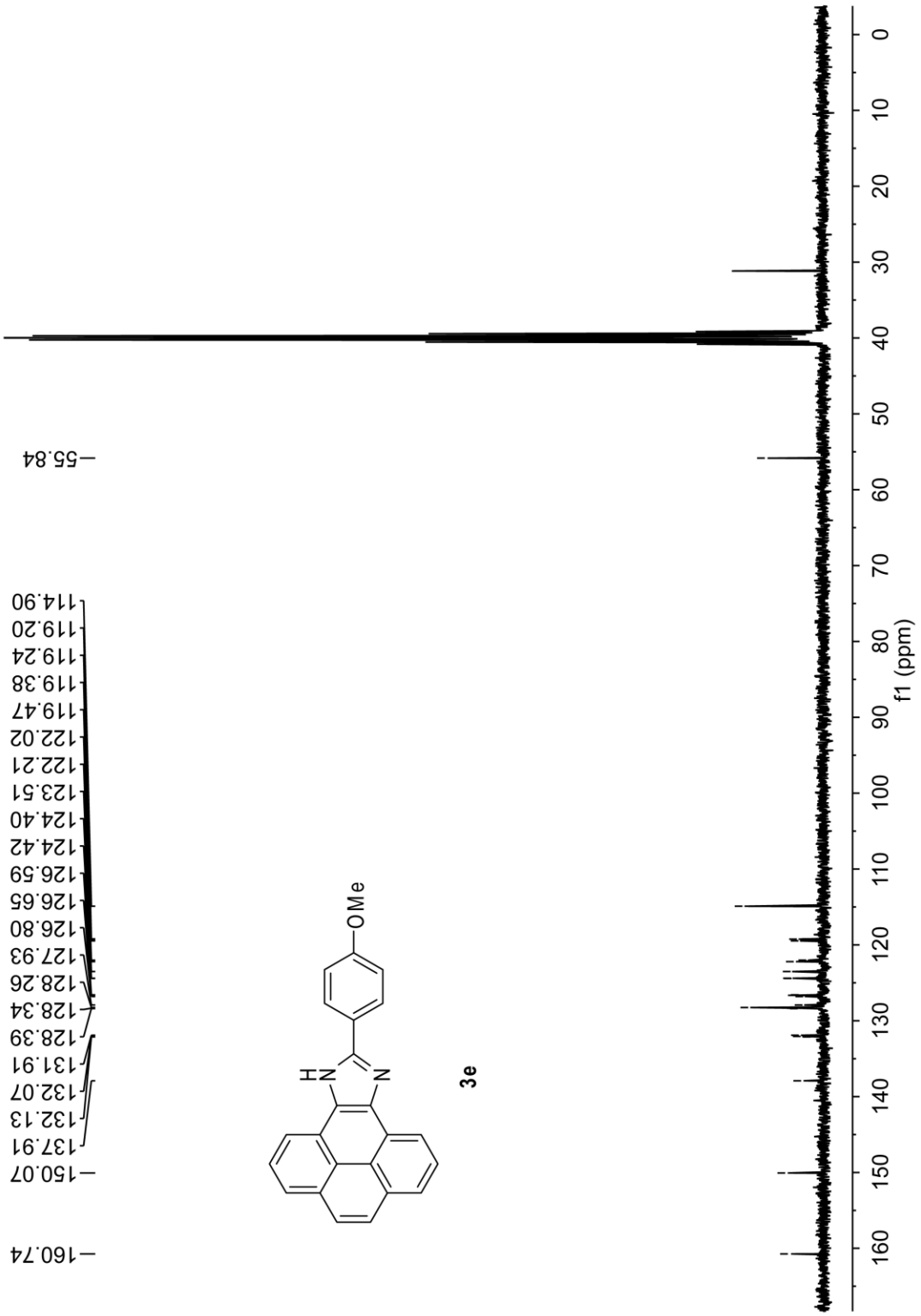

Fig. S-10 ^{13}C NMR (75 MHz, DMSO-d_6) spectrum of compound **3e**.

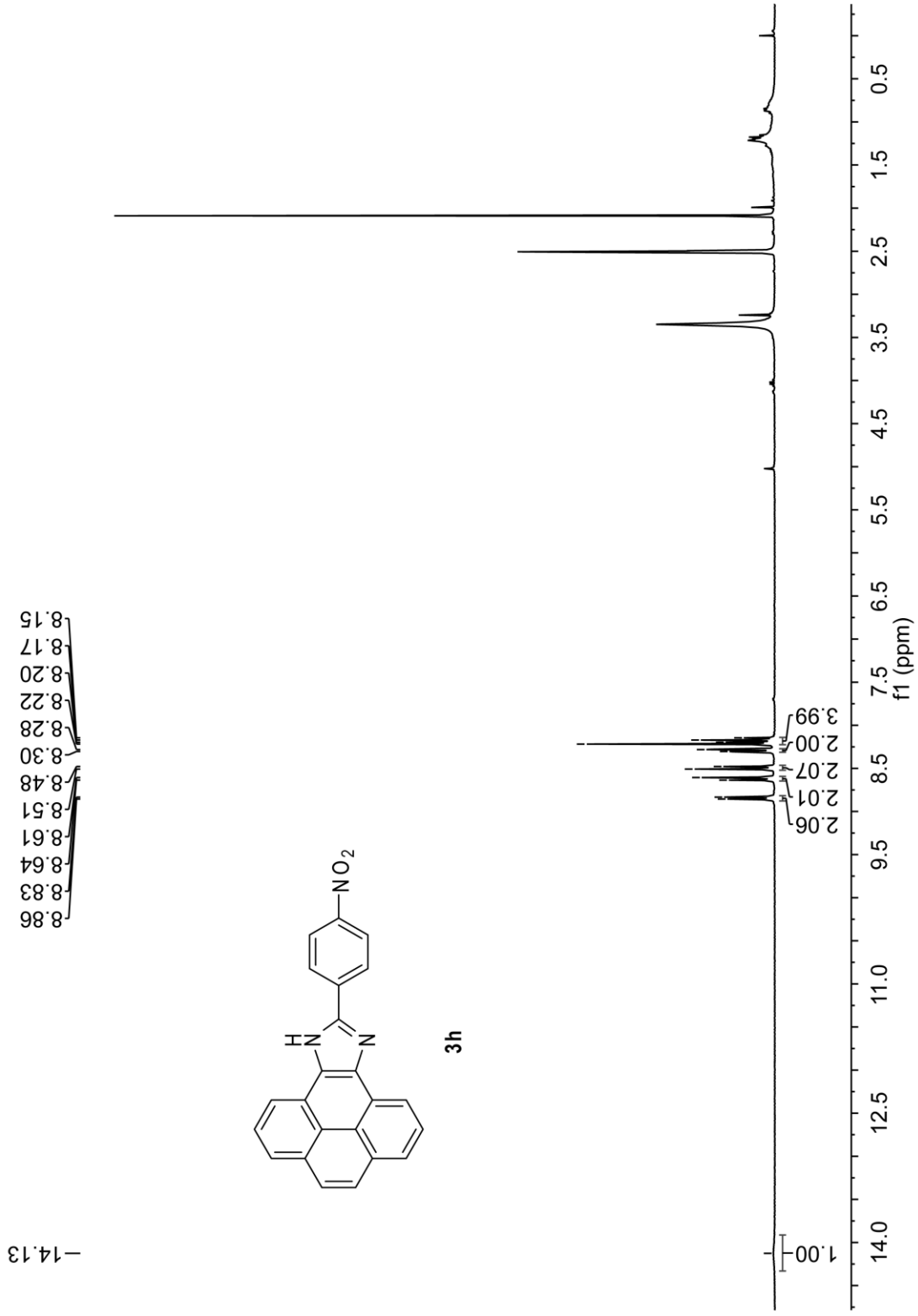

Fig. S-11 ^{1}H NMR (300 MHz, DMSO-d_6) spectrum of compound **3h**.

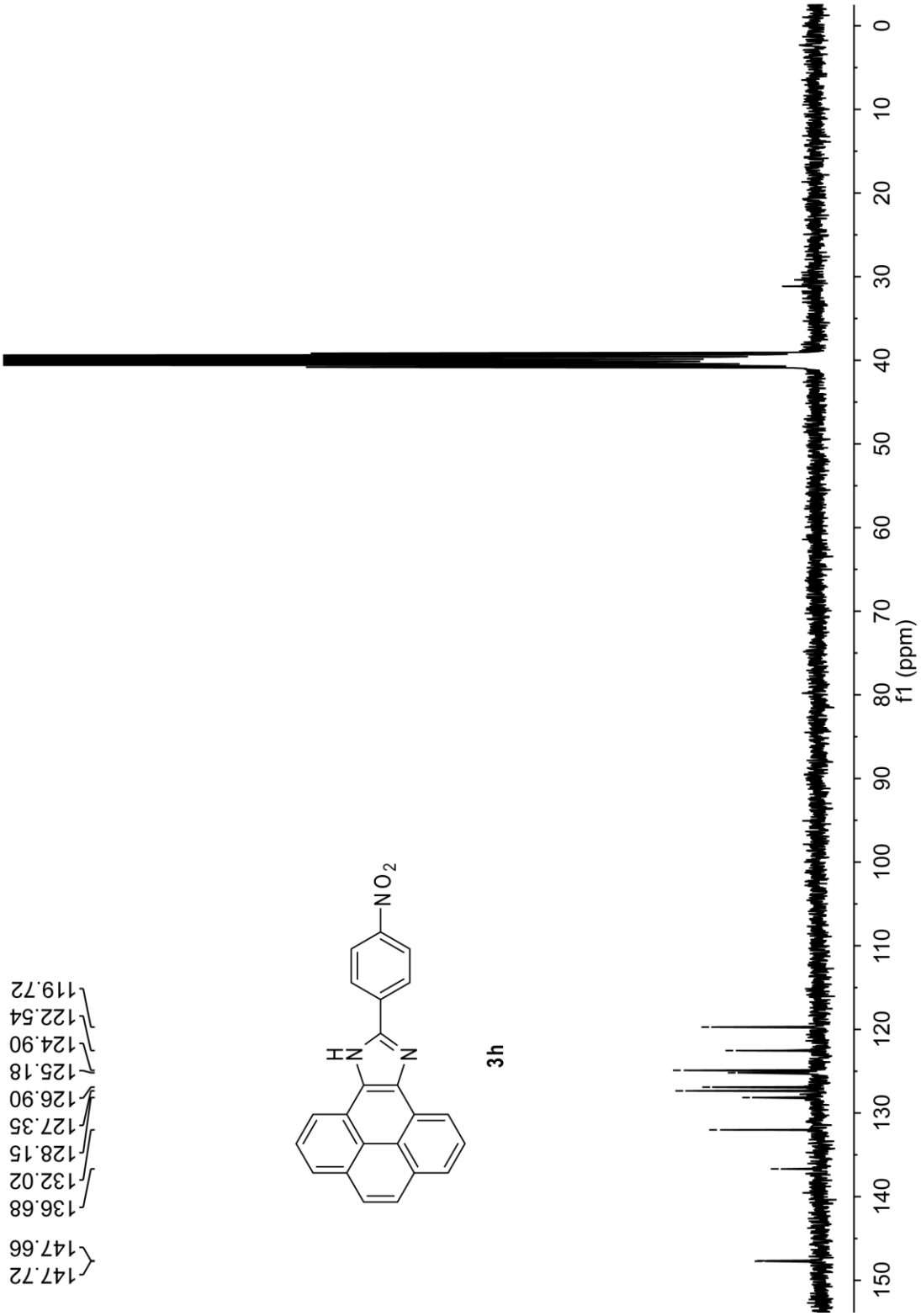

Fig. S-12 ^{13}C NMR (75 MHz, DMSO-d_6) spectrum of compound **3h**.

3. DFT and TD-DFT Computational Results

3.1 Geometry Optimization

Molecular geometries of compounds **3a-h** were optimized at the M06-2X/Def2-SV(P) level using Spartan'18 Parallel Suite (Wavefunction Inc.). Detailed Cartesian coordinates are provided below.

Table S-1 Cartesian coordinates of optimized structures of **3a-h**

3a				[**3b** – H]$^-$ anion				**3b**			
H	-4.626273	-0.046530	2.436749	H	4.630607	-0.002574	2.347412	H	4.647183	0.055163	3.040838
C	-3.534060	-0.035208	2.418490	C	3.536489	-0.002242	2.336692	C	3.555004	0.041711	3.023115
C	-0.715632	-0.005918	2.369580	C	0.720591	-0.000529	2.307520	C	0.736331	0.007204	2.975367
C	-2.863544	-0.024052	1.195123	C	2.857281	-0.002302	1.118985	C	2.883713	0.028034	1.800113
C	-2.820029	-0.031866	3.610291	C	2.834752	-0.001565	3.539277	C	2.841548	0.038137	4.215230
C	-1.415172	-0.016753	3.607736	C	1.429643	-0.000842	3.541623	C	1.436511	0.020384	4.213246
C	-1.466754	-0.010142	1.153666	C	1.457349	-0.001452	1.079591	C	1.486608	0.011481	1.759039
H	-3.438736	-0.025554	0.265121	H	3.392668	-0.002803	0.166712	H	3.458347	0.029806	0.869773
H	-3.347444	-0.040802	4.567710	H	3.367715	-0.001536	4.494980	H	3.369395	0.049002	5.172363
C	0.725553	0.009924	2.362400	C	-0.720591	0.000529	2.307520	C	-0.704525	-0.010918	2.968592
C	3.540754	0.042027	2.378308	C	-3.536489	0.002242	2.336692	C	-3.519900	-0.047687	2.985440
C	1.462087	0.020232	1.142282	C	-1.457349	0.001452	1.079591	C	-1.441138	-0.023066	1.748525
C	1.436894	0.015262	3.594251	C	-1.429643	0.000842	3.541623	C	-1.415591	-0.016666	4.200710
C	2.841058	0.031517	3.579697	C	-2.834752	0.001565	3.539277	C	-2.819833	-0.035321	4.186624
C	2.856940	0.036328	1.161877	C	-2.857281	0.002302	1.118985	C	-2.836246	-0.041479	1.768842
H	3.379573	0.035969	4.531182	H	-3.367715	0.001536	4.494980	H	-3.358055	-0.040226	5.138248
H	3.392027	0.044824	0.210064	H	-3.392668	0.002803	0.166712	H	-3.371459	-0.051521	0.817103
H	4.633276	0.055097	2.386273	H	-4.630607	0.002574	2.347412	H	-4.612379	-0.062615	2.993718
C	-0.661519	-0.011554	4.836881	C	0.678701	-0.000471	4.773018	C	0.683233	0.014842	5.442551
H	-1.214167	-0.020321	5.780153	H	1.235732	-0.000674	5.715425	H	1.236050	0.025283	6.385686
C	0.694899	0.003549	4.829809	C	-0.678701	0.000471	4.773018	C	-0.673179	-0.002984	5.435952
H	1.255911	0.007558	5.768350	H	-1.235732	0.000674	5.715425	H	-1.233744	-0.007386	6.374741
C	-0.689553	0.000403	-0.053504	C	0.706309	-0.001147	-0.146304	C	0.709429	-0.001503	0.552285
C	0.697531	0.012520	-0.080569	C	-0.706309	0.001147	-0.146304	C	-0.677503	-0.015108	0.525347
N	-1.066663	-0.000697	-1.373036	N	1.146587	-0.002073	-1.420336	N	1.086260	-0.000967	-0.767543
H	-2.013060	-0.039804	-1.726259	N	-1.146587	0.002073	-1.420336	H	2.032221	0.040192	-1.121634
N	1.154976	0.015633	-1.366157	C	0.000000	0.000000	-2.129728	N	-1.135680	-0.019393	-0.759965
C	0.082380	0.007495	-2.124976	C	0.000000	0.000000	-3.600669	C	-0.063181	-0.010581	-1.519123
C	0.091036	0.003874	-3.594276	C	-0.000000	0.000000	-6.416655	C	-0.070719	-0.007170	-2.987671
C	0.205733	-0.014125	-6.394255	C	1.206839	-0.012377	-4.317405	C	-0.182711	0.019038	-5.812230
C	-1.077027	0.145225	-4.354553	C	-1.206839	0.012377	-4.317405	C	1.092725	-0.159014	-3.750420
C	1.319817	-0.142314	-4.253891	C	-1.205166	0.012724	-5.710048	C	-1.293644	0.154471	-3.652443
C	1.374685	-0.150931	-5.643020	C	1.205166	-0.012724	-5.710048	C	-1.342973	0.167982	-5.040865
C	-1.019498	0.135080	-5.746385	H	2.137032	-0.022384	-3.744756	C	1.033880	-0.142855	-5.141684
H	-2.048360	0.281025	-3.870185	H	-2.137031	0.022384	-3.744756	H	2.064230	-0.303925	-3.268820
H	2.222923	-0.247393	-3.649595	H	-2.154973	0.024302	-6.253619	H	-2.198211	0.272809	-3.052646
H	2.338035	-0.268326	-6.144530	H	2.154973	-0.024302	-6.253619	H	-2.305748	0.302407	-5.542430
H	-1.938897	0.248772	-6.325112	H	-0.000000	0.000000	-7.510481	H	1.955431	-0.261578	-5.718669
H	0.250301	-0.020022	-7.485688					C	-0.248581	0.003697	-7.317145
								H	0.696869	0.350866	-7.762803
								H	-1.062411	0.647499	-7.686262
								H	-0.437560	-1.018042	-7.691095
3c				**3e**				**3f**			
H	-4.627827	-0.028604	2.460383	H	4.812222	0.000000	3.190593	H	-4.754355	-0.051809	2.839716
C	-3.535646	-0.021468	2.440354	C	3.719773	0.000000	3.184990	C	-3.662636	-0.039121	2.803620
C	-0.717002	-0.003021	2.387041	C	0.900987	0.000000	3.168672	C	-0.844985	-0.006638	2.708926
C	-2.866949	-0.011725	1.215925	C	3.035202	0.000000	1.969469	C	-3.011919	-0.030597	1.569463
C	-2.819564	-0.022095	3.630864	C	3.019763	0.000000	4.385156	C	-2.928994	-0.031674	3.983396
C	-1.414612	-0.012481	3.626272	C	1.614848	0.000000	4.398634	C	-1.524224	-0.015267	3.958290
C	-1.470268	-0.003152	1.172543	C	1.637689	0.000000	1.943766	C	-1.616168	-0.014652	1.505646
H	-3.443813	-0.010285	0.286940	H	3.599824	0.000000	1.033007	H	-3.602272	-0.036526	0.648969
H	-3.345488	-0.029876	4.589092	H	3.558242	0.000000	5.336470	H	-3.440659	-0.038601	4.949317
C	0.724258	0.007213	2.377798	C	-0.539905	0.000000	3.177458	C	0.596038	0.010043	2.679084
C	3.539710	0.027568	2.389797	C	-3.354876	0.000000	3.224990	C	3.411329	0.042796	2.649780
C	1.459259	0.016180	1.156854	C	-1.289896	0.000000	1.965217	C	1.313366	0.018706	1.448017

C	1.437304	0.008061	3.608615	C	-1.237457	0.000000	4.417328	C	1.327001	0.017978	3.899300
C	2.841571	0.018447	3.591990	C	-2.641700	0.000000	4.418706	C	2.730853	0.034460	3.861941
C	2.854101	0.026355	1.174294	C	-2.684753	0.000000	2.001006	C	2.708113	0.034935	1.444236
H	3.381434	0.019304	4.542694	H	-3.169478	0.000000	5.376216	H	3.284516	0.040729	4.804678
H	3.388291	0.033605	0.221975	H	-3.230641	0.000000	1.055258	H	3.228361	0.041463	0.484197
H	4.632253	0.035933	2.396263	H	-4.447373	0.000000	3.245112	H	4.503758	0.055701	2.640050
C	-0.659262	-0.011524	4.854350	C	0.875027	0.000000	5.636307	C	-0.750976	-0.006924	5.175254
H	-1.210586	-0.019172	5.798368	H	1.438501	0.000000	6.573240	H	-1.288544	-0.013891	6.127168
C	0.697194	-0.002107	4.845276	C	-0.481449	0.000000	5.644469	C	0.605167	0.008832	5.146541
H	1.259632	-0.001514	5.782941	H	-1.032128	0.000000	6.589142	H	1.181024	0.014962	6.075993
C	-0.694588	0.005504	-0.035760	C	0.847112	0.000000	0.746211	C	-0.857893	-0.005434	0.285984
C	0.692484	0.012823	-0.064714	C	-0.539616	0.000000	0.733779	C	0.528872	0.009787	0.237865
N	-1.074204	0.006553	-1.354814	N	1.209824	0.000000	-0.578228	N	-1.255537	-0.009425	-1.027572
H	-2.022171	-0.025218	-1.704504	H	2.153543	0.000000	-0.939950	H	-2.209062	-0.021793	-1.362672
N	1.147665	0.015596	-1.351019	N	-1.011202	0.000000	-0.547253	N	0.966073	0.014321	-1.053897
C	0.073909	0.011325	-2.107916	C	0.053097	0.000000	-1.318115	C	-0.117160	0.002127	-1.795815
C	0.085450	0.007171	-3.576095	C	0.028981	0.000000	-2.785175	C	-0.120681	0.000690	-3.265076
C	0.212763	-0.017037	-6.365643	C	-0.125238	0.000000	-5.595664	C	-0.037526	-0.002372	-6.069867
C	-1.080768	0.114531	-4.343396	C	1.193869	0.000000	-3.568825	C	1.107747	-0.001780	-3.932346
C	1.319451	-0.106919	-4.232192	C	-1.208251	0.000000	-3.435360	C	-1.304676	0.002160	-4.019229
C	1.387581	-0.118953	-5.619530	C	-1.295042	0.000000	-4.824837	C	-1.265032	0.000432	-5.411847
C	-1.023538	0.101306	-5.734649	C	1.121306	0.000000	-4.952833	C	1.146673	-0.003352	-5.326528
H	-2.059279	0.223222	-3.867576	H	2.183753	0.000000	-3.103224	H	2.037577	-0.002631	-3.358950
H	2.224127	-0.185616	-3.626321	H	-2.112908	0.000000	-2.823877	H	-2.279972	0.006006	-3.524146
H	2.346399	-0.209688	-6.132752	H	-2.279166	0.000000	-5.294368	H	-2.196505	0.001874	-5.981866
H	-1.931969	0.185708	-6.333350	H	2.020748	0.000000	-5.571120	H	0.006613	-0.003501	-7.163178
Cl	0.292700	-0.035948	-8.100397	O	-0.102024	0.000000	-6.944191	C	2.462450	-0.006382	-6.025402
				C	-1.324222	0.000000	-7.633606	H	2.399726	-0.009616	-7.142602
				H	-1.919584	-0.900440	-7.397377	O	3.524520	-0.006016	-5.466439
				H	-1.077821	0.000000	-8.703819				
				H	-1.919584	0.900440	-7.397377				
3g				**3h**							
H	4.639477	0.000000	2.863502	H	4.640295	0.000000	2.873281				
C	3.547341	0.000000	2.843444	C	3.548228	0.000000	2.849664				
C	0.728286	0.000000	2.790329	C	0.729296	0.000000	2.787673				
C	2.878434	0.000000	1.619104	C	2.883079	0.000000	1.623181				
C	2.831021	0.000000	4.033622	C	2.828082	0.000000	4.037279				
C	1.425875	0.000000	4.029438	C	1.423021	0.000000	4.028833				
C	1.481971	0.000000	1.576424	C	1.486992	0.000000	1.576466				
H	3.455294	0.000000	0.690141	H	3.463033	0.000000	0.696059				
H	3.357033	0.000000	4.991817	H	3.351136	0.000000	4.997115				
C	-0.713269	0.000000	2.781157	C	-0.712327	0.000000	2.774694				
C	-3.528759	0.000000	2.794186	C	-3.527771	0.000000	2.780138				
C	-1.448905	0.000000	1.560643	C	-1.444835	0.000000	1.552777				
C	-1.425677	0.000000	4.012136	C	-1.427993	0.000000	4.003579				
C	-2.830156	0.000000	3.995866	C	-2.832399	0.000000	3.983450				
C	-2.843500	0.000000	1.578371	C	-2.839208	0.000000	1.566135				
H	-3.369651	0.000000	4.946754	H	-3.374594	0.000000	4.932823				
H	-3.378433	0.000000	0.626468	H	-3.372004	0.000000	0.612991				
H	-4.621283	0.000000	2.800987	H	-4.620311	0.000000	2.783898				
C	0.670885	0.000000	5.257684	C	0.664794	0.000000	5.254876				
H	1.222368	0.000000	6.201589	H	1.213463	0.000000	6.200428				
C	-0.685473	0.000000	5.248790	C	-0.691501	0.000000	5.242148				
H	-1.247728	0.000000	6.186501	H	-1.256333	0.000000	6.178326				
C	0.706195	0.000000	0.367726	C	0.714482	0.000000	0.365379				
C	-0.681998	0.000000	0.338672	C	-0.673992	0.000000	0.333211				
N	1.086256	0.000000	-0.949391	N	1.097966	0.000000	-0.950846				
H	2.035475	0.000000	-1.297404	H	2.048527	0.000000	-1.295327				
N	-1.135780	0.000000	-0.946594	N	-1.124096	0.000000	-0.953176				
C	-0.061306	0.000000	-1.703807	C	-0.048023	0.000000	-1.707624				
C	-0.072385	0.000000	-3.171291	C	-0.062295	0.000000	-3.174422				
C	-0.190361	0.000000	-5.966538	C	-0.197108	0.000000	-5.941385				
C	1.108319	0.000000	-3.932884	C	1.111955	0.000000	-3.941691				
C	-1.313357	0.000000	-3.824947	C	-1.307599	0.000000	-3.823362				
C	-1.368146	0.000000	-5.212854	C	-1.381005	0.000000	-5.208884				
C	1.049800	0.000000	-5.319236	C	1.050969	0.000000	-5.330912				
H	2.087935	0.000000	-3.447096	H	2.095701	0.000000	-3.465643				
H	-2.219310	0.000000	-3.216463	H	-2.211407	0.000000	-3.211988				
H	-2.336129	0.000000	-5.723389	H	-2.336778	0.000000	-5.732689				
H	1.957052	0.000000	-5.928082	H	1.950679	0.000000	-5.946017				

C	-0.245211	0.000000	-7.450611	N	-0.268603	0.000000	-7.414613	
H	-1.276387	0.000000	-7.883540	O	0.774881	0.000000	-8.021386	
O	0.724189	0.000000	-8.161222	O	-1.366397	0.000000	-7.914437	

3.2 Results of QTAIM Analysis

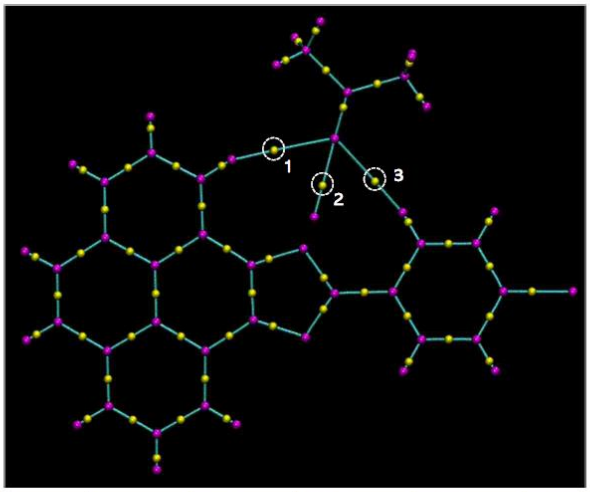

CP	Type	ρ	∇ρ²	G(r)	V(r)	H(r)
1	(3,-1)	0.00782	0.0269	0.00619	-0.00565	0.000541
2	(3,-1)	0.0223	0.0950	0.0220	-0.0202	0.00179
3	(3,-1)	0.00963	0.0322	0.00767	-0.00730	0.000367

Fig. S-13 Molecular graph of compound **3c** complexed with acetone. Bond critical points (BCPs) for hydrogen bonding interactions are highlighted. Calculated at the M06-2X/Def2-SV(P) level.

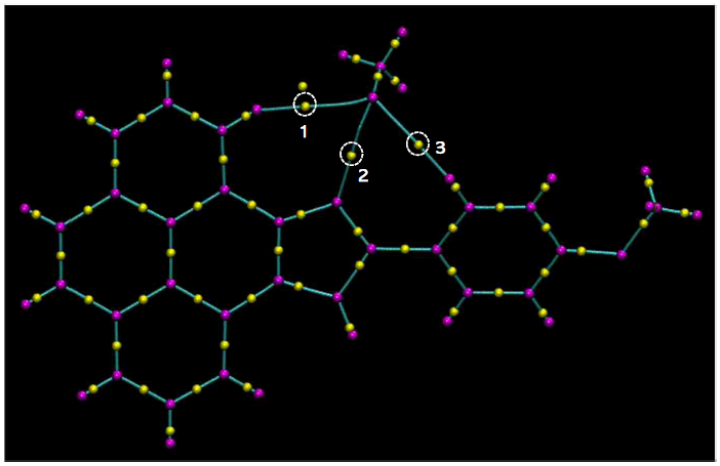

CP	Type	ρ	∇ρ²	G(r)	V(r)	H(r)
1	(3,-1)	0.0311	0.109	0.0268	-0.0264	0.000391
2	(3,-1)	0.00909	0.0316	0.00746	-0.00703	0.000433
3	(3,-1)	0.00625	0.0257	0.00558	-0.00473	0.000845

Fig. S-14 Molecular graph of compound **3e** complexed with methanol. Bond critical points (BCPs) for hydrogen bonding interactions are highlighted. Calculated at the M06-2X/Def2-SV(P) level.

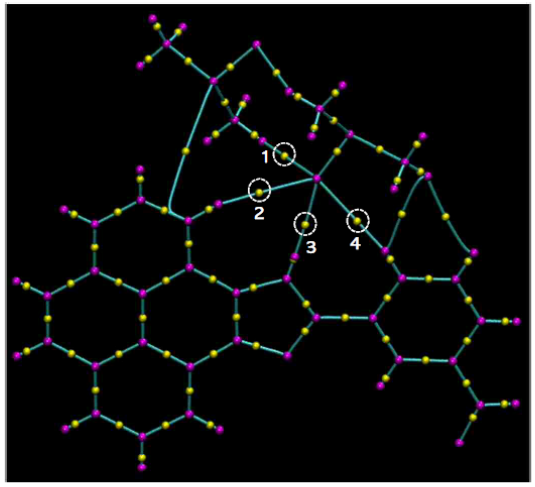

CP	Type	ρ	$\nabla\rho^2$	G(r)	V(r)	H(r)
1	(3,-1)	0.0111	0.0378	0.00920	-0.00896	0.000242
2	(3,-1)	0.0719	0.0263	0.00594	-0.00530	0.000640
3	(3,-1)	0.0165	0.0715	0.0165	-0.0152	0.00133
4	(3,-1)	0.00866	0.0287	0.00679	-0.00642	0.000380

Fig. S-15 Molecular graph of compound **3f** complexed with two molecules of DMSO. Bond critical points (BCPs) for hydrogen bonding interactions are highlighted. Calculated at the M06-2X/Def2-SV(P) level.

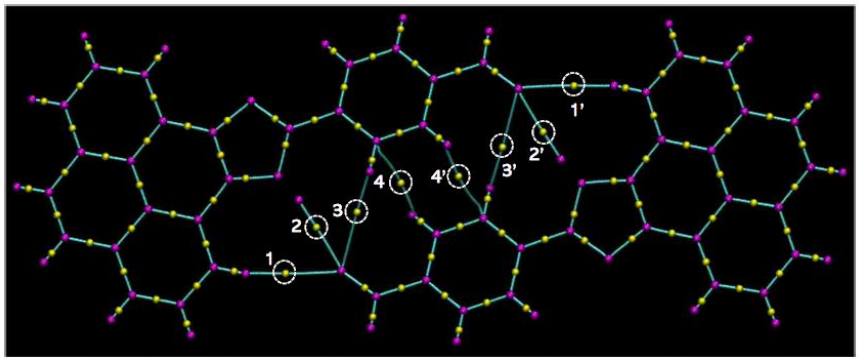

CP	Type	ρ	$\nabla\rho^2$	G(r)	V(r)	H(r)
1/1′	(3,-1)	0.0622	0.0209	0.00475	-0.00428	0.000467
2/2′	(3,-1)	0.0113	0.0373	0.00886	-0.00840	0.000464
3/3′	(3,-1)	0.00307	0.0133	0.00249	-0.00166	0.000826
4/4′	(3,-1)	0.00762	0.0306	0.00582	-0.00399	0.00184

Fig. S-16 Molecular graph of hydrogen bonded dimer of **3g**. Bond critical points (BCPs) for hydrogen bonding interactions are highlighted. Calculated at the M06-2X/Def2-SV(P) level.

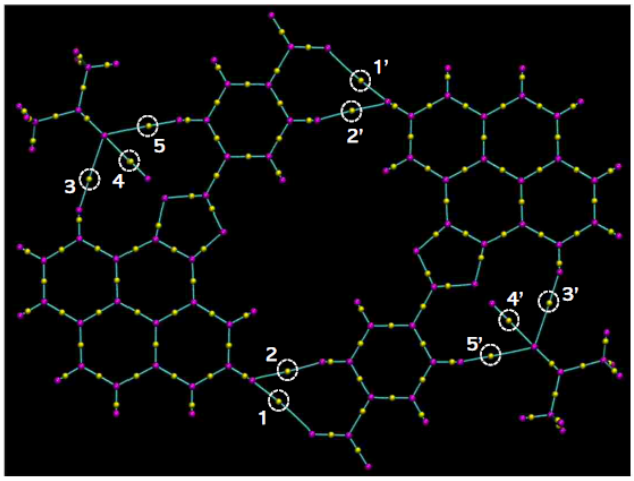

CP	Type	ρ	∇ρ²	G(r)	V(r)	H(r)
1/1′	(3,-1)	0.00612	0.0241	0.00525	-0.00447	0.000782
2/2′	(3,-1)	0.00402	0.0193	0.00366	-0.00249	0.00117
3/3′	(3,-1)	0.00806	0.0275	0.00637	-0.00586	0.000510
4/4′	(3,-1)	0.0233	0.0988	0.0228	-0.0210	0.00185
5/5′	(3,-1)	0.0102	0.0337	0.00813	-0.00785	0.000286

Fig. S-17 Molecular graph of hydrogen bonded dimer of **3h**. Bond critical points (BCPs) for hydrogen bonding interactions are highlighted. Calculated at the M06-2X/Def2-SV(P) level.

3.3 Electronic Absorption Properties of Compound 3a and 3a Anion Calculated by TD-DFT

Table S-2 Vertical electronic transitions of **3a** calculated at the TD-B3LYP/6-311+G(d,p) level

Wavelength (nm)	Osc. Strength	Major Contributions
368.4	0.3762	HOMO→LUMO (91%)
357.2	0.3052	HOMO→L+1 (82%)
328.2	0.1637	H-1→LUMO (16%), HOMO→L+1 (11%), HOMO→L+2 (65%)
297.8	0.3172	H-2→LUMO (28%), H-1→LUMO (55%)
289.4	0.1383	H-2→LUMO (54%), H-1→LUMO (11%), HOMO→L+2 (15%)
288.4	0.0319	HOMO→L+3 (83%)
276.0	0.0206	H-2→L+1 (13%), H-1→L+1 (38%), HOMO→L+4 (40%)
273.1	0.0896	H-1→L+1 (44%), HOMO→L+4 (43%)
269.3	0.0852	H-2→L+1 (67%)
257.3	0.0006	HOMO→L+5 (95%)

Table S-3 Vertical electronic transitions of **3a** anion calculated at the TD-B3LYP/6-311+G(d,p) level

Wavelength (nm)	**Osc. Strength**	**Major Contributions**
428.9	0.1372	HOMO→LUMO (95%)
383.9	0.4334	HOMO→L+1 (89%)
346.7	0.3759	HOMO→L+2 (89%)
323.4	0.2509	H-1→LUMO (85%)
320.2	0.0054	HOMO→L+3 (96%)
301.2	0.0461	H-2→LUMO (74%), HOMO→L+5 (18%)
295.4	0.0016	H-1→L+1 (43%), HOMO→L+5 (46%)
288.6	0.0002	HOMO→L+4 (93%)
276.9	0.2561	H-1→L+1 (50%), HOMO→L+5 (28%)
276.1	0.0002	H-3→LUMO (32%), H-2→L+1 (49%)

4. UV-Vis Absorption and Fluorescence Data

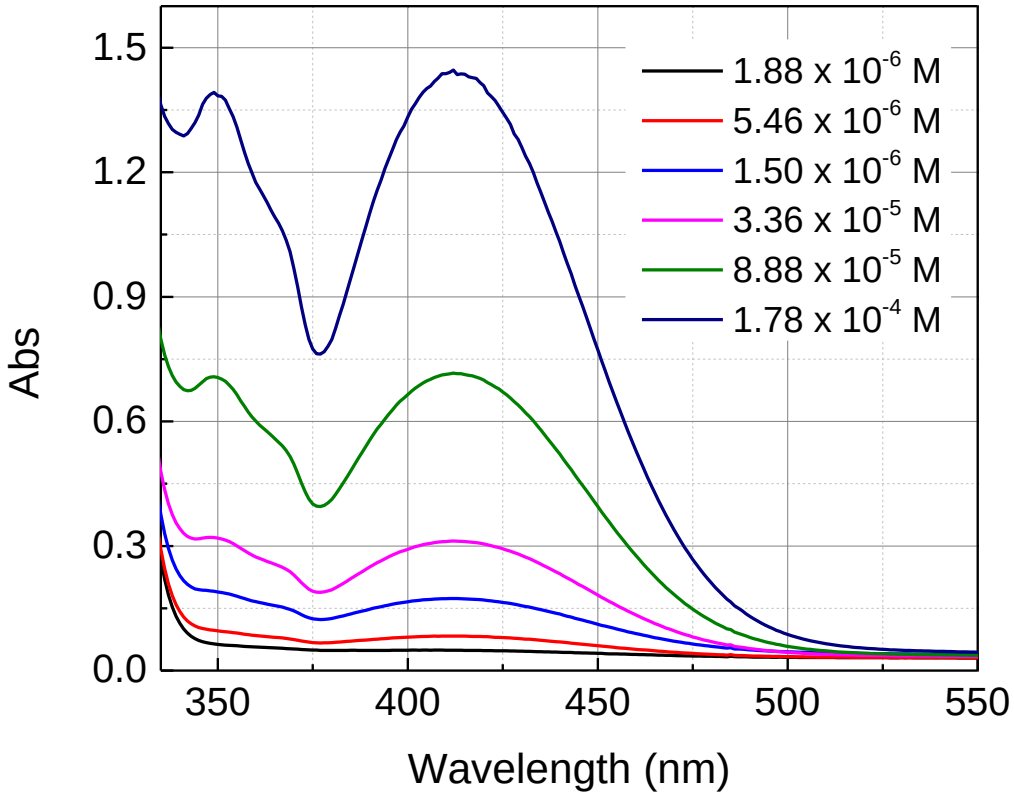

Fig. S-18 UV-Vis absorption spectra of **3h** measured at various concentrations (in acetone, at room temperature).

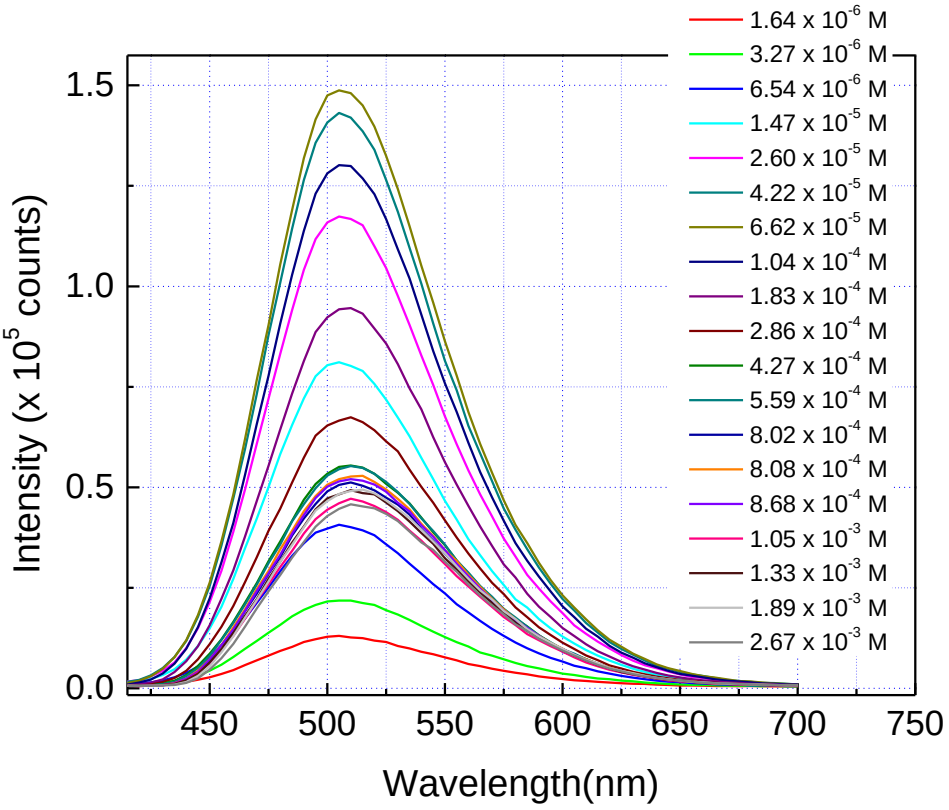

Fig. S-19 Fluorescence spectra of **3g** measured at various concentrations (in acetone, at room temperature).

Supporting Information

Designed Synthesis and Crystallization of Pyrenoimidazole-based Supramolecular Synthons

*Zahra A. Tabasi, Joshua C. Walsh, Graham J. Bodwell, and Yuming Zhao**

Department of Chemistry, Memorial University, St. John's, Newfoundland and Labrador, CANADA A1B 3X7; yuming@mun.ca

Table of Content

1. NMR Spectra of Compounds 1-3 S1

2. Crystallographic Data for Compounds 1-4 and Co-crystals S23

1. NMR Spectra of Compounds 1-3

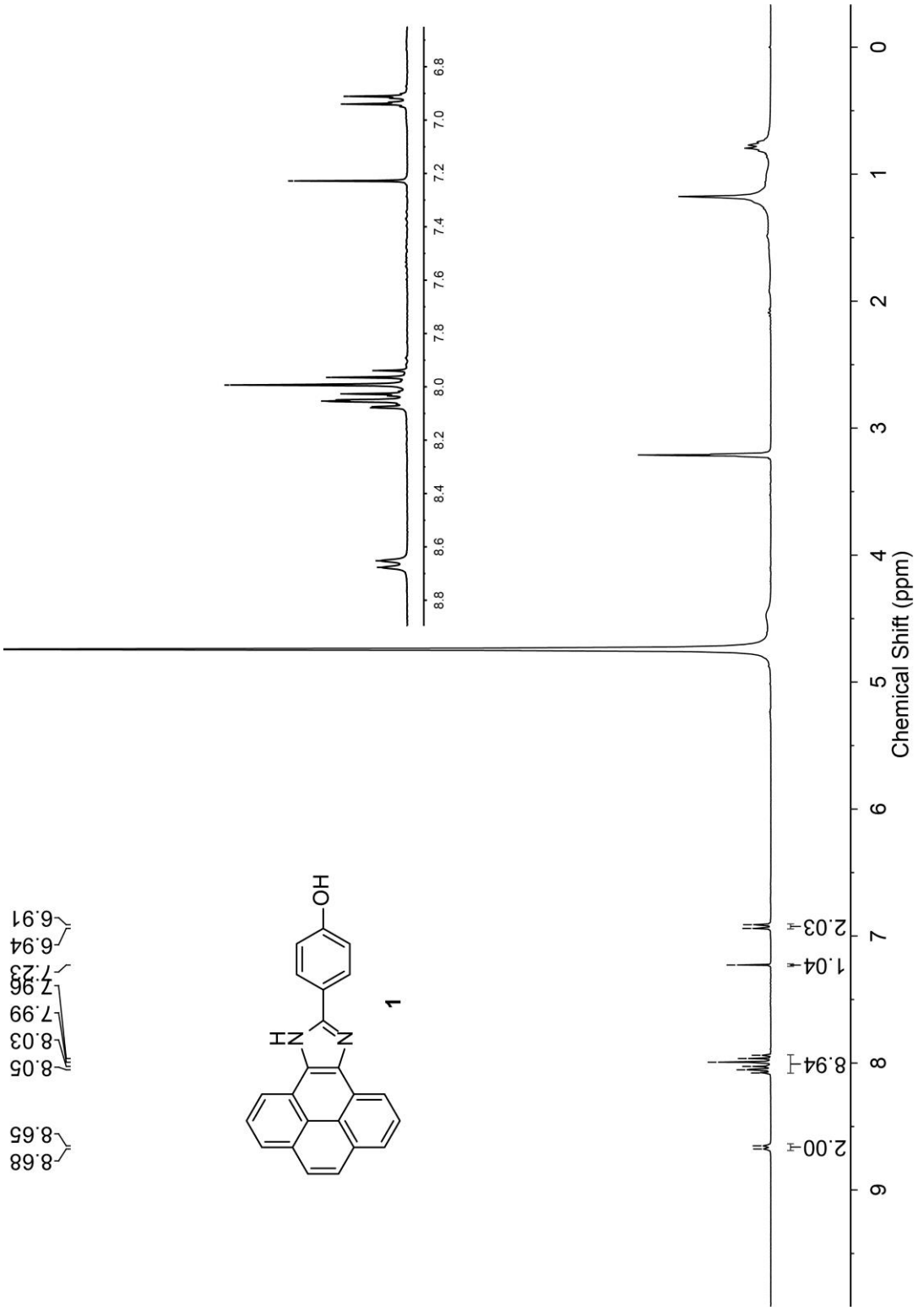

Fig. S-1 ^{1}H NMR (300 MHz, CD_3OD) spectrum of compound **1**.

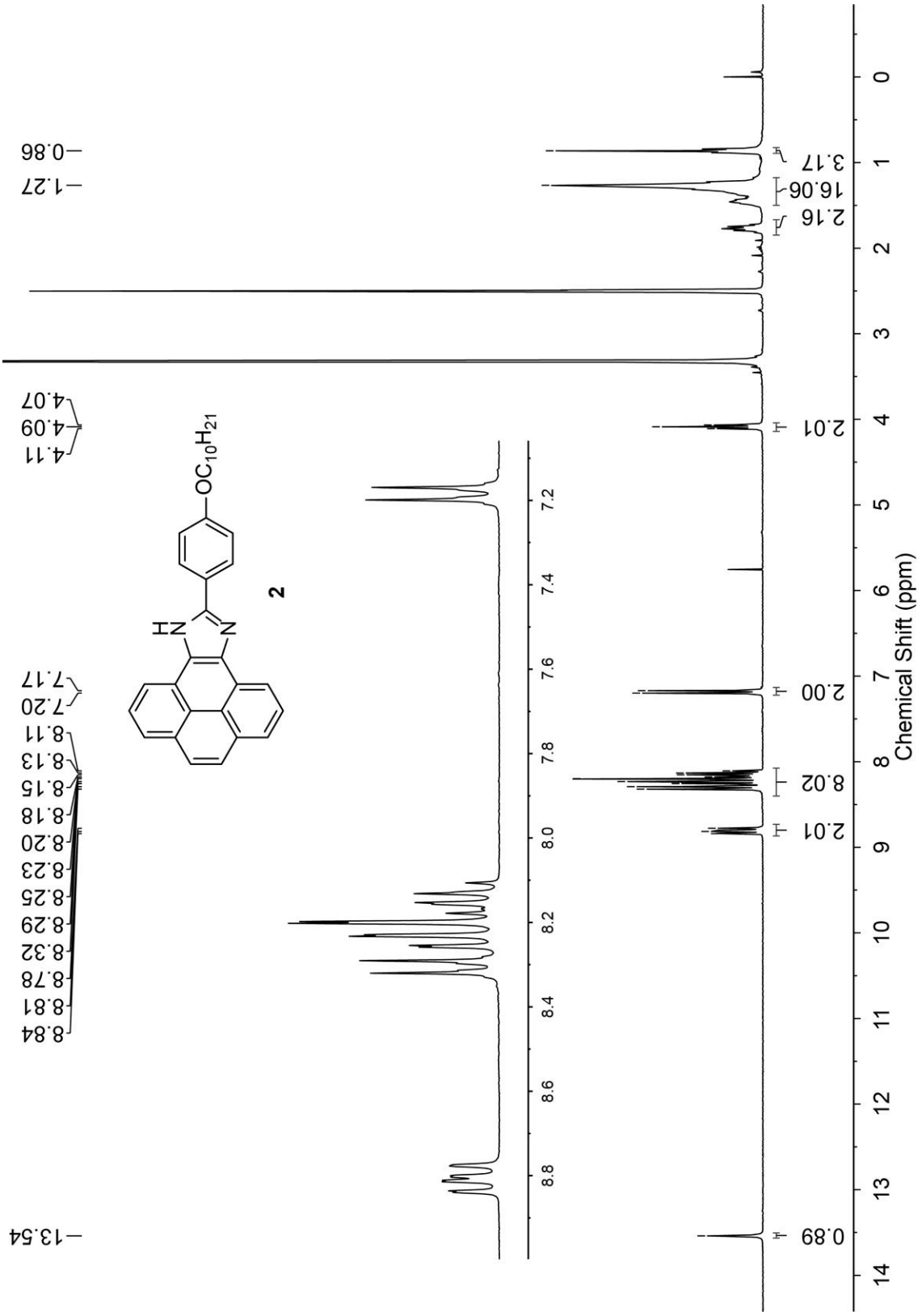

Fig. S-2 ^{1}H NMR (300 MHz, acetone-d_6) spectrum of compound **2**.

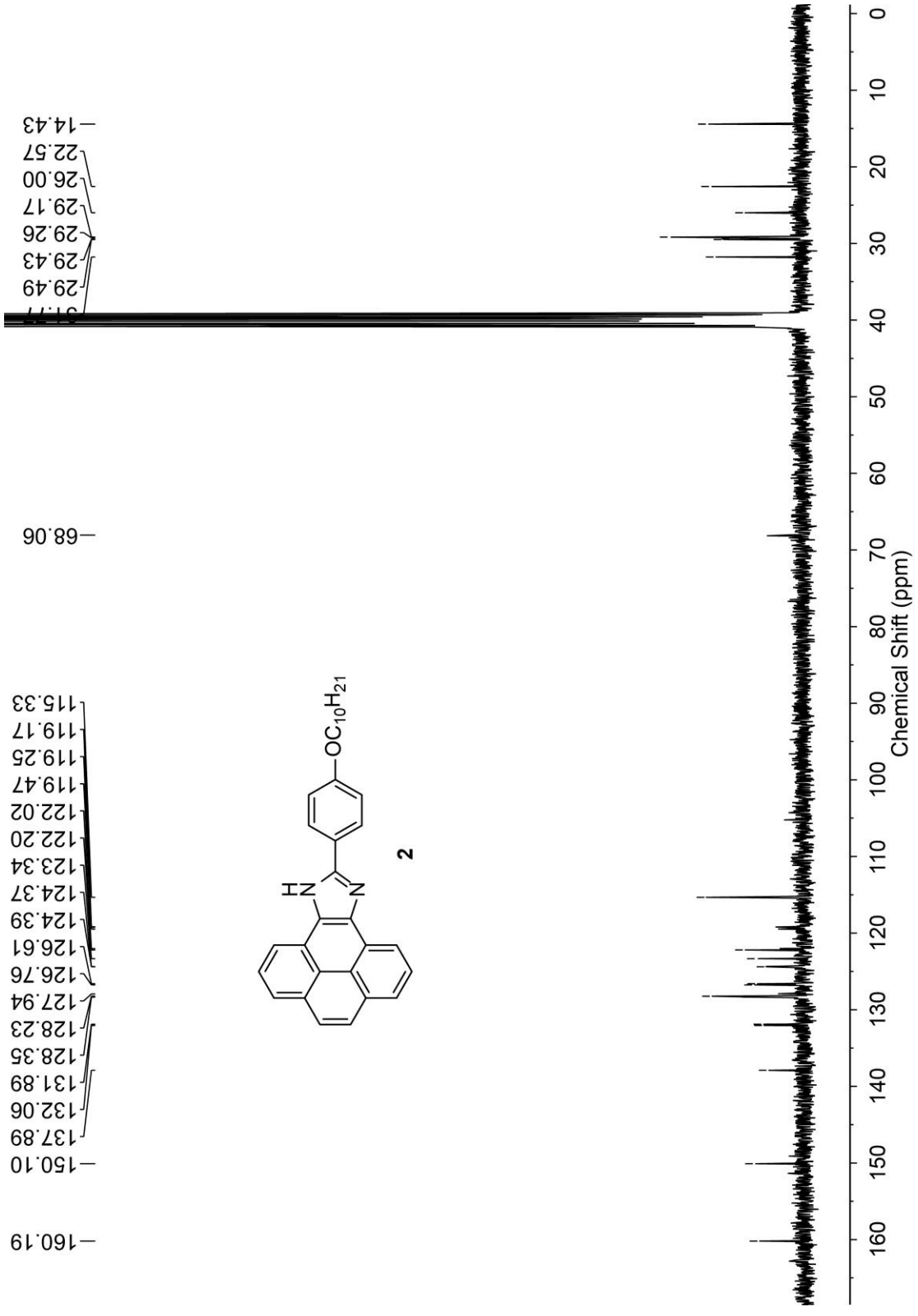

Fig. S-3 ^{13}C NMR (75 MHz, acetone-d_6) spectrum of compound **2**.

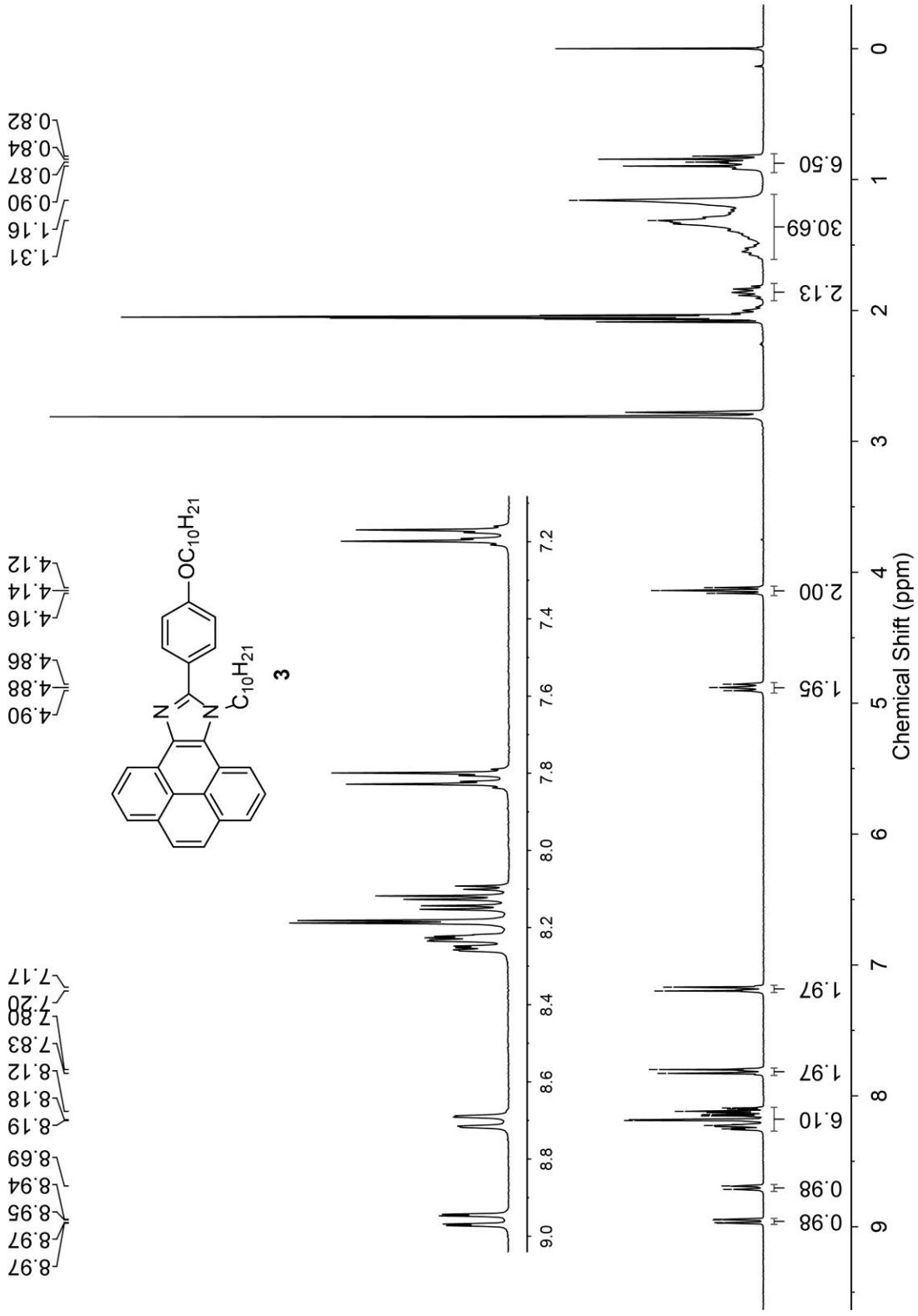

Fig. S-4 ^{1}H NMR (300 MHz, acetone-d_6) spectrum of compound **3**.

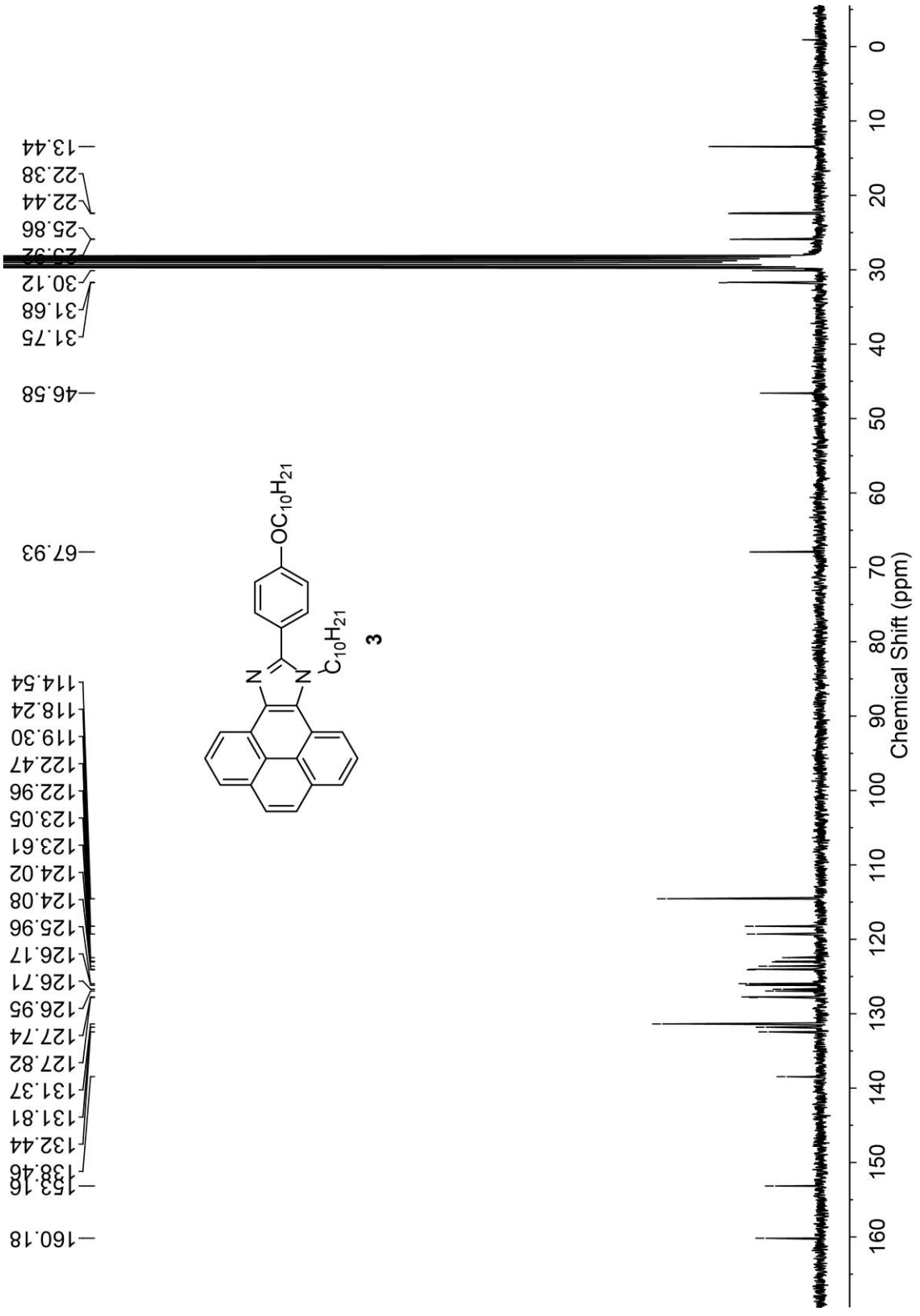

Fig. S-5 ^{13}C NMR (75 MHz, acetone-d_6) spectrum of compound **3**.

2. Crystallographic Data for Compounds 1-4 and Co-crystals

Table S-1 Crystallographic and experimental data for compound **1**

Empirical formula	$C_{24}H_{18}N_2O_2$
Formula weight	366.40
Temperature/K	-173
Crystal system	monoclinic
Space group	$P2_1/n$ (an alternate setting of $P2_1/c$ [No. 14])
a/Å	12.6038(2)
b/Å	8.2717(2)
c/Å	18.3638(4)
β/°	109.1087(12)
Volume/Å^3	1809.02(7)
Z	4
ρ_{calc} g/cm3	1.345
μ/mm^{-1}	0.691
Crystal size/mm^3	0.14 × 0.13 × 0.10
Radiation	Cu K_α (1.54178) (microfocus source)
2Θ range for data collection/°	7.50 to 147.70
Index ranges	$-15 \le h \le 15$, $-10 \le k \le 10$, $-22 \le l \le 22$
Reflections collected	12501
Independent reflections	3591 [R_{int} = 0.0212]
Data/restraints/parameters	3591/0/266
Goodness-of-fit (S) [all data]	1.079
Final R_1 [$F_o^2 \ge 2\sigma(F_o^2)$]	0.0425
Final ωR_2 [all data]	0.1314
Largest diff. peak/hole / e Å-3	0.285/-0.325

Table S-2 Crystallographic and experimental data for compound **2**

Empirical formula	$C_{33}H_{38}N_2O_3$
Formula weight	510.65
Temperature/K	100(2)
Crystal system	triclinic
Space group	P-1
a/Å	8.9659(3)
b/Å	8.9998(3)
c/Å	19.2836(7)
α/°	87.414(3)
β/°	79.965(3)

γ/°	63.475(3)
Volume/Å^3	1369.99(9)
Z	2
ρ_{calc} g/cm3	1.238
μ/mm^{-1}	0.620
F(000)	548.0
Crystal size/mm^3	0.15 × 0.1 × 0.05
Radiation	Cu K_α (λ = 1.54184)
2Θ range for data collection/°	4.656 to 155.11
Index ranges	-11 ≤ h ≤ 10, -11 ≤ k ≤ 11, -18 ≤ l ≤ 24
Reflections collected	19003
Independent reflections	5677 [R_{int} = 0.0325, R_{sigma} = 0.0229]
Data/restraints/parameters	5677/0/364
Goodness-of-fit on F2	1.058
Final R indexes [I>=2σ (I)]	R_1 = 0.0479, ωR_2 = 0.1304
Final R indexes [all data]	R_1 = 0.0550, ωR_2 = 0.1371
Largest diff. peak/hole / e Å-3	0.28/-0.30

Table S-3 Crystallographic and experimental data for compound **3**

Empirical formula	$C_{43}H_{54}N_2O$
Formula weight	614.88
Temperature/K	-173
Crystal system	triclinic
Space group	$P\bar{1}$ (No. 2)]
a/Å	9.4376(3)
b/Å	11.2292(4)
c/Å	17.0583(6)
α/°	90.117(2)
β/°	93.940(2)
γ/°	101.967(2)
Volume/Å^3	1764.07(11)
Z	2
ρ_{calc} g/cm3	1.158
μ/mm^{-1}	0.516
Crystal size/mm^3	0.63 × 0.09 × 0.07
Radiation	Cu K_α (λ = 1.54178) (microfocus source)
2Θ range for data collection/°	5.20 to 147.82
Index ranges	-11 ≤ h ≤ 11, -13 ≤ k ≤ 14, -21 ≤ l ≤ 21
Reflections collected	60985
Independent reflections	6879 (R_{int} = 0.0843)
Data/restraints/parameters	6879/0 /417
Goodness-of-fit (*S*) [all data]	1.017

Final R_1 [$F_o^2 \geq 2\sigma(F_o^2)$]	0.0555
Final ωR_2 [all data]	0.1633
Largest diff. peak/hole / e Å-3	0.210/-0.331

Table S-4 Crystallographic and experimental data for co-crystal of **4** and benzoic acid

Empirical formula	$C_{30}H_{19}N_3O_4$
$D_{calc.}$/ g cm^{-3}	1.415
μ/mm^{-1}	0.780
Formula weight	485.48
Color	orange
Shape	block
Size/mm^3	0.16×0.14×0.09
T/K	291(2)
Crystal system	monoclinic
Space group	$P2_1/n$
a/Å	9.27810(10)
b/Å	9.15590(10)
c/Å	26.8645(2)
β/°	93.0520(10)
V/Å^3	2278.89(4)
Z	4
Wavelength/Å	1.54184
Radiation type	Cu K_α (λ = 1.54184)
Θ_{min}/°	3.295
Θ_{max}/°	77.294
Measured reflections	29507
Independent reflections	4783
Reflections with I > 2(I)	3830
R_{int}	0.0522
Parameters	341
Restraints	0
Largest peak	0.232
Deepest hole	-0.307
GooF	1.073
wR_2 (all data)	0.1322
wR_2	0.1238
R_1 (all data)	0.0545
R_1	0.0449

Table S-5 Crystallographic and experimental data for single crystal of **4**

Empirical formula	$C_{23}H_{13}N_3O_2$

Formula weight	363.36
Temperature/K	100(2)
Crystal system	monoclinic
Space group	$P2_1/n$
a/Å	21.97397(18)
b/Å	6.78000(8)
c/Å	22.09565(19)
β/°	96.0991(8)
Volume/Å^3	3273.26(5)
Z	8
ρ_{calc}g/cm^3	1.475
μ/mm^{-1}	0.783
F(000)	1504.0
Crystal size/mm^3	0.26 × 0.13 × 0.08
Radiation	Cu $K\alpha$ (λ = 1.54184)
2θ range for data collection/°	5.392 to 154.744
Index ranges	$-27 \leq h \leq 26$, $-8 \leq k \leq 8$, $-27 \leq l \leq 27$
Reflections collected	42102
Independent reflections	6860 [R_{int} = 0.0437, R_{sigma} = 0.0325]
Data/restraints/parameters	6860/0/514
Goodness-of-fit on F^2	1.050
Final R indexes [I>=2σ (I)]	R_1 = 0.0409, wR_2 = 0.1146
Final R indexes [all data]	R_1 = 0.0457, wR_2 = 0.1193
Largest diff. peak/hole / e Å^{-3}	0.29/-0.28

Table S-6 Crystallographic and experimental data for co-crystal of **4** and trimesic acid

Empirical formula	$C_{61}H_{46}N_6O_{13}$
Formula weight	1071.04
Temperature/K	100(2)
Crystal system	triclinic
Space group	P-1
a/Å	7.87677(11)
b/Å	15.1110(3)
c/Å	22.6336(3)
α/°	70.7760(15)
β/°	80.7734(12)
γ/°	75.8511(14)
Volume/Å^3	2457.21(7)
Z	2

ρ_{calc}g/cm^3	1.448
μ/mm^{-1}	0.855
F(000)	1116.0
Crystal size/mm^3	0.238 × 0.193 × 0.037
Radiation	Cu *K*α (λ = 1.54184)
2θ range for data collection/°	4.15 to 154.702
Index ranges	$-9 \leq h \leq 9$, $-18 \leq k \leq 19$, $-28 \leq l \leq 28$
Reflections collected	48246
Independent reflections	10239 [R_{int} = 0.0607, R_{sigma} = 0.0441]
Data/restraints/parameters	10239/1/753
Goodness-of-fit on F^2	1.043
Final *R* indexes [*I*>=2σ (I)]	R_1 = 0.0561, wR_2 = 0.1497
Final *R* indexes [all data]	R_1 = 0.0624, wR_2 = 0.1550
Largest diff. peak/hole / e Å^{-3}	0.35/-0.34